KTH Engineering Sciences

Boundary integral methods for Stokes flow: Quadrature techniques and fast Ewald methods

OANA MARIN

PhD Thesis
Stockholm, Sweden, 2012

TRITA-NA 2012:14
ISSN-0348-2952
KTH/NA/–12/14–SE
ISBN 978-91-7501-578-1

KTH School of Engineering Sciences
SE-100 44 Stockholm
SWEDEN

Akademisk avhandling som med tillstånd av Kungl Tekniska högskolan framlägges till offentlig granskning för avläggande av teknologie doktorsexamen fredagen den 14:e december 2012 klockan 10.15 i D2, Lindstedtsvägen 5, KTH, Stockholm.

Abstract

Fluid phenomena dominated by viscous effects can, in many cases, be modeled by the Stokes equations. The boundary integral form of the Stokes equations reduces the number of degrees of freedom in a numerical discretization by reformulating the three-dimensional problem to two-dimensional integral equations to be discretized over the boundaries of the domain. Hence for the study of objects immersed in a fluid, such as drops or elastic/solid particles, integral equations are to be discretized over the surfaces of these objects only. As outer boundaries or confinements are added these must also be included in the formulation.

An inherent difficulty in the numerical treatment of boundary integrals for Stokes flow is the integration of the singular fundamental solution of the Stokes equations, *e.g.* the so called Stokeslet. To alleviate this problem we developed a set of high-order quadrature rules for the numerical integration of the Stokeslet over a flat surface. Such a quadrature rule was first designed for singularities of the type $1/|\mathbf{x}|$. To assess the convergence properties of this quadrature rule a theoretical analysis has been performed. The slightly more complicated singularity of the Stokeslet required certain modifications of the integration rule developed for $1/|\mathbf{x}|$. An extension of this type of quadrature rule to a cylindrical surface is also developed. These quadrature rules are tested also on physical problems that have an analytic solution in the literature.

Another difficulty associated with boundary integral problems is introduced by periodic boundary conditions. For a set of particles in a periodic domain periodicity is imposed by requiring that the motion of each particle has an added contribution from all periodic images of all particles all the way up to infinity. This leads to an infinite sum which is not absolutely convergent, and an additional physical constraint which removes the divergence needs to be imposed. The sum is decomposed into two fast converging sums, one that handles the short range interactions in real space and the other that sums up the long range interactions in Fourier space. Such decompositions are already available in the literature for kernels that are commonly used in boundary integral formulations. Here a decomposition in faster decaying sums than the ones present in the literature is derived for the periodic kernel of the stress tensor.

However the computational complexity of the sums, regardless of the decomposition they stem from, is $\mathcal{O}(N^2)$. This complexity can be lowered using a fast summation method as we introduced here for simulating a sedimenting fiber suspension. The fast summation method was initially designed for point particles, which could be used for fibers discretized numerically almost without any changes. However, when two fibers are very close to each other, analytical integration is used to eliminate numerical inaccuracies due to the nearly singular behavior of the kernel and the real space part in the fast summation method was modified to allow for this analytical treatment. The method we have developed for sedimenting fiber suspensions allows for simulations in large periodic domains and we have performed a set of such simulations at a larger scale (larger domain/more fibers) than previously feasible.

To Philipp

Contents

Part I

Introductory chapters

Chapter 1

Introduction

Integral equations, ever since they were introduced by Abel 1823 [1], have been widely studied by mathematicians and engineers alike. An integral equation corresponds to a differential equation reformulated as the convolution of a kernel, a so-called Green's function, with a force density of equal magnitude as the forcing term of the underlying differential equation [19]. The Green's function is specific to the differential operator and in some situations it even bears a name which hints to the equation it is associated with, *e.g.* the kernel of the Stokes equations is often called a *Stokeslet*, name which was coined by Hancock [29]. Only after the independent proofs provided by Ehrenpreis [21, 22] and Malgrange [51] it became clear that only the limited class of differential operators with constant coefficients admits a representation in terms of a Green's function. An integral equation has the advantage that it reduces a partial differential equation stated in a three-dimensional domain to an integral expressed over two-dimensional surfaces. In general, regardless of the dimension of the initial problem the boundary integral equation is defined on a manifold of co-dimension one. Another aspect that favors integral equations is that problems over infinite domains can be studied with ease in integral form. In the field of fluid dynamics, however, only particular types of flows are governed by linear equations that can be transformed into integral equations, namely irrotational and inviscid potential flow and highly viscous flow (Stokes flow).

We shall focus on problems that are modeled by the Stokes equations and give a brief background on integral equations as applied to viscous flow. The applications that make use of the boundary integral form range from blood cells in Stokes flow [66] to the motion of microorganisms [35]. In general multiple bodies immersed in a viscous flow can be simulated with less difficulty by stating the system of equations in integral form than by solving the differential equations with the aid of *e.g.* grid based methods with moving meshes. Characteristic to boundary integral equations is the description of physical quantities such as velocity or pressure in terms of integrals over smooth distributions of forces multiplying specific kernels. These kernels, or fundamental solutions, depend on the physical quantity they are associated with but also on the geometry of the domain. Hence we may have free-space kernels or *e.g.* half-space kernels which assume that the observation field is bounded by an infinite wall. The method of images is a technique used to obtain a modified fundamental solution which accounts for certain boundaries that confine the flow, see Blake [8]. This approach however is amenable only for confinements with a simple geometry and only allows for a no-slip boundary condition.

Large scale simulations of particles immersed in a Stokesian flow are usually performed in periodic domains to reproduce phenomena matching those provided by experimental work.

In the field of boundary integrals periodicity is imposed by requiring that the particle motion in the primary computational cell is identical in all other cells periodically replicated all the way up to infinity. To this end all periodic images of all particles have an added contribution to the motion of the particles in the periodic domain under consideration. Mathematically this translates into an infinite sum which has to be truncated in numerical computations. This however is not straight-forward since the sum is not absolutely convergent. To alleviate this inconvenience additional suitable physical constraints have to be imposed on the system, *e.g.* zero mean flow for the Stokes equations. The method of choice to speed-up the convergence of the aforementioned infinite sum over all periodic images is the Ewald technique [24] of decomposing the sum such that the short range interactions are summed up in real space and the long range ones in Fourier space. The Ewald decomposition thus leads to two sums both of computational complexity $\mathcal{O}(N^2)$, where N is the number of particles in the periodic domain. By introducing a fast summation method, *e.g.* Spectral Ewald [47] or Smooth Particle Mesh Ewald [23] the complexity can be reduced to $\mathcal{O}(N \log N)$.

The purpose of this thesis is to address certain issues pertaining to the numerical integration of specific singular functions and the treatment of periodicity in the framework of boundary integrals. In the first part of this thesis we introduce the Stokes equations with their corresponding integral formulation and describe the fundamental solutions of Stokes flow, *e.g.* the Stokeslet and the Stresslet. Subsequently we illustrate how to apply the boundary integral equation to a series of problems that are modeled by the Stokes equations. Further we describe how to approximate numerically an integral equation and give a brief overview of the existing discretization and numerical integration techniques. Another chapter is dedicated to a discussion on confinements and how they are approximated in the boundary integral set-up. Moving on to the treatment of periodicity in the boundary integral framework the classical decomposition by Ewald of the kernel of the Laplace equations is being derived. Thereon several decomposition techniques for the kernel of the Stokes flow are being presented. The introductory part of this thesis is concluded with a chapter on fast summation methods, here with special focus on the Spectral Ewald.

The second part of this thesis contains five manuscripts which present more detailed studies of numerical integration of singularities and treatments of periodic boundary conditions. The first paper treats the development of a set of quadrature rules that handle singular functions of the type $1/|\mathbf{x}|$ in two dimensions and $1/|x|^\gamma$ with $\gamma < 1$ in one dimension. The type of quadrature rules we consider here are specific to the singularity they have been developed for. Our paper presents a theoretical study of the accuracy of such quadrature rules.

The second paper applies the concepts of the quadrature rules developed for a $1/|\mathbf{x}|$ singularity to the singular fundamental solution of Stokes flow. This quadrature rule is validated against the physical problem of a sphere sedimenting towards a flat plate due to gravity.

The third manuscript applies the Spectral Ewald method coupled with the Linked Cell List to perform large scale simulations of fibers submersed in Stokes flow. The fiber-fiber interaction is modeled using the slender body theory and the emerging system of integral equations is treated using a hybrid analytical-numerical approach. Analytical integration is not generally possible, however for fibers in near vicinity of each other it can be applied to a term of the real space sum. This procedure requires the adaptation of the entire real space sum treatment. The remaining part of the system is integrated numerically using a convenient quadrature rule.

The fourth manuscript deals with the periodic treatment of the fundamental solution of the stress kernel, *i.e.* the Stresslet. The Stresslet has so far been periodized based on the decomposition provided by Beenakker [7]. However we were able to derive a new decomposition starting from a decomposition by Hasimoto [31] which yields faster converging sums in both real and Fourier space.

The last article reverts back to the numerical integration of singularities, it is a first step towards extending the work in the first and second paper over a flat surface to a general parameterizable surface. The focus is mainly on integrating across cylindrical surfaces and is restricted to obtaining third order accuracy, as opposed to the higher-order methods obtained in Papers I and II.

Chapter 2

Stokes flow

The motion of a Newtonian fluid can be accurately modeled by the Navier–Stokes equations which in their incompressible form are given as

$$\begin{aligned} \rho\frac{\partial \mathbf{u}}{\partial t} + \rho\mathbf{u}\cdot\nabla\mathbf{u} &= -\nabla p + \mu\Delta\mathbf{u} + \rho\mathbf{f} \ , \quad \text{in} \quad \Omega \ , \\ \nabla\cdot\mathbf{u} &= 0 \ . \end{aligned} \tag{2.1}$$

Here $\mathbf{u}$ denotes the flow velocity vector, p the pressure, ρ the density of the fluid, ν the kinematic viscosity, while $\mathbf{f}$ is a volume force. The viscosity is assumed to be constant. The equations can be non-dimensionalized by using a reference velocity U and length scale L, $\cdot^*$ denotes dimensionless quantities

$$\mathbf{x}^* = \frac{\mathbf{x}}{L} \ , \quad \mathbf{u}^* = \frac{\mathbf{u}}{U} \ , \quad t^* = t\frac{U}{L} \ , \quad p^* = \frac{pL}{\mu U} \ .$$

With this change of variables and a subsequent multiplication of the equations by $L^2/(U\mu)$ we obtain

$$\begin{aligned} \frac{\rho U L^2}{\mu L}\frac{\partial \mathbf{u}^*}{\partial t^*} + \frac{\rho U L}{\mu}\mathbf{u}^*\cdot\nabla\mathbf{u}^* &= -\nabla p^* + \Delta\mathbf{u}^* + \frac{\rho L^2}{U\mu}\mathbf{f} \ , \quad \text{in} \quad \Omega \ , \\ \nabla\cdot\mathbf{u}^* &= 0 \ . \end{aligned} \tag{2.2}$$

By denoting the time scale of the flow $T = L/U$ and using $\nu = \mu/\rho$ together with the following non-dimensional numbers

$$\beta = \frac{L^2}{\nu T} \ , \quad Re = \frac{UL}{\nu} \ , \quad Fr = \frac{U}{\sqrt{gL}} \ ,$$

we obtain the non-dimensional form

$$\begin{aligned} \beta\frac{\partial \mathbf{u}^*}{\partial t^*} + Re\mathbf{u}^*\cdot\nabla\mathbf{u}^* &= -\nabla p^* + \Delta\mathbf{u}^* + \frac{Re}{Fr^2}\frac{\mathbf{f}}{f} \ , \quad \text{in} \quad \Omega \ , \\ \nabla\cdot\mathbf{u}^* &= 0 \ . \end{aligned} \tag{2.3}$$

where $f = |\mathbf{f}|$, Re is the Reynolds number, β the Stokes number and Fr the Froude number. If both $\beta \ll 1$ and $Re \ll 1$ the terms on the left-hand side vanish and the incompressible Navier–Stokes equations simplify to the linear Stokes equations which by reverting to dimensional variables can be written

$$\begin{aligned} \nabla p - \mu \Delta \mathbf{u} &= \mathbf{f}\ , \quad \text{in} \quad \Omega\ , \\ \nabla \cdot \mathbf{u} &= 0\ . \end{aligned} \tag{2.4}$$

The Stokes equations are linear with constant coefficients. Such partial differential equations are easier to solve both mathematically and numerically compared to the Navier–Stokes equations. Furthermore they can be rewritten as integral equations over the boundaries present in the physical problem at hand. This reduces the dimensionality of the problem, *e.g.* instead of discretizing an entire volume it is sufficient to treat numerically only the boundaries. Such a boundary integral formulation of Stokes flow lies at the basis of the studies presented in this thesis, and will be discussed in more detail in the sections to follow.

2.1 Fundamental solutions of Stokes flow

The fundamental solutions of the Stokes flow have various expressions according to the dimension of the space in which they are derived. A two-dimensional fundamental solution of the Stokes flow is of logarithmic type while the three-dimensional one is of the type $1/r$, with r being the inter-particle distance. Since the present work concerns only three-dimensional problems we restrict the presentation of the fundamental solutions of Stokes flow only to this dimensionality. The kernels differ also according to whether they represent a free-space solution or certain boundaries present in the problem are already embedded in the kernel as will be seen in Section 5.1. To start with we discuss only the free-space Green's functions and for this reason the subscript 0 is used.

Consider a point force of magnitude $\mathbf{f}$ located at $\mathbf{x}$ within a highly viscous flow. This corresponds mathematically to the Stokes equations (2.4) with the right-hand side given in terms of the Dirac delta function as $\mathbf{f}\delta(\mathbf{x}-\mathbf{x}_0)$. The velocity $\mathbf{u}$, pressure p or stress $\boldsymbol{\tau}$ at an observation point $\mathbf{x}_0$ can be computed as functions of the relative distance to the point force $\mathbf{f}$ as follows

$$u_i(x_0) = \frac{1}{8\pi\mu} G_{0,ij}(\mathbf{x}-\mathbf{x}_0) f_j\ , \tag{2.5}$$

where

$$G_{0,ij}(\mathbf{x}-\mathbf{x_0}) = \frac{\delta_{ij}}{|\hat{\mathbf{x}}|} + \frac{\hat{x}_i \hat{x}_j}{|\hat{\mathbf{x}}|^3}\ , \tag{2.6}$$

with $\hat{\mathbf{x}} = \mathbf{x} - \mathbf{x_0}$ and δ_{ij} the Kronecker delta. Written in tensor notation we have

$$\mathbf{G}_0(\mathbf{x}-\mathbf{x_0}) = \frac{\mathbf{I}}{|\hat{\mathbf{x}}|} + \frac{\hat{\mathbf{x}} \otimes \hat{\mathbf{x}}}{|\hat{\mathbf{x}}|^3}\ , \tag{2.7}$$

with the outer product $\hat{\mathbf{x}} \otimes \hat{\mathbf{x}}$ and he identity matrix $\mathbf{I}$ t. The fundamental solution $\mathbf{G}_0$ is also known as the Stokeslet, term coined by Hancock [29]. It is important to notice that if the points $\mathbf{x}$ and $\mathbf{x}_0$ coincide the Stokeslet is singular.

In a similar fashion the pressure can be expressed as

$$p(\mathbf{x}_0) = \frac{1}{8\pi} P_{0,j}(\mathbf{x}-\mathbf{x}_0) f_j\ , \tag{2.8}$$

with the fundamental solution

$$\mathbf{P}_0(\mathbf{x}-\mathbf{x_0}) = 2\frac{\hat{\mathbf{x}}}{|\hat{\mathbf{x}}|^3}\ . \tag{2.9}$$

The stress tensor $\boldsymbol{\tau}$ can be expressed in terms of the Stresslet, $\mathbf{T}_0$, as

$$\tau_{ik}(\mathbf{x}_0) = \frac{1}{8\pi} T_{0,ijk}(\mathbf{x} - \mathbf{x}_0) f_j \ , \tag{2.10}$$

with

$$\mathbf{T}_0(\mathbf{x} - \mathbf{x_0}) = -6 \frac{\hat{\mathbf{x}}\hat{\mathbf{x}}\hat{\mathbf{x}}}{|\hat{\mathbf{x}}|^5} \ . \tag{2.11}$$

Using these fundamental solutions we can state integral equations for Stokes flow as will be discussed in the next section. However, one may encounter also high-order derivatives of these solutions in integral formulations of a more advanced nature, details can be found in Pozrikidis [55]. In this thesis we shall use only the Dipole, the Laplacian of the Stokeslet, which appears in the expressions of slender body theory, see Section 3.2.

Vector calculus derivation of the Stokeslet

To give some more background to what will follow we will demonstrate here how to obtain the Stokeslet starting from the Stokes equations stated as partial differential equations. Several derivations of the Stokeslet can be found in textbooks, such as the derivation using Fourier transforms in [55] and also the derivation using the vector calculus approach. However the proof based on vector calculus in [55] is quite terse and a more detailed description is provided here.

In order to find the fundamental solution to (2.4) we consider a single point force located at $\mathbf{x}_0$ of magnitude $\mathbf{f}_0$ and rewrite

$$\begin{aligned} \nabla p - \mu \Delta \mathbf{u} &= \mathbf{f}_0 \delta(\mathbf{x} - \mathbf{x}_0) \ , \quad \text{in} \quad \Omega \ , \\ \nabla \cdot \mathbf{u} &= 0 \ . \end{aligned} \tag{2.12}$$

where δ is the three-dimensional Dirac delta function.

We denote $\Delta \mathbf{G} = \delta(\mathbf{x} - \mathbf{x}_0)$ and set $\Delta \mathbf{H} = \mathbf{G}$. By using this change of variables we identify $\mathbf{G}$ to be the fundamental solution of the Laplace equation, and $\mathbf{H}$ the solution of the biharmonic equation $\Delta\Delta\mathbf{H} = \delta(\mathbf{x} - \mathbf{x}_0)$.

As a first step we take the divergence of (2.12) and use the fact that the Laplacian and the divergence operator commute. If we apply the identity $\nabla \cdot (\mathbf{a}b) = b\nabla \cdot \mathbf{a} + \mathbf{a} \cdot \nabla b$ to $\nabla \mathbf{f}_0 \delta$ (in distribution sense) we obtain

$$\Delta p = \mathbf{f}_0 \nabla \delta \ ,$$

which ultimately leads to

$$p = \mathbf{f}_0 \cdot \nabla \mathbf{G} \ . \tag{2.13}$$

By substituting (2.13) in (2.12) a new relation is obtained

$$\mu \mathbf{u} = \mathbf{f}_0 (\nabla\nabla - \mathbf{I}\Delta) \mathbf{H} \ . \tag{2.14}$$

This enables us to find an expression for $\mathbf{u}$ if $\mathbf{H}$ is known. It remains to solve the biharmonic equation for a point force located at $\mathbf{x}_0$

$$\Delta\Delta\mathbf{H} = \delta$$

To expedite the derivation we consider the fundamental solution of the Laplace equation to be known, *i.e.* $1/4\pi r$, where $r = |\mathbf{x}|$. If such a solution was not known it may be quickly obtained in the same manner in which we shall compute $\mathbf{H}$. To find $\mathbf{H}$ such that $\Delta\mathbf{H} = 1/(4\pi r)$ we express the Laplacian in spherical coordinates

$$\Delta H = \mathbf{H}_{rr} + \frac{\mathbf{H}}{r} + \frac{1}{r^2\sin(\theta)}(\sin\theta\mathbf{H}_\theta)_\theta + \frac{1}{r^2\sin^2\theta}\mathbf{H}_{\phi\phi} \ , \tag{2.15}$$

Since ΔH is radial the terms exhibiting an angle dependency may be dropped leaving us with an ordinary differential equation

$$H''(r) + \frac{2}{r}H'(r) = \frac{1}{4\pi r} \ ,$$

which can be rewritten as

$$\frac{1}{r^2}(r^2H'(r))' = \frac{1}{4\pi r} \ . \tag{2.16}$$

We solve this for $H(0) = 0$ and obtain $H(r) = r/(8\pi)$. Returning to (2.14) we have

$$\mathbf{u}(\mathbf{x}) = \frac{1}{8\pi\mu}\mathbf{f}_0(\nabla\nabla - \mathbf{I}\Delta)r \ , \tag{2.17}$$

which provides us with

$$\mathbf{u}(\mathbf{x}) = \frac{1}{8\pi\mu}\mathbf{f}_0\left(\frac{\delta_{ij}}{|\hat{\mathbf{x}}|} + \frac{\hat{x}_i\hat{x}_j}{|\hat{\mathbf{x}}|^3}\right) \ . \tag{2.18}$$

The derivation is concluded by noting that this expression is identical to (2.5).

2.2 Boundary integral equations

Consider an immersed object with surface S and a force distribution $\mathbf{f}$ over the surface. A set of derivations based on the Lorentz reciprocal theorem, to be found in [55], yields an expression for the velocity at a point $\mathbf{x}_0$

$$\begin{aligned} u_j(\mathbf{x}_0) = &-\frac{1}{8\pi\mu}\int_S f_i(\mathbf{x})G_{0,ij}(\mathbf{x}-\mathbf{x}_0)\mathrm{d}S_{\mathbf{x}} \\ &+\frac{1}{8\pi}\int_S u_i(\mathbf{x})T_{0,ijk}(\mathbf{x}-\mathbf{x}_0)n_k(\mathbf{x})\mathrm{d}S_{\mathbf{x}} \ . \end{aligned} \tag{2.19}$$

The first term on the right-hand side is called the *single-layer potential* and the second term *double-layer potential.* The double layer potential will have a different limiting value as we let $\mathbf{x}_0$ approach the surface S either from the inside or outside. Introducing $\psi(\mathbf{x}_0)$ to denote the double layer integral in (2.19) we have

$$\lim_{\epsilon\to 0}\psi(\mathbf{x}_0 \pm \epsilon\mathbf{n}(\mathbf{x}_0)) = \pm 4\pi u_j + \int_S^{PV} u_iT_{0,ijk}n_k\mathrm{d}S_{\mathbf{x}} \ , \tag{2.20}$$

where the principal value (PV) is defined as the improper integral when $\mathbf{x}_0$ on S. Equation (2.19) can be further simplified to obtain simpler formulations, also called indirect boundary integral representations. The single-layer formulation for Stokes flow reads

$$u_i(\mathbf{x}_0) = \frac{1}{8\pi\mu}\int_S G_{0,ij}(\mathbf{x}-\mathbf{x}_0)f_j(\mathbf{x})\mathrm{d}S_{\mathbf{x}} \ , \tag{2.21}$$

and is valid for any $\mathbf{x}_0$ on S, or away from S. This formulation can represent successfully flows that are internal as well as external to the domain S. A disadvantage of the single-layer representation, which is in fact a Fredholm equation of the first kind, is that it is ill-conditioned. This formulation nevertheless is still widely used [30] despite its ill-conditioning. The same formulation is employed extensively in Paper II of this manuscript were we also derive a highly accurate quadrature for the single layer formulation for the Stokes flow over a flat plate.

From (2.19) a second formulation, called the double-layer formulation, can be derived to be

$$u_j(\mathbf{x}_0) = \frac{1}{8\pi} \int_S q_i(\mathbf{x}) T_{0,ijk}(\mathbf{x} - \mathbf{x}_0) n_k(\mathbf{x}) \mathrm{d}S_{\mathbf{x}} \ , \tag{2.22}$$

where $\mathbf{n}(\mathbf{x})$ is the outward normal to S. Again using (2.20) the equation for $\mathbf{x}_0 \in S$ is obtained. As stated here this representation is not complete. It can be shown by eigenvalue analysis that the double-layer potential is not capable of representing an arbitrary external flow, see Pozrikidis [55]. However the double-layer potential can be applied to model flows external to torque-free and force-free bodies, for other fluid phenomena the double layer can be regularized as explained in [55]. With proper modification the double-layer formulation is well suited to model also flows external to immersed bodies such as sedimenting particles [40] or clusters of spheres in elasticity problems [54]. The double layer formulation however, as compared to the single layer formulation is well conditioned.

Similar integral equations can be written for the pressure and for the stress. We refer the reader for more details concerning integral equations for Stokes flow to Pozrikidis [55]. A comparison of the limitations and advantages of various direct or indirect boundary integral formulations is available in [37]. The expressions (2.19)–(2.22) listed here to describe the flow can be used to model various multiphase flow problems as will be presented in Chapter 3.

Chapter 3

Integral formulations for particulate flows

Boundary integral formulations hold a great advantage over other methods of simulating particulate flows since the equations are stated only over the surfaces of the particles. In other words the size of the problem to be discretized does not depend on the size of the computational domain but only on the surfaces of the particles. This reduces the dimensionality of the discrete problem in numerical simulations while maintaining a controllable accuracy. Particles can be tracked in a Lagrangian fashion independent of the computational domain. In the current chapter we introduce a set of boundary integral models used in simulating particulate flows in a Stokesian regime.

3.1 Solid particles

Assume a single solid body immersed in a Stokesian fluid. Over the body surface S we consider a distribution of forces $\mathbf{f}$. The velocity field $\mathbf{u}$ at some point $\mathbf{x}_0$ in the fluid or on the body surface can be computed using the single-layer formulation as

$$\mathbf{u}(\mathbf{x_0}) = \frac{1}{8\pi\mu}\int_S \mathbf{G_0}(\mathbf{x}-\mathbf{x_0})\mathbf{f}(\mathbf{x})\mathrm{d}S_{\mathbf{x}} \ . \tag{3.1}$$

We are interested in computing either the impact of a moving particle on the surrounding fluid or the behavior of a particle subject to an imposed background flow or a given external force. The same type of boundary integral formulation can address both problems. Since we considered a solid particle we must require that the rigid body equation of motion is obeyed, *i.e.*

$$\mathbf{u}(\mathbf{x_0}) = \mathbf{V} + \mathbf{\Omega} \times (\mathbf{x_0} - \mathbf{x_c}),\ \mathbf{x}_0 \in S \ , \tag{3.2}$$

where $\mathbf{x}_c$ is the center of mass of the object, $\mathbf{V}$ and $\mathbf{\Omega}$ represent the translational and angular velocity. A no-slip boundary condition yields that for $\mathbf{x}_0 \in S$ both (3.1) and (3.2) have to be simultaneously satisfied, *i.e.*

$$\mathbf{V} + \mathbf{\Omega} \times (\mathbf{x_0} - \mathbf{x_c}) = \frac{1}{8\pi\mu}\int_S \mathbf{G_0}(\mathbf{x}-\mathbf{x_0})\mathbf{f}(\mathbf{x})\mathrm{d}S_{\mathbf{x}} \ . \tag{3.3}$$

Let us assume that the solid particle is subject to gravity and we intend to compute the flow as the particle sediments. Then we have two extra conditions: i) the total integrated force over the surface of the solid particle must balance the buoyancy force and, ii) no torques are applied to the particle, *i.e.*

$$\begin{aligned}\mathbf{F} &= \int_S \mathbf{f}(\mathbf{x})\mathrm{d}S_{\mathbf{x}} = \Delta\rho V g \mathbf{e_g} \;, \qquad (3.4)\\ \mathbf{L} &= \int_S (\mathbf{x}-\mathbf{x}_c)\times\mathbf{f}(\mathbf{x})\mathrm{d}S_{\mathbf{x}} = 0 \;.\end{aligned}$$

Here $\Delta\rho$ denotes the density difference, V volume of the object and $g\mathbf{e_g}$ the gravitational acceleration acting in the $\mathbf{e_g}$ direction.

In (3.3) the translation and angular velocities $\mathbf{V}$ and $\mathbf{\Omega}$ as well as the distribution of forces $\mathbf{f}$ are unknown. The constraints in (3.4) close the system. Naturally, different conditions on the integrated force and torque can be applied depending on the problem.

Consider now a neutrally buoyant particle immersed in a flow of velocity $\mathbf{u}_\infty$, *e.g.* a shear flow. By the superposition principle the correction due to the immersed particle is added to the background flow to yield the total velocity

$$\mathbf{u}(\mathbf{x_0}) = \mathbf{u}_\infty(\mathbf{x}_0) + \frac{1}{8\pi\mu}\int_S \mathbf{G_0}(\mathbf{x}-\mathbf{x_0})\mathbf{f}(\mathbf{x})\mathrm{d}S_{\mathbf{x}} \;. \qquad (3.5)$$

To solve for the distribution of forces constraints of the type (3.4) are required together with the no-slip boundary conditions. In this case we demand that the integrated force vanishes over the surface of the particle.

All these simple modeling principles can be applied to a wide class of solid particles ranging from spherical particles to fibers. We have used the same ideas as presented here to study a sphere sedimenting in an infinite or wall bounded flow, as it will be further discussed in Paper II.

3.2 Slender bodies

Bodies that have a slender or elongated shape admit an approximate boundary integral representation that is very efficient from the viewpoint of numerical simulations. In Fig. 3.1 we display such a body, a rotation ellipsoid of axes a, b, c with $b = c$. If the principal axes of the ellipsoid, b and a, are such that one is much longer than the other, $a/b \ll 1$, we call the ellipsoid a slender body. In this case it can be assumed that the disturbance flow due to the presence of the body is approximately the same as that due to a line distribution of fundamental solutions along its long axis, a. This concept and consequent derivations were reintroduced by Batchelor [6] following the work of Burgers [11]. Higher order approximations were provided by Keller and Rubinow [42] and Johnson [39]. Several extensions and applications of the slender body approximation have been used for fibers [14, 62], helical swimmers [35] and more recently for elongated drops [38]. The simulations of fiber suspensions performed in Paper III of this thesis rely also on the slender body theory and for this reason we describe here in greater length the guiding principles.

A slender body is characterized by the slenderness parameter $\epsilon = a/b \ll 1$, which is the ratio of its axes. If we consider the filament of a slender body of length L to be given by the parametrization $\mathbf{x}(s,t) = (x(s,t), y(s,t), z(s,t))$. Following Johnson [39] the velocity field is taken to be an integral over the centerline parametrized by s with $s \in [0, L]$ of a distribution $\mathbf{f}$ of Stokeslets $\mathbf{G}$ and a distribution $\mathbf{g}$ of Doublets $\mathbf{G}^D$. Thus the following ansatz is made

$$\mathbf{u}(\mathbf{x}_0) = \mathbf{u}_\infty(\mathbf{x}_0) + \frac{1}{8\pi\mu}\int_0^L \mathbf{f}(s)\mathbf{G}(\mathbf{x}(s)-\mathbf{x}_0) + \mathbf{g}(s)\mathbf{G}^D(\mathbf{x}(s)-\mathbf{x}_0))\mathrm{d}s \;, \qquad (3.6)$$

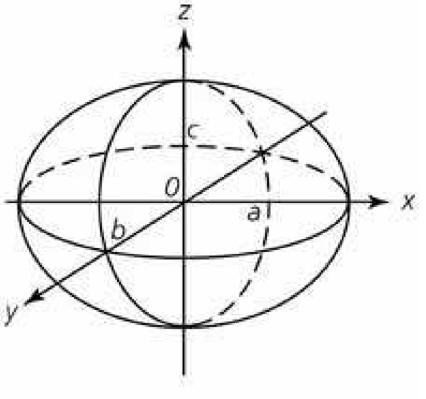

Figure 3.1: Sketch of an ellipsoid. If $b/a \ll 1$ this can be assumed to be a slender body.

with

$$\begin{aligned} G_{ij}(\hat{\mathbf{x}}) &= \frac{\delta_{ij}}{|\hat{\mathbf{x}}|} + \frac{\hat{x}_i \hat{x}_j}{|\hat{\mathbf{x}}|^3} , \\ G^D_{ij}(\hat{\mathbf{x}}) &= \frac{\delta_{ij}}{|\hat{\mathbf{x}}|^3} - 3\frac{\hat{x}_i \hat{x}_j}{|\hat{\mathbf{x}}|^5} , \end{aligned}$$

where $\hat{\mathbf{x}} = \mathbf{x}(s) - \mathbf{x}_0$.

In order to obtain a unified expression for the distribution of point forces $\mathbf{f}$ and $\mathbf{g}$ the technique of matched asymptotic expansions is used. Without any technical details we outline the steps as described by Götz [26] :

I. Construct an outer expansion of the ansatz as a power series of ϵ, for points parametrized by t away from s, $|t - s| \gg \epsilon$.

II. Obtain an inner expansion in terms of the slenderness parameter ϵ, for points close to s.

III. Match the two expansion using the principle *"Outer limit of the inner expansion = Inner limit of the outer expansion"*.

   This will yield a composite expansion where the common part of the inner and outer expansion that matches is removed.

IV. Apply boundary conditions (no-slip) on the slender body surface. Neglecting higher order terms in ϵ an expression is obtained which is $\mathcal{O}(\epsilon)$.

V. An integral equation depending on the parameter ϵ is obtained.

We can write a unified equation for a distribution of Stokeslets and Doublets of strength $\mathbf{f}$ across the centerline parametrized by s for $\mathbf{x}_0$ not on the filament of the slender body

$$\mathbf{u}(\mathbf{x}_0) = \mathbf{u}_\infty(\mathbf{x}_0) + \frac{1}{8\pi\mu} \int_0^L \left[\mathbf{G}(\mathbf{x}(s) - \mathbf{x}_0) + \frac{\epsilon^2}{2} \mathbf{G}^D(\mathbf{x}(s) - \mathbf{x}_0) \right] \mathbf{f}(s) \mathrm{d}s \ , \tag{3.7}$$

which coincides with (3.6) where we have set

$$\mathbf{g}(s) = \frac{\epsilon^2}{2} \mathbf{f}(s) \ .$$

This relationship between $\mathbf{f}$ and $\mathbf{g}$ is chosen such that the angular dependence which occurs in the composite expansion is eliminated. This is needed since the no-slip boundary condition on the slender body is only imposed along the centerline and does not take into account the cross section of the slender body.

For a point $\mathbf{x}$ point on the filament the velocity is given as

$$\mathbf{u}(\mathbf{x}) = \frac{\partial \mathbf{x}(s,t)}{\partial t} = \mathbf{u}_\infty(\mathbf{x}) + \frac{1}{8\pi\mu}(-\Delta[\mathbf{f}](s) - K[\mathbf{f}](s)) \ , \tag{3.8}$$

where $\mathbf{f}$ is a force per unit length on the filament. The operators Δ and K are defined as follows

$$\Delta[\mathbf{f}](s) = [-c(\mathbf{I} + \hat{\mathbf{s}}(s)\hat{\mathbf{s}}(s)) + 2(\mathbf{I} - \hat{\mathbf{s}}(s)\hat{\mathbf{s}}(s))]\mathbf{f}(s) \tag{3.9}$$

where $\hat{\mathbf{s}} = \frac{\partial \mathbf{x}(s,t)}{\partial s}$ and $c = \log(\epsilon^2 \mathrm{e})$ and

$$K[\mathbf{f}](s) = \int_0^L \left(\frac{\mathbf{I} + \hat{\mathbf{R}}(s,s')\hat{\mathbf{R}}(s,s')}{|\mathbf{R}(s,s')|}\mathbf{f}(s') - \frac{\mathbf{I} + \hat{\mathbf{s}}(s)\hat{\mathbf{s}}(s)}{|s-s'|}\mathbf{f}(s) \right) \mathrm{d}s' \tag{3.10}$$

with $\mathbf{R}(s,s') = \mathbf{x}(s,t) - \mathbf{x}(s',t)$ for a certain t. The formulation in (3.8) is valid for a slender body of any shape which has the property that it does not re-approach itself. If however a particular slender body is considered, *i.e.* a rigid straight fiber then the operator K simplifies to

$$K[\mathbf{f}](s) = \int_0^L \frac{\mathbf{f}(s') - \mathbf{f}(s)}{|s-s'|} \mathrm{d}s' \ . \tag{3.11}$$

Details can be found in Tornberg and Shelley [63].

The slender body formulation (3.7) depends on the slenderness parameter ϵ and the velocity of the center-line is of order $\mathcal{O}(\epsilon^2 \log \epsilon)$ accurate. The fluid velocity at a point outside the slender body is of order $\mathcal{O}(\epsilon)$ accurate all the way up to the fiber surface.

If we now consider a set of N fibers with a distribution of forces $\mathbf{f}_l(s)$ along their filament, $l = 1, \ldots, N$. To compute the velocity at a point $\mathbf{x}_l(s)$ on the fiber the contribution from the fiber itself given by (3.8) is added to the contribution form all other fibers given by (3.7) yielding

$$\begin{aligned} \mathbf{u}(\mathbf{x}_l(s)) &= \mathbf{u}_\infty(\mathbf{x}_l(s)) + \frac{1}{8\pi\mu}(-\Delta[\mathbf{f}_l](s) - K[\mathbf{f}_l](s)) \\ &\quad + \frac{1}{8\pi\mu} \sum_{\substack{n=1 \\ n \neq l}}^{N} \int_0^L \mathbf{S}(\mathbf{x}_l(s) - \mathbf{x}_n(s))\mathbf{f}_n(s) \mathrm{d}s \ , \end{aligned}$$

where for $\mathbf{x} = \mathbf{x}_l(s) - \mathbf{x}_n(s)$ the total Green's function is given by

$$\mathbf{S}(\mathbf{x}) = \mathbf{G}(\mathbf{x}) + \frac{\epsilon^2}{2}\mathbf{G}^D(\mathbf{x}) \ .$$

This set of equations has been used in simulations of flexible and rigid fibers, see [62, 63]. The same formulation is used in Paper III in the present manuscript, in the context of large scale simulations of fiber suspensions.

Chapter 4

Numerical methods for integral equations

This chapter addresses aspects of the numerical treatment of integral equations. A common difficulty shared by most integral equations is the treatment of singular kernels. Several numerical integration methods that deal with such kernels have been developed over the years. In some cases it is possible to analytically integrate the isolated kernel, in other cases specially designed quadrature rules can be used to numerically evaluate the integral. Nonetheless the integration of singularities is still problem dependent and as such a rather difficult task.

In the context of numerical treatment of singular integrands we introduce our work on the development of quadrature rules tailored to specific singular kernels. This set of quadrature rules is developed in the framework of Nyström's method. In this chapter we provide only an overview of the method, theoretical details are given in Paper I and applications in Paper II and Paper V.

The most used classes of numerical methods are collocation methods [5, 43] from where emerge the boundary element method [56] and Nyström's method [18, 5]. The collocation method is based on the idea of enforcing the solution to be valid at a set of grid points. In the Boundary element method the solution to an integral equation is expressed as a linear combination of basis functions and the accuracy is given by the choice of basis functions. Nyström's method however requires no ansatz on the *shape* of the function as the integral equation is solved directly at the discrete grid points, *i.e.* the quadrature points and collocation points are the same.

The singularity of a boundary integral problem can be treated by using a quadrature rule which has been designed to handle this specific singularity, *e.g.* Gaussian quadrature rules as developed for one-dimensional problems in [61], ideas extended to the boundary integral set-up in [44]. Using Nyström's method in a two dimensional set-up [32] integrates the singular kernel using a Gauss-Legendre quadrature. In higher dimensions the Duffy quadrature [20] can be used to integrate the singularity over triangulated surfaces. Alternatively Bremer and Gimbutas [10] introduced a method which uses appropriately scaled functions to integrate weekly singular kernels over non-conformal surfaces.

4.1 Nyström's method

As a brief prerequisite to Nyström's method which shall be used in Papers I, II and V we provide two examples. Consider the one-dimensional integration

$$u(t) = \int_a^b G(t-s)f(s)\mathrm{d}s,\ t \in [a,\ b]\ , \tag{4.1}$$

By discretizing the segment $[a,\ b]$ at points s_i with $s_i \in [a,\ b]$ we can evaluate the above integral as

$$u(t) = \sum_{i=1}^{N+1} \frac{\Delta_{i-1}+\Delta_i}{2} G(t-s_i)f(s_i),\ t \in [a,\ b]\ . \tag{4.2}$$

In the higher dimensional case Nyström's method is most suitable for integrating surfaces that have a parametric representation. For example a sphere of radius R can be parametrized using spherical coordinates. The integral can then be written as

$$\int_S \mathbf{G}(\mathbf{x}-\mathbf{x}_0)\mathbf{f}(\mathbf{x})\mathrm{d}S_{\mathbf{x}} = \int_0^{\pi}\int_0^{2\pi} \mathbf{G}(\phi-\phi_0, \theta-\theta_0)\mathbf{f}(\phi,\theta)R^2\sin(\theta)\mathrm{d}\phi\mathrm{d}\theta\ . \tag{4.3}$$

This integral can be numerically evaluated by discretizing the angles ϕ and θ and subsequently using *e.g.* the trapezoidal rule. This example illustrates that in certain situations Nyström's method offers a simpler solution to the problem than the collocation method in terms of domain discretization and numerical integration. The actual integration of the singularity however has not been discussed yet. The singularity subtraction method may be employed as described in Paper II. In the same paper we develop a quadrature rule for integrating to high order the Stokeslet over flat surfaces. This is extended in Paper V to the curvilinear surface of a cylinder. Both quadratures rules are based on the corrected trapezoidal ruled which is analyzed theoretically in Paper I.

4.2 Corrected trapezoidal rules for singular kernels

A part of this thesis is concerned with the integration of kernels of the type $s(x) = |x|^{\gamma}$ with $\gamma > -1$ in one dimension and $s(\mathbf{x}) = |\mathbf{x}|^{-1}$ in two dimensions by using a specially designed quadrature rule in the framework of Nyström's method. The same approach to the numerical integration of singular but integrable kernels that we employ in Paper I was explored by Lyness [50] and later Kapur et al. [41]. They propose a quadrature which uses the trapezoidal rule wherever the integrand is non-singular, thus skipping the singular point. Close to the singularity a correction term is constructed to compensate for the omitted point. These ideas have been extended to singularities of the type $\log(|\mathbf{x}|)$ [2] or $1/|\mathbf{x}|$ in the three-dimensional space in [3], though their work lacks formal convergence proofs. Our work fills in this gap by proving for specific singular functions that the order of accuracy that can be observed in practice is also confirmed by theoretical analysis.

As a preview to Paper I we describe the designed quadrature rule without detailing the entire construction process. Assume we intend to numerically integrate the integral $\int_S f(\mathbf{x})s(\mathbf{x})\mathrm{d}\mathbf{x}$ where s defined as above is singular at the origin. As a first step we use the *punctured* trapezoidal rule, where the singular point is not included in the summation

$$T_h^0[f\cdot s] = \sum_{\boldsymbol{\beta}h\in S, \boldsymbol{\beta}\neq 0} h^d f(\boldsymbol{\beta}h)s(\boldsymbol{\beta}h) - \frac{1}{2}\sum_{\boldsymbol{\beta}h\in\partial S} h^d f(\boldsymbol{\beta}h)s(\boldsymbol{\beta}h). \tag{4.4}$$

Here $\boldsymbol{\beta} \in \mathbb{Z}^2$ and h is the interval in space given by the discretization of the domain, homogeneous in all directions. We shall construct a quadrature rule, Q_h^p which is applied to the integrand $f(\mathbf{x})s(\mathbf{x})$ in the following fashion

$$Q_h^p[f \cdot s] = T_h^0[f \cdot s] + A_h^p[f]. \tag{4.5}$$

with the correction operator given as

$$A_h^p[f] = a(h) \sum_{|\boldsymbol{\beta}| \leq p} \omega_{\boldsymbol{\beta}} f(\boldsymbol{\beta} h), \tag{4.6}$$

where $a(h)$ has a simple expression which depends on the singularity $s(\mathbf{x})$ and on the grid spacing h. In the two-dimensional framework with $s(\mathbf{x}) = 1/|\mathbf{x}|$ case $a(h) = h$. The correction provided by the operator A_h^p is a local correction, *i.e.* acting solely in a close vicinity of the singularity.

The main task in developing the rule Q_h^p is the computation of the weights $\omega_{\boldsymbol{\beta}}$. Note that in the correction operator A_h^p the weights $\omega_{\boldsymbol{\beta}}$ take the place of the singular function in every discrete point $\boldsymbol{\beta} h$ and that the correction operator spans a set of discrete points at a distance of maximum ph from the origin. The parameter p determines the number of weights $\omega_{\boldsymbol{\beta}}$ and ultimately determines the convergence order of the modified trapezoidal rule.

Details on the computation of the weights $\omega_{\boldsymbol{\beta}}$ are available in Paper I together with a theoretical analysis of the accuracy and existence of such modified trapezoidal rules. The set of rules developed for *e.g.* $1/|\mathbf{x}|$ are $\mathcal{O}(h^{2p+3})$ accurate and are available in Paper I up to $\mathcal{O}(h^{11})$. Furthermore in Paper I we provide an expression based on which we can directly compute the weights for the one-dimensional quadrature rules applied to $s(x) = |x|^\gamma$ for any $\gamma > -1$. The same type of method can be used to develop a set of high-order quadrature rules for the Stokeslet and the extension to the Stokeslet is presented in Paper II.

4.3 Modified quadrature rules for singular kernels over parameterizable surfaces

Modified quadrature rules can be extended also to curvilinear surfaces. In the two dimensional set-up Aguilar [2] devised a corrected trapezoidal rule for the logarithmic singularity over a circle, a curved line. In paper V in this thesis we show how to apply the principles of a modified quadrature rules to smooth parameterizable surfaces. Since the trapezoidal rule applies to multi-dimensional integrals using equidistant spacing it can only be extended to parameterizable surfaces defined on a hypercube. Here we are concerned solely with surfaces that arise in practice, surfaces which are typically mappings defined on a square domain, let us say $D = [0\ a_1] \times [0\ a_2]$.

Consider the integral

$$\int_D f(\mathbf{x}) \mathrm{d}D_{\mathbf{x}}$$

The trapezoidal rule applied to this integral reads

$$\int_D f(\mathbf{x}) \mathrm{d}\mathbf{x} \approx T_{\underline{h}}[f] = \sum_{i=0}^{N} \sum_{j=0}^{M} \mathcal{W}_i(h_1) \mathcal{W}_j(h_2) f(ih_1, jh_2)\ , \tag{4.7}$$

where $h_1 = a_1/N$ and $h_2 = a_2/M$ and the weights are defined as

$$\mathcal{W}(h) = [h/2,\ h, \ldots, h,\ h/2]\ .$$

The notation $\underline{h} = (h_1, h_2)$ as a subscript on T indicates that different spacing is assumed in the two spatial directions.

Consider a parametrization defined on D, *i.e.* a smooth mapping $\gamma : D \to S$ which takes points $\mathbf{x}$ such that $\gamma(\mathbf{x}) = \mathbf{y} \in S$. This leads to the integral

$$\int_D (f \circ \gamma)(\mathbf{x}) \left| \frac{\partial \gamma}{\partial x_1} \times \frac{\partial \gamma}{\partial x_2} \right| \mathrm{d}D_{\mathbf{x}} \ , \tag{4.8}$$

where $|\frac{\partial \gamma}{\partial x_1} \times \frac{\partial \gamma}{\partial x_2}|$ is the surface element that arises from the change of variables brought by the parametrization γ.

Let us define $\psi(\mathbf{x}) = (f \circ \gamma)(\mathbf{x})|\frac{\partial \gamma}{\partial x_1} \times \frac{\partial \gamma}{\partial x_2}|$. To this function the trapezoidal rule can be applied as above without any modifications. Assume now that we intend to compute for a point $\mathbf{y}_0 = \gamma(\mathbf{x}_0)$ the convolution $(s * f)(\mathbf{y}_0)$ over a surface S which is given by the mapping γ defined over the domain D, where s is a singular function. The corresponding integral can then be expressed as

$$\int\limits_S s(\mathbf{y} - \mathbf{y}_0) f(\mathbf{y}) \mathrm{d}S_{\mathbf{y}} = \int\limits_D s \circ (\gamma(\mathbf{x}) - \gamma(\mathbf{x}_0))(f \circ \gamma)(\mathbf{x}) \left| \frac{\partial \gamma}{\partial x_1} \times \frac{\partial \gamma}{\partial x_2} \right| \mathrm{d}D_{\mathbf{x}} \ , \tag{4.9}$$

To integrate singular functions defined over parameterizable surfaces we can devise a quadrature rule of the type (4.5) for $p = 0$ given as

$$Q^0_{\underline{h}}[(s \circ \gamma_{\mathbf{x}_0}) \cdot \psi] = T^0_{\underline{h}}[(s \circ \gamma_{\mathbf{x}_0}) \cdot \psi] + A^0_{\underline{h}}[\psi] \ , \tag{4.10}$$

where $T^0_{\underline{h}}$ is the punctured trapezoidal rule and we used the notation $\gamma_{\mathbf{x}_0}(\mathbf{x}) = \gamma(\mathbf{x}) - \gamma(\mathbf{x}_0)$ for the shift of the function γ by $\gamma(\mathbf{x}_0)$. The correction operator is then

$$A^0_{\underline{h}}[\psi] = a(\gamma(\underline{h}))\omega_0 \psi(\mathbf{x}_0) \ , \tag{4.11}$$

where $a(\gamma(\underline{h})) = |\gamma(\underline{h})|_2$ with $| \cdot |_2$ being the Euclidian norm.

Such quadrature rules will typically be generated by weights ω_0 which depend on the position of ω_0 on the surface S. In Paper V we identify the requirements on the parametrization such that we can devise a quadrature rule that yields a unique weight, *i.e.* independent on the position on the surface. From this class of surfaces the cylinder given by a parameterization in cylindrical coordinates has been selected and explicit quadrature rules were developed for various ratios h_1/h_2.

4.4 Other approaches to singular integrals – regularized kernels

So far we have regarded the exact integration of the singular kernel as being possible either analytically or by using special numerical techniques. It is worth mentioning that there is another type of approach namely to replace the singular kernel by a regularized kernel. This technique was developed and analyzed in [13]. The regularized Stokeslet which is the non-singular version of the Stokeslet takes the form

$$\mathbf{G}_\epsilon(\mathbf{x} - \mathbf{x_0}) = (|\hat{\mathbf{x}}|^2 + 2\epsilon^2) \frac{\mathbf{I}}{(|\hat{\mathbf{x}}|^2 + \epsilon^2)^{3/2}} + \frac{\hat{\mathbf{x}} \otimes \hat{\mathbf{x}}}{(|\hat{\mathbf{x}}|^2 + \epsilon^2)^{3/2}}, \tag{4.12}$$

where $\hat{\mathbf{x}} = \mathbf{x} - \mathbf{x_0}$ and ϵ is the regularization parameter. This is an approximation of the Stokeslet and is obtained by considering that the point force acting at $\mathbf{x}_0$ is in fact a smooth function which acts with maximum intensity in the point $\mathbf{x}_0$ and away from $\mathbf{x}_0$

decays smoothly. The role of ϵ is to *smoothen* the Stokeslet. This parameter is chosen to be fairly small but still not too small compared to the grid resolution in the discrete case. The regularization has an error of $\mathcal{O}(\epsilon)$ in a region of size $\mathcal{O}(\sqrt{\epsilon})$ that surrounds the boundaries. Further away from the boundaries the error is $\mathcal{O}(\epsilon^2)$.

Chapter 5

Boundaries in Stokes flow

The field of fluid dynamics amassed a significant block of studies pertaining to particle-particle interactions in Stokes flow. Experimentalists [53] and numerical analysts alike [9] have explored the intricate hydrodynamics of particles, fibers or drops in the attempt of achieving a better understanding of phenomena such as clustering or dispersion. The time evolution of a suspension exhibits different behavior when the mutual interactions between particles are left unhindered, as opposed to the case where constraints such as solid walls are introduced. We survey here the main approaches to wall modeling for Boundary Integral Equations.

A simple solid boundary such as a flat wall is introduced in the classical theory of boundary integrals by the method of images. This method served for a long time as the main tool for wall modeling in applications such as drop deformation in the vicinity of walls [65], or fiber alignment [12]. To begin with we shall present the basic principles of the method of images followed by a brief analysis of its limitations. Our work however is directed towards providing an alternative to this classical method of modeling solid walls. The approach we suggest involves a direct numerical treatment of the solid boundary. In the last section of this chapter we offer some details concerning our approach to confinement treatment which is further analyzed in Paper II. This wall treatment can be extended to slightly more complicated confinements and a first attempt of third order accuracy has been made to model cylindrical surfaces in Paper V.

5.1 Method of images

The method of images originated in the field of electrostatics. In order to calculate the distribution of the electric field of a charge in the vicinity of a conducting surface the mirror image with respect to a symmetry hyperplane is added. This is done in such a way that the tangential component of the electrical field to the surface of a conductor is zero and the field is uniquely defined by the normal component. In electrostatics the potential corresponding to a point charge at $\mathbf{x}_0$ is of the type $1/|\hat{\mathbf{x}}|$ which is similar in expression to a point force in Stokes flow which is $1/|\hat{\mathbf{x}}| + \hat{\mathbf{x}} \otimes \hat{\mathbf{x}}/|\hat{\mathbf{x}}|^3$, here $\hat{\mathbf{x}} = \mathbf{x} - \mathbf{x}_0$, with $\mathbf{x}$ being an observation point.

The seminal paper by Blake, [8], gives the recipe of applying the method of images to Stokes flow to obtain a modified fundamental solution. This fundamental solution contains implicitly the presence of a wall over which a no-slip boundary condition is imposed. Not all details are reproduced here but a short description of the derivation is needed in order to stress the advantages and also the limitations of the method of images.

To start with we consider a point force at $\mathbf{x}_0$ of some strength F, see Fig. 5.1 situated at a distance h from a flat wall given by $x_3 = 0$. The Stokeslet $\mathbf{G}$ for an observation point $\mathbf{x}$ is given as

$$G_{ij}(\mathbf{r}) = \frac{1}{8\pi\mu}\left(\frac{\delta_{ij}}{|\mathbf{r}|} + \frac{r_i r_j}{|\mathbf{r}|^3}\right) ,$$

where $\mathbf{r} = \mathbf{x} - \mathbf{x}_0$ as indicated in Fig. 5.1.

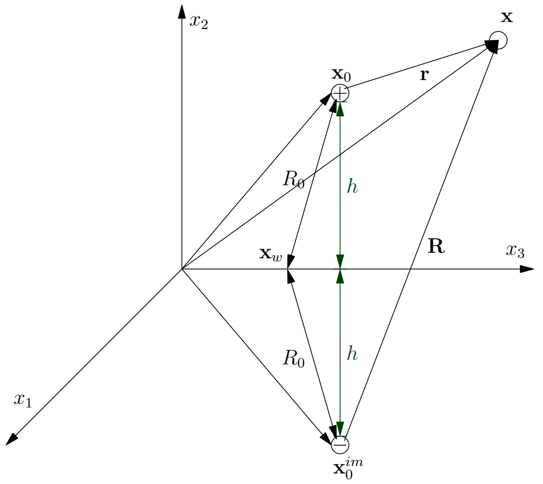

Figure 5.1: Point force at $\mathbf{x}_0$ and its mirror image $\mathbf{x}_0^{im}$.

The mirror image of the point $\mathbf{x}_0$ is taken to be $\mathbf{x}_0^{im}$ and is of negative strength $-F$. The contribution of the image point $\mathbf{x}_0^{im}$ yields a fundamental solution

$$G^{im}_{ij}(\mathbf{R}) = \frac{1}{8\pi\mu}\left(\frac{\delta_{ij}}{|\mathbf{R}|} + \frac{R_i R_j}{|\mathbf{R}|^3}\right) + \omega_{ij} ,$$

where $\mathbf{R} = \mathbf{x} - \mathbf{x}_0^{im}$ and ω_{ij} is a complementary solution which remains to be determined.

We may write the fundamental solution given by the Stokeslet and the mirror image as

$$G^w_{ij}(\mathbf{r}) = G_{ij}(\mathbf{r}) + G^{im}_{ij}(\mathbf{R}).$$

We require that at the wall we have a no-slip boundary condition, thus $G^w_{ij}(\tilde{\mathbf{r}}) = 0$ for $\mathbf{r} = \mathbf{x}_w - \mathbf{x}_0$ with $\mathbf{x}_w$ a point of the wall $x_3 = 0$, thus

$$G^{im}_{ij}(\mathbf{x}_w - \mathbf{x}_0^{im}) = -G_{ij}(\mathbf{x}_w - \mathbf{x}_0) . \tag{5.1}$$

From this we can determine ω_{ij} such that it satisfies the Stokes equations and also the boundary conditions over the wall surface. Finally we obtain an expression for $G^w_{ij}(\mathbf{r})$ in terms of a potential dipole $\mathbf{G}^D$ and a Stokeslet doublet $\mathbf{G}^{SD}$

$$G^w_{ij}(\mathbf{r}) = G_{ij}(\mathbf{r}) - G_{ij}(\mathbf{R}) + 2h^2 G^D_{ij}(\mathbf{R}) - 2h G^{SD}_{ij}(\mathbf{R}) .$$

where

$$\begin{aligned} G^D_{ij}(\mathbf{R}) &= \pm\left(\frac{\delta_{ij}}{|\mathbf{R}|^3} - 3\frac{R_i R_j}{|\mathbf{R}|^5}\right), \\ G^{SD}_{ij}(\mathbf{R}) &= R_3 G^D_{ij}(\mathbf{R}) \pm \frac{\delta_{j3}R_i - \delta_{i3}R_j}{|\mathbf{R}|^3}. \end{aligned}$$

with a minus sign for $j = 3$ and plus sign for $j = 1, 2$.

We can notice from this derivation of the modified Stokeslet G_{ij}^w that it has been developed specifically for a flat wall. A similar type of reasoning can be applied to consider the influence of a second parallel wall, see [48]. This is not without difficulties since the formulation involves slowly converging series in terms of Fourier-Bessel integrals. To circumvent this Staben et al. [60] use the regularized Fourier-Bessel integrals which lead to fast converging sums. However none of these models based on the method of reflections allow for imposing a non-homogeneous velocity field at the surface of the wall. Non-homogeneous boundary conditions arise in physical models such as the modeling of pumping/suction walls. An example concerning Sampson flow over an orifice is provided in the last section of this chapter. Confinements given by curvilinear surfaces are even more difficult to explore by using the method of images. In the next section we will discuss the alternative approach of explicitly discretizing the wall and numerically imposing boundary conditions over its surface.

5.2 Direct numerical discretization

In the method of images the boundary condition to be imposed at the wall - such as no-slip and impermeability - is used explicitly in the derivation. The fact that the boundary condition is *hard-coded* in the modified kernel does not allow for modelling *e.g.* moving walls. To our knowledge there is no way to alleviate this restriction other than re-deriving the modified kernel for a certain boundary condition. Thus it is of interest to seek a method for treating a wall that entails a higher degree of flexibility in handling non-homogeneous boundary conditions.

Assume first that the wall Γ is the only boundary in the computational domain. The flow velocity at any point $\mathbf{x}_0 \in \Gamma$ is then given

$$\mathbf{u}(\mathbf{x}_0) = \frac{1}{8\pi\mu} \int_\Gamma \mathbf{G}(\mathbf{x} - \mathbf{x}_0)\mathbf{f}_w(\mathbf{x})\mathrm{d}\Gamma_{\mathbf{x}} \ , \tag{5.2}$$

where $\mathbf{G}$ is the fundamental solution of Stokes flow (Stokeslet) and $\mathbf{f}_w$ represents the force densities at the wall. We seek to solve the problem (5.2) and compute the distribution of forces that satisfies given boundary conditions on the velocity $\mathbf{u}$. In order to avoid end effects of a finite plate, we employ periodic boundary conditions in the wall parallel directions, effectively rendering the wall infinite. In the boundary integral formulation periodic boundary conditions are imposed by using rather intricate formulas that differ according to whether periodicity is imposed in all three spatial directions or only in two directions (possibly even one direction). We discuss periodicity starting from the kernel of the Laplace equations and illustrate also decompositions of the periodic kernels of the Stokes equations in Section 6. However in Paper II which focuses on the wall treatment introduced here we use a *bi-periodic* Stokeslet to account for periodic boundary conditions solely in the wall parallel directions.

Equation (5.2) is singular whenever $\mathbf{x} = \mathbf{x}_0$. We therefore developed a high-order method to numerically integrate the singularity of the Stokeslet. The quadrature rule is based on the trapezoidal rule to which a correction operator is added to account for the singular behavior of the integrand. The idea is the same as described in Section 4.2 for singular functions of the type $1/|\mathbf{x}|$.

To study the advantages and shortcomings of the present approach to wall treatment we analyze the problem of a sphere in a free-fall trajectory towards a plane wall. By using superposition we add to equation (5.2) the velocity due to a sedimenting sphere. On the surface of the wall we impose the no-slip and impermeability conditions $\mathbf{u}(\mathbf{x}_0) = 0$ for any $\mathbf{x}_0 \in \Gamma$ and solve a coupled system for the distribution of point forces over the surfaces of the wall and sphere and also for the sphere velocity. A complete description of the system in continuous and discrete form is given in Paper II, where we also compare the simulation results to the wall-corrected Stokes law.

The discretization of a two-dimensional surface leads to a large, full matrix. However, we have found that certain symmetries of the matrix arising from the discretization of the wall allow us to store only three of its columns. The wall used in conjunction with a falling sphere can thus be algebraically solved by using *e.g.* the Schur complement method.

The high-order and memory efficient method we developed can be extended to two parallel walls in a straightforward manner. Although we impose homogeneous Dirichlet boundary conditions over the surface of the wall, we can use the same method in combination with non-homogeneous boundary conditions.

5.3 Non-homogeneous boundary conditions

A wide set of exact solutions have been obtained analytically for Stokes flow past various obstacles or inside various confinements. These expressions can be used in practice to impose boundary conditions which yield a valid viscous flow solution. Such boundary conditions enable the study of complex flows which do not admit immediate exact solutions. Many of the applications of interest involve flow above a flat plate with gaps or channel flow between moving/pumping walls.

The wall treatment developed in Paper II allows for any non-homogeneous boundary condition which corresponds to a solution of Stokes flow. Non-homogeneous boundary conditions are imposed in this set-up by simply prescribing the velocity field at the wall surface in the right hand side of the equation (5.2). Subsequently the distribution of point forces corresponding to this boundary condition can be computed and used to evaluate the velocity field on either side of the wall.

In Paper II we illustrate how to impose non-homogeneous boundary conditions using the aforementioned wall treatment on a simple sine wave. In this introduction however we choose an application that has a corresponding analytic solution. To this end we represent the flow inside a domain due to a boundary condition imposed over the wall surface on the Sampson flow problem. Sampson flow is the flow due to pressure difference past a flat plate with a circular orifice and an exact solution has been derived by Davis [17]. The orifice is represented in cylindrical coordinates ρ, ϕ, x_3 and the exact solution is computed in oblate spheroidal coordinates. Although the solution is provided in the latter system of coordinates we can transform back to cylindrical coordinates and obtain the velocity $\mathbf{u} = (u_1, u_2, u_3)$. Inside the domain the velocity field is given as

$$u_1 = \frac{x_3 \rho \xi}{(2\xi^2 + \rho^2 + x_3^2 - 1)(\xi^2 + \rho^2 + x_3^2)} \cos(\phi), \tag{5.3}$$

$$u_2 = \frac{x_3 \rho \xi}{(2\xi^2 + \rho^2 + x_3^2 - 1)(\xi^2 + \rho^2 + x_3^2)} \sin(\phi), \tag{5.4}$$

$$u_3 = \frac{\xi^3}{2\xi^2 + \rho^2 + x_3^2 - 1}, \tag{5.5}$$

with

$$\xi = \frac{1}{2}\sqrt{2 + 2\sqrt{\rho^4 + 2\rho^2 x_3^2 - 2\rho^2 + x_3^4 + 2x_3^2 + 1} - 2\rho^2 - 2x_3^2}$$

where $\rho \in [0, 1]$, $\phi \in [0, 2\pi)$ and x_3 the coordinate in the wall normal direction. At the boundary the velocity is $\mathbf{u} = (0, 0, \sqrt{1 - \rho^2})$ over the orifice and $\mathbf{u} = (0, 0, 0)$ over the wall surface.

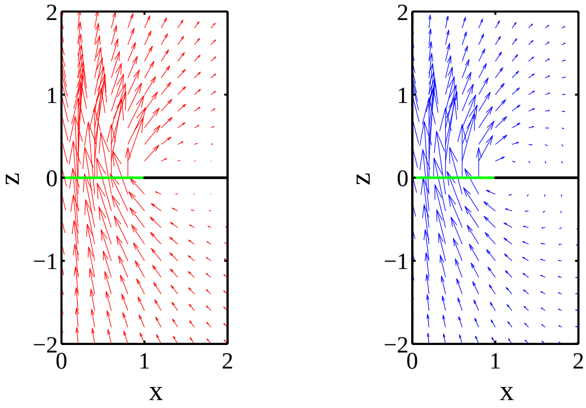

(a) Analytic solution (b) Simulated solution

Figure 5.2: Sampson flow; axisymmetric flow through an orifice (green) above a flat plate (black). Velocity field u, w in the xz plane.

Imposing this boundary condition we compute the velocity field in the entire domain. In Fig. 5.2b we reproduce the simulation results corresponding to the analytic velocity field (5.3) and by comparing to Fig. 5.2a find the expected qualitative match. However the solution in this case is no more than first order accurate over the surface of the wall due to the imposed velocity profile of class C^0 which leads to a force density of class C^0 over the wall surface. The quadrature rule derived in Paper II to integrate the Stokeslet with high-order accuracy is not specially suited to handle to high order integrands of a low differentiability class. However it is possible in practice to *mollify* $\mathbf{u}$ such that it is smooth. The purpose of this example has been solely to assess the capacity of the set-up in Paper II to replicate physically relevant problems, pin-pointing possible issues that may arise in practice.

Chapter 6

Periodic boundary conditions for Boundary Integral equations

In the field of fluid dynamics, depending on the nature of the problem at hand, we can distinguish between three main settings: free-space problems — where the flow and immersed particles are allowed to move freely in the infinite space, periodic problems — where the infinite space is assumed to be divided in cuboids and the flow physics is constrained to behave identically in each computational box, and confined problems — where the flow is subject to specific boundary conditions, such as solid walls and particles are restricted to move only inside the confined domain. Combinations of these types of settings are of course possible, *e.g.* periodicity in conjunction with solid walls, see Paper II. The kernel of an integral equation may change according to the type of problem under consideration. In Section 2.1 the free space kernels of Stokes flow were provided. The kernel of Stokes flow subject to a solid wall boundary condition was derived in Section 5.1. It remains now to discuss how the kernel of the Stokeslet modifies under periodic boundary conditions.

When dealing with boundary integral representations the flow is modeled implicitly through the influence of the immersed objects on the surrounding fluid. As mentioned in Chapter 3 the flow velocity at a point $\mathbf{x}_0$ due to a set of N point particles $i = 1, \dots, N$ is

$$\mathbf{u}(\mathbf{x}_0) = \frac{1}{8\pi\mu} \sum_i \mathbf{G}_0(\mathbf{x}_i - \mathbf{x}_0)\mathbf{f}(\mathbf{x}_i) \ . \tag{6.1}$$

Consider that the point particles at positions $\mathbf{x}_i$, $i = 1, \dots, N$, and also the evaluation point $\mathbf{x}_0$, lie within a domain, $\Omega = [0,\ L)^3$. If this computational domain is now periodically replicated in every direction then the velocity at a point $\mathbf{x}_0$ would be determined not only by the presence of the objects immersed in the current domain Ω but also their periodic images. For a particle at position $\mathbf{x}$ the periodic image is given by $\mathbf{x} + \tau(\mathbf{p})$ with $\tau(\mathbf{p}) = p_1 L\mathbf{e}_1 + p_2 L\mathbf{e}_2 + p_3 L\mathbf{e}_3$ where $p_i \in \mathbb{Z},\ i = 1, \dots, 3$, see Fig. 6.1 for one particle and its periodic images. The contribution of all particles and their periodic replicas is then

$$\mathbf{u}(\mathbf{x}_0) = \frac{1}{8\pi\mu} \sum_i \sum_{\mathbf{p}}{}' \mathbf{G}_0(\mathbf{x}_i - \mathbf{x}_0 + \tau(\mathbf{p}))\mathbf{f}(\mathbf{x}_i) \ , \tag{6.2}$$

where the prime superscript designates that the term $\mathbf{x}_i = \mathbf{x}_0$ was omitted for $\mathbf{p} = 0$.

Due to the nature of the Stokeslet ($1/r$-like decay) the sum is only conditionally convergent. To render the sum convergent a look back at the underlying physics is needed to assess whether further assumptions can be made in order to remove the divergence. For Stokes

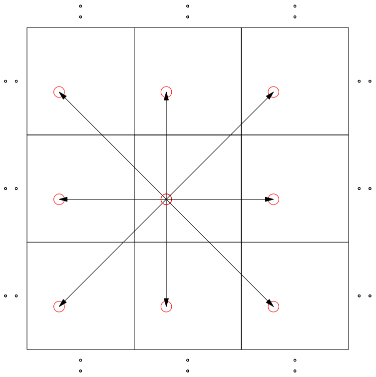

Figure 6.1: Two-dimensional sketch of a periodically replicated computational domain. The particle (red) and its images are summed up to infinity.

flow problems the assumption to make is that $\int_V \mathbf{u} \mathrm{d}V = 0$, which corresponds physically to zero mass flux. Equivalently it is assumed that the forces acting onto the fluid are balanced by a mean pressure gradient. For an electrostatics problem however the additional constraint needed is that of charge, *i.e.* that the sum of all charges within the primary periodic cell sum to zero. It remains nonetheless to explain how to actually make good use of such constraints in practice.

The classic mathematical tool for speeding up the convergence of sums of the type (6.2) has been provided by Ewald [24] in the context of electrostatic interactions. At the core of Ewald's procedure lies the idea of decomposing the interaction potential into a short-range component and a long-range one, the two terms being balanced by a scalar known as the Ewald parameter. This decomposition will lead to two sums, the one over the short range interactions to be evaluated in real space and the long range components in Fourier space, thus both sums being quickly convergent.

6.1 Ewald summation

The Ewald summation formalism has been long explored both theoretically [64], [34] and in physical applications such as molecular dynamics and flow phenomena simulations [47]. To outline the Ewald summation method we shall start from the classical electrostatics problem, following [45]. Thereafter we pursue the Ewald summation for Stokes flow problems, which is among one of the main interests of this thesis.

Ewald summation for molecular dynamics

Consider a basic molecular dynamics problem: N point particles located at positions $\mathbf{x}_n$, $n = 1, \ldots, N$ in a domain $\Omega = [0,\ L)^3$. The particles are assumed to have charges q_n and the configuration is charge neutral, *i.e.* $\sum_n q_n = 0$. To find the electrostatic potential due this set of charges in a periodic setup we need to solve the following Laplace problem

$$-\Delta\phi(\mathbf{x}) = 4\pi \sum_{n=1}^{N} \sigma^n(\mathbf{x}), \quad \sigma^n(\mathbf{x}) = \sum_{\mathbf{p}\in\mathbb{Z}^3} q_n \delta(\mathbf{x} - \mathbf{x}_n + \tau(\mathbf{p})) \tag{6.3}$$

where $\tau(\mathbf{p}) = p_1 L\mathbf{e}_1 + p_2 L\mathbf{e}_2 + p_3 L\mathbf{e}_3$ with $p_i \in \mathbb{Z},\ i = 1, \ldots, 3$. From (6.3) we can obtain the expression for the potential to be

$$\phi(\mathbf{x}) = \frac{1}{4\pi} \sum_{n=1}^{N} \sum_{\mathbf{p}\in\mathbb{Z}^3} \frac{q_n}{|\mathbf{x} - \mathbf{x}_n + \tau(\mathbf{p})|} \tag{6.4}$$

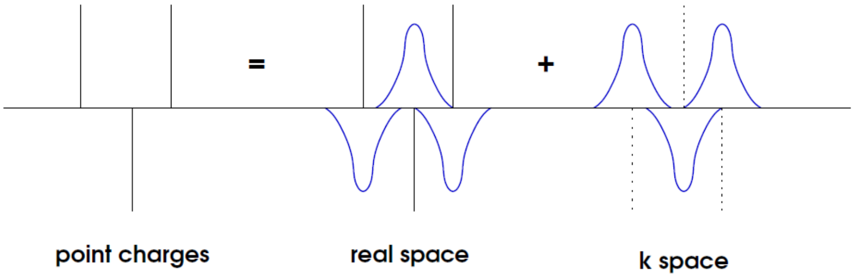

Figure 6.2: Ewald summation sketch. Point charges are being screened using a function γ and by this the sum in (6.4) is split into a real space sum and a Fourier space sum.

Ewald's outstanding contribution was to introduce a screening function $\gamma(\xi, \mathbf{x})$ to split the source term in (6.3) as

$$\sigma^n(\mathbf{x}) = \sigma^n(\mathbf{x}) - (\sigma^n * \gamma)(\mathbf{x}) + (\sigma^n * \gamma)(\mathbf{x}) \tag{6.5}$$

The requirements on the screening function are that $\gamma(\xi, 0) = 1$, $\gamma(\xi, |\mathbf{x}| \to \infty) \to 0$ and at the same time $|\gamma(\xi, \mathbf{x})|_{L_2} = 1$. A set of such functions is being explored in [34], however the most popular choice due to its fast decay is a Gaussian. To gain more intuition on how the decomposition is performed see the illustration in Fig.6.2. The decomposition in (6.5) leads to a component $\sigma^{n,R}(\xi, \mathbf{x}) = \sigma^n(\mathbf{x}) - (\sigma^n * \gamma)(\mathbf{x})$ which will be evaluated in the real space and the remaining $\sigma^{n,F}(\xi, \mathbf{x}) = (\sigma^n * \gamma)(\mathbf{x})$ in Fourier space. By the linearity of the Laplace operator the two problems can be handled separately

$$\begin{aligned} -\Delta\phi^{n,R}(\mathbf{x}) &= 4\pi\sigma^{n,R}(\mathbf{x}), && (6.6)\\ -\Delta\phi^{n,F}(\mathbf{x}) &= 4\pi\sigma^{n,F}(\mathbf{x}) && (6.7) \end{aligned}$$

To retrieve the full potential solution of the Laplace problem subject to periodic boundary conditions it remains to sum up $\phi(\mathbf{x}) = \sum_n \phi^{n,R}(\mathbf{x}) + \phi^{n,F}(\mathbf{x})$.

The traditional screening function is a Gaussian with carefully chosen prefactors that lead to suitable expressions, *i.e.* $\gamma = \xi^3 \pi^{-3/2} e^{-\xi^2|\mathbf{x}|^2}$. The real space sum can be evaluated directly by computing the convolution

$$\begin{aligned} \phi^{n,R}(\mathbf{x}) &= \int_{\mathbb{R}^3} \frac{q_n}{|\mathbf{y} - \mathbf{x}_n|} \sum_{\mathbf{p}\in\mathbb{Z}^3} (\delta(\mathbf{y} - \mathbf{x}_n + \tau(\mathbf{p})) - \gamma(\mathbf{y} - \mathbf{x}_n + \tau(\mathbf{p})))\mathrm{d}\mathbf{y} \\ &= \sum_{\mathbf{p}\in\mathbb{Z}^3} q_n \frac{\operatorname{erfc}(\xi|\mathbf{x} - \mathbf{x}_n + \mathbf{p}|)}{|\mathbf{x} - \mathbf{x}_n + \mathbf{p}|}, \qquad \mathbf{x} \neq \mathbf{x}_n \end{aligned}$$

where the complementary error function $\operatorname{erfc}(x) = 1 - \operatorname{erf}(x)$ is defined in terms of the error function

$$\operatorname{erf}(x) = \frac{2}{\sqrt{\pi}} \int_0^x e^{-t^2} \mathrm{d}t\ .$$

To proceed to the solution of the second Laplace problem we write in the frequency domain

$$-\Delta\phi^{n,F} = \sum_{\mathbf{k}} k^2 \hat{\phi}^{n,F}(\mathbf{k}) e^{i\mathbf{k}(\mathbf{x}-\mathbf{x}_n)} \tag{6.8}$$

Using the Poisson summation we express the right hand side of $-\Delta\phi^{n,F}(\mathbf{x}) = 4\pi\sigma^{n,F}(\mathbf{x})$ as being

$$\begin{aligned} \sigma^{n,F} &= \sum_{\mathbf{p}\in\mathbb{Z}^3} q_n \gamma(\mathbf{x}-\mathbf{x}_n+\mathbf{p}) = \frac{q_n}{V}\sum_{\mathbf{k}} \hat{\gamma}(\mathbf{k}) e^{i\mathbf{k}\cdot(\mathbf{x}-\mathbf{x}_n)} \\ &= \frac{q_n}{V}\sum_{\mathbf{k}} e^{-k^2/4\xi^2} e^{i\mathbf{k}(\mathbf{x}-\mathbf{x}_n)} \end{aligned} \tag{6.9}$$

where the wavenumber $\mathbf{k}$ is defined as $\mathbf{k} \in 2\pi\boldsymbol{\kappa}/L,\ \boldsymbol{\kappa} \in \mathbb{Z}^3$ and $k = |\mathbf{k}|$, and V stands for the volume of the domain. From both (6.8) and (6.9) we obtain

$$\phi^{n,F} = \frac{4\pi q_n}{V}\sum_{\mathbf{k}} \frac{e^{-k^2/4\xi^2}}{k^2} e^{i\mathbf{k}\cdot(\mathbf{x}-\mathbf{x}_n)} \tag{6.10}$$

To remove the ambiguity brought by the fact that the solution to a Laplace equation is determined only up to a constant we need to set the requirement $\int_{\mathbb{R}^3} \phi(\mathbf{x})\mathrm{d}\mathbf{x} = 0$. It follows that $\hat{\phi^F}(\mathbf{k}=0) = 0$, so it is reasonable to remove the term $\mathbf{k} = 0$ from the Fourier space sum.

Summing up over all point particles n we have the final expression for the potential in a periodic setup

$$\begin{aligned} \phi(\mathbf{x}_m) &= \sum_n \sum_{\mathbf{p}\in\mathbb{Z}^3}{}' q_n \frac{\operatorname{erfc}(\xi|\mathbf{x}_m-\mathbf{x}_n+\mathbf{p}|)}{|\mathbf{x}_m-\mathbf{x}_n+\mathbf{p}|} \\ &+ \frac{4\pi}{V}\sum_{\mathbf{k}\neq 0} \frac{e^{-k^2/4\xi^2}}{k^2} \sum_n e^{i\mathbf{k}(\mathbf{x}_m-\mathbf{x}_n)} q_n - \frac{2\xi}{\sqrt{\pi}} q_m \end{aligned} \tag{6.11}$$

The prime superscript over the real space sum indicates that the term $\mathbf{p} = 0, m = n$ is being skipped. When we subtract off the point at $n = m$ we get

$$\lim_{|\mathbf{x}|\to 0} \left(\frac{\operatorname{erfc}(\xi|\mathbf{x}|)}{|\mathbf{x}|} - \frac{1}{|\mathbf{x}|} \right) = -\frac{2\xi}{\sqrt{\pi}} \ .$$

from which stems the last term in (6.11), the so-called *self interaction.*

The parameter ξ introduced through the Ewald decomposition controls at which rate either the real space sum, or the Fourier space sum decays. Both sums are of complexity $\mathcal{O}(N^2)$.

6.2 Ewald summation for Stokes flow

The Ewald summation for Stokes flow can be found in the literature under two more popular names, the Beenakker decomposition [7], or the Hasimoto decomposition [31]. Both these decompositions are revised in a more modern framework in [46]. These are both based on Gaussian decompositions multiplying polynomials and have similar decays, with a slightly faster convergence observed in the case of the Hasimoto decomposition [46]. Both decompositions will be discussed briefly in the following section.

A set of point particles immersed in a Stokesian flow at positions $\mathbf{x}_n$ of forces $\mathbf{f}_n$ give a velocity at a point $\mathbf{x}_m$ of

$$\mathbf{u}(\mathbf{x}_m) = \sum_n \sum_{\mathbf{p}\in\mathbb{Z}^3}{}' \mathbf{S}(\mathbf{x}_n - \mathbf{x}_m)\mathbf{f}_n \ , \tag{6.12}$$

where the prime denotes that the point $\mathbf{x}_m = \mathbf{x}_n$ is skipped for $\mathbf{p} = 0$ and

$$\mathbf{S}(\mathbf{x}) = \frac{1}{8\pi\mu}\left(\frac{\mathbf{I}}{|\mathbf{x}|} + \frac{\mathbf{x}\mathbf{x}}{|\mathbf{x}|^3}\right) . \tag{6.13}$$

The procedure to obtain a decomposition in two fast converging sums is idem to the one pertaining to the Laplace equation and leads to an expression of the type

$$\mathbf{u}(\mathbf{x}_m) = \mathbf{u}^r(\mathbf{x}_m) + \mathbf{u}^F(\mathbf{x}_m) + \mathbf{u}_{self}(\mathbf{x}_m) \tag{6.14}$$

with the notation $\mathbf{u}^r$ for the real space sum, $\mathbf{u}^F$ the Fourier space sum, and $\mathbf{u}_{self}$ the self-interaction term.

Both decompositions that we present here have the form in (6.14) however the terms in the real space sum and Fourier space sum differ from each other as will be seen.

The Hasimoto decomposition

The Hasimoto decomposition can be derived in a similar way as previously explained for the kernel of the Laplace equation using a screening function, as indicated in [33],

$$\gamma(\xi, r) = \xi^3/\pi^{-3/2}\mathrm{e}^{-\xi^2 r^2}(5/2 - \xi^2 r^2) \ .$$

The real space sum of the Hasimoto decomposition reads

$$\mathbf{u}^r(\mathbf{x}_m) = \sum_{n=1}^{N} \sum_{\mathbf{p}}{}' \Gamma(\xi, \mathbf{x}_m - \mathbf{x}_n + \mathbf{p})\mathbf{f}_n \ , \tag{6.15}$$

with

$$\Gamma(\xi, \mathbf{x}) = C(\xi r)\frac{\mathbf{I}}{r} + D(\xi r)\frac{\hat{\mathbf{x}}\hat{\mathbf{x}}}{r} \ ,$$

and

$$C(\xi r) = \operatorname{erfc}(\xi r) - \frac{2\xi r}{\sqrt{\pi}}e^{-\xi^2 r^2}, \quad D(\xi r) = \operatorname{erfc}(\xi r) + \frac{2\xi r}{\sqrt{\pi}}e^{-\xi^2 r^2}$$

where we used the notation $\hat{\mathbf{x}} = \mathbf{x}/|\mathbf{x}|$, $r = |\mathbf{x}|$.

The Fourier space sum is

$$\mathbf{u}^F(\mathbf{x}_m) = \frac{1}{V}\sum_{n=1}^{N}\sum_{\mathbf{k}\neq 0} \Phi(\xi, \mathbf{x}_m - \mathbf{x}_n, \mathbf{k})\mathbf{f}_n \ , \tag{6.16}$$

with terms given by

$$\Phi(\xi, \mathbf{k}) \quad = \quad B(\xi, \mathbf{k})e^{-k^2/4\xi^2}e^{-i\mathbf{k}\cdot\mathbf{x}} \ .$$

where for a wavenumber $\mathbf{k}$ is defined as $\mathbf{k} \in 2\pi\boldsymbol{\kappa}/L, \ \boldsymbol{\kappa} \in \mathbb{Z}^3$ and $k = |\mathbf{k}|$

$$B(\xi, \mathbf{k}) = 8\pi\left(1 + \frac{k^2}{4\xi^2}\right)\frac{1}{k^4}(k^2\mathbf{I} - \mathbf{k}\mathbf{k}) \ . \tag{6.17}$$

and

$$\mathbf{u}_{self}(\mathbf{x}_m) = \frac{4\xi}{\sqrt{\pi}}. \tag{6.18}$$

The Beenakker decomposition

The Beenakker decomposition can be derived using a screening function

$$\gamma(\xi, r) = \xi^3/\pi^{-3/2}\mathrm{e}^{-\xi^2 r^2}(10 - 11\xi^2 r^2 + 2\xi^4 r^4)\ .$$

This choice yields a real space sum component given as

$$\mathbf{u}^r(\mathbf{x}_m) = \sum_{n=1}^{N} \sum_{\mathbf{p}}{}' \Gamma(\xi, \mathbf{x}_m - \mathbf{x}_n + \mathbf{p})\mathbf{f}_n\ , \tag{6.19}$$

with

$$\Gamma(\xi, \mathbf{x}) \quad = \quad C(\xi r)\frac{\mathbf{I}}{r} + D(\xi r)\frac{\hat{\mathbf{x}}\hat{\mathbf{x}}}{r}\ ,$$

and

$$C(\xi r) = \operatorname{erfc}(\xi r) - \frac{2}{\sqrt{\pi}}(2\xi^2 r^2 - 3)e^{-\xi^2 r^2}, \quad D(\xi r) = \operatorname{erfc}(\xi r) + \frac{2}{\sqrt{\pi}}(1 - 2\xi^2 r^2)e^{-\xi^2 r^2}$$

where we used the notation $\hat{\mathbf{x}} = \mathbf{x}/|\mathbf{x}|$, $r = |\mathbf{x}|$.

The Fourier space sum is

$$\mathbf{u}^F(\mathbf{x}_m) = \frac{1}{V}\sum_{n=1}^{N} \sum_{\mathbf{k}\neq 0} \Phi(\xi, \mathbf{x}_m - \mathbf{x}_n, \mathbf{k})\mathbf{f}_n\ , \tag{6.20}$$

with terms given by

$$\Phi(\xi, \mathbf{k}) \quad = \quad B(\xi, \mathbf{k})e^{-k^2/4\xi^2}e^{-i\mathbf{k}\cdot\mathbf{x}}\ .$$

where for a wavenumber $\mathbf{k}$ is defined as $\mathbf{k} \in 2\pi\boldsymbol{\kappa}/L,\ \boldsymbol{\kappa} \in \mathbb{Z}^3$ and $k = |\mathbf{k}|$

$$B(\xi, \mathbf{k}) = 8\pi\left(1 + \frac{k^2}{4\xi^2} + \frac{k^4}{8\xi^4}\right)(k^2\mathbf{I} - \mathbf{k}\mathbf{k})\ . \tag{6.21}$$

and

$$\mathbf{u}_{self}(\mathbf{x}_m) = \frac{8\xi}{\sqrt{\pi}}. \tag{6.22}$$

Note that both decompositions contain in the real space sum the complementary error function, $\operatorname{erfc}(r)$, which for positive arguments can be approximated by $\operatorname{erfc}(r) \leq \mathrm{e}^{-r^2}$. Thus the real space sum in both decompositions features an exponential decay, *i.e.* $\mathrm{e}^{-\xi^2 r^2}$, that depends proportionally on the splitting parameter ξ. The Fourier space sum decays also exponentially, like $\mathrm{e}^{-k^2/4\xi^2}$, but this decay is inversely proportional to the parameter ξ.

The sole difference between the Beenakker and Hasimoto's decomposition is in the polynomial expressions that multiply these exponentials. A lower order polynomial, such as in the Hasimoto decomposition, gives a faster decay of the sum, albeit the difference is small in practice. For each of the sums to be computed all the pair-wise interactions between the N particles have to be considered, thus the computation of the sums is $\mathcal{O}(N^2)$. As higher accuracy is desired the constant grows and using a direct method becomes unfeasible unless N is small. This computational complexity can be however reduced by using a fast Ewald summation method, as will be seen in Section 7.

6.3 Error estimates and parameter choice

In numerical computations both infinite sums given in (6.14) must be truncated. Here we focus on the Hasimoto decomposition which is used in the present thesis. The parameter ξ affects both the accuracy and the efficiency. The computational cost of evaluating the Fourier space sum can balance the cost of the real space sum for a carefully picked ξ. Also for a chosen ξ the truncation can be performed such that the method is of a certain accuracy δ. An error analysis already performed in [46] can be used to assess the loss of accuracy due to truncation. The error analysis is performed in euclidean norm for a particle positioned at $\mathbf{x}_n$. For the Stokeslet it has been shown that if the sum $\Gamma(\xi, \mathbf{x}+\mathbf{p})$, is truncated at a certain cut-off r_c then the truncation error is

$$\left|\sum_{\mathbf{p}}\Gamma(\xi,\mathbf{x}+\mathbf{p})\mathbf{f}-\sum_{|\mathbf{x}+\mathbf{p}|\le r_c}\Gamma(\xi,\mathbf{x}+\mathbf{p})\mathbf{f}\right|\le\sum_{|\mathbf{x}+\mathbf{p}|>r_c}||\Gamma(\xi,\mathbf{x}+\mathbf{p})\mathbf{f}||_2\le E_R^S(\xi,r_c)||\mathbf{f}||_2\ ,$$

and $E_R(\xi, r_c)$ can be estimated as

$$E_R(\xi,r_c)\le(12\pi+16\sqrt{\pi}r_c\xi)\frac{1}{\xi^2}e^{-\xi^2r_c^2}\ . \tag{6.23}$$

Similarly for the Fourier space sum it was obtained that the truncation error at a certain k_∞ is

$$\left|\sum_{\mathbf{k}}|\Phi(\xi,\mathbf{k})\mathbf{f}-\sum_{|\mathbf{k}|\le k_\infty}|\Phi(\xi,\mathbf{k})\mathbf{f}\right|\le\sum_{|\bar{\mathbf{k}}|>k_\infty}||\Phi(\xi,\mathbf{k})\mathbf{f}||_2\le E_F^S(\xi,k_\infty)||\mathbf{f}||_2$$

where for $\mathbf{k}=2\pi\bar{\mathbf{k}}$ with $\bar{\mathbf{k}}=(k_1/L,\ k_2/L,\ k_3/L)$ and $k_i\in\mathbb{Z}, i=1,\dots,N$ and $k_\infty=|\bar{\mathbf{k}}|$

$$E_F(\xi,k_\infty)\le(2\sqrt{\pi}k_\infty+3\xi)\frac{2}{\sqrt{\pi}}e^{-k_\infty^2(\pi/\xi)^2}.$$

These estimates intertwine the cut-off in the real space r_c, and the cut-off in the Fourier space k_∞ through the splitting parameter ξ for a fixed accuracy demand δ. However the expressions are not easily invertible for a given δ, *i.e.* it is hard to solve $E_R(\xi, r_c) \approx \delta$ using the expression in (6.23), and similarly for the expression in (6.24). Using the observation that each error estimate follows a certain *law* with respect to ξ we establish in Paper III using a curve fitting approach a set of relations between parameters r_c, ξ and k_∞, ξ. Thus we have that

$$E_R(\xi,r_c)\le(12\pi+16\sqrt{\pi}r_c\xi)\frac{1}{\xi^2}e^{-\xi^2r_c^2}\quad\to\quad r_c(\xi,\delta)=a_r(\delta)\cdot\xi^{-b_r(\delta)}$$
$$E_F(\xi,k_\infty)\le(2\sqrt{\pi}k_\infty+3\xi)\frac{2}{\sqrt{\pi}}e^{-k_\infty^2(\pi/\xi)^2}\quad\to\quad k_\infty(\xi,\delta)=a_k(\delta)\cdot\xi+b_k(\delta)$$

with $a(\delta)$ and $b(\delta)$ to be determined through curve fitting at a fixed δ.

This gives us the possibility to shift back and forth from r_c to k_∞ through ξ. In Paper III we offer a thorough description on how the parameter choice is to be performed and also how both sums are to be balanced for optimal efficiency at a given accuracy.

6.4 Periodic Stresslet – Beenakker decomposition

Consider the same framework as previously, *i.e.* a set of points particles $\mathbf{x}_i$, $i=1,\dots,N$ in a periodic domain, $\Omega=[0,L)^3$ subject to periodic boundary conditions. For any point particle $\mathbf{x}$ the periodic image is given by $\mathbf{x}+\tau(\mathbf{p})$ with $\tau(\mathbf{p}) = p_1L\mathbf{e}_1 + p_2L\mathbf{e}_2 + p_3L\mathbf{e}_3$, $\mathbf{p} \in \mathbb{Z}^3$. The discrete equivalent of the double layer formulation in Section 2.2 reads

$$u_l(\mathbf{x}_i) = \frac{1}{8\pi} \sum_{\mathbf{p}\in\mathbb{Z}^3}{}' \sum_j T_{0,lmp}(\mathbf{x}_j - \mathbf{x}_i + \tau(\mathbf{p})) f_m(\mathbf{x}_j) n_p(\mathbf{x}_j) \ , \quad i = 1,\ldots,N \tag{6.24}$$

where the prime over the sum over $\mathbf{p}$ stands for skipping the singular point $i=j$ for $|\mathbf{p}|=0$ and

$$T_{0,lmp}(\mathbf{x}) = -6\frac{x_l x_m x_p}{|\mathbf{x}|^5}. \tag{6.25}$$

The decomposition that stands out in the literature [15, 25, 49] is the one based on Beenakker's decomposition. According to Beenakker we can split the sum in (6.24) as follows

$$u_l^T(\mathbf{x}_i) = u_l^{T,r}(\mathbf{x}_i) + u_l^{T,F}(\mathbf{x}_i) \tag{6.26}$$

The Fourier space sum is given in terms of the wavenumber $\mathbf{k} \in 2\pi\boldsymbol{\kappa}/L$, $\boldsymbol{\kappa} \in \mathbb{Z}^3$ and $k = |\mathbf{k}|$ as

$$u_l^{T,F}(\mathbf{x}_i) = -\frac{1}{V}\sum_{\mathbf{k}\neq 0}\sum_j \Phi_{lmp}(\xi,\mathbf{k}) S_{mp}(\mathbf{x}_j) i\mathrm{e}^{-i\mathbf{k}\cdot(\mathbf{x}_i-\mathbf{x}_j)} \ ,$$

with $S_{mp}(\mathbf{x}) = f_m(\mathbf{x})n_p(\mathbf{x})$, V the volume of the domain Ω and

$$\Phi_{lmp}(\xi,\mathbf{k}) = \pi\left[-\frac{2}{k^4}k_l k_m k_p + \frac{1}{k^2}(\delta_{mp}k_l + \delta_{lp}k_m + \delta_{lm}k_p)\right]\left(8 + 2\frac{k^2}{\xi^2} + \frac{k^4}{\xi^4}\right)\mathrm{e}^{-k^2/4\xi^2}$$

With the same notation for S_{mp} the real space sum is given as

$$u_l^{T,r}(\mathbf{x}_i) = \sum_{\mathbf{p}\in\mathbb{Z}^3}{}' \sum_j \Gamma_{lmp}(\xi, \mathbf{x}_j - \mathbf{x}_i + \tau(\mathbf{p})) S_{mp}(\mathbf{x}_j) \ , \tag{6.27}$$

with

$$\Gamma_{lmp}(\xi,\mathbf{x}) = C(\xi,|\mathbf{x}|)\hat{x}_l\hat{x}_m\hat{x}_p + D(\xi,|\mathbf{x}|)(\delta_{lm}\hat{x}_p + \delta_{lp}\hat{x}_m + \delta_{mp}\hat{x}_l) \ , \tag{6.28}$$

where $\hat{\mathbf{x}} = \mathbf{x}/|\mathbf{x}|$ and

$$\begin{aligned} C(\xi,r) &= -\frac{6}{r^2}\,\mathrm{erfc}(\xi r) + \left(-\frac{12\xi}{r\sqrt{\pi}} - \frac{8\xi^3 r}{\sqrt{\pi}} + \frac{16\xi^5 r^3}{\sqrt{\pi}}\right)\mathrm{e}^{-\xi^2 r^2} \\ D(\xi,r) &= \frac{8\xi^3}{\sqrt{\pi}}(2-\xi^2 r^2)\mathrm{e}^{-\xi^2 r^2} \ . \end{aligned}$$

According to [25] the stress tensor can be expressed in terms of an operator $T_{lmp}(\mathbf{x}) = \Xi[r]$ where $r = |\mathbf{x}|$ and

$$\Xi(r) = [(\delta_{lm}\nabla_m + \delta_{mp}\nabla_l + \delta_{lp}\nabla_m)\nabla^2 - 2\nabla_l\nabla_m\nabla_p](r) \ ,$$

It can be easily verified that $\Xi(r)$ leads to the expression (6.25). If now we decompose the $r = r\,\mathrm{erfc}(\xi r) + r\,\mathrm{erf}(\xi r)$ we can compute two sums

$$\begin{aligned} T^r_{lmp}(\mathbf{x}) &= \Xi(r\,\mathrm{erfc}(\xi r)) \ , \\ T^F_{lmp}(\mathbf{x}) &= \Xi(r\,\mathrm{erf}(\xi r)) \ , \end{aligned}$$

By evaluating the above expressions the Beenakker decomposition of the Stresslet as provided in (6.26) can be obtained.

As an alternative to this decomposition in Paper IV of this thesis a decomposition with faster decaying properties was derived. The approach taken in Paper IV to obtain the two final sums in (6.26) is however different. In Paper IV we start from the expression of the stress tensor in terms of the pressure and gradient of the velocity. Using the fact the fundamental solution of the pressure can also be obtained as a function of the gradient of the kernel of the Laplace equation we can use the decompositions stemming from the screening function that yields the Hasimoto decomposition for Stokes flow, see Section 6.2 to obtain what proves to be a decomposition with faster decaying sums.

Chapter 7

Fast Ewald summation methods

An Ewald type of decomposition such as the one mentioned in Section 6.2 involves a sum in real space of decay $\mathrm{e}^{-\xi^2 r^2}$, as discussed in Section 6.2, where r is the distance between particles and ξ the splitting parameter, and a sum in Fourier space of decay $\mathrm{e}^{-k^2/4\xi^2}$, where k is the wavenumber. For large ξ the real space sum decays fast while the Fourier space sum decays slower and vice-versa. It seems natural to choose a larger ξ such that the real space sum decays faster and seek ways to use the Fast Fourier Transform (FFT) for the Fourier space sum evaluation. This very idea is at the basis of fast Ewald summation methods.

To provide a brief overview of FFT based Ewald methods we follow [58]. Consider we intend to evaluate $\phi^F = \sum_n \phi^{n,F}(\mathbf{x})$, with $\phi^{n,F}(\mathbf{x})$ solving the Laplace problem (6.7). Construct a function $g(\mathbf{x}) = \gamma * 1/4\pi|\mathbf{x}|$, $1/4\pi|\mathbf{x}|$ kernel of the Laplace equation. To compute $\phi^F(\mathbf{x}_m) = \sum_n (g * \sigma^n)(\mathbf{x}_m)$ at a particle position $\mathbf{x}_m$ we follow the outline of a FFT-based Ewald method

- Introduce a regular grid over the basic periodic cell.

- *Spread* or *interpolate* point sources over the regular grid, by considering a mollified $\tilde{\sigma}^n$; *to grid* smearing step.

- Compute the FFT of this grid function, *i.e.* $\tilde{\sigma}^n$,

- Multiply by a modified Green's function in Fourier space, $\hat{\phi^F} = \sum_n \hat{g}\hat{\tilde{\sigma}}^n$

- Compute the IFFT of the obtained grid function, $\hat{\phi^F}$.

- Evaluate at target points using grid values, *i.e.* evaluate $\phi^F(\mathbf{x}_m)$; same interpolation procedure as in the *spreading* step above; *from grid* recovery step.

Extensive work on fast Ewald methods has been conducted in the field of molecular dynamics and some of the methods in this field have been picked up also by fluid dynamicists. The Particle-Particle Particle-Mesh algorithm (PPPM) due to [36] and Particle Mesh Ewald (PME) [16] are some of the most cited and used algorithms. The PME method was first applied to the study of hydrodynamics between suspended spheres by [28] and further systematized in the work on 'Stokesian dynamics' by [59]. A further refinement of the PME method, known as the Smooth PME (SPME) [23] was also extended to flow problems by [57]. The *'to-grid'* and *'from-grid'* steps in the FFT based Ewald method have been improved in the SPME method by introducing high-order B-splines which lead to more accurate interpolating schemes. However the polynomial interpolation can be bypassed altogether by choosing properly scaled Gaussians that lead to a spectrally accurate Ewald method (SE) [47].

The large scale simulations of fibers in periodic domains performed in Paper III use the Spectral Ewald method to expedite the computations. Here we shall describe how the Fourier space sum is to be treated using the Spectral Ewald on the Hasimoto decomposition of the periodic Stokeslet, see 6.2.

7.1 Fourier space sum treatment

Consider a set of N point particles at positions $\mathbf{x}_n$ in a domain $\Omega = [0,\ L)^3$ of volume V. The distribution of particles is assumed uniform and of number density $\rho = N/V$. Here we outline the principle of the fast summation method and for brevity of the description the domain is a cube of side L, however in Paper III we consider general rectangular domains.

The Fourier space sum in (6.14) using the Hasimoto decomposition takes the form

$$\mathbf{u}^F(\mathbf{x}_m) = \frac{1}{V}\sum_{n=1}^{N}\sum_{\mathbf{k}\neq 0}\Phi(\xi, \mathbf{x}_m - \mathbf{x}_n, \mathbf{k})\mathbf{q}_n \ , \tag{7.1}$$

with terms given by

$$\Phi(\xi, \mathbf{k}) \quad = \quad B(\xi, \mathbf{k})e^{-k^2/4\xi^2}e^{-i\mathbf{k}\cdot\mathbf{x}} \ .$$

where for a wavenumber $\mathbf{k}$ is defined as $\mathbf{k} \in 2\pi\boldsymbol{\kappa}/L,\ \boldsymbol{\kappa} \in \mathbb{Z}^3$ and $k = |\mathbf{k}|$, the amplification factor is

$$B(\xi, \mathbf{k}) = 8\pi\left(1 + \frac{k^2}{4\xi^2}\right)\frac{1}{k^4}(k^2\mathbf{I} - \mathbf{kk}) \ . \tag{7.2}$$

The basic idea of the Spectral Ewald method is to use the fact that a convolution in real space is a product in Fourier space. Split

$$\mathbf{u}^F(\mathbf{x}_m) = \frac{1}{V}\sum_{\mathbf{k}\neq 0}B(\xi, \mathbf{k})\mathrm{e}^{-(1-\eta)k^2/4\xi^2}\mathrm{e}^{-i\mathbf{k}\cdot\mathbf{x}_m}\sum_{n=1}^{N}\mathbf{f}(\mathbf{x}_n)\mathrm{e}^{i\mathbf{k}\cdot\mathbf{x}_n}\mathrm{e}^{-\eta k^2/8\xi^2} \ .$$

and by setting

$$\widehat{H}_k = \sum_{n=1}^{N}\mathbf{f}(\mathbf{x}_n)\mathrm{e}^{i\mathbf{k}\cdot\mathbf{x}_n}\mathrm{e}^{-\eta k^2/8\xi^2} \tag{7.3}$$

rewrite

$$\mathbf{u}^F(\mathbf{x}_m) = \frac{1}{V}\sum_{\mathbf{k}\neq 0}B(\xi, \mathbf{k})\mathrm{e}^{-(1-\eta)k^2/4\xi^2}\mathrm{e}^{-i\mathbf{k}\cdot\mathbf{x}_m}\mathrm{e}^{-\eta k^2/8\xi^2}\widehat{H}_{-k} \ . \tag{7.4}$$

Note that $\widehat{H}_k = \sum_n \mathbf{f}_n\widehat{v}_k\widehat{w}_k$ with $\widehat{v}_k = \mathrm{e}^{-\eta k^2/8\xi^2}$ and $\widehat{w}_k = e^{-i\mathbf{k}\cdot\mathbf{x}_n}$. This product in Fourier space has a corresponding convolution in real space of the functions $v = \left(\frac{2\xi^2}{\pi\eta}\right)^{3/2}\mathrm{e}^{-2\xi^2r^2/\eta}$ and $w = \delta(\mathbf{x} - \mathbf{x}_n)$.

This implies that we can write in real space

$$H(\mathbf{x}) = \sum_n \mathbf{f}(\mathbf{x}_n)\left(\frac{2\xi^2}{\pi\eta}\right)^{3/2}\mathrm{e}^{-2\xi^2r^2/\eta}\mathrm{e}^{-2\xi^2|\mathbf{x}-\mathbf{x}_n|_*^2/\eta} \ , \tag{7.5}$$

where $|\cdot|_*$ denotes the distance to closest periodic image.

This representation of H is a sum of n properly scaled Gaussians with the peak values centered at each point particle $\mathbf{x}_n$.

Let us define

$$\widehat{\widetilde{H}}_k = B(\xi, \mathbf{k})\mathrm{e}^{-(1-\eta)k^2/4\xi^2}\widehat{H}_k \tag{7.6}$$

then the Fourier space sum can be written

$$\mathbf{u}^F(\mathbf{x}_m) = \frac{1}{V}\sum_{\mathbf{k}\neq 0}\widehat{\widetilde{H}}_{-k}\mathrm{e}^{-\eta k^2/8\xi^2}\mathrm{e}^{-i\mathbf{k}\cdot\mathbf{x}_m} \ .$$

Reverting to a computation in real space the Fourier component becomes

$$\mathbf{u}^F(\mathbf{x}_m) = \int_\Omega \widetilde{H}(x)\left(\frac{2\xi^2}{\pi\eta}\right)^{3/2}\mathrm{e}^{-2\xi^2|\mathbf{x}-\mathbf{x}_m|_*^2/\eta}\mathrm{d}\mathbf{x} \ . \tag{7.7}$$

The advantage is that integrating in real space on a equidistant grid (here of M_g grid points) over a full period can be performed with spectral accuracy using the trapezoidal rule. A thorough discussion on the algorithm is offered in Paper III and is based on the descriptions offered by [47]. The algorithm is reproduced here only to assure a better understanding of the section to follow on fast Gaussian gridding.

Consider the domain $\Omega = [0,\ L)$ to be discretized in a number of M_g points, yielding a grid spacing $h = L/M_g$. The size of the grid to be considered in real space (M_g grid points) is connected to the truncation of the Fourier space sum. If a grid of M_g odd grid points is considered then, with the scaling $\mathbf{k} = 2\pi\boldsymbol{\kappa}$, $\boldsymbol{\kappa} \in \mathbb{Z}^3$, we have that $\kappa \in \{-(M_g - 1)/2, \dots, 0, \dots, (M_g - 1)/2\}$. Thus if the sum is truncated at a certain κ_∞ (in the aforementioned scaling) then $M_g = 2\kappa_\infty + 1$.

The only free parameter in (7.5) is η which controls the shape of the Gaussians $e^{-2\xi^2|\mathbf{x}-\mathbf{x}_m|_*^2/\eta}$. If we consider the width of a Gaussian after truncation to be w then for a set of P discrete points in the support of the Gaussian at a spacing h away from each other we have $w = Ph/2$. If now, as explained in [46], we take the width to correspond to m standard deviations $w = \sigma m$, $\sigma^2 = \eta/4\xi^2$, we obtain that

$$\eta = \left(\frac{Ph\xi}{m}\right)^2 \ .$$

The number of points in the support of a Gaussian P and the parameter m, giving the shape of the Gaussian, and by that the level of the Gaussian at the truncation point are fixed for a certain accuracy requirement and guidelines for values to chosen were provided already in [47].

A simple operation count gives the following complexity of the algorithm

$$\underbrace{\mathcal{O}(NP^3)}_{Eq.(7.5)} + \underbrace{\mathcal{O}({M_g}^3\log {M_g}^3)}_{FFT+IFFT} + \underbrace{\mathcal{O}({M_g}^3)}_{Eq.(7.6)} + \underbrace{\mathcal{O}(NP^3)}_{Eq.(7.7)} \tag{7.8}$$

7.2 Fast Gaussian gridding

The fast Gaussian gridding provides a mean of expediting sums of the form

$$H(\mathbf{x}) = C\sum_n \mathbf{f}_n\mathrm{e}^{-\alpha|\mathbf{x}-\mathbf{x}_n|_*^2} \tag{7.9}$$

Algorithm 1 Algorithm for fast computation of Fourier space sum

```
[1] Construct a uniform grid over the domain $\Omega = [0,\ L)^3$ with $M_g$ grid points and a spacing $h = L/M_g$.
[2] Set $P$ and evaluate $H$ using (7.5) for $\eta = (P\xi h/m)^2$. For this a fast Gaussian gridding algorithm is used [47]. ($m$ can be chosen as a function of $P$ as explained in Paper III)
[3] Use a three-dimensional FFT to evaluate $\widehat{H}$.
[4] Compute $\widehat{\widehat{H}}$ using (7.6).
[5] Use a inverse FFT to retrieve $\widetilde{H}$.
[6] Evaluate (7.7) using the trapezoidal rule, yielding spectral accuracy due to the periodicity of the integrand. This again yields sums over Gaussians which calls once more for the fast Gaussian gridding algorithm.
```

Adapting the ideas of Greeengard and Lee [27] we assume that $H(\mathbf{x})$ is to be evaluated over a constant grid $\mathbf{x} = [ih, jh, kh]$, where $i, j, k = 0, \dots, M-1$. In one dimension, $x = ih$, the exponential can be evaluated as follows

$$\mathrm{e}^{-\alpha(x-x_n)^2} = \mathrm{e}^{-\alpha(ih-x_n)^2} = \mathrm{e}^{-\alpha((ih)^2-2ihx_n+x_n^2)} = \mathrm{e}^{-\alpha(ih)^2}\left(\mathrm{e}^{\alpha 2hx_n}\right)^i \mathrm{e}^{-\alpha x_n^2} \tag{7.10}$$

The first term in (7.10) is independent of x_n therefore all evaluations of $\mathrm{e}^{-\alpha(ih)^2}$ depend only on the grid spacing and can be performed once and reused for each evaluation point x_n. However the remaining terms depend on the source location and have to be computed for each x_n. The same procedure can be applied in all directions. In applications the term $\left(\mathrm{e}^{\alpha 2hx_n}\right)^i$ is at the risk of becoming very large, thus incurring a loss of precision in ensuing computations. This is alleviated in [47] by introducing a shift of the exponent $t = x - x_n$.

If the sum (7.9) is evaluated directly on a grid of P^3 points it requires NP^3 evaluations of the exponential. By using instead the fast gridding in (7.10) only $4N$ evaluations of the exponential are needed followed by roughly $N(P^3 + 3P)$ multiplications. The speed-up of this procedure is, as reported in [47], of approximately 15-20 times faster for a three dimensional problem.

The fast gridding technique is used in conjunction with the Spectral Ewald method in steps [1] and [5] in Algorithm 1. The Gaussians used in the algorithm have a support of P points however they are spread over the entire grid of M_g points.

7.3 Real space sum treatment

Regarding the real space sum it has been mentioned that we seek to truncate it at a lower cut-off to shift more of the work to the Fourier space sum. Let us assume that the cut-off is less than the size of the domain, *i.e.* $r_c < L$. It suffices then to compute the real space sum only for particles within a sphere of radius r_c. However even if the cut-off is less than the domain size all pair-wise interactions have to be computed to find those particles that lie at a distance less than r_c away from each other. This is highly inconvenient since it is an $\mathcal{O}(N^2)$ operation. A more efficient approach is to use what is known as the Linked Cell List algorithm [4].

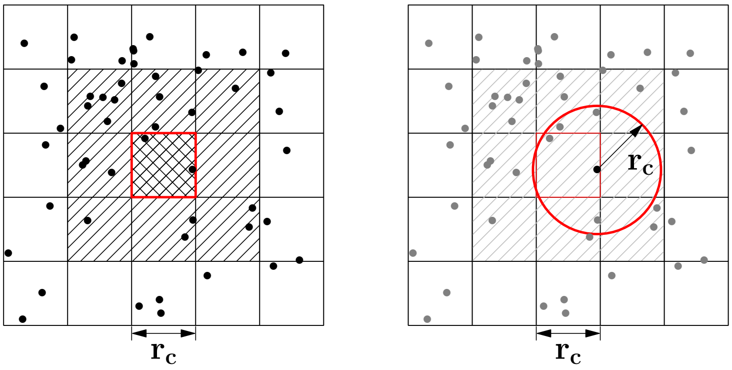

(a) Linked cell list (b) Verlet list

Figure 7.1: Linked cell list division of the computational domain ($r_c = L/5$).

Assume that for the domain $\Omega = [0,\ L)^3$ the real space sum can be truncated at a cut-off r_c such that $r_c = L/5$. Then if we divide the domain as in Fig. 7.1a we can perform a logical operation of assigning to each particle the box it belongs to. Afterwards we can resume the computation of pair-wise interactions for each particle and all of those in the 26 immediate neighbor boxes. Since each sub-box is of volume r_c^3 and we regard here a uniform distribution of particles then we can assume that the number of particles from all neighboring sub-boxes is $N_c \approx 27\rho r_c^3$. The number of pairwise interactions that have to computed then is $(N_c - 1)N/2$ instead of $(N - 1)N/2$. This can be further reduced through a refinement of the list of neighbors for each particle by eliminating those particles that lie in the cube of side $3r_c$ but are at more than r_c away from the current particle. This refinement is known also as the Verlet list, for a graphical representation see Fig. 7.1b. The number of neighboring particles reduces now to $N_c^* \approx 4\pi/3\rho r_c^3$. With this algorithm if N_c^* is preserved constant then the computation of the real space sum has a complexity of $\mathcal{O}(N)$.

7.4 Parameter choice for the Fast summation

The parameter ξ controls the decay of both sums and in Section 6.3 we have discussed how error estimates can be used to connect the cut-off in the real space r_c to the cut-off in Fourier space k_∞. In practice we can use the relations explained in Section 6.3 and detailed in Paper III to establish what parameters to choose for a certain accuracy requirement to be met. However for the fast summation method to be efficient we need to commit the real space truncation at a very small r_c and shift more computational work in the Fourier space where FFTs can speed up computations. This is the key-point of the fast summation method since the real space sum is $\mathcal{O}(N)$ only if the truncation of the real space sum r_c is preserved proportional to the number density ρ, *i.e.* $r_c \approx \sqrt[3]{1/\rho}$. Also the constant of the complexity cost is large if r_c not significantly smaller than the size of the domain.

The key steps, also described in Paper III, are

Key steps

[1] Identify the simulation input data: N number of particles, $\Omega = [0,\ B)^3$ the domain, δ desired accuracy.

[2] Choose ξ_0 such that $r_c < B/3$.

[3] Perform a set of simulation for $\xi = \xi_i$, $i = 1, \dots, p$, and $\xi_0 < \xi_1 < \dots \xi_p$.

[4] For each new ξ_i compute the cut-offs r_c, k_∞ that yield an accuracy δ.

[5] Find $\xi = \min_i(t(N, \xi_i))$, where $t(N, \xi_i)$ is the computational time for a simulation with N particles at a ξ_i.

The choice $r_c < B/3$ as a starting parameter is needed since as noted in Section 7.3 the Linked Cell list is efficient only if the number of pairwise computations is reduced to a subvolume of the domain Ω. However for fiber suspensions, see Paper III, we have already computed the optimal ξ for a set of input parameters. The optimality of ξ mentioned here is in terms of computational cost. If one optimal ξ is known then the problem can be scaled to find an optimal ξ for any other set of input parameters. Details on this procedure can be found in Paper III.

Chapter 8

Summary of papers and division of work

Paper I

The first paper entitled *'Corrected trapezoidal rules for a class of singular kernels'* develops a type of high-order quadrature that handles singular kernels. In one-dimension we consider kernels $s(x) = |x|^\gamma$ with $\gamma > -1$ and in two-dimensions $\gamma = -1$. The core of the manuscript deals with the theoretical analysis of the accuracy of the developed quadrature rules. We also provide careful descriptions concerning the techniques used together with implementation considerations. The rules that have been constructed are investigated numerically and shown to match the theoretical results. Under the supervision of Olof Runborg and Anna-Karin Tornberg the author of this thesis has written a large part of the manuscript, performed the proofs in two dimensions and the numerical computations.

Paper II

The second paper, *'A highly accurate boundary treatment for confined Stokes flow'* extends the principles of the same type of quadrature rule that has been analyzed in Paper I to the singular kernel given by the fundamental solution of Stokes equations (*i.e.* the Stokeslet). A quadrature rule that integrates the Stokeslet over a flat plate is developed and validated numerically. This quadrature rule is used to model a wall in the classical problem of a sphere sedimenting towards a straight wall. The analytical solution of the sphere-wall problem provides a good reference case against which we can analyze the strengths and short-comings of our approach to wall treatment. The author of this thesis developed the quadrature rule with feed-back from Anna-Karin Tornberg and also the algebraic treatment of the system. The author also performed the numerical computations and wrote the manuscript with feed-back from Anna-Karin Tornberg and Katarina Gustavsson. Appendix B was contributed by Katarina Gustavsson. This work is based on a parallel Fortran code developed by the author for fibers sedimenting onto a flat plate which was the initial research project of this thesis. However this project was canceled after two and a half years since the slender body theory proved to not yield satisfactory results in conjunction with fully discretized walls. The quadrature rule developed in this paper stemmed from the studies in Paper I and the fiber suspension was replaced by a sphere in the initial code to offer a proper validation of the method.

Paper II is published in *Computers & Fluids*, vol. 66, pp. 215–230 (2012) [52].

Paper III

The third paper *A fast summation method for fiber simulations* deals with the simulation of a large suspension of fibers in periodic domains. The fiber-fiber interaction model is based on the slender body theory and involves integrals in terms of both the Stokeslet and the Laplacian of the Stokeslet (Dipole). The Stokeslet is periodized using the Hasimoto decomposition presented in Section 6 and to obtain similar decay of the constituent sums the periodic Dipole had to be derived starting from the same decomposition. A straightforward method of obtaining the truncation parameters needed by the fast Ewald method was derived for both the periodic Stokeslet and periodic Dipole that enter the fiber-fiber interaction model. The Spectral Ewald method initially designed for point particles was adapted to handle analytic integrals over fibers in close vicinity to each other. Based on the idea of Anna-Karin Tornberg to perform large scale simulations using the Spectral Ewald method the author of this thesis derived the aforementioned numerical treatment. The numerical tests, followed by the numerical simulations were performed under the supervision of Anna-Karin Tornberg. The author of this thesis wrote the manuscript with feedback from Anna-Karin Tornberg on the mathematical model and numerical method and Katarina Gustavsson on the fiber suspension simulations.

Paper IV

A new fast converging decomposition for the periodic Stresslet establishes a new decomposition for the periodic kernel of the stress tensor (Stresslet). Based on the knowledge that the stress tensor can be expressed in terms of the pressure and the gradient of the velocity it was possible to obtain a new decomposition with faster decaying sums than the decomposition already present in the literature which is derived using the Beenakker approach. The novel decomposition stems from the splitting scheme by Hasimoto for the periodic kernel of the Stokes flow (Stokeslet) presented in Section 6 and a new decomposition for the Laplace kernel, as will be explained in Paper IV. The entire manuscript from idea, derivation and numerical implementation to the redaction of the paper has been performed by the author of this thesis.

Paper V

A numerical integration technique for the singular kernels of Laplace and Stokes equations over some curvilinear surfaces extends the work in Paper I and II to a set of curvilinear surfaces. It is more difficult to obtain modified weights for the singular kernels of Laplace and Stokes over non-flat surfaces since it is not possible to compute analytical solutions using exponentials as it is done in Papers I and II. Thus an approach using repeated Richardson extrapolation is used. For complex geometries the modified weights used in the correction operator are not universal. Therefore we identify a class of parameterizable surfaces that yield correction operators which do not require the computation of modified weights in each discrete point. The author of this thesis wrote the manuscript and performed the numerical tests based on a self-directed idea.

Bibliography

[1] N. H. Abel. Solution de quelques problémes á l'aide d'intégrales definies. *Magazin for Naturvidenskaberne*, Aargang I(Bind 2):11–27, 1823.

[2] J. C. Aguilar. High-order corrected trapezoidal quadrature rules for functions with a logarithmic singularity on a circle. *Int. J. Contemp. Math. Sciences*, 3(23):1133–1140, 2008.

[3] J. C. Aguilar and Y. Chen. High-order corrected trapezoidal quadrature rules for the Coulomb potential in three dimensions. *Comput. Math. Appl.*, 49:625–631, 2005.

[4] M. P. Allen and D. J. Tildesley. *Computer Simulation of Liquids.* Clarendon Press, New York, U.S.A., 1989.

[5] K. E. Atkinson. *The Numerical Solution of Integral Equations of the Second Kind.* Cambridge University Press, Cambridge, U.K., 1997.

[6] G. K. Batchelor. Slender-body theory for particles of arbitrary cross-section in Stokes flow. *J. Fluid Mech.*, 44:419–440, 1970.

[7] C. W. J. Beenakker. Ewald sums of the Rotne-Prager tensor. *J. Chem. Phys.*, 85:1581–1582, 1986.

[8] J. R. Blake. A note on the image system for a Stokeslet in a no-slip boundary. *Proc. Camb. Philos. Soc.*, 70:303–310, 1971.

[9] J. F. Brady and G. Bossis. Stokesian dynamics. *Annu. Rev. Fluid Mech.*, 20:111–157, 1988.

[10] J. Bremer and Z. Gimbutas. A Nyström method for weakly singular integral operators on surfaces. *J. Comput. Phys.*, 231(14):4885–4903, 2012.

[11] J. M. Burgers. *Second Report on Viscosity and Plasticity.* North Holland Publishing Companiy, Amsterdam, The Netherlands, 1938.

[12] A. Carlsson. *Near Wall Fibre Orientation in Flowing Suspensions.* PhD thesis, KTH Mechanics, Royal Institute of Technology, Sweden, 2009.

[13] R. Cortez. The method of regularized Stokeslets. *SIAM J. Sci. Comput.*, 23(4):1204–1225, 2001.

[14] R. G. Cox. The motion of long slender bodies in a viscous fluid. Part 1. General theory. *J. Fluid Mech.*, 44:791–810, 1970.

[15] F. R. Cunha and M. Loewenberg. A study of emulsion expansion by a boundary integral method. *Mech. Res. Commun.*, 30(6):639–649, 2003.

[16] T. Darden, D. York, and L. Pedersen. Particle mesh Ewald: An $n \cdot \log(n)$ method for Ewald sums in large systems. *J. Chem. Phys.*, 98(12):10089–10092, 1993.

[17] A. M. J. Davis. Shear flow disturbance due to a hole in the plane. *Phys. Fluids A*, 3:478–480, 1991.

[18] L. M. Delves and J. L. Mohamed. *Computational Methods for Integral Equations.* Cambridge University Press, Cambridge, U.K., 1988.

[19] D. G. Duffy. *Green's Functions with Applications.* Chapman & Hall/CRC Press, 2001.

[20] M. G. Duffy. Quadrature over a pyramid or cube of integrands with a singularity at a vertex. *SIAM J. Numer. Anal.*, 19(6):1260–1262, 1982.

[21] L. Ehrenpreis. Solution of some problems of division: Part I. Division by a polynomial of derivation. *Am. J. Math.*, 76(4):883–903, 1954.

[22] L. Ehrenpreis. Solution of some problems of division: Part II. Division by a punctual distribution. *Am. J. Math.*, 77(2):286–292, 1955.

[23] U. Essmann, L. Perera, M. L. Berkowitz, T. Darden, H. Lee, and L. G. Pedersen. A smooth particle mesh Ewald method. *J. Chem. Phys.*, 103(19):8577–8593, 1995.

[24] P. P. Ewald. Die Berechnung optischer und elektrostatischer Gitterpotentiale. *Ann. Phys.*, 369(3):253–287, 1921.

[25] X.-J. Fan, N. Phan-Thien, and R. Zheng. Completed double layer boundary element method for periodic suspensions. *Z. Angew. Math. Phys.*, 49:167–193, 1998.

[26] T. Götz. *Interactions of Fibers and Flow: Asymptotics, Theory and Numerics.* PhD thesis, Universität Kaiserslautern, Germany, 2000.

[27] L. Greengard and J. Y. Lee. Accelerating the nonuniform fast Fourier transform. *SIAM Rev.*, 46(3):443–454, 2004.

[28] E. K. Guckel. *Large scale simulations of particulate systems using the PME method.* PhD thesis, University of Illinois at Urbana-Champaign, 1999.

[29] G. J. Hancock. The self-propulsion of microscopic organisms through liquids. *Proc. Royal Soc. London. A*, 217(1128):96–121, 1953.

[30] J. Happel and H. Brenner. *Low Reynolds Number Hydrodynamics.* Kluwer, Dordrecht, The Netherlands, 1983.

[31] H. Hasimoto. On the periodic fundamental solutions of the Stokes equations and their application to viscous flow past a cubic array of spheres. *J. Fluid Mech.*, 5:317–328, 1959.

[32] J. Helsing and R. Ojala. On the evaluation of layer potentials close to their sources. *J. Comput. Phys.*, 227(5):2899–2921, 2008.

[33] J. P. Hernández-Ortiz, J. J. de Pablo, and M. D. Graham. Fast computation of many-particle hydrodynamic and electrostatic interactions in a confined geometry. *Phys. Rev. Lett.*, 98(140602), 2007.

[34] D. M. Heyes and F. von Swol. The electrostatic potential and field in the surface region of lamina and semi infinite point charge lattices. *J. Chem. Phys.*, 75(10):5051–5058, 1981.

[35] J. J. L. Higdon. A hydrodynamic analysis of flagellar propulsion. *J. Fluid Mech.*, 90:685–711, 1979.

[36] R. W. Hockney and J. W. Eastwood. *Computer Simulation Using Particles.* Taylor & Francis, New York, U.S.A, 1988.

[37] M. S. Ingber and A. A. Mammoli. A comparison of integral formulations for the analysis of low Reynolds number flows. *Eng. Anal. Bound. Elem.*, 23:307–315, 1999.

[38] P. J. A. Janssen, Anderson P. D., and Loewenberg M. A slender-body theory for low-viscosity drops in shear flow between parallel walls. *Phys. Fluids*, 22(042002), 2010.

[39] R. E. Johnson. An improved slender-body theory for Stokes flow. *J. Fluid Mech.*, 99:411–431, 1980.

[40] S. Jung, S. E. Spagnolie, K. Parikh, M. J. Shelley, and A.-K. Tornberg. Periodic sedimentation in a Stokesian fluid. *Phys. Rev. E*, 74(035302), 2006.

[41] S. Kapur and V. Rokhlin. High-order corrected trapezoidal quadrature rules for singular functions. *SIAM J. Numer. Anal.*, 34(4):1331–1356, 1997.

[42] J. B. Keller and S. I. Rubinow. Slender-body theory for slow viscous flow. *J. Fluid Mech.*, 75:705–714, 1976.

[43] R. Kress. *Linear Integral Equations.* Springer, New York, U.S.A., 1999.

[44] M. H. Lean and A. Wexler. Accurate numerical integration of singular boundary element kernels over boundaries with curvature. *Int. J. Num. Meth. Eng.*, 21(3):211–228, 1985.

[45] D. Lindbo. *Spectral Accuracy in Fast Ewald Methods and Topics in Fluid Interface Simulation.* PhD thesis, KTH Numerical Analysis, Royal Institute of Technology, Sweden, 2011.

[46] D. Lindbo and A.-K. Tornberg. Spectrally accurate fast summation for periodic Stokes potentials. *J. Comput. Phys.*, 229(23):8994–9010, 2010.

[47] D. Lindbo and A.-K. Tornberg. Spectral accuracy in fast Ewald-based methods for particle simulations. *J. Comput. Phys.*, 230(24):8744–8761, 2011.

[48] N. Liron and S. Mochon. Stokes flow for a Stokeslet between two parallel flat plates. *J. Eng. Math.*, 10:287–303, 1976.

[49] M. Loewenberg and E. J. Hinch. Numerical simulation of a concentrated emulsion in shear flow. *J. Fluid Mech.*, 321:395–419, 1996.

[50] J. N. Lyness. An error functional expansion for N-dimensional quadrature with an integrand function singular at a point. *Math. Comput.*, 30(133):1–23, 1976.

[51] B. Malrgrange. Existence et approximation des solutions des équations aux dérivées partielles et des équations de convolution. *Ann. Inst. Fourier*, 6:271–355, 1956.

[52] O. Marin, K. Gustavsson, and A.-K. Tornberg. A highly accurate boundary treatment for confined Stokes flow. *Comput. Fluids*, 66:215–230, 2012.

[53] B. Metzger, M. Nicolas, and É. Guazelli. Falling clouds of particles in viscous fluids. *J. Fluid Mech.*, 580:283–301, 2007.

[54] N. Phan-Thien and D. Tullock. Completed double layer boundary element method in elasticity. *J. Mech. Phys. Sol.*, 41(6):1067–1086, 1993.

[55] C. Pozrikidis. *Boundary Integral and Singularity Methods for Linearized Viscous Flow.* Cambridge University Press, Cambridge, U.K., 1992.

[56] C. Pozrikidis. *A Practical Guide to Boundary-Element Methods with the Software Library BEMLIB.* Chapman & Hall/CRC Press, 2002.

[57] D. Saintillan, E. Darve, and E. S. G. Shaqfeh. A smooth particle-mesh Ewald algorithm for Stokes suspension simulations: The sedimentation of fibers. *Phys. Fluids*, 17(033301), 2005.

[58] Y. Shan, J. L. Klepeis, M. P. Eastwood, R. O. Dror, and D. E. Shaw. A fast Ewald mesh method for molecular simulations. *J. Chem. Phys.*, 122(054101), 2005.

[59] A. Sierou and J. F. Brady. Accelerated Stokesian Dynamics simulations. *J. Fluid Mech.*, 448:115–146, 2001.

[60] M. E. Staben, A. Z. Zinchenko, and R. H. Davis. Motion of a particle between two parallel walls in low-Reynolds number Poiseuille flow. *Phys. Fluids*, 15:1711–1733, 2003.

[61] A. H. Stroud and D. Secrest. *Gaussian Quadrature Rules.* Prentice Hall, Upper Saddle River, U.S.A., 1966.

[62] A.-K. Tornberg and K. Gustavsson. A numerical method for simulations of rigid fiber suspensions. *J. Comput. Phys.*, 215:172–196, 2005.

[63] A.-K. Tornberg and M. J. Shelley. Simulating the dynamics and interactions of flexible fibers in stokes flows. *J. Comput. Phys.*, 196:8–40, 2004.

[64] A. Y. Toukmaji and J.A. Board Jr. Ewald summation techniques in perspective: a survey. *Comput. Phys. Commun.*, 95(3):73–92, 1996.

[65] L. C. Wrobel, D. Soares Jr., and C. L. Das Bhaumik. Drop deformation in Stokes flow through converging channels. *Eng. Anal. Bound. Elem.*, 33(7):993–1000, 2009.

[66] H. Zhao, A. H. G. Isfahani, L. N. Olson, and J. B. Freund. A spectral boundary integral method for flowing blood cells. *J. Comput. Phys.*, 229:3726–3744, 2010.

Part II

Included papers

Corrected trapezoidal rules for a class of singular functions

Oana Marin[1,2], Olof Runborg[2], Anna-Karin Tornberg[1,2]
[1]Linné FLOW Centre
[2]KTH-CSC (NA), SE-100 44 Stockholm, Sweden

Abstract

A set of accurate quadrature rules applicable to a class of integrable functions with isolated singularities is designed and analyzed theoretically in one and two dimensions. These quadrature rules are based on the trapezoidal rule with corrected quadrature weights for points in the vicinity of the singularity. To compute the correction weights small size ill-conditioned systems have to be solved. The convergence of the correction weights is accelerated by the use of compactly supported functions that annihilate boundary errors. Convergence proofs with error estimates for the resulting quadrature rules are given in both one and two dimensions. The tabulated weights are specific for the singularities under consideration, but the methodology extends to a large class of functions with integrable isolated singularities. Furthermore in one dimension we have obtained a closed form expression based on which the modified weights can be computed directly.

1 Introduction

This paper focuses on the design of accurate quadrature rules for functions with isolated singularities. The need to numerically evaluate such integrals arises in *e.g.* methods based on boundary integral equations, where the fundamental solution, or Green's function, has an integrable singularity.

In the literature one can find several different approaches to the numerical integration of singular functions. These include different semi-analytical techniques and singularity subtraction approaches [17]. Different mappings and changes of coordinates in order to remove the singularity have also been applied [10, 7, 6, 19, 13, 16]. The approach that we will follow here is to modify the trapezoidal rule to render it high order accurate for singular functions. The resulting quadrature rules are very attractive due to their simplicity – the trapezoidal rule is modified with a small number of correction weights, and the simple structure is retained.

The trapezoidal rule is spectrally accurate for smooth, compactly supported or periodic functions. For other functions it is in general at most second order accurate. There are two sources of these larger errors: singularities and boundaries. Both these error sources can be reduced by modifying the quadrature weights locally, in a vicinity of the singularity (which is assumed here to be isolated) or at the boundaries. Hence, by adjusting the weights locally, high order accurate versions of the trapezoidal rule can be constructed also in the presence of singularities and boundaries. The new weights are pre-computed and tabulated; once constructed, the modified trapezoidal rule can easily be applied. In the case of a singularity, the modified weights are however specific to the singularity that is being considered.

The first singularity corrected trapezoidal methods introduced by Rokhlin in [18] were restricted in practice to rather low orders of accuracy, since the magnitude of the correction weights became very large for higher order methods. To alleviate this problem, Alpert

[4] used more correction weights than the optimal number, and minimized their sum of squares. The integration interval is split at the singularity into two subintervals, such that the singularity is always at a boundary. Kapur and Rokhlin [11] introduced additional quadrature points and weights outside the interval of integration and could thereby obtain much smaller correction weights. Such a method is not always convenient to apply, and yet another approach by Alpert, [5] was to introduce a hybrid Gauss-Trapezoidal rule, where a few of the regularly spaced nodes towards the interval end points are replaced with irregularly spaced nodes. The computed weights at the irregular nodes are both bounded and positive.

In the papers [18, 4, 11, 5], quadrature rules are designed for singular functions of the form $f(x) = \phi(x)s(x) + \psi(x)$ and $f(x) = \phi(x)s(x)$, where $\phi(x)$ and $\psi(x)$ are regular functions and $s(x)$ has an isolated integrable singularity such as $s(x) = |x|^\gamma$, $\gamma > -1$ or $s(x) = \log(|x|)$. The integration interval is split at the singularity, and for each subinterval there is a regular end and a singular end. Corrections to the trapezoidal rule are applied at both ends, to reduce the boundary errors at the regular end, and to control the error from the singularity and the boundary at the other end. Theoretical analysis is offered for all these methods.

It is inconvenient to split the domain of integration at the singularity in higher dimensions. Aguilar and Chen designed singularity corrected trapezoidal rules for the $s(\mathbf{x}) = \log(|\mathbf{x}|)$ singularity in $\mathbb{R}^2$ [2], and for $s(\mathbf{x}) = 1/|\mathbf{x}|$ in $\mathbb{R}^3$ [3]. The singularities are interior to the domain, and a singularity correction in the interior is combined with boundary corrections to yield higher order methods. No theoretical analysis is provided in these papers, but the expected order of accuracy is given for the method, which is consistent with numerical examples.

One procedure for constructing a set of increasingly accurate quadrature rules is to require the exact integration of monomials of increasing degree, see [12]. A similar procedure is followed here to determine the modified weights of the corrected trapezoidal rules. The exact integration of monomials, up to a desired degree, multiplying the singular function $s(x)$ is first enforced for a specific uniform grid spacing h. This leads to a linear system of equations for the modified weights. The obtained correction weights will then depend on h. This is not very practical. Instead, one wants to use the converged weights that are defined as the weights obtained in the limit as $h \to 0$. They are grid independent, universal for the given singularity, and can be tabulated once computed. As Aguilar and Chen [2, 3] note, the system to be solved for the weights becomes severely ill-conditioned, more so for smaller h, and multi-precision arithmetic is needed to perform this task.

Duan and Rokhlin [9] apply similar techniques to design singularity corrected trapezoidal rules for $s(\mathbf{x}) = \log(|\mathbf{x}|)$ singularities in two dimensions. They however do not seek converged correction weights, but compute weights that depend on the grid size h. They are able to derive analytical, although very lengthy, expressions for the weights, and thereby avoid solving an ill-conditioned system. The analytical formulas that they derive are however approximated numerically, but to very high accuracy. A theoretical proof is offered regarding the accuracy of the quadrature rules, using also some theoretical results developed in [14].

In this paper we consider singularities of the kind $s(x) = |x|^\gamma$, $\gamma > -1$ in one dimension and $s(\mathbf{x}) = 1/|\mathbf{x}|$ in two dimensions. The singularities are interior to the domain. As in Aguilar and Chen [2], our singularity corrections can be combined with boundary corrections [4] to reduce boundary errors as needed.

One difference in our approach compared to all previous works cited above lies in the procedure for computing the weights. The corrected trapezoidal rule is based on the punctured trapezoidal rule (excluding the point of singularity) together with a correction operator that applies in grid points in the vicinity of the singularity. In order to accelerate the convergence of the weights, the boundary errors in the punctured trapezoidal rule must be reduced. The approach used previously is to introduce a boundary correction for the trapezoidal rule. Here, we suggest an alternative approach where we multiply $s(x)$ by a fixed, compactly supported function $g(x)$. This completely annihilates the boundary errors. The convergence rate of the weights will now instead depend on the number of derivatives of g that vanish at the point of singularity. This is proven for the one-dimensional case in Section 3; see Lemma 5. For the two-dimensional case, we cannot offer a rigorous proof, but note the same behavior in practice. With a faster convergence rate for the weights, larger values of h can be used, which to some extent reduces the ill-conditioning of the system. To compute converged weights to double precision, we use a multi-precision library that allows for computations in multi-precision arithmetic.

In the one-dimensional case we are able to show that the converged weights are the solution to a linear system of equations, where the system matrix is a Vandermonde matrix and where the right hand side has an analytic expression in terms of the Riemann zeta function (see Appendix A). Hence in this case, we can directly compute the converged weights by solving this system of equations.

The singularity corrections that we design are of order $\mathcal{O}\left(h^{2+\gamma+d+2p}\right)$ in $\mathbb{R}^d$, $d = 1, 2$, as weights are modified at grid points in p layers around the singularity, see Theorem 4. In two dimensions ($\gamma = -1$), for $p = 0$, which corresponds to a single correction weight at the singularity, we have a third order rule. For each additional layer of correction weights, the order of accuracy increases by two. Compared to Aguilar and Chen [2] our layers differ somewhat, with the number of correction weights in our approach growing slower as the number of layers is increased. We also have a theoretical analysis of the method's convergence rate.

In two-dimensions, we have considered the singularity $1/|\mathbf{x}|$, which is the Green's function for Laplace's equation in three dimensions, instead of $\log(|\mathbf{x}|)$ as in [2, 9]. A boundary integral equation for the three-dimensional Laplace contains integrals over two-dimensional surfaces, that are the boundaries of the domain. This method would apply when the boundary is flat. Extensions based on the approach and the theory presented in this paper are discussed in the conclusions.

The outline of the paper is as follows. In section 2, we describe the modified trapezoidal rules and their structure, and we define the system of equations from which the correction weights can be obtained. The theoretical analysis is presented in Section 3, starting with the accuracy of the punctured trapezoidal rule, before we prove the accuracy of the modified trapezoidal rules. We also give a proof of convergence for the correction weights in one dimension. Numerical results to validate the constructed quadrature rules together with discussions concerning implementation aspects are provided in Section 4.

Notations

In order to render the text more legible the multi-index notation will be used. A multi-index in the d-dimensional set-up is $\boldsymbol{\alpha} = (\alpha_1, \ldots, \alpha_d)$. For $\boldsymbol{\alpha} \in \mathbb{R}^d, \mathbb{Z}^d$, including multi-indices, we define the norms $|\boldsymbol{\alpha}| = \sum_{i=1}^{d} |\alpha_i|$ and $|\boldsymbol{\alpha}|_2 = \sqrt{\sum_{i=1}^{d} \alpha_i^2}$. To be more explicit we write at times $|\boldsymbol{\alpha}|_1$ instead of $|\boldsymbol{\alpha}|$. We also use $\boldsymbol{\alpha}! = \alpha_1! \cdots \alpha_d!$. For $\mathbf{x} \in \mathbb{R}^d$ we define monomials $\mathbf{x}^{\boldsymbol{\alpha}} = x_1^{\alpha_1} \cdot .. x_d^{\alpha_d}$ and for the partial derivatives

$$\partial^{\boldsymbol{\alpha}} f(\mathbf{x}) = \frac{\partial^{|\boldsymbol{\alpha}|}}{\partial x_1^{\alpha_1} .. \partial x_d^{\alpha_d}} f(\mathbf{x}).$$

Occasionally we will make use of the basis vectors in $\mathbb{R}^d$ which shall be denoted by $\mathbf{e}_i$ with $1 \le i \le d$.

The notations $[x]$ - integer part of x and $\{x\}$ - fractional part of x will also be used; recall $x = [x] + \{x\}$. Throughout the manuscript C will denote a constant which is independent of other parameters relevant in the particular context where it is used, typically the grid spacing h and position $\mathbf{x}$. It may at times be accompanied by a numeral subscript to differentiate it from other similar constants.

Trapezoidal rule

Consider a function $f \in C^{2p+2}(\mathbb{R}^d)$, defined on the interval $S = [-a,\ a]$ for $d = 1$, and on the square $S = [-a,\ a]^2$ for $d = 2$. The standard trapezoidal rule in one dimension is then given by

$$\int_S f(x)\mathrm{d}x \approx T_h[f] := \sum_{\beta=-N}^{N} hf(\beta h) - \frac{1}{2}\left(hf(a) + hf(-a)\right), \qquad h = 2a/N, \tag{1}$$

and in two dimensions, with the same h,

$$\int_S f(\mathbf{x})\mathrm{d}\mathbf{x} \approx T_h[f] := \sum_{\substack{\boldsymbol{\beta}h\in S\\ \boldsymbol{\beta}\in\mathbb{Z}^2}} h^2 f(\boldsymbol{\beta}h) - \frac{1}{2}\sum_{\substack{\boldsymbol{\beta}h\in \partial S\\ \boldsymbol{\beta}\in\mathbb{Z}^2}} h^2 f(\boldsymbol{\beta}h) - \frac{1}{4}\sum_{\substack{\boldsymbol{\beta}h\in \partial S_c\\ \boldsymbol{\beta}\in\mathbb{Z}^2}} h^2 f(\boldsymbol{\beta}h), \tag{2}$$

where we used ∂S_c to denote the four corner points of S. Typically for a smooth integrand over a bounded interval the numerical integration using the trapezoidal rule exhibits second order convergence. To delve further into the error analysis of the trapezoidal rule and later the modified trapezoidal rule we will use two main approaches: the Euler-Maclaurin expansion and Fourier analysis. We use the following precise form of the Euler-Maclaurin expansion:

Theorem 1 (Euler-Maclaurin expansion)**.** *For a function $f \in C^{2p+2}([a,b])$*

$$\begin{aligned}\int_a^b f(x)\mathrm{d}x =& T_h[f] + \sum_{\ell=1}^{p}\frac{h^{2\ell}b_{2\ell}}{(2\ell)!}(f^{(2\ell-1)}(b) - f^{(2\ell-1)}(a))\\ &+ \frac{h^{2p+2}}{(2p+2)!}\int_a^b B_{2p+2}\left(\left\{\frac{x-a}{h}\right\}\right)f^{(2p+2)}(x)\mathrm{d}x.\end{aligned} \tag{3}$$

The expression uses the Bernoulli polynomials B_p and the Bernoulli numbers defined as $b_p = B_p(0)$. The periodized versions $B_p(\{x\})$ are piecewise smooth and bounded functions. See the book by Cohen [8, Proposition 9.3.1 and Remark 2] for more details.

From the Euler-Maclaurin expansion (3) we see that there are two main sources of errors in the trapezoidal rule, corresponding to the terms in the error expression. First, we have the contribution to the error from the boundaries given by

$$\sum_{\ell=1}^{p}\frac{h^{2\ell}b_{2\ell}}{(2\ell)!}(f^{(2\ell-1)}(b) - f^{(2\ell-1)}(a)) \tag{4}$$

Second, we have the contribution of the error which is determined by the regularity of the function,

$$\frac{h^{2p+2}}{(2p+2)!}\int_a^b B_{2p+2}\left(\left\{\frac{x-a}{h}\right\}\right)f^{(2p+2)}(x)\mathrm{d}x.$$

There are two common situations when the sum in (4) vanishes for integrands of class $C^{2p+2}(\mathbb{R})$: when the integrand is periodic on $[a,b]$ and when the integrand is compactly supported within (a,b). In this case the error of the trapezoidal rule is $\mathcal{O}\left(h^{2p+2}\right)$. If the integrand is C^∞ and there are no boundary errors the trapezoidal rule exhibits spectral convergence.

The accuracy of the trapezoidal rule may also be studied through Fourier analysis. In this approach we use the Poisson summation formula for $f \in C_c^2(\mathbb{R})$ and note that

$$T_h[f] = \sum_j hf(jh) = \sum_k \hat{f}\left(\frac{k}{h}\right) = \int f(x)\mathrm{d}x + \sum_{k\neq 0} \hat{f}\left(\frac{k}{h}\right),$$

where

$$\hat{f}(k) = \int f(x)e^{-2\pi i k x}\mathrm{d}x. \tag{5}$$

Our aim is to show that this oscillatory integral can be estimated by

$$|\hat{f}(k)| \leq \frac{C}{|k|^p}, \qquad p > 1,$$

from which it will then follow that

$$\left|T_h[f] - \int f(x)\mathrm{d}x\right| \leq \sum_{k\neq 0}\left|\hat{f}\left(\frac{k}{h}\right)\right| \leq Ch^p \sum_{k\neq 0}\frac{1}{|k|^p} \leq C'h^p.$$

2 Modified trapezoidal rules

We will construct modified trapezoidal rules with a singularity correction for functions with isolated singularities. More precisely, we consider functions $f(\mathbf{x}) = s(\mathbf{x})\phi(\mathbf{x})$ where $\phi(\mathbf{x})$ is regular and

$$s(\mathbf{x}) = |\mathbf{x}|^\gamma \text{ with } \begin{cases} \gamma \in (-1,0) & \mathbf{x} \in \mathbb{R}, \\ \gamma = -1 & \mathbf{x} \in \mathbb{R}^2 \end{cases}. \tag{6}$$

Simple correction

Let us define the punctured trapezoidal rule, as applied to a compactly supported function f,

$$T_h^0[f] = \sum_{\boldsymbol{\beta}\neq 0} h^d f(\boldsymbol{\beta} h), \qquad \boldsymbol{\beta} \in \mathbb{Z}^d. \tag{7}$$

Introduce the simply corrected quadrature rule $Q_h^0[\phi\cdot s] = T_h^0[\phi\cdot s] + a(h)\omega_0\phi(0)$ where $a(h)$ is a weight factor. The correction weight $\omega_0(h)$ is defined by

$$a(h)\omega_0(h)g(0) = \int g(\mathbf{x})s(\mathbf{x})\mathrm{d}x - T_h^0[g\cdot s], \tag{8}$$

where $g(x)$ is a compactly supported function with $g(x) \neq 0$. The function $g(x)$ is introduced to annihilate the boundary errors from the punctured trapezoidal rule.

If the weight factor $a(h)$ is chosen correctly $\omega_0(h) \to \overline{\omega}_0$ as $h \to 0$ where $\overline{\omega}_0$ does not depend on h nor on g. The convergence rate $\omega_0(h) \to \overline{\omega}_0$, however, depends strongly on the choice of g. The convergence is fast when the function g is *flat* at the singularity, *i.e.* it has several derivatives that vanish at the origin, see Section 4.

The modified quadrature rule reads

$$Q_h^0[\phi \cdot s] = T_h^0[\phi \cdot s] + a(h)\overline{\omega}_0\phi(0), \tag{9}$$

where for a space of dimension d

$$a(h) = h^d s(h) = h^{\gamma+d}. \tag{10}$$

We will show below that adding a modification at the origin in this way will lead to a method of order $\mathcal{O}\left(h^{2+d+\gamma}\right)$ for $s(\mathbf{x})$ given by (6). This assumes that the function $\phi(x)$ is regular enough, and also compactly supported within the integration domain. If it is not compactly supported, T_h^0 should be replaced by a boundary corrected punctured trapezoidal rule, see [4].

Higher order correction

A higher order quadrature rule will involve more correction weights. Define

$$Q_h^p[\phi \cdot s] = T_h^0[\phi \cdot s] + a(h) \sum_{\boldsymbol{\beta} \in \mathcal{L}_p} \overline{\omega}_{\boldsymbol{\beta}}\phi(\boldsymbol{\beta}h), \tag{11}$$

where

$$\mathcal{L}_p = \{\boldsymbol{\beta} \in \mathbb{Z}^d \text{ s.t.} |\boldsymbol{\beta}|_1 \leq p\}. \tag{12}$$

In analogy with (8), the weights should satisfy the following equations

$$\int g(\mathbf{x})s(\mathbf{x})\mathbf{x}^{2\boldsymbol{\alpha}}\mathrm{d}\mathbf{x} = T_h^0[g \cdot s \cdot \mathbf{x}^{2\boldsymbol{\alpha}}] + a(h) \sum_{\boldsymbol{\beta} \in \mathcal{L}_p} \omega_{\boldsymbol{\beta}}(h)(\boldsymbol{\beta}h)^{2\boldsymbol{\alpha}} g(\boldsymbol{\beta}h), \quad \forall\, \boldsymbol{\alpha} \text{ s.t. } |\boldsymbol{\alpha}|_1 \leq p. \tag{13}$$

Temporarily denote the weight associated with a point (x_i, y_j) $(\beta = (i,j))$ by $w_{i,j}$. We then require $w_{\pm i,\pm j} = w_{\pm j,\pm i}$ for all possible combinations of signs. Such a weight will be denoted by w_q^m, where $q = |i| + |j|$, and m will be defined below. Due to these symmetry assumptions for the weights, the equations in (13) are stated only for even order monomials since the equations for odd monomials are automatically satisfied. We will show that the number of unknown weights equals the number of equations in (13).

Let us now consider the two-dimensional case. Consider sets $\mathcal{L}_p$ as in (12), with $d = 2$ (see Fig. 1). Introduce the subsets $\mathcal{G}_q^m \subset \mathcal{L}_p$ over which weights are equal,

$$\mathcal{G}_q^m = \{\boldsymbol{\beta} \in \mathbb{Z}^2 \quad s.t. \quad |\boldsymbol{\beta}|_1 = q \ , \ |\boldsymbol{\beta}|_2 = \sqrt{m^2 + (q-m)^2}\}. \tag{14}$$

for $q = 0, \dots, p$ and $m = 0, \dots, [q/2]$. This defines disjoint subsets of $\mathcal{L}_p$ such that $\mathcal{G}_q^m \cap \mathcal{G}_{q'}^{m'} = 0$ for $m \neq m'$, or $q \neq q'$ and $\bigcup_{q \leq p} \bigcup_{m \leq [q/2]} \mathcal{G}_q^m = \mathcal{L}_p$.

To each of these sets $\mathcal{G}_q^m$ we associate one weight ω_q^m. The number of all distinct weights associated with $\mathcal{L}_p$ is

$$N_p = \sum_{m=0}^{p} ([m/2] + 1) = \begin{cases} (p/2)^2 + p + 1, & \text{if } p \text{ is even,} \\ (p+1)^2/4 + (p+1)/2, & \text{if } p \text{ is odd.} \end{cases} \tag{15}$$

We want to enforce (13) for all $\boldsymbol{\alpha}$ such that $|\boldsymbol{\alpha}| \leq p$. This set can be described by $\alpha \in \mathcal{M}_p$ with

$$\mathcal{M}_p = \bigcup_{q \leq p} \bigcup_{m \leq [q/2]} \{(q-m, m)\}. \tag{16}$$

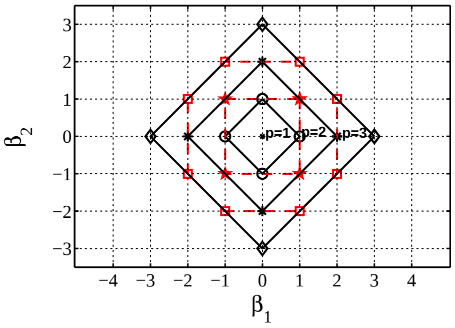

Figure 1: The sets $\mathcal{L}_p$ include all grid points on and inside the layers indicated in the figure.

For this set, we have $|\mathcal{M}_p| = N_p$, and (13) constitutes a square system. Relating to the notation above, we have $\boldsymbol{\alpha}_q^m = (q-m, m)$.

In Table 1 we list the monomials along with the sets of discretization points where the weights are corrected for layers up to $q = 4$. The first column provides the levels q and m at which we take a monomial $\mathbf{x}^{2\boldsymbol{\alpha}}$ where $\boldsymbol{\alpha} = \boldsymbol{\alpha}_q^m$ is listed in the third column. The last two columns list the sets of points, $\mathcal{G}_q^m$ and the associated weights $\bar{\omega}_q^m$.

Hence we solve the following $N_p \times N_p$ linear system of equations

$$a(h) \sum_{q=0}^{p} \sum_{m=0}^{[q/2]} \omega_q^m \sum_{\boldsymbol{\beta} \in \mathcal{G}_q^m} g(\boldsymbol{\beta} h)(\boldsymbol{\beta} h)^{2\boldsymbol{\alpha}} \\ = \int g(\mathbf{x}) s(\mathbf{x}) \mathbf{x}^{2\boldsymbol{\alpha}} \mathrm{d}\mathbf{x} - T_h^0[g \cdot s \cdot \mathbf{x}^{2\boldsymbol{\alpha}}], \qquad \forall \boldsymbol{\alpha} \in \mathcal{M}_p. \tag{17}$$

In order to recast this system in matrix notation we introduce an index $i = 0, \ldots, N_p - 1$ and define $\boldsymbol{\alpha}_i$, ω_i and $\mathcal{G}_i$ from $\boldsymbol{\alpha}_q^m$, ω_q^m and $\mathcal{G}_q^m$, respectively, by letting $i = N_q + m$, where N_q is given by (15). We can then introduce the matrices K, $\tilde{I} \in \mathbb{R}^{N_p \times N_p}$ with elements

$$K_{ij} = \sum_{\boldsymbol{\beta} \in \mathcal{G}_j} \boldsymbol{\beta}^{2\boldsymbol{\alpha}_i}, \qquad i, j = 0, \ldots, N_p - 1,$$

and

$$\tilde{I}_{ij} = g(\boldsymbol{\beta} h)\delta_{ij}, \qquad \boldsymbol{\beta} \in \mathcal{G}_j, \qquad i, j = 0, \ldots, N_p - 1.$$

which is well defined since the function $g(\boldsymbol{\beta} h)$ takes the same value for all $\boldsymbol{\beta} \in \mathcal{G}_i$.

The right-hand side of the system becomes

$$c_i(h) = \frac{1}{h^{2|\boldsymbol{\alpha}_i|} a(h)} \left(\int g(\mathbf{x}) s(\mathbf{x}) \mathbf{x}^{2\boldsymbol{\alpha}_i} \mathrm{d}\mathbf{x} - T_h^0[g \cdot s \cdot \mathbf{x}^{2\boldsymbol{\alpha}_i}] \right), i = 0, \ldots, N_p - 1.$$

These expressions lead to the system

$$K \tilde{I}(h) \boldsymbol{\omega}(h) = \boldsymbol{c}(h). \tag{18}$$

Here the solution vector $\boldsymbol{\omega}(h) = (\omega_0(h), \ldots, \omega_{N_p-1}(h))$ and the right-hand side $\boldsymbol{c}(h) = (c_0(h), \ldots, c_{N_p-1}(h))$ have the ordering provided by the new indexing.

Table 1: Sets of discrete points $\mathcal{G}_q^m$ for different values of q.

q	m	$\boldsymbol{\alpha}_q^m =$ $(q-m,m)$	$\mathbf{x}^{2\boldsymbol{\alpha}}$	$\mathcal{G}_q^m$	Associated weight $\overline{\varpi}_q^m$
0	0	(0,0)	1	(0,0)	$\overline{\varpi}_0^0$
1	0	(1,0)	x_1^2	$(\pm1,0)$ $(0,\pm1)$	$\overline{\varpi}_1^0$
2	0	(2,0)	x_1^4	$(\pm2,0)$ $(0,\pm2)$	$\overline{\varpi}_2^0$
	1	(1,1)	$x_1^2x_2^2$	$(\pm1,\pm1)$	$\overline{\varpi}_2^1$
3	0	(3,0)	x_1^6	$(\pm3,0)$ $(0,\pm3)$	$\overline{\varpi}_3^0$
	1	(2,1)	$x_1^4x_2^2$	$(\pm2,\pm1)$ $(\pm1,\pm2)$	$\overline{\varpi}_3^1$
4	2	(2,2)	$x_1^4x_2^4$	$(\pm2,\pm2)$	$\overline{\varpi}_4^2$
	1	(3,1)	$x_1^6x_2^2$	$(\pm3,\pm1)$ $(\pm1,\pm3)$	$\overline{\varpi}_4^1$
	0	(4,0)	x_1^8	$(\pm4,0)$ $(0,\pm4)$	$\overline{\varpi}_4^0$
5	2	(3,2)	$x_1^6x_2^4$	$(\pm3,\pm2)$ $(\pm2,\pm3)$	$\overline{\varpi}_5^2$
	1	(4,1)	$x_1^8x_2^2$	$(\pm4,\pm1)$ $(\pm1,\pm4)$	$\overline{\varpi}_5^1$
	0	(5,0)	x_1^{10}	$(\pm5,0)$ $(0,\pm5)$	$\overline{\varpi}_5^0$

For a given p consider the converged solution $\boldsymbol{\omega}(h) \to \overline{\boldsymbol{\varpi}}$ of the system (18) and define the modified quadrature rule for a singularity $s(\mathbf{x})$ with modified weights $\overline{\varpi}_q^m$

$$Q_h^p[\phi \cdot s] = T_h^0[\phi \cdot s] + A_h^p[\phi], \tag{19}$$

with

$$A_h^p[\phi] = a(h) \sum_{q=0}^{p} \sum_{m=0}^{[q/2]} \overline{\varpi}_q^m \sum_{\beta \in \mathcal{G}_q^m} \phi(\beta h), \tag{20}$$

where $\mathcal{G}_q^m$ as in (14). The constructed rule Q_h^p has accuracy $\mathcal{O}\left(h^{2p+3}\right)$, see Theorem 4.

In one dimension the expressions for the sets $\mathcal{L}_p$, $\mathcal{M}_p$ greatly simplify since in this context $N_p = p+1$ and

$$\mathcal{L}_p = \{\beta \in \mathbb{Z}, |\beta| = j,\ j \le p\}, \qquad \mathcal{M}_p = \{\alpha \in \mathbb{N}, \alpha = j,\ j \le p\}, \qquad \mathcal{G}_i = \{\pm i\}.$$

So $K \in \mathbb{R}^{(p+1)\times(p+1)}$ has elements $K_{00} = 1$ and otherwise the Vandermonde structure $K_{ij} = 2j^{2i}$. Moreover, $\tilde{I}_{ij}(h) = g(ih)\delta_{ij}$. The right-hand side entries are simply

$$c_i(h) := \frac{1}{h^{2i}a(h)} \left[\int g(x)s(x)x^{2i}\mathrm{d}x - T_h^0[g \cdot s \cdot x^{2i}] \right].$$

The corrected punctured trapezoidal rule Q_h^p defined as in (19) has the correction operator

$$A_h^p[\phi] := a(h) \sum_{j=0}^{p} \overline{\varpi}_j (\phi(jh) + \phi(-jh)). \tag{21}$$

3 Theoretical analysis

The techniques used to prove the accuracy of the modified quadrature rule differ in the one-dimensional set-up from the two-dimensional one. The Fourier approach is chosen for the lower dimension while in two dimensions the Euler-Maclaurin formula is applied in each direction. In this analysis, we focus on the errors due to the singularities and the accuracy of the singularity corrections. Therefore, we consider the integration of $f(x) = \phi(x)s(x)$, where $\phi(x)$ is compactly supported within the integration domain.

To begin with we provide an accuracy result for the punctured trapezoidal rule. Using this result we obtain an error estimate of the modified trapezoidal rule in terms of h and the difference $\boldsymbol{\omega}(h) - \overline{\boldsymbol{\varpi}}$ in Theorem 4, where $\boldsymbol{\omega}(h) - \overline{\boldsymbol{\varpi}}$ can be made sufficiently small with a proper choice of g so that it does not alter the asymptotic order. This is proven in the one-dimensional case, where we show that $\boldsymbol{\omega}(h) \to \overline{\boldsymbol{\varpi}}$ and also obtain an estimate of $|\boldsymbol{\omega}(h) - \overline{\boldsymbol{\varpi}}|$, thus yielding a complete error estimate for the modified trapezoidal rule in one dimension. In two dimensions, we offer no rigorous proofs for the convergence of the weights, but note the same behaviour as in one dimension in numerical experiments.

Accuracy of punctured trapezoidal rule

To prove the order of convergence of the constructed quadrature rule we start by deriving an error estimate for the punctured trapezoidal rule. Theorem 2 states the one-dimensional result. The corresponding two dimensional result in Theorem 3 is weaker; note that the function $f = \tilde{g} \cdot s$ vanishes at the origin, thus $\mathcal{T}_h[f] = \mathcal{T}_h^0[f]$. General error estimates of the type below were derived in [14]. However, those include also the boundary errors and do not cover the cases we are interested in here.

Theorem 2. *Consider* $f : \mathbb{R} \to \mathbb{R}$ *given as* $f = g(x)s(x)$ *where* $s(x) = |x|^\gamma$ *with* $\gamma > -1$. *Let* p *and* q *be integers such that* $0 \leq p < q$ *and* $2q + 1 > \gamma$. *Take* $g(x) \in C_c^{2q+2}(\mathbb{R})$ *with* $g^{(k)}(0) = 0$ *for* $k = 2, 4, \ldots, 2p$. *Then*

$$\left| \int f(x)\mathrm{d}x - T_h^0[f] - g(0)h^{\gamma+1}\overline{c}(\gamma) \right| \leq C\left(h^{2p+\gamma+3} + h^{2q+2}\right),$$

where $\overline{c}(\gamma)$ *depends on* γ *but is independent of* h *and* g.

We note that if $\gamma > 0$ this also gives an estimate for the standard trapezoidal rule since then $f(0) = 0$ and $T_h[f] = T_h^0[f]$. The proof of this theorem is given in Section 3. In Lemma A.1 in Appendix A, a closed form expression for $\overline{c}(\gamma)$ is given.

Theorem 3. *Consider* $f : \mathbb{R}^2 \to \mathbb{R}$ *given as* $f(\mathbf{x}) = \tilde{g}(\mathbf{x})s(\mathbf{x})$ *where* $s(\mathbf{x}) = 1/|\mathbf{x}|$. *Let* q *and* p *be integers such that* $q > p$. *Take* $\tilde{g} \in C_c^{2q+3}(\mathbb{R}^2)$ *with* $\partial^{\boldsymbol{k}}\tilde{g}(\mathbf{0}) = 0$ *for* $\forall \boldsymbol{k} \in \mathbb{N}^2$ *such that* $|\boldsymbol{k}| < 2p + 2$. *Then it holds that*

$$\left| \int f(\mathbf{x})\mathrm{d}\mathbf{x} - \mathcal{T}_h[f] \right| \leq Ch^{2p+3}.$$

This theorem is proven in Section 3.

One-dimensional case

In this section we prove Theorem 2. We begin by introducing a cut-off function $\psi \in C^\infty$ satisfying $\psi(x) = \psi(-x)$ and

$$\psi(x) = \begin{cases} 0, & |x| \leq 1/2, \\ 1, & |x| \geq 1. \end{cases} \tag{22}$$

We then have

$$T_h^0[f] = T_h[f\psi(\cdot/h)].$$

Consequently,

$$\int f(x)\mathrm{d}x - T_h^0[f] = \int f(x)(1-\psi(x/h))\mathrm{d}x + \int f(x)\psi(x/h)\mathrm{d}x - T_h[f\psi(\cdot/h)], \tag{23}$$

and we can estimate the two parts separately. For the first term we have

$$\begin{aligned}\int f(x)(1-\psi(x/h))\mathrm{d}x &= \int_{-h}^{h} g(x)s(x)(1-\psi(x/h))\mathrm{d}x \\ &= h^{\gamma+1}\int_{-1}^{1} g(hx)s(x)(1-\psi(x))\mathrm{d}x,\end{aligned} \tag{24}$$

where we have used the definition of ψ in (22) and a rescaling of the interval. By the symmetry of $\psi(x), s(x)$ and the assumption of vanishing derivatives

$$\begin{aligned}&\int_{-1}^{1} (g(hx)-g(0))\, s(x)(1-\psi(x))\mathrm{d}x \\ &\quad = \int_{-1}^{1}\left(g(hx) - \sum_{j=0}^{2p+1}\frac{g^{(j)}(0)}{j!}(hx)^j\right) s(x)(1-\psi(x))\mathrm{d}x.\end{aligned}$$

Therefore, after estimating the remainder term in the Taylor expansion of $g(x)$, which is bounded by $\tilde{C}h^{2p+2}|x|^{2p+2}$,

$$\begin{aligned}&\left|\int_{-1}^{1}(g(hx)-g(0))s(x)(1-\psi(x))\mathrm{d}x\right| \\ &\qquad \le \tilde{C}h^{2p+2}\int_{-1}^{1}|x|^{\gamma+2p+2}|1-\psi(x)|\mathrm{d}x \le Ch^{2p+2}.\end{aligned} \tag{25}$$

Define

$$\bar{c}_1(\gamma) = \int_{-1}^{1} s(x)(1-\psi(x))\, dx.$$

Then we obtain from (25) and (24),

$$\begin{aligned}&\left|\int f(x)(1-\psi(x))\mathrm{d}x - g(0)h^{\gamma+1}\bar{c}_1(\gamma)\right| \\ &\qquad = h^{\gamma+1}\left|\int_{-1}^{1}(g(hx)-g(0))s(x)(1-\psi(x))\mathrm{d}x\right| \le Ch^{2p+\gamma+3}.\end{aligned} \tag{26}$$

For the second term in (23) we can use the strategy based on the Fourier analysis as in Section 1 for the standard trapezoidal rule applied to $f(x)\psi(x/h)$. Hence, since $f(x)\psi(x/h) \in C_c^{2q+2}(\mathbb{R})$ we obtain from the Poisson summation formula (5)

$$\begin{aligned}T_h[f\psi(\cdot/h)] &= \int f(x)\psi(x/h)\mathrm{d}x + \sum_{k\neq 0}\hat{f}_\psi(k/h,h), \\ \hat{f}_\psi(k,h) &= \int f(x)\psi(x/h)e^{-2\pi i k x/h}\mathrm{d}x.\end{aligned} \tag{27}$$

Moreover, by the symmetry of $\psi(x)$,

$$\begin{aligned}\hat{f}_\psi(k/h,h) + \hat{f}_\psi(-k/h,h) &= 2\int g(x)s(x)\psi(x/h)\cos(2\pi kx/h)\mathrm{d}x \\ &= 2\Re\int_0^\infty (g(x)+g(-x))s(x)\psi(x/h)e^{2\pi i k x/h}\mathrm{d}x.\end{aligned} \tag{28}$$

We will now use Lemma 1 stated and proven below, which provides estimates on oscillatory integrals of this type. Since the even derivatives of $g(x)$ are zero up to order $2p$ in $x = 0$, all derivatives of $\tilde{g}(x) = g(x) + g(-x)$ are zero up to order $2p + 1$ in $x = 0$. We can therefore apply Lemma 1 to the integral with $2p + 1$ for p and $2q + 2$ for q. We obtain

$$\begin{aligned}\int_0^\infty (g(x) + g(-x))s(x)\psi(x/h)e^{2\pi ikx/h}\mathrm{d}x =& \tilde{g}(0)W(2\pi k)h^{\gamma+1}(2\pi k)^{-2(q+1)} \\ &+ \mathcal{O}\left(k^{-2(q+1)}(h^{\gamma+2p+3} + h^{2q+2})\right).\end{aligned} \tag{29}$$

Using (28) combined with (29), an expression for $\hat{f}_\psi(k/h, h) + \hat{f}_\psi(-k/h, h)$ is obtained. Rewriting the sum in (27) to use this expression, we get

$$\begin{aligned}T_h[f\psi(\cdot/h)] &= \int f(x)\psi(x/h)\mathrm{d}x + 2\Re\sum_{k=1}^\infty \int_0^\infty (g(x) + g(-x))s(x)\psi(x/h)e^{2\pi ikx/h}\mathrm{d}x \\ &= \int f(x)\psi(x/h)\mathrm{d}x + 4g(0)h^{\gamma+1}\Re\sum_{k=1}^\infty \frac{W(2\pi k)}{(2\pi k)^{2(q+1)}} \\ &\quad + [h^{\gamma+2p+3} + h^{2q+2}]\sum_{k=1}^\infty \mathcal{O}\left(k^{-2(q+1)}\right) \\ &= \int f(x)\psi(x/h)\mathrm{d}x + g(0)h^{\gamma+1}\bar{c}_2(\gamma) + \mathcal{O}\left(h^{\gamma+2p+3} + h^{2q+2}\right),\end{aligned} \tag{30}$$

where

$$\bar{c}_2(\gamma) = 4\Re\sum_{k=1}^\infty \frac{W(2\pi k)}{(2\pi k)^{2(q+1)}}.$$

Note that this is well-defined since $q \geq 0$ and $W(k)$ is bounded in k. Using (23) we get

$$\begin{aligned}&\left|\int f(x)dx - T_h^0(f) - g(0)h^{\gamma+1}\left(\bar{c}_1(\gamma) - \bar{c}_2(\gamma)\right)\right| \\ &\qquad \leq \left|\int f(x)(1 - \psi(x/h))dx - g(0)h^{\gamma+1}\bar{c}_1(\gamma)\right| \\ &\qquad\quad + \left|\int f(x)\psi(x/h)dx - T_h(f\psi(./h)) + g(0)h^{\gamma+1}\bar{c}_2(\gamma)\right|.\end{aligned}$$

The result of Theorem 2 now follows from (26) and (30) with

$$\bar{c}(\gamma) = \bar{c}_1(\gamma) - \bar{c}_2(\gamma) = \int_{-1}^1 s(x)(1 - \psi(x))\,dx - 4\Re\sum_{k=1}^\infty \frac{W(2\pi k)}{(2\pi k)^{2(q+1)}},$$

which is independent of h and $g(x)$. It remains to state and prove Lemma 1.

Lemma 1. *Let p and q be integers such that $0 \leq p < q$ and h and k are positive real numbers, and γ any real number. Suppose $g(x) \in C_c^q$ with $\operatorname{supp} g \subset [0, L]$ and $g^{(\ell)}(0) = 0$ for $\ell = 1, \ldots, p$. If $q > \gamma + 1$ and $\psi(x)$ as given in (22) then there is a function $W(k)$ such that*

$$\left|\int_0^\infty \psi(x/h)g(x)x^\gamma e^{ikx/h}\mathrm{d}x - g(0)W(k)h^{\gamma+1}k^{-q}\right| \leq C_q k^{-q}(h^{\gamma+2+p} + h^q), \tag{31}$$

where $W(k)$ is bounded in k and independent of h and $g(x)$ (but depends on q).

Proof. We let $s(x) = x^\gamma$ and note that $|s^{(j)}(x)| \le Cx^{\gamma-j}$. Since supp $\psi(x/h)g(x) \subset [h/2, L] \subset (0,\infty)$ we have after q integrations by parts,

$$\begin{aligned} I(h,k) &:= \int_0^\infty \psi(x/h)g(x)s(x)e^{ikx/h}\mathrm{d}x \\ &= \left(\frac{ih}{k}\right)^q \int_0^\infty \left(\frac{\mathrm{d}^q}{\mathrm{d}x^q}\psi(x/h)g(x)s(x)\right) e^{ikx/h}\mathrm{d}x, \end{aligned}$$

Define $W(k)$ as

$$W(k) = i^q \int_0^\infty \left(\frac{\mathrm{d}^q}{\mathrm{d}x^q}\psi(x)s(x)\right) e^{ikx}\mathrm{d}x. \tag{32}$$

Clearly $W(k)$ does not depend on h. Moreover, $\psi^{(j)}(x)$ is compactly supported for $j \ge 1$ and $|s^{(q)}(x)| \le x^{\gamma-q}$ is integrable because $q > \gamma+1$. Therefore,

$$|W(k)| \le \int_0^\infty |\psi(x)s^{(q)}(x)|\mathrm{d}x + \sum_{j=1}^{q} d_{q,j} \int_0^\infty |\psi^{(j)}(x)s^{(q-j)}(x)|\mathrm{d}x \le C,$$

where $d_{q,j}$ are the binomial coefficients. The estimate is independent of k, showing the boundedness of $W(k)$. After rescaling the integral we also have,

$$\begin{aligned} W(k) =& i^q h^{q-1} \int_0^\infty \left(\frac{\mathrm{d}^q}{\mathrm{d}x^q}\psi(x/h)s(x/h)\right) e^{ikx/h}\mathrm{d}x \\ =& i^q h^{q-1-\gamma} \int_0^\infty \left(\frac{d^q}{\mathrm{d}x^q}\psi(x/h)s(x)\right) e^{ikx/h}\mathrm{d}x. \end{aligned}$$

Then, with $r(x) := \psi(x/h)g(x)$,

$$\begin{aligned} &I(h,k) - g(0)W(k)h^{\gamma+1}k^{-q} \\ &\quad = \left(\frac{ih}{k}\right)^q \int_0^\infty \left(\frac{\mathrm{d}^q}{\mathrm{d}x^q}[r(x) - g(0)\psi(x/h)]s(x)\right) e^{ikx/h}\mathrm{d}x \\ &\quad = \left(\frac{h}{ik}\right)^q \sum_{j=0}^{q} d_{q,j} \int_0^\infty [r^{(j)}(x) - g(0)h^{-j}\psi^{(j)}(x/h)]s^{(q-j)}(x)e^{ikx/h}\mathrm{d}x. \end{aligned} \tag{33}$$

We have the following expression for the derivatives of $r(x)$,

$$r^{(j)}(x) = \begin{cases} \sum_{\ell=0}^{j} \frac{d_{j,\ell}}{h^{j-\ell}}\psi^{(j-\ell)}(x/h)g^{(\ell)}(x), & h/2 \le x \le h, \\ g^{(j)}(x), & h < x \le L, \end{cases}$$

since $\psi^{(j)}(x) \equiv 0$ for $j > 0$ and $x > h$. Let $\delta_{i,j}$ be the Kronecker delta. Exploiting the facts that $\psi(x/h) \equiv 0$ for $x < h/2$ and $\psi(x/h) \equiv 1$ for $x > h$ we obtain for $0 \leq j \leq q$,

$$\begin{aligned}
&\int_0^\infty [r^{(j)}(x) - g(0)h^{-j}\psi^{(j)}(x/h)]s^{(q-j)}(x)e^{ikx/h}\mathrm{d}x \\
&\quad = \int_{h/2}^h \left[\sum_{\ell=0}^j \frac{d_{j,\ell}}{h^{j-\ell}}\psi^{(j-\ell)}(x/h)g^{(\ell)}(x) - \frac{1}{h^j}\psi^{(j)}(x/h)g(0)\right] s^{(q-j)}(x)e^{ikx/h}\mathrm{d}x \\
&\quad + \int_h^L g^{(j)}(x)s^{(q-j)}(x)e^{ikx/h}\mathrm{d}x - \delta_{0,j}g(0)\int_h^\infty s^{(q)}(x)e^{ikx/h}\mathrm{d}x \\
&\quad = \sum_{\ell=0}^j \frac{d_{j,\ell}}{h^{j-\ell}}\int_{h/2}^h \psi^{(j-\ell)}(x/h)\left[g^{(\ell)}(x) - \delta_{0,\ell}g(0)\right] s^{(q-j)}(x)e^{ikx/h}\mathrm{d}x \\
&\quad + \int_h^L [g^{(j)}(x) - \delta_{0,j}g(0)]s^{(q-j)}(x)e^{ikx/h}\mathrm{d}x \\
&\quad - \delta_{0,j}g(0)\int_L^\infty s^{(q)}(x)e^{ikx/h}\mathrm{d}x. \qquad (34)
\end{aligned}$$

We will now use the assumption that $g^{(\ell)}(0) = 0$ for $1 \leq \ell \leq p$. From Taylor's theorem we get

$$|g^{(j)}(x) - g^{(j)}(0)| \leq |g^{(p+1)}|_\infty \frac{|x|^{p+1-j}}{(p+1-j)!} = C|x|^{p+1-j}, \qquad 0 \leq j \leq p,$$

and therefore also

$$|g^{(j)}(x) - \delta_{0,j}g(0)| \leq Cx^{\max(p+1-j,0)}.$$

We use this to estimate the integrals in (34). First, for $0 \leq j \leq q$ and $0 \leq \ell \leq j$,

$$\begin{aligned}
&\frac{1}{h^{j-\ell}}\left|\int_{h/2}^h \psi^{(j-\ell)}(x/h)\left[g^{(\ell)}(x) - \delta_{0,\ell}g(0)\right] s^{(q-j)}(x)e^{ikx/h}\mathrm{d}x\right| \\
&\qquad \leq \frac{C}{h^{j-\ell}}\int_{h/2}^h x^{\max(p+1-\ell,0)+\gamma-q+j}\mathrm{d}x \leq Ch^{\max(p+1-\ell,0)+\gamma-q+1+\ell} \\
&\qquad \leq Ch^{p+2+\gamma-q},
\end{aligned}$$

where we used the fact that $h^{\max(r,0)} \leq h^r$ when $h < 1$. Moreover, for the second integral in (34),

$$\begin{aligned}
&\left|\int_h^L [g^{(j)}(x) - \delta_{0,j}g(0)]s^{(q-j)}(x)e^{ikx/h}\mathrm{d}x\right| \\
&\qquad \leq C\int_h^L x^{\max(p+1-j,0)+\gamma-q+j}\mathrm{d}x \leq C(h^{\max(p+1-j,0)+\gamma-q+j+1} + 1) \\
&\qquad \leq C(h^{p+2+\gamma-q} + 1).
\end{aligned}$$

Finally, for the last integral in (34),

$$\left|\int_L^\infty s^{(q)}(x)e^{ikx/h}\mathrm{d}x\right| \leq C\int_L^\infty x^{\gamma-q}\mathrm{d}x \leq C,$$

since $q > \gamma + 1$. Together with (33) these estimates show that

$$|I(h,k) - g(0)W(k)h^{\gamma+1}k^{-q}| \leq C\left(\frac{h}{k}\right)^q (h^{p+2+\gamma-q} + 1) \leq Ck^{-q}(h^{\gamma+2+p} + h^q).$$

This proves the lemma. □

Two-dimensional case

The Euler-Maclaurin expansion formula is the basis for the theoretical analysis in two dimensions. Since it provides an error estimate based on the cancellation and boundedness of higher order derivatives — see (1) — we first evaluate the higher order derivatives of the singular function $s(\mathbf{x}) = 1/|\mathbf{x}|$. The concluding result of this subsection is the proof of Theorem 3 that was stated in Section 3.

Lemma 2. *The partial derivatives of order $\boldsymbol{k}$ of $\mathbf{x}^{\boldsymbol{\alpha}}/|\mathbf{x}|$ with $\mathbf{x} = (x_1, x_2)$ are given as*

$$\partial^{\boldsymbol{k}} \frac{\mathbf{x}^{\boldsymbol{\alpha}}}{|\mathbf{x}|} = \frac{1}{|\mathbf{x}|^{|\boldsymbol{k}|-|\boldsymbol{\alpha}|+1}} P_{\boldsymbol{k},\boldsymbol{\alpha}}\left(\frac{\mathbf{x}}{|\mathbf{x}|}\right), \tag{35}$$

where $P_{\boldsymbol{k},\boldsymbol{\alpha}}$ is a polynomial of $\deg P_{\boldsymbol{k},\boldsymbol{\alpha}} = |\boldsymbol{k}| + |\boldsymbol{\alpha}|$ in two variables $P_{\boldsymbol{k},\boldsymbol{\alpha}}(\mathbf{x}) = P_{\boldsymbol{k},\boldsymbol{\alpha}}(x_1, x_2)$.

Proof. For $\boldsymbol{k} = (0, 0)$ we have

$$\partial^{\boldsymbol{k}} \frac{\mathbf{x}^{\boldsymbol{\alpha}}}{|\mathbf{x}|} = \left(\frac{\mathbf{x}}{|\mathbf{x}|}\right)^{\boldsymbol{\alpha}} \frac{1}{|\mathbf{x}|^{1-|\boldsymbol{\alpha}|}},$$

which agrees with (35) with $P_{\boldsymbol{k},\boldsymbol{\alpha}}(\boldsymbol{z}) = \boldsymbol{z}^{\boldsymbol{\alpha}}$. We let $P^{(j)}_{\boldsymbol{k},\boldsymbol{\alpha}}(x_1, x_2) := \partial_{x_j} P_{\boldsymbol{k},\boldsymbol{\alpha}}(x_1, x_2)$ and note that these are polynomials of degree one less than the degree of $P_{\boldsymbol{k},\boldsymbol{\alpha}}(x_1, x_2)$ itself. Assume the theorem statement is true for $\boldsymbol{k}$ and let $\boldsymbol{k} \to \boldsymbol{k} + \mathbf{e}_1$. Then we want to show that

$$\partial^{\boldsymbol{k}+\boldsymbol{e}_1} \frac{\mathbf{x}^{\boldsymbol{\alpha}}}{|\mathbf{x}|} = \frac{1}{|\mathbf{x}|^{|\boldsymbol{k}|-|\boldsymbol{\alpha}|+2}} P_{\boldsymbol{k}+\boldsymbol{e}_1,\boldsymbol{\alpha}}\left(\frac{\mathbf{x}}{|\mathbf{x}|}\right),$$

for some polynomial $P_{\boldsymbol{k}+\mathbf{e}_1,\boldsymbol{\alpha}}$ of degree $|\boldsymbol{k}| + |\boldsymbol{\alpha}| + 1$. By applying the chain rule and evaluating, we get

$$\begin{aligned}
&\partial_{x_1} \frac{1}{|\mathbf{x}|^{|\boldsymbol{k}|-|\boldsymbol{\alpha}|+1}} P_{\boldsymbol{k},\boldsymbol{\alpha}}\left(\frac{\mathbf{x}}{|\mathbf{x}|}\right) = \\
&\quad = P_{\boldsymbol{k},\boldsymbol{\alpha}}\left(\frac{\mathbf{x}}{|\mathbf{x}|}\right) \partial_{x_1} \frac{1}{|\mathbf{x}|^{|\boldsymbol{k}|-|\boldsymbol{\alpha}|+1}} + \\
&\quad + \frac{1}{|\mathbf{x}|^{|\boldsymbol{k}|-|\boldsymbol{\alpha}|+1}} \left(\left(\frac{1}{|\mathbf{x}|} - \frac{x_1^2}{|\mathbf{x}|^3} \right) P^{(1)}_{\boldsymbol{k},\boldsymbol{\alpha}}\left(\frac{\mathbf{x}}{|\mathbf{x}|}\right) + \left(\frac{x_1 x_2}{|\mathbf{x}|^3} \right) P^{(2)}_{\boldsymbol{k},\boldsymbol{\alpha}}\left(\frac{\mathbf{x}}{|\mathbf{x}|}\right) \right) \\
&\quad = \frac{-(|\boldsymbol{k}| - |\boldsymbol{\alpha}| + 1) x_1}{|\mathbf{x}|^{|\boldsymbol{k}|-|\boldsymbol{\alpha}|+3}} P_{\boldsymbol{k},\boldsymbol{\alpha}}\left(\frac{\mathbf{x}}{|\mathbf{x}|}\right) + \\
&\quad + \frac{1}{|\mathbf{x}|^{|\boldsymbol{k}|-|\boldsymbol{\alpha}|+2}} \left(\left(1 - \frac{x_1^2}{|\mathbf{x}|^2} \right) P^{(1)}_{\boldsymbol{k},\boldsymbol{\alpha}}\left(\frac{\mathbf{x}}{|\mathbf{x}|}\right) + \left(\frac{x_1 x_2}{|\mathbf{x}|^2} \right) P^{(2)}_{\boldsymbol{k},\boldsymbol{\alpha}}\left(\frac{\mathbf{x}}{|\mathbf{x}|}\right) \right) \\
&\quad =: \frac{1}{|\mathbf{x}|^{|\boldsymbol{k}|-|\boldsymbol{\alpha}|+2}} P_{\boldsymbol{k}+\mathbf{e}_1,\boldsymbol{\alpha}}\left(\frac{\mathbf{x}}{|\mathbf{x}|}\right)
\end{aligned}$$

where $\deg P_{\boldsymbol{k}+\mathbf{e}_1,\boldsymbol{\alpha}} = |\boldsymbol{k}| + |\boldsymbol{\alpha}| + 1$, which is what we needed to show. The case $\boldsymbol{k} \to \boldsymbol{k} + \mathbf{e}_2$ can be proved in the same way. This induction step proves that the expression provided by the lemma is valid.

$\square$

Lemma 3. *Let $\Omega \subset \mathbb{R}^2$ be a compact set. Consider $f{:}\Omega \to \mathbb{R}$ given as $f(\mathbf{x}) = \tilde{g}(\mathbf{x}) \cdot s(\mathbf{x})$ where $s(\mathbf{x}) = 1/|\mathbf{x}|$ and $\tilde{g} \in C^q(\Omega)$ has vanishing derivatives upto order $p \le q$ in the origin: $\partial^{\boldsymbol{k}} \tilde{g}(\mathbf{0}) = 0$ for all $\boldsymbol{k} \in \mathbb{N}^2$ such that $|\boldsymbol{k}| < p$. Then, for each $|\boldsymbol{n}| \le q$ there is a constant $C(\boldsymbol{n})$ independent of $\mathbf{x}$ and p, such that*

$$|\partial^{\boldsymbol{n}} f(\mathbf{x})| \le C(\boldsymbol{n}) |\mathbf{x}|^{p-1-|\boldsymbol{n}|}, \qquad \forall \mathbf{x} \in \Omega \setminus \{0\}.$$

Proof. In order to compute the higher order derivatives of f the Leibniz rule is applied

$$\partial^{\boldsymbol{n}}(f(\mathbf{x})) = \partial^{\boldsymbol{n}}(\tilde{g}(\mathbf{x}) \cdot s(\mathbf{x})) = \sum_{\boldsymbol{\ell}+\boldsymbol{r}=\boldsymbol{n}} b^n_{\ell r} \partial^{\boldsymbol{\ell}} \tilde{g}(\mathbf{x}) \partial^{\boldsymbol{r}} s(\mathbf{x}),$$

where $b^n_{\ell r}$ are binomial coefficients. By Taylor expanding $\partial^{\boldsymbol{\ell}}\tilde{g}$ and recalling that $\partial^{\boldsymbol{k}}\tilde{g}(\mathbf{0}) = 0$ for all $\boldsymbol{k} \in \mathbb{N}^2$ such that $|\boldsymbol{k}| < p$ we have for $|\boldsymbol{\ell}| < p$

$$\partial^{\boldsymbol{\ell}}\tilde{g}(\mathbf{x}) = \sum_{|\boldsymbol{k}|=0}^{p-1-|\boldsymbol{\ell}|} \frac{\mathbf{x}^{\boldsymbol{k}}}{\boldsymbol{k}!} \frac{\partial^{(\boldsymbol{\ell}+\boldsymbol{k})}\tilde{g}(\mathbf{0})}{\partial \mathbf{x}^{\boldsymbol{k}}} + R_\ell(\mathbf{x})|\mathbf{x}|^{p-|\boldsymbol{\ell}|} = R_\ell(\mathbf{x})|\mathbf{x}|^{p-|\boldsymbol{\ell}|}.$$

On the other hand, when $p \leq |\boldsymbol{\ell}| \leq q$ we just use the boundedness of $\partial^{\boldsymbol{\ell}}\tilde{g}$ over Ω and obtain, for all $\mathbf{x} \in \Omega$,

$$|\partial^{\boldsymbol{\ell}}\tilde{g}(\mathbf{x})| \leq C_0 \begin{cases} |\mathbf{x}|^{p-|\boldsymbol{\ell}|} & : |\boldsymbol{\ell}| < p, \\ 1 & : p \leq |\boldsymbol{\ell}| \leq q, \end{cases} \qquad C_0 = \max_{|\ell| \leq |n|} \sup_{x \in \Omega} \max\left(|R_\ell(\mathbf{x})|, |\partial^{\boldsymbol{\ell}}\tilde{g}(\mathbf{x})|\right).$$

By using Lemma 2 with $\boldsymbol{\alpha} = 0$ for $\partial^{\boldsymbol{r}}s(\mathbf{x})$ we have for $\boldsymbol{r} \leq \boldsymbol{n}$,

$$|\partial^{\boldsymbol{r}}s(\mathbf{x})| = \frac{1}{|\mathbf{x}|^{|\boldsymbol{r}|+1}} P_{\boldsymbol{r},0}\left(\frac{\mathbf{x}}{|\mathbf{x}|}\right) \leq \frac{C_1}{|\mathbf{x}|^{|\boldsymbol{r}|+1}}, \qquad C_1 = \max_{|r| \leq |n|} \sup_{x} \left| P_{\boldsymbol{r},0}\left(\frac{\mathbf{x}}{|\mathbf{x}|}\right)\right|,$$

where C_1 is bounded since $\{\mathbf{x}/|\mathbf{x}|,\ \mathbf{x} \in \mathbb{R}^2\}$ is compact. Together these estimates yield

$$\begin{aligned} |\partial^{\boldsymbol{n}}(f(\mathbf{x}))| \leq & \sum_{\boldsymbol{\ell}+\boldsymbol{r}=\boldsymbol{n}} b^n_{\ell r} |\partial^{\boldsymbol{\ell}}\tilde{g}(\mathbf{x})||\partial^{\boldsymbol{r}}s(\mathbf{x})| \\ \leq & C_0 C_1 \sum_{\boldsymbol{\ell}+\boldsymbol{r}=\boldsymbol{n}} \frac{b^n_{\ell r}}{|\mathbf{x}|^{|\boldsymbol{r}|+1}} \begin{cases} |\mathbf{x}|^{p-|\boldsymbol{\ell}|} & : |\boldsymbol{\ell}| < p, \\ 1 & : p \leq |\boldsymbol{\ell}| \leq q, \end{cases} \\ = & C_0 C_1 \sum_{\boldsymbol{\ell}+\boldsymbol{r}=\boldsymbol{n}} b^n_{\ell r} \begin{cases} |\mathbf{x}|^{p-1-|\boldsymbol{n}|} & : |\boldsymbol{\ell}| < p, \\ |\mathbf{x}|^{-|\boldsymbol{r}|-1} & : p \leq |\boldsymbol{\ell}| \leq q. \end{cases} \end{aligned} \tag{36}$$

Let $\eta := \sup_{x \in \Omega} |\mathbf{x}|$. Then, when $p \leq |\boldsymbol{\ell}| \leq |\boldsymbol{n}| \leq q$,

$$\begin{aligned} \max_{\ell+r=n} |\mathbf{x}|^{-|\boldsymbol{r}|-1} &= \max_{\ell+r=n} \frac{1}{\eta^{|\boldsymbol{r}|+1}} \left|\frac{\mathbf{x}}{\eta}\right|^{-|\boldsymbol{r}|-1} \\ &\leq \left(\max_{\ell+r=n} \frac{1}{\eta^{|\boldsymbol{r}|+1}}\right) \left|\frac{\mathbf{x}}{\eta}\right|^{p-1-|\boldsymbol{n}|} =: C_2 \, |\mathbf{x}|^{p-1-|\boldsymbol{n}|} \ . \end{aligned}$$

Entering this in (36) we finally have

$$|\partial^{\boldsymbol{n}}(f(\mathbf{x}))| \leq |\mathbf{x}|^{p-1-|\boldsymbol{n}|} \, C_0 C_1 \sum_{\boldsymbol{\ell}+\boldsymbol{r}=\boldsymbol{n}} b^n_{\ell r}(1 + C_2),$$

which proves the lemma since the sum is bounded independent of p. □

Lemma 4. *Consider* $f{:}\mathbb{R}^2 \to \mathbb{R}$ *given as* $f(\mathbf{x}) = \tilde{g}(\mathbf{x}) \cdot s(\mathbf{x})$ *where* $s(\mathbf{x}) = 1/|\mathbf{x}|$. *Take* $\tilde{g} \in C_c^{2m+3}(\mathbb{R}^2)$ *with* $\partial^{\boldsymbol{k}}\tilde{g}(\mathbf{0}) = 0$ *for all* $\boldsymbol{k} \in \mathbb{N}^2$ *such that* $|\boldsymbol{k}| < 2p + 2$. *Then*

$$\int_{-a}^{a} |\partial^{\boldsymbol{n}}(\tilde{g}(\mathbf{x})s(\mathbf{x}))| \mathrm{d}x_1 \leq C|x_2|^{2p-2m}, \quad |\boldsymbol{n}| = 2m + 2,$$

with $\mathbf{x} = (x_1, x_2)$, $x_2 \neq 0$, *when* $m > p$. *This estimate is also true when* $m = p$ *if* $\mathbf{n}$ *contains at least one derivative in the* x_1*-direction,* i.e. *if we can write* $\mathbf{n} = \tilde{\mathbf{n}} + \mathbf{e}_1$ *for some multi-index* $\tilde{\mathbf{n}}$.

Proof. We first consider the case $m > p$. By using Lemma 3 with $2p+2$ for p we estimate the integrand

$$\int_{-a}^{a} |\partial^{\boldsymbol{n}} \tilde{g}(\mathbf{x}) s(\mathbf{x})| \mathrm{d}x_1 \leq C(\boldsymbol{n}) \int_{-a}^{a} |\mathbf{x}|^{2p+1-|\boldsymbol{n}|} \mathrm{d}x_1 = C(\boldsymbol{n}) \int_{-a}^{a} |\mathbf{x}|^{2p-2m-1} \mathrm{d}x_1. \tag{37}$$

Since $x_2 \neq 0$ we can perform the change of variables $x_1 = x_2 s$ and $\mathrm{d}x_1 = x_2 \mathrm{d}s$. We obtain

$$\begin{aligned} \int_{-a}^{a} |\mathbf{x}|^{2p-2m-1} \mathrm{d}x_1 &= |x_2|^{2p-2m} \int_{-a/x_2}^{a/x_2} \sqrt{1+s^2}^{\,2p-2m-1} \mathrm{d}s \\ &\leq |x_2|^{2p-2m} \int_{-\infty}^{\infty} \frac{1}{\sqrt{1+s^2}^{\,2m-2p+1}} \mathrm{d}s \leq C |x_2|^{2p-2m}, \end{aligned} \tag{38}$$

since here $2m - 2p + 1 > 1$, which means that the integral is bounded.

Now we turn to the case $m = p$ and define the polynomial

$$Q(\mathbf{x}) = \sum_{|\ell| = 2p+2} \frac{\partial^{\boldsymbol{\ell}} \tilde{g}(0)}{\partial \mathbf{x}^{\ell}} \frac{\mathbf{x}^{\boldsymbol{\ell}}}{\boldsymbol{\ell}!}.$$

Since $\partial^{\boldsymbol{k}} Q(0) = 0$ for $|\boldsymbol{k}| < 2p+2$, this polynomial has the property that

$$\partial^{\boldsymbol{k}} [\tilde{g}(\mathbf{x}) - Q(\mathbf{x})]|_{\mathbf{x}=0} = 0, \quad |\boldsymbol{k}| \leq 2p+2. \tag{39}$$

The function f can be split as

$$f(\mathbf{x}) = (\tilde{g}(\mathbf{x}) - Q(\mathbf{x})) s(\mathbf{x}) + Q(\mathbf{x}) s(\mathbf{x}). \tag{40}$$

We can now use Lemma 3 for $(\tilde{g} - Q)s$ with $2p+2$ zero derivatives instead of only $2p+1$ as in the case $m > p$. This is allowed since $\tilde{g}$ has $2m+3 = 2p+3$ continuous derivatives. Then, in the same way as in (38) we find a constant C_1 such that

$$\int_{-a}^{a} \Big| \partial^{\boldsymbol{n}} [\tilde{g}(\mathbf{x}) - Q(\mathbf{x})] s(\mathbf{x}) \Big| \mathrm{d}x_1 \leq C_1 |x_2|^{2p-2m} = C_1. \tag{41}$$

Next we seek to bound the $\boldsymbol{n}$-th derivative of $Q(\mathbf{x})s(\mathbf{x})$ and proceed by splitting $\boldsymbol{n} = \tilde{\boldsymbol{n}} + \mathbf{e}_1$. We first take the $\tilde{\boldsymbol{n}}$-th derivative and from Lemma 2 with $|\boldsymbol{k}| = 2p+1$ and $|\boldsymbol{\alpha}| = 2p+2$ we obtain

$$\partial^{\tilde{\boldsymbol{n}}} [Q(\mathbf{x}) s(\mathbf{x})] = \sum_{|\ell| = 2p+2} \frac{\partial^{\ell} \tilde{g}(0)}{\ell! \partial \mathbf{x}^{\ell}} P_{\tilde{\boldsymbol{n}}, \boldsymbol{\ell}} \left(\frac{\mathbf{x}}{|\mathbf{x}|} \right) =: P \left(\frac{\mathbf{x}}{|\mathbf{x}|} \right). \tag{42}$$

By further taking the derivative in the $\mathbf{e}_1$ direction and using the same differentiation as in Lemma 2 we have

$$\partial^{\boldsymbol{n}} [Q(\mathbf{x}) s(\mathbf{x})] = \partial_{x_1} P \left(\frac{\mathbf{x}}{|\mathbf{x}|} \right) = \frac{x_2}{|\mathbf{x}|^2} E \left(\frac{\mathbf{x}}{|\mathbf{x}|} \right) \tag{43}$$

where E is another polynomial. We note that $\sup_x |E(\mathbf{x}/|\mathbf{x}|)| =: C_2 < \infty$ as before. In order to bound the integral over $\partial^{\boldsymbol{n}}[Q(\mathbf{x})s(\mathbf{x})]$ we apply once more the change of variables $x_1 = s x_2$ and obtain

$$\begin{aligned} \int_{-a}^{a} \Big| \partial^{\boldsymbol{n}} [Q(\mathbf{x}) s(\mathbf{x})] \Big| \mathrm{d}x_1 &= \int_{-a}^{a} \left| \frac{x_2}{|\mathbf{x}|^2} E \left(\frac{\mathbf{x}}{|\mathbf{x}|} \right) \right| \mathrm{d}x_1 \leq C_2 \int_{-a}^{a} \frac{|x_2|}{|\mathbf{x}|^2} \mathrm{d}x_1 \\ &= C_2 \int_{-a/x_2}^{a/x_2} \frac{1}{1+s^2} \mathrm{d}x_1 \leq \ C \int_{-\infty}^{\infty} \frac{1}{1+s^2} \mathrm{d}s = \pi C_2, \end{aligned} \tag{44}$$

Gathering (41) and (44) we finally have that for $p = m$

$$\begin{aligned}\int_{-a}^{a} |\partial^{\boldsymbol{n}}(\tilde{g}(\mathbf{x})s(\mathbf{x}))|\mathrm{d}x_1 &\leq \int_{-a}^{a} \left|\partial^{\boldsymbol{n}}[\tilde{g}(\mathbf{x}) - Q(\mathbf{x})]s(\mathbf{x})\right|\mathrm{d}x_1 + \int_{-a}^{a} \left|\partial^{\boldsymbol{n}}[Q(\mathbf{x})s(\mathbf{x})]\right|\mathrm{d}x_1 \\ &\leq C_1 + \pi C_2,\end{aligned}$$

which concludes the proof of the lemma. □

We are now ready to prove Theorem 3. Let the compact support of f be denoted D and suppose that $D \subset [-a,\ a]^2$. The error estimate will be obtained by evaluating two consequent approximations according to the split

$$\begin{aligned}\int_D f(\mathbf{x})\mathrm{d}\mathbf{x} - \mathcal{T}_h[f] &= \int_D f(\mathbf{x})\mathrm{d}\mathbf{x} - \int_{-a}^{a} T_h[f(\cdot, x_2)]\mathrm{d}x_2 + \int_{-a}^{a} T_h[f(\cdot, x_2)]\mathrm{d}x_2 - \mathcal{T}_h[f] \\ &= \int_{-a}^{a} I_1(x_2)\mathrm{d}x_2 + \sum_{j\in\mathbb{Z}} I_2(jh)h,\end{aligned} \tag{45}$$

with

$$\begin{aligned}I_1(x) &= \int_{-a}^{a} f(x_1, x)\mathrm{d}x_1 - T_h[f(\cdot, x)], \\ I_2(x) &= \int_{-a}^{a} f(x, x_2)\mathrm{d}x_2 - T_h[f(x, \cdot)].\end{aligned} \tag{46}$$

We note that by Lemma 3 with p set to $2p+2$ we have $\lim_{x\to 0} f(\mathbf{x}) = 0$ and f can therefore be defined by continuity at the origin. This implies that both $I_1(x)$ and $I_2(x)$ are continuous at $x = 0$.

Since $f(\mathbf{x})$ is smooth when $x_2 \neq 0$ we obtain from the Euler-Maclaurin expansion (3) that

$$I_1(x_2) = \frac{h^{2m+2}}{(2m+2)!} \int_{-a}^{a} B_{2m+2}\left(\left\{\frac{x_1 + a}{h}\right\}\right)\partial_{x_1}^{2m+2} f(\mathbf{x})\mathrm{d}x_1,$$

for any $m \leq q$ and $x_2 \neq 0$. Therefore, since $B_{2m+2}(\{x\})$ is bounded,

$$|I_1(x_2)| \leq C_m h^{2m+2} \int_{-a}^{a} |\partial_{x_1}^{2m+2} f(\mathbf{x})|\mathrm{d}x_1,$$

for $m \leq q$ and $x_2 \neq 0$. We distinguish two cases according to whether x_2 is in a vicinity of the origin where the singularity plays a higher role or x_2 is away from the origin.

When $0 < |x_2| < h$ we take $m = p$ and obtain from Lemma 4 with $\boldsymbol{n} = (2p+2, 0)$ that

$$|I_1(x_2)| \leq C_1 h^{2p+2}$$

When $|x_2| \geq h$ we take $m = q > p$ and obtain from Lemma 4 that

$$|I_1(x_2)| \leq C_2 h^{2q+2} |x_2|^{2p-2q}.$$

Now, since $I_1(x_2)$ is continuous at $x_2 = 0$ the integral can be bounded as

$$\begin{aligned}\int_{-a}^{a} |I_1(x_2)|\mathrm{d}x_2 &\leq C_1 h^{2p+2} \int_{-h}^{h} \mathrm{d}x_2 + C_2 h^{2q+2} \int_{a \geq |x_2| > h} |x_2|^{2p-2q} \mathrm{d}x_2 \\ &= 2Ch^{2p+3} + 2Ch^{2q+2} \frac{h^{2p-2q+1} - a^{2p-2q+1}}{2p-2q+1} < Ch^{2p+3}.\end{aligned} \tag{47}$$

For $I_2(jh)$ we obtain exactly as above

$$|I_2(jh)| \leq Ch^{2q+2} |jh|^{2p-2q} = Ch^{2p+2} |j|^{2p-2q}, \quad |j| > 1.$$

For $j = 0$ we use the fact that I_2 is continuous at $x = 0$. The same estimate as above then gives

$$|I_2(0)| = \lim_{x \to 0} |I_2(x)| \leq Ch^{2p+2}.$$

This leads to

$$\sum_{j \in \mathbb{Z}} |I_2(jh)|h \leq |I_2(0)|h + \sum_{|j| \geq 1} |I_2(jh)|h \leq Ch^{2p+3} + Ch^{2p+3} \sum_{|j| \geq 1} j^{2p-2q} \leq Ch^{2p+3}.$$

Using this and (47) we get finally get from (45),

$$\left| \int\limits_D f(\mathbf{x})\mathrm{d}\mathbf{x} - \mathcal{T}_h[f] \right| \leq \int\limits_{-a}^{a} |I_1(x_2)|\mathrm{d}x_2 + \sum_{j \in \mathbb{Z}} |I_2(jh)h| \leq Ch^{2p+3},$$

which concludes the proof of Theorem 3.

Accuracy of the corrected trapezoidal rule

The corrected trapezoidal rule consists of the punctured trapezoidal rule and a correction operator (20). The vector of correction weights $\overline{\boldsymbol{\omega}}$ are defined as the solution to the system (18)

$$KI(h)\boldsymbol{\omega}(h) = \mathbf{c}(h),$$

as $h \to 0$. We assume throughout this text that the weights $\boldsymbol{\omega}(h)$ are well defined solutions of this system for sufficiently small h. In two dimensions we also need to assume that the converged values $\overline{\boldsymbol{\omega}}$ obtained as the limit $\boldsymbol{\omega}(h) \to \overline{\boldsymbol{\omega}}$ when $h \to 0$ are well defined; in one dimension this follows from Lemma 5. Theorem 4 gives a proof of the convergence rate for the new quadrature rule in both one and two dimensions based on the assumption that the modified weights are bounded. When the non-converged weights $\boldsymbol{\omega}(h)$ are used the convergence rate is $\mathcal{O}\left(h^{2p+2+\gamma+d}\right)$. In the more practical case, when the converged weights $\overline{\boldsymbol{\omega}}$ are used, we prove that the convergence rate of the full rule depends on the convergence rate of the weights — if this rate is fast enough for some g the overall convergence rate is unaffected. In one dimension we furthermore show that this fast rate can be obtained by choosing a flat enough g, see Lemma 5. Although we do not prove it, strong numerical evidence confirms that Lemma 5 and the overall rate $\mathcal{O}\left(h^{2p+2+\gamma+d}\right)$ hold also in two dimensions.

Theorem 4. *Given a function $\phi \in C^{2q+2}(\mathbb{R}^d)$ compactly supported and a singular function*

$$s(\mathbf{x}) = |\mathbf{x}|^{\gamma} \textit{ with } \begin{cases} \gamma \in (-1, 0) & \mathbf{x} \in \mathbb{R}, \\ \gamma = -1, & \mathbf{x} \in \mathbb{R}^2. \end{cases}$$

Consider the modified quadrature applied to $f = \phi \cdot s$ written in operator form

$$Q_h^p[\phi \cdot s] = T_h^0[\phi \cdot s] + A_h^p[\phi],$$

which corresponds to (19) with the correction operators (21) in one dimension and (20) in two dimensions. Let $g \in C_c^{2q+2}(\mathbb{R}^d)$ be a radially symmetric function such that $g(0) = 1$ and $\partial^{\boldsymbol{k}} g(0) = 0$ for $\boldsymbol{k} \leq 2p+1$ with $p < q$. Moreover let $\boldsymbol{\omega}(h)$ be the solution of (18) for this g. Then the approximation error satisfies

$$|Q_h^p[\phi \cdot s] - I[\phi \cdot s]| \leq C \left(h^{2p+2+\gamma+d} + h^{\gamma+d} |\boldsymbol{\omega}(h) - \overline{\boldsymbol{\omega}}| \right), \tag{48}$$

where $I[\phi \cdot s]$ is the analytical integral. In one dimension by using Lemma 5 the estimate leads to

$$|Q_h^p[\phi \cdot s] - I[\phi \cdot s]| \leq C h^{2p+2+\gamma+d}. \tag{49}$$

Finally, if $\tilde{Q}_h^p$ is the quadrature rule where the non-converged weights $\boldsymbol{\omega}(h)$ are used instead of $\overline{\boldsymbol{\omega}}$ in the correction operator,

$$|\tilde{Q}_h^p[\phi \cdot s] - I[\phi \cdot s]| \leq C h^{2p+2+\gamma+d}, \tag{50}$$

in both one and two dimensions.

Proof. We start by defining $P_\phi(\mathbf{x})$ as the Taylor polynomial of order $2p+1$ of ϕ at the origin,

$$P_\phi(\mathbf{x}) := \sum_{|\boldsymbol{\alpha}|=0}^{2p+1} \frac{\mathbf{x}^{\boldsymbol{\alpha}}}{\boldsymbol{\alpha}!} \frac{\partial^{\boldsymbol{\alpha}} \phi(0)}{\partial \mathbf{x}^{\boldsymbol{\alpha}}}. \tag{51}$$

We furthermore define the compactly supported function $\tilde{\phi}(\mathbf{x}) = P_\phi(\mathbf{x}) g(\mathbf{x})$ which is an approximation of $\phi(\mathbf{x})$ close to $\mathbf{x} = 0$. Indeed, for $|\boldsymbol{k}| < 2p+2$,

$$\partial^{\boldsymbol{k}} \tilde{\phi}(\mathbf{x}) \Big|_{\mathbf{x}=\mathbf{0}} = \sum_{\boldsymbol{\ell}+\boldsymbol{r}=\boldsymbol{k}} \frac{\boldsymbol{k}!}{\boldsymbol{r}!\boldsymbol{\ell}!} \partial^{\boldsymbol{\ell}} P_\phi(\mathbf{x}) \partial^{\boldsymbol{r}} g(\mathbf{x}) \Big|_{\mathbf{x}=\mathbf{0}} = \partial^{\boldsymbol{k}} P_\phi(\mathbf{x}) \Big|_{\mathbf{x}=\mathbf{0}} = \partial^{\boldsymbol{k}} \phi(\mathbf{0}),$$

and as a consequence

$$\partial^{\boldsymbol{k}} [\phi(\mathbf{x}) - \tilde{\phi}(\mathbf{x})]|_{\mathbf{x}=\mathbf{0}} = 0, \quad |\boldsymbol{k}| < 2p+2. \tag{52}$$

In order to determine the order of convergence of $Q_h^p[f] - I[f]$ we split

$$\begin{aligned} Q_h^p[\phi \cdot s] - I[\phi \cdot s] &= T_h^0[\phi \cdot s] + A_h^p[\phi] - I[\phi \cdot s] \\ &= A_h^p[\phi - \tilde{\phi}] + (T_h^0 - I)[(\phi - \tilde{\phi}) \cdot s] + (Q_h^p - I)[\tilde{\phi} \cdot s] \\ &:= E_1 + E_2 + E_3, \end{aligned} \tag{53}$$

and treat these three terms separately.

To estimate E_1 we first note that (52) implies that, for all $\mathbf{x} \in \mathbb{R}^d$,

$$|\phi(\mathbf{x}) - \tilde{\phi}(\mathbf{x})| \leq C|\mathbf{x}|^{2p+2}, \qquad C = \sup_{\substack{\mathbf{x} \in \mathbb{R}^d \\ |\boldsymbol{k}|=2p+2}} \frac{1}{\boldsymbol{k}!} \left| \partial^{\boldsymbol{k}} (\phi(\mathbf{x}) - \tilde{\phi}(\mathbf{x})) \right| < \infty.$$

Using also (10) and (20) we then get

$$\begin{aligned} |E_1| = |A_h^p[\phi - \tilde{\phi}]| &\leq C a(h) \sup_{\boldsymbol{\beta} \in \mathcal{L}_p} [\phi(\boldsymbol{\beta} h) - \tilde{\phi}(\boldsymbol{\beta} h)] \leq C h^{\gamma+d} \sup_{\boldsymbol{\beta} \in \mathcal{L}_p} |\boldsymbol{\beta} h|^{2p+2} \\ &\leq C h^{2p+2+\gamma+d}, \end{aligned} \tag{54}$$

where we assumed that the weights $\overline{\boldsymbol{\varpi}}$ are bounded.

To bound E_2 we use Theorem 3 in two dimensions and Theorem 2 in one dimension, yielding

$$|E_2| = |(T_h^0 - I)[\phi \cdot s - \tilde{\phi} \cdot s]| \leq Ch^{2p+2+\gamma+d}. \tag{55}$$

It remains to bound E_3. Using the fact that $\tilde{\phi}$ has the form $\tilde{\phi} = P_\phi g$ with P_ϕ defined in (51) we have

$$\begin{aligned} |E_3| = |Q_h^p[\tilde{\phi} \cdot s] - I[\tilde{\phi} \cdot s]| &\leq \sum_{|\boldsymbol{\alpha}|=0}^{2p+1} \frac{1}{\boldsymbol{\alpha}!} \left| \frac{\partial^{\boldsymbol{\alpha}} \phi(0)}{\partial \mathbf{x}^{\boldsymbol{\alpha}}} \right| |Q_h^p[g \cdot s \cdot \mathbf{x}^{\boldsymbol{\alpha}}] - I[g \cdot s \cdot \mathbf{x}^{\boldsymbol{\alpha}}]| \\ &\leq C \sum_{|\boldsymbol{\alpha}|=0}^{2p+1} |T_h^0[g \cdot s \cdot \mathbf{x}^{\boldsymbol{\alpha}}] - I[g \cdot s \cdot \mathbf{x}^{\boldsymbol{\alpha}}] + A_h^p[g \cdot \mathbf{x}^{\boldsymbol{\alpha}}]|. \end{aligned} \tag{56}$$

We now want to show that the terms inside the sum in (56) are zero if α_1 and/or α_2 in $\boldsymbol{\alpha} = (\alpha_1, \alpha_2)$ is odd. Since g is radially symmetric, $g(x_1, x_2) = g(\pm x_1, \pm x_2)$ for all combinations of signs. The same holds for s. Therefore,

$$\begin{aligned} I[g \cdot s \cdot \mathbf{x}^{\boldsymbol{\alpha}}] &= \int g(\mathbf{x}) s(\mathbf{x}) \mathbf{x}^{\boldsymbol{\alpha}} \mathrm{d}\mathbf{x} \\ &= \int\limits_{x_1 \geq 0, x_2 \geq 0} g(\mathbf{x}) s(\mathbf{x}) [x_1^{\alpha_1} x_2^{\alpha_2} + (-x_1)^{\alpha_1} x_2^{\alpha_2} \\ &\qquad + x_1^{\alpha_1} (-x_2)^{\alpha_2} + (-x_1)^{\alpha_1} (-x_2)^{\alpha_2}] \mathrm{d}\mathbf{x} \\ &= \int\limits_{x_1 \geq 0, x_2 \geq 0} g(\mathbf{x}) s(\mathbf{x}) x_1^{\alpha_1} x_2^{\alpha_2} [1 + (-1)^{\alpha_1} + (-1)^{\alpha_2} + (-1)^{\alpha_1 + \alpha_2}] \mathrm{d}\mathbf{x}, \end{aligned}$$

and this sum vanishes for α_1 and/or α_2 odd. In a similar way we obtain $T_h^0[g \cdot s \cdot \mathbf{x}^{\boldsymbol{\alpha}}] = 0$ for α_1 and/or α_2 odd. In one dimension the corresponding expressions are clearly zero if α is odd. For the operator A_h^p in (20) we have

$$\begin{aligned} A_h^p[g \cdot \mathbf{x}^{\boldsymbol{\alpha}}] &= a(h) \sum_{q=0}^{p} \sum_{m=0}^{[q/2]} \overline{\omega}_q^m \sum_{\boldsymbol{\beta} \in \mathcal{G}_q^m} g(\boldsymbol{\beta} h) (\boldsymbol{\beta} h)^{\boldsymbol{\alpha}} \\ &= a(h) \sum_{q=0}^{p} \sum_{m=0}^{[q/2]} C_q^m \overline{\omega}_q^m h^{\boldsymbol{\alpha}} \sum_{\boldsymbol{\beta} \in \mathcal{G}_q^m} \boldsymbol{\beta}^{\boldsymbol{\alpha}}. \end{aligned} \tag{57}$$

Here we used the fact that $g(\boldsymbol{\beta} h)$ is constant for all $\boldsymbol{\beta} \in \mathcal{G}_q^m$ and we have called this constant C_q^m. Furthermore, let $\boldsymbol{\beta} = (\beta_1, \beta_2)$. Since $(\pm\beta_1, \pm\beta_2) \in \mathcal{G}_q^m$ if $\boldsymbol{\beta} \in \mathcal{G}_q^m$,

$$\begin{aligned} \sum_{\boldsymbol{\beta} \in \mathcal{G}_q^m} \boldsymbol{\beta}^{\boldsymbol{\alpha}} &= \sum_{\boldsymbol{\beta} \in \mathcal{G}_q^m} \frac{\beta_1^{\alpha_1} \beta_2^{\alpha_2} + (-\beta_1)^{\alpha_1} \beta_2^{\alpha_2} + \beta_1^{\alpha_1} (-\beta_2)^{\alpha_2} + (-\beta_1)^{\alpha_1} (-\beta_2)^{\alpha_2}}{4} \\ &= \sum_{\boldsymbol{\beta} \in \mathcal{G}_q^m} \boldsymbol{\beta}^{\boldsymbol{\alpha}} \frac{1 + (-1)^{\alpha_1} + (-1)^{\alpha_2} + (-1)^{\alpha_1} (-1)^{\alpha_2}}{4} = 0, \end{aligned} \tag{58}$$

if α_1 or α_2 is odd. Hence, we have shown that the terms in (56) containing odd polynomials vanish. Retaining only the even polynomials, we write the sum as

$$|E_3| \leq C \sum_{|\boldsymbol{\alpha}|=0}^{p} |T_h^0[g \cdot s \cdot \mathbf{x}^{2\boldsymbol{\alpha}}] - I[g \cdot s \cdot \mathbf{x}^{2\boldsymbol{\alpha}}] + A_h^p[g \cdot \mathbf{x}^{2\boldsymbol{\alpha}}]|. \tag{59}$$

This sum is over all $\boldsymbol{\alpha} \in \mathcal{M}_p$ as defined in (16). By (17) the first difference in the sum may be rewritten

$$T_h^0[g \cdot s \cdot \mathbf{x}^{2\boldsymbol{\alpha}}] - I[g \cdot s \cdot \mathbf{x}^{2\boldsymbol{\alpha}}] = -a(h) \sum_{q=0}^{p} \sum_{m=0}^{[q/2]} \omega_q^m(h) \sum_{\boldsymbol{\beta} \in \mathcal{G}_q^m} g(\boldsymbol{\beta} h)(\boldsymbol{\beta} h)^{2\boldsymbol{\alpha}}.$$

From (59), using the formula above and also the definition of A_h^p in (20), we obtain

$$\begin{aligned} |E_3| &\leq C' a(h) \sum_{\boldsymbol{\alpha} \in \mathcal{M}_p} \sum_{q=0}^{p} \sum_{m=0}^{[q/2]} |\omega_q^m(h) - \overline{\omega}_q^m| |g(\boldsymbol{\beta} h)| |(\boldsymbol{\beta} h)|^{2|\boldsymbol{\alpha}|} \\ &\leq C h^{\gamma + d} |\boldsymbol{\omega}(h) - \overline{\boldsymbol{\omega}}|. \end{aligned}$$

By using also (54), (55) and the split (53) the result in (48) follows. Finally, to prove (50) we just note that if the weights are changed the estimate (54) for E_1 can be done in precisely the same way, while clearly $E_3 = 0$. ☐

The estimate (49) of the Theorem is a consequence of the following Lemma 5, upon noting that we can always find a function $g(x)$ satisfying the assumptions of the Theorem with $q \geq 2p + (1+\gamma)/2$. Then $\mathcal{O}\left(h^{2q+1-\gamma-2p}\right) \leq \mathcal{O}\left(h^{2p+2}\right)$ and (60) inserted in (48) gives (49).

Lemma 5. *Let* p *and* q *be integers such that* $0 \leq p < q$ *and* $2q + 1 > \gamma + 2p$. *Suppose* $g(x) \in C_c^{2q+2}(\mathbb{R})$ *an even function with* g *as in Theorem 4. Then the approximate weights* $\boldsymbol{\omega}(h)$ *given as the solution of (18) for this* g *converge to* $\overline{\boldsymbol{\omega}}$ *and satisfy the error estimate*

$$|\boldsymbol{\omega}(h) - \overline{\boldsymbol{\omega}}| \leq C\left(h^{2p+2} + h^{2q+1-\gamma-2p}\right). \tag{60}$$

Proof. We claim that $\overline{\boldsymbol{\omega}}$ is given as a solution to

$$K \overline{\boldsymbol{\omega}} = \overline{\boldsymbol{c}}(\gamma),$$

where $\overline{\boldsymbol{c}}(\gamma)$ is defined as $\overline{\boldsymbol{c}} = (\overline{c}_0, \ldots, \overline{c}_{N_p - 1})$ with $\overline{c}_i = \overline{c}(\gamma + 2i)$ and $\overline{c}(\gamma)$ given in Theorem 2. Note that since K is a Vandermonde matrix with $K_{ij} = 2j^{2i}$ it is non-singular, so $\overline{\boldsymbol{\omega}}$ is well-defined. Furthermore with the notations in Section 2 and by Theorem 2,

$$\begin{aligned} h^{\gamma+1+2i} c_i(h) = &\int g(x) s(x) x^{2i} \mathrm{d}x - T_h^0[g \cdot s \cdot x^{2i}] \\ =& g(0) h^{\gamma+1+2i} \overline{c}_i + O(h^{2p+\gamma+3+2i} + h^{2q+2}). \end{aligned} \tag{61}$$

Therefore,

$$|c_i(h) - \overline{c}_i| \leq C(h^{2p+2} + h^{2q+2-\gamma-1-2i}) \leq C'(h^{2p+2} + h^{2q+1-\gamma-2p}). \tag{62}$$

We also have by Taylor expanding $\tilde{I}(h)$ around the origin and using the fact that $g(x)$ has $2p+1$ vanishing derivatives at the origin

$$|\tilde{I}(h) - I| \leq C h^{2p+2}, \tag{63}$$

with I the identity matrix. The result (60) now follows since

$$\begin{aligned} |\boldsymbol{\omega}(h) - \overline{\boldsymbol{\omega}}| &= |\tilde{I}(h)^{-1} K^{-1} \boldsymbol{c}(h) - K^{-1} \overline{\boldsymbol{c}}(\gamma)| \\ &= \left| K^{-1}(\boldsymbol{c}(h) - \overline{\boldsymbol{c}}(\gamma)) + (\tilde{I}(h)^{-1} - I) K^{-1} \boldsymbol{c}(h) \right| \\ &\leq C |\boldsymbol{c}(h) - \overline{\boldsymbol{c}}(\gamma)| + C' |\tilde{I}(h) - I|. \end{aligned} \tag{64}$$

Using (62) and (63), this proves the lemma. ☐

4 Numerical results

The correction weights for the quadrature rules depend on the singularity and must be computed and tabulated for each singularity under consideration. In this section we first discuss the computation of the weights, and then provide tabulated weights and discuss examples in one and two dimensions.

Computing the correction weights

The vector of correction weights $\boldsymbol{\omega}(h)$ can be obtained as solutions to the system (18) with the aid of a smooth and compactly supported function. How fast these weights converge to their limiting values $\overline{\boldsymbol{\omega}}$ depends on the number of vanishing derivatives that the compactly supported function has in the origin — see Lemma 5. In practice we do not choose a compactly supported function but $g(x) = e^{-|x|^{2k}}$ in such way that it is properly decayed at the boundaries of the domain. Note that for increasing values of k this function has an increasing number of derivatives that vanish at the origin.

In one dimension the vector of converged weights $\overline{\boldsymbol{\omega}}$ can be obtained as the solution of (A.2), using the closed form expression of $\bar{c}(\gamma)$, and we use these to measure the errors in $\boldsymbol{\omega}(h)$. In Fig. 2 the convergence rate of the weights is displayed for $g(x) = e^{-x^2}$, and $g(x) = e^{-x^4}$ respectively. In the first case, only the first derivative vanishes at the origin and therefore by Lemma 5 we expect a convergence order $\mathcal{O}\left(h^2\right)$. Similarly for e^{-x^4} all the derivatives up to third order evaluate to zero at the origin and thus we expect $\mathcal{O}\left(h^4\right)$ convergence. The numerical tests confirm the expected orders of convergence.

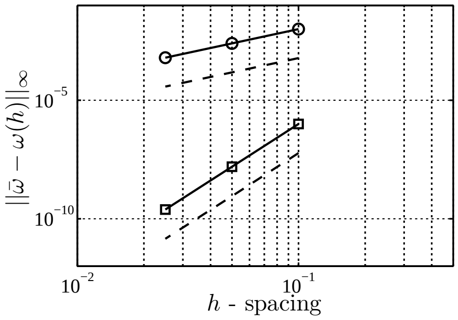

Figure 2: Error of the weights estimation for: □ — e^{-x^4}; ○ — e^{-x^2}; dashed lines — slopes of the expected order of convergence: $\mathcal{O}\left(h^2\right)$; $\mathcal{O}\left(h^4\right)$.

In two dimensions, we do not have a direct way to obtain the converged weights and the system (18) has to be solved as $h \to 0$. A bottleneck in this procedure is the ill-conditioning of the linear system; as the number of modified weights increases the reciprocal condition number of the system reaches epsilon of the machine. The aim is to obtain the value of the weights with double precision. Therefore the systems are solved in multiple precision arithmetic through straight forward Gaussian elimination followed by repeated Richardson extrapolation.

For $g(\mathbf{x}) = e^{-|\mathbf{x}|^{2k}}$ the order of convergence of the weights is $\mathcal{O}\left(h^{2k}\right)$ and a larger value of k can be used to speed up the convergence. In Fig. 3 we show for the system (18) with $p = 3$ how the choice of k controls the convergence of the weights with respect to the condition number of the system, $\kappa(A)$. Note that the condition number depends only weakly on the choice of g for a fixed h (the data points corresponding to the same h essentially line up along vertical lines). On the horizontal axis we can follow the growth of the condition number $\kappa(A)$, while on the vertical axis we can read the error in approximating the weights. To achieve an error $||\overline{\boldsymbol{\varpi}} - \boldsymbol{\omega}(h)||_\infty$ below a prescribed tolerance, the condition number will be lower for a larger k, and fewer digits will be lost in the calculations. Hence, not as many digits are needed in the multi-precision arithmetic, and the system can be solved much faster. It can however also be seen from Fig. 3 that once we use $e^{-|\mathbf{x}|^8}$ the computations for large h display a worse error than for lower exponents of the Gaussian. This is due to the difficulty in numerically resolving the Gaussian once the exponent of $e^{-|\mathbf{x}|^{2k}}$ increases. This implies that it will not be feasible to increase k indefinitely and we must settle for some intermediary value. Consequently, in practice we shall set up the system (18) for the function $e^{-|\mathbf{x}|^6}$, compute several solutions $\boldsymbol{\omega}(h)$ and use Richardson extrapolation as a final step in retrieving $\overline{\boldsymbol{\varpi}}$ as given in Table 4.

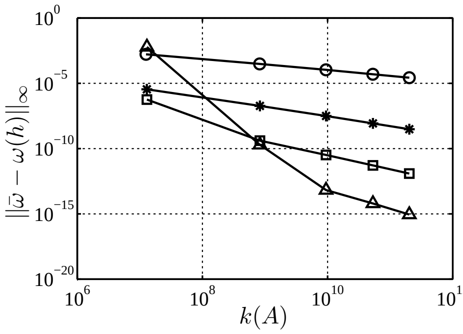

Figure 3: Error in estimating the weights $||\overline{\boldsymbol{\varpi}} - \boldsymbol{\omega}(h)||_\infty$ versus condition number of the system $\kappa(A)$ ($p = 3$, two-dimensional): $\circ$ — $e^{-|\mathbf{x}|^2}$; $*$ — $e^{-|\mathbf{x}|^4}$; $\square$ — $e^{-|\mathbf{x}|^6}$; $\triangle$ — $e^{-|\mathbf{x}|^8}$.

Applying the quadrature rules - a one-dimensional example

In this section, we study the convergence rates of the newly developed quadrature rules when applied to a singularity of type $|x|^\gamma$. We use (19) and (21) with correction weights in $2p+1$ points, obtained by solving the system (A.2). We consider two cases.

In the first case, we take $f(x) = \cos(x)|x|^\gamma$ with $\gamma = -0.8$ and $p = 2$. We include boundaries, but use high order boundary corrections given in [4] so that the boundaries yield lower errors than the singularity. The expected convergence rate is $\mathcal{O}\left(h^{2p+3+\gamma}\right) = \mathcal{O}\left(h^{6.2}\right)$ and to preserve this accuracy we use boundary corrections of order $\mathcal{O}\left(h^{8}\right)$. The result agrees well with the theory, as reported in Fig. 4a.

In the second case, we take $f(x) = \exp^{-x^2}\cos(x)|x|^\gamma$ with $\gamma = -0.5$ and $p = 4$. In this case the function is essentially zero on the boundaries and no boundary correction is needed. Theory predicts a convergence rate of $\mathcal{O}\left(h^{10.5}\right)$ which holds up well, see Fig. 4b. We also record in Table 2 the correction weights for the quadrature rule used in this case, ($p = 4$ and $\gamma = -0.5$).

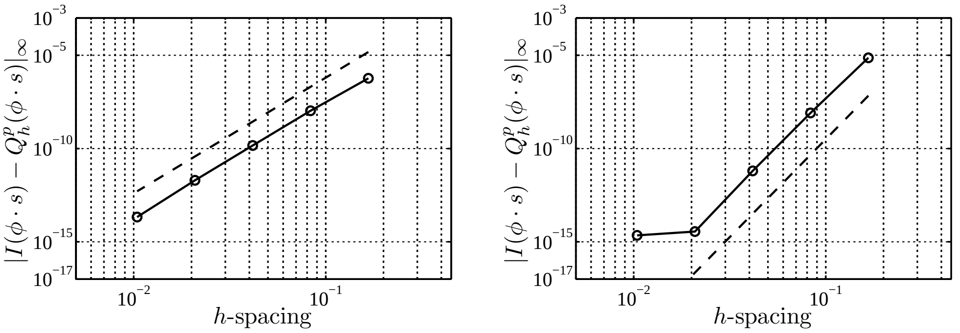

(a) $p = 2$, $\gamma = -0.8$; $\mathcal{O}\left(h^{8.2}\right)$; boundary corrections are used

(b) $p = 4$, $\gamma = -0.5$; $\mathcal{O}\left(h^{10.5}\right)$; compactly supported integrand

Figure 4: Convergence tests for various singularities: ○ — computed accuracy; dashed line — slope of the theoretical order of convergence.

Table 2: Weights for the quadrature rule Q_h^p, with $p = 4$ for $s(x) = |x|^{-0.5}$.

Discretization points	Weights
$j = \quad 0$	$\omega_0 = \quad 2.84364764808899424$
$j = \pm 1$	$\omega_1 = \quad 4.4010623268195800 \times 10^{-2}$
$j = \pm 2$	$\omega_2 = -6.2404540776693907 \times 10^{-3}$
$j = \pm 3$	$\omega_3 = \quad 8.1883632187304387 \times 10^{-4}$
$j = \pm 4$	$\omega_4 = -5.8320747783912244 \times 10^{-4}$

Applying the quadrature rules – a two-dimensional example

Consider an essentially compactly supported function, *e.g.* $\phi(x, y) = \cos(x)e^{-(x^2+y^2)}$ and evaluate

$$\int_{-8}^{8}\int_{-8}^{8}\frac{\phi(x,y)}{\sqrt{x^2+y^2}}\mathrm{d}x\mathrm{d}y. \tag{65}$$

On this chosen integral we test the set of quadrature rules Q_h^p, with $p = 0, \ldots, 5$, as defined in (19). The improvement in accuracy as p increases can be observed in Fig. 5 and in Table 3 where the order of convergence obtained through numerical experiment is compared to the theoretical one. The expected order of convergence for Q_h^p is 13. In practice even higher order quadrature rules ($p > 5$) do not seem to result in better accuracy; in the asymptotic range, round-off errors dominate in double precision.

5 Conclusion

We have constructed and also proved the accuracy of high-order quadrature rules that handle singular functions of the type $s(x) = |x|^\gamma$ with $\gamma > -1$ in one dimension and $\gamma = -1$ in two dimensions. The quadrature rules are based on the well-known trapezoidal rule, but with modified weights close to the singularity. They can be applied in a straight-forward manner by using the modified weights which have been computed and tabulated in this paper.

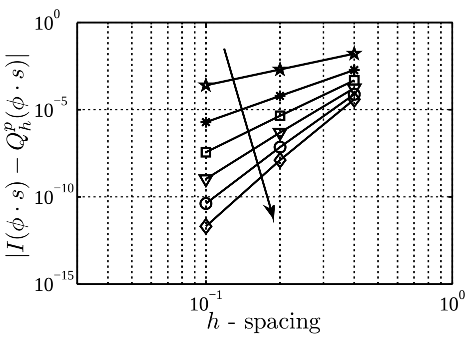

Figure 5: Accuracy results for increasing values of p (in direction of arrow) : ($\star$) $p = 0$; ($*$) $p = 1$; ($\Box$) $p = 2$; ($\bigtriangledown$) $p = 3$; ($\circ$) $p = 4$; ($\diamond$) $p = 5$.

Table 3: Computed order of convergence, numerical versus theoretical – two-dimensional case.

p	Convergence order	
	Theoretical	Numerical
0	3	3.0040
1	5	4.9854
2	7	6.9356
3	9	8.8563
4	11	10.7476
5	13	12.6107

In the construction of the quadrature rules we used compactly supported functions to annihilate boundary errors and accelerate the convergence of the correction weights. If the quadrature rule is to be applied to functions that are neither periodic nor compactly supported within the domain, it should be combined with boundary corrections for the trapezoidal rule of sufficiently high order to exhibit the full convergence order it has been designed to have. The correction operator associated with the singularity remains the same whether or not boundary corrections are necessary.

The modified weights are obtained as the solution of an ill-conditioned linear system of equations. We have described how this system is set-up and discussed its ill-conditioning. The convergence rate of the weights depends on the *flatness* of the compactly supported function used to annihilate boundary errors, *i.e.* on the number of derivatives that vanish at the singular point. We illustrate this property in numerical examples and prove mathematically its validity in the one-dimensional case. With an improved convergence rate for the weights, a larger h can be used, which to some extent alleviates the ill-conditioning problem. To be able to compute the weights with 16 correct digits, a multi-precision library is used. In one-dimension, we were able to find an analytical expression for the right hand side of the system such that converged weights can be computed directly (see Appendix A).

The methodology for setting up the system for the weights can be extended also to other singularities, *e.g.* the fundamental solution of the Stokes equations, [15], which is not radially symmetric in all its tensorial components as the functions $|x|^\gamma$, and more

Table 4: Modified weights for the $1/|\mathbf{x}|$ singularity in two dimensions.

q	$\mathcal{O}\left(h^{2q+3}\right)$	Discretization points	Modified weights
0	3	$\mathcal{G}_0^0 = \{(0,0)\}$	$\overline{\varpi}_0^0 = 3.9002649200019564 \times 10^0$
1	5	$\mathcal{G}_0^0 = \{(0,0)\}$	$\overline{\varpi}_0^0 = 3.6714406096247369 \times 10^0$
		$\mathcal{G}_1^0 = \{(\pm 1,0),(0,\pm 1)\}$	$\overline{\varpi}_1^0 = 5.7206077594304738 \times 10^{-2}$
2	7	$\mathcal{G}_0^0 = \{(0,0)\}$	$\overline{\varpi}_0^0 = 3.6192550095006482 \times 10^0$
		$\mathcal{G}_1^0 = \{(\pm 1,0),(0,\pm 1)\}$	$\overline{\varpi}_1^0 = 7.0478261675350094 \times 10^{-2}$
		$\mathcal{G}_2^1 = \{(\pm 1,\pm 1)\}$	$\overline{\varpi}_2^1 = 6.1845239404762928 \times 10^{-3}$
		$\mathcal{G}_2^0 = \{(\pm 2,0),(0,\pm 2)\}$	$\overline{\varpi}_2^0 = -6.4103079904994854 \times 10^{-3}$
3	9	$\mathcal{G}_0^0 = \{(0,0)\}$	$\overline{\varpi}_0^0 = 3.5956326153661837 \times 10^0$
		$\mathcal{G}_1^0 = \{(\pm 1,0),(0,\pm 1)\}$	$\overline{\varpi}_1^0 = 7.6498210003072550 \times 10^{-2}$
		$\mathcal{G}_2^1 = \{(\pm 1,\pm 1)\}$	$\overline{\varpi}_2^1 = 1.0726043096799093 \times 10^{-2}$
		$\mathcal{G}_2^0 = \{(\pm 2,0),(0,\pm 2)\}$	$\overline{\varpi}_2^0 = -1.0861970941933728 \times 10^{-2}$
		$\mathcal{G}_3^1 = \{(\pm 2,\pm 1),(\pm 1,\pm 2)\}$	$\overline{\varpi}_3^1 = -5.6768989454035010 \times 10^{-4}$
		$\mathcal{G}_3^0 = \{(\pm 3,0),(0,\pm 3)\}$	$\overline{\varpi}_3^0 = 9.3117379008582382 \times 10^{-4}$
4	11	$\mathcal{G}_0^0 = \{(0,0)\}$	$\overline{\varpi}_0^0 = 3.5816901196890991 \times 10^0$
		$\mathcal{G}_1^0 = \{(\pm 1,0),(0,\pm 1)\}$	$\overline{\varpi}_1^0 = 8.0270822919205118 \times 10^{-2}$
		$\mathcal{G}_2^1 = \{(\pm 1,\pm 1)\}$	$\overline{\varpi}_2^1 = 1.3733352021301174 \times 10^{-2}$
		$\mathcal{G}_2^0 = \{(\pm 2,0),(0,\pm 2)\}$	$\overline{\varpi}_2^0 = -1.4045613458587681 \times 10^{-2}$
		$\mathcal{G}_3^1 = \{(\pm 2,\pm 1),(\pm 1,\pm 2)\}$	$\overline{\varpi}_3^1 = -1.1741498011806794 \times 10^{-3}$
		$\mathcal{G}_3^0 = \{(\pm 3,0),(0,\pm 3)\}$	$\overline{\varpi}_3^0 = 1.9899412695107586 \times 10^{-3}$
		$\mathcal{G}_4^2 = \{(\pm 2,\pm 2)\}$	$\overline{\varpi}_4^2 = 6.2476521748914537 \times 10^{-6}$
		$\mathcal{G}_4^1 = \{(\pm 3,\pm 1),(\pm 1,\pm 3)\}$	$\overline{\varpi}_4^1 = 9.6911549656793913 \times 10^{-5}$
		$\mathcal{G}_4^0 = \{(\pm 4,\pm 0),(0,\pm 4)\}$	$\overline{\varpi}_4^0 = -1.5657382234231533 \times 10^{-4}$
5	13	$\mathcal{G}_0^0 = \{(0,0)\}$	$\overline{\varpi}_0^0 = 3.5724020676062076 \times 10^0$
		$\mathcal{G}_1^0 = \{(\pm 1,0),(0,\pm 1)\}$	$\overline{\varpi}_1^0 = 8.2931084474334645 \times 10^{-2}$
		$\mathcal{G}_2^1 = \{(\pm 1,\pm 1)\}$	$\overline{\varpi}_2^1 = 1.5807226557430198 \times 10^{-2}$
		$\mathcal{G}_2^0 = \{(\pm 2,0),(0,\pm 2)\}$	$\overline{\varpi}_2^0 = -1.6446295482375981 \times 10^{-2}$
		$\mathcal{G}_3^1 = \{(\pm 2,\pm 1),(\pm 1,\pm 2)\}$	$\overline{\varpi}_3^1 = -1.6998553930113205 \times 10^{-3}$
		$\mathcal{G}_3^0 = \{(\pm 3,0),(0,\pm 3)\}$	$\overline{\varpi}_3^0 = 2.9905345964354009 \times 10^{-3}$
		$\mathcal{G}_4^2 = \{(\pm 2,\pm 2)\}$	$\overline{\varpi}_4^2 = 1.5896929239405025 \times 10^{-5}$
		$\mathcal{G}_4^1 = \{(\pm 3,\pm 1),(\pm 1,\pm 3)\}$	$\overline{\varpi}_4^1 = 2.4136953002238568 \times 10^{-4}$
		$\mathcal{G}_4^0 = \{(\pm 4,\pm 0),(0,\pm 4)\}$	$\overline{\varpi}_4^0 = -4.0746367252001358 \times 10^{-4}$
		$\mathcal{G}_5^2 = \{(\pm 3,\pm 2),(\pm 2,\pm 3)\}$	$\overline{\varpi}_5^2 = -8.0410642204279767 \times 10^{-7}$
		$\mathcal{G}_5^1 = \{(\pm 4,\pm 1),(\pm 1,\pm 4)\}$	$\overline{\varpi}_5^1 = -1.7655194334677572 \times 10^{-5}$
		$\mathcal{G}_5^0 = \{(\pm 5,\pm 0),(0,\pm 5)\}$	$\overline{\varpi}_5^0 = 2.8620023884705339 \times 10^{-5}$

complicated symmetries must be taken into account.

The integration of $1/|\mathbf{x}|$ in $\mathbb{R}^2$ as considered here, can also be viewed as an integration of the fundamental solution of Laplace over a flat surface in $\mathbb{R}^3$. This relates to the discretization of boundary integral formulations, where integrals are to be evaluated over the boundaries of the domain, may it be an outer boundary, the surface of a scattering object in an electromagnetic application or the surface of an immersed particle in Stokes flow. We therefore plan to extend this work also to consider the integration of weakly singular integrals over more general smooth surfaces.

Acknowledgements

The support and enthusiasm with which Hans Riesel has met all our questions on Bernoulli numbers and the Riemann zeta function is gratefully acknowledged.

Appendix A Analytical expression for weights (one-dimensional case)

For the one-dimensional case we are able to provide an analytical expression for the weights. The weights are a solution, as a function of h, of the system (18) which reads

$$K\tilde{I}(h)\boldsymbol{\omega}(h) = \boldsymbol{c}(h). \tag{A.1}$$

From Lemma 5 we know that $\tilde{I}(h)$ converges to the identity matrix and if we could obtain an analytical expression, $\overline{\boldsymbol{c}}(\gamma)$ which is the limit value of the right hand side the weights could be simply computed by solving a system independent of the discretization such as

$$K\overline{\boldsymbol{\omega}} = \overline{\boldsymbol{c}}(\gamma), \tag{A.2}$$

where the vector $\overline{\boldsymbol{c}}(\gamma)$ has elements $(\overline{c}_0, \dots, \overline{c}_{N_p-1})$ with $\overline{c}_i = \overline{c}(\gamma + 2i)$. The function $\overline{c}(\gamma)$ was first encountered in Theorem 2 and consequently shown to have the form[1]

$$\overline{c}(\gamma) = \int_{-1}^{1} s(x)(1 - \psi(x) - 1)\mathrm{d}x - 4\Re\sum_{k=1}^{\infty} \frac{W(2\pi k)}{(2\pi k)^{2q}}.$$

In Lemma A.1 below we will show that $\overline{c}(\gamma) = -2\zeta(-\gamma)$, where ζ is the Riemann zeta function. In the proof we will make use of the expansion of $\zeta(\gamma)$ around the pole at $\gamma = 1$,

Theorem A.1 (Riemann zeta function)**.** *For all integers $q \geq 1$ and complex values γ with $\Re\gamma < 2q$,*

$$\zeta(-\gamma) = -\frac{1}{\gamma+1} + \frac{1}{2} - \sum_{j=1}^{q} \frac{B_{2j}}{(2j)!} s^{(2j-1)}(1) - \frac{1}{(2q)!}\int_{1}^{\infty} s^{(2q)}(x) B_{2q}(\{x\})\mathrm{d}x,$$

where $s(x) = x^{\gamma}$.

The result in Theorem A.1 can be found for instance in [1, Formula 23.2.3, page 807].

Lemma A.1. *The expression of $\overline{c}(\gamma)$ corresponding to a singularity $s(x) = |x|^{\gamma}$ which generates the right hand side to the system (A.2) has the closed form expression*

$$\overline{c}(\gamma) = -2\zeta(-\gamma),$$

where ζ is the Riemann zeta function.

---

[1] We use q instead of $q + 1$ here for notational simplicity.

Using the definition (32) of $W(k)$ we have

$$\begin{aligned}
4\Re\sum_{k=1}^{\infty}\frac{W(2\pi k)}{(2\pi k)^{2q}} &= 4\Re\sum_{k=1}^{\infty}(2\pi ik)^{-2q}\int_0^{\infty}\left(\frac{d^{2q}}{\mathrm{d}x^{2q}}\psi(x)s(x)\right)e^{2\pi ikx}\mathrm{d}x \\
&= 2\Re\sum_{k=1}^{\infty}(2\pi ik)^{-2q}\int\left(\frac{d^{q}}{\mathrm{d}x^{2q}}\psi(x)s(x)\right)e^{2\pi ikx}\mathrm{d}x \\
&= \int\left(\frac{d^{2q}}{\mathrm{d}x^{2q}}\psi(x)s(x)\right)\sum_{k\neq 0}\frac{e^{2\pi ikx}}{(2\pi ik)^{2q}}\mathrm{d}x \\
&= -\frac{1}{(2q)!}\int\left(\frac{d^{2q}}{\mathrm{d}x^{2q}}\psi(x)s(x)\right)B_{2q}(\{x\})\mathrm{d}x,
\end{aligned}$$

where we used the formula for the Fourier series of $B_q(x)$, $0 \leq x < 1$. Thus,

$$\overline{c}(\gamma) = \int_{-1}^{1}s(x)(1-\psi(x))\mathrm{d}x + \frac{1}{(2q)!}\int\left(\frac{d^{2q}}{\mathrm{d}x^{2q}}\psi(x)s(x)\right)B_{2q}(\{x\})\mathrm{d}x.$$

Since $B_{2q}(1-x) = B_{2q}(x)$ and therefore by the symmetry of all functions,

$$\frac{1}{2}\overline{c}(\gamma) = \int_0^1 s(x)(1-\psi(x))\mathrm{d}x + \frac{1}{(2q)!}\int_0^{\infty}\left(\frac{d^{2q}}{\mathrm{d}x^{2q}}\psi(x)s(x)\right)B_{2q}(\{x\})\mathrm{d}x. \tag{A.3}$$

To evaluate the last integral in (A.3), we will now use the Euler–Maclaurin, (Theorem 1) summation formula for the integral over $[0,1]$ and Theorem A.1 for the rest. We also need that fact that since $\psi(x) \equiv 1$ for $x \geq 1$,

$$\left.\frac{d^j}{\mathrm{d}x^j}\psi(x)s(x)\right|_{x=1} = s^{(j)}(1), \qquad j \geq 0.$$

We get

$$\begin{aligned}
\frac{1}{(2q)!}\int_0^{\infty}\left(\frac{\mathrm{d}^{2q}}{\mathrm{d}x^{2q}}\psi(x)s(x)\right)B_{2q}(\{x\})\mathrm{d}x &= \frac{1}{(2q)!}\int_0^{1}\left(\frac{\mathrm{d}^{2q}}{\mathrm{d}x^{2q}}\psi(x)s(x)\right)B_{2q}(\{x\})\mathrm{d}x+ \\
&\quad + \frac{1}{(2q)!}\int_1^{\infty}s^{(2q)}(x)B_{2q}(\{x\})\mathrm{d}x \\
&= \int_0^1\psi(x)s(x)\mathrm{d}x - \frac{1}{2}s(1) + \sum_{j=1}^{q}\frac{B_{2j}}{(2j)!}s^{(2j-1)}(1) \\
&\quad - \zeta(-\gamma) - \frac{1}{\gamma+1} + \frac{1}{2} - \sum_{j=1}^{q}\frac{B_{2j}}{(2j)!}s^{(2j-1)}(1) \\
&= \int_0^1\psi(x)s(x)\mathrm{d}x - \zeta(-\gamma) - \int_0^1 s(x)\mathrm{d}x.
\end{aligned}$$

Together with (A.3), this shows that

$$\overline{c}(\gamma) = -2\zeta(-\gamma). \tag{A.4}$$

References

[1] M. Abramowitz and I. A. Stegun. *Handbook of Mathematical Functions with Formulas, Graphs, and Mathematical Tables.* Dover Publications, Mineola, U.S.A., 9th edition, 1964.

[2] J. C. Aguilar and Y. Chen. High-order corrected trapezoidal quadrature rules for functions with a logarithmic singularity in 2-D. *Comput. Math. Appl.*, 44:1031–1039, 2002.

[3] J. C. Aguilar and Y. Chen. High-order corrected trapezoidal quadrature rules for the Coulomb potential in three dimensions. *Comput. Math. Appl.*, 49:625–631, 2005.

[4] B. K. Alpert. High-order quadratures for integral operators with singular kernels. *J. Comput. Appl. Math.*, 60:367–378, 1995.

[5] B. K. Alpert. Hybrid Gauss-trapezoidal quadrature rules. *SIAM J. Sci. Comput.*, 20:1551–1584, 1999.

[6] K. Atkinson. Quadrature of singular integrands over surfaces. *Electron. T. Numer. Ana.*, 17:133–150, 2004.

[7] O. P. Bruno and L. A. Kunyansky. A fast, high-order algorithm for the solution of surface scattering problems: Basic implementation. *J. Comput. Phys.*, 169:80–110, 2001.

[8] H. Cohen. *Number Theory. Vol. II. Analytic and Modern Tools.* Springer, New York, U.S.A., 2007.

[9] R. Duan and V. Rokhlin. High-order quadratures for the solution of scattering problems in two dimensions. *J. Comput. Phys.*, 228:2152–2174, 2009.

[10] M. G. Duffy. Quadrature over a pyramid or cube of integrands with a singularity at a vertex. *SIAM J. Numer. Anal.*, 19(6):1260–1262, 1982.

[11] S. Kapur and V. Rokhlin. High-order corrected trapezoidal quadrature rules for singular functions. *SIAM J. Numer. Anal.*, 34(4):1331–1356, 1997.

[12] P. Keast and J. N. Lyness. On the structure of fully symmetric multidimensional quadrature rules. *SIAM J. Numer. Anal.*, 16(1):11–29, 1979.

[13] M. A. Khayat and D. R. Wilton. Numerical evaluation of singular and near-singular potential integrals. *IEEE Trans. Antennas Propag.*, 53:3180–3190, 2005.

[14] J. N. Lyness. An error functional expansion for N-dimensional quadrature with an integrand function singular at a point. *Math. Comput.*, 30(133):1–23, 1976.

[15] O. Marin, K. Gustavsson, and A.-K. Tornberg. A highly accurate boundary treatment for confined Stokes flow. *Comput. Fluids*, 66:215–230, 2012.

[16] S. E. Mousavi and N. Sukumar. Generalized Duffy transformation for integrating vertex singularities. *Comput. Mech.*, 45:127–140, 2010.

[17] C. Pozrikidis. *Boundary Integral and Singularity Methods for Linearized Viscous Flow.* Cambridge University Press, Cambridge, U.K., 1992.

[18] V. Rokhlin. Endpoint corrected trapezoidal quadrature rules for singular functions. *Comput. Math. Appl.*, 20:51–62, 1990.

[19] A. Sidi. Application of class $\mathcal{S}$m variable transformations to numerical integration over surfaces of spheres. *J. Comput. Appl. Math.*, 184:475–492, 2005.

A highly accurate boundary treatment for confined Stokes flow

Oana Marin, Katarina Gustavsson, Anna-Karin Tornberg
Linné FLOW Centre, KTH-CSC (NA), SE-100 44 Stockholm, Sweden

Abstract

Fluid flow phenomena in the Stokesian regime abounds in nature as well as in microfluidic applications. Discretizations based on boundary integral formulations for such flow problems allow for a reduction in dimensionality but have to deal with dense matrices and the numerical evaluation of integrals with singular kernels. The focus of this paper is the discretization of wall confinements, and specifically the numerical treatment of flat solid boundaries (walls), for which a set of high-order quadrature rules that accurately integrate the singular kernel of the Stokes equations are developed. Discretizing by Nyström's method, the accuracy of the numerical integration determines the accuracy of the solution of the boundary integral equations, and a higher order quadrature method yields a large gain in accuracy at negligible cost. The structure of the resulting submatrix associated with each wall is exploited in order to substantially reduce the memory usage. The expected convergence of the quadrature rules is validated through numerical tests, and this boundary treatment is further applied to the classical problem of a sedimenting sphere in the vicinity of solid walls.

1 Introduction

Microfluidics [6] is a growing branch of fluid mechanics which focuses on applications such as: transport in micro-channels [12], microorganism locomotion [7], lab-on-a-chip [9], etc. In many of these cases the flows are characterized by dominating viscous effects and a low Reynolds number. Flows at low Reynolds number can be modeled by neglecting the inertia terms in the Navier-Stokes equations, yielding the so-called Stokes equations, see e.g. [24]. For finite-size objects immersed in Stokes flow, the governing differential equations can be equivalently formulated as boundary integral equations on the surfaces of the immersed bodies or by asymptotic analysis along the centerline of a slender body [13, 29]. This reduces the dimensionality of the problem, and is especially advantageous for discretization of moving immersed objects since there is no volume grid that requires remeshing. For particle motion in confined geometries, such as droplet and particle motion in channels [17], and the suspensions of particles or fibers in wall-bounded shear flow [18], external boundaries must also be included.

Traditionally, external solid boundaries are included in the formulation using the method of images. The idea behind the method of images is to regard the wall as a mirror which reflects the velocities due to point forces such that a *no-slip* boundary condition is satisfied at the wall. This leads to an analytic expression of a modified fundamental solution, the half-space Stokeslet, for one single infinite flat wall. Most popular in the literature is the derivation by Blake [5] which has been used in many different applications, see e.g. [8, 26]. An extension of the method of images to two parallel walls has been derived by Liron and Mochon [20] obtaining a Green's function for a point force singularity between two parallel walls. However, this formulation involves slowly convergent series and a further study by Staben *et al.* [28] provides a different set of expressions based on rapidly convergent integrals.

Still, these expressions are lengthy and require a large computational effort. The method of images does not allow for other boundary conditions than the velocity equal to zero at the walls, nor does it easily adapt to more complicated geometries. Thus extensive analytic work is needed to address each particular problem to take into account special geometries e.g. flow past a wall with an orifice [23] or flow due to a Stokeslet in a pipe [21].

In the present contribution we propose to use a direct numerical treatment of a flat solid boundary/wall by discretizing its entire surface. A similar technique was employed in e.g. [18] to study the dynamics of short fibers under the influence of such a wall. This approach extends straight-forwardly to the problem of two parallel walls and also readily permits the use of non-homogeneous boundary conditions. The inclusion of a wall in the boundary integral formulation adds an integral involving the unknown force density on the boundary convolved with the Green's function of Stokes flow. Boundary conditions are imposed on the velocity at the solid boundaries leading to a system to be solved for the force density distribution. This requires the evaluation of singular integrals over the underlying surfaces. The evaluation of such integrals usually poses difficulties in solving problems modeled using boundary integrals.

Integral equations stated over solid boundaries can be discretized by means of either the boundary element method [24] or Nyström's method [24]. The latter approach is convenient when applied to smooth, parameterizable geometries since it is straight-forward to implement and, as we shall observe, yields under certain circumstances matrices with a specific homogeneous structure. In the field of boundary integrals where discretized problems lead to dense matrices it is highly advantageous to exploit a specific matrix structure in order to reduce the memory requirements. A drawback, however, of the Nyström method is that it does not possess a degree of generality in treating singular kernels to high-order. Several techniques have been developed in the framework of Nyström's method to numerically integrate the Stokeslet over certain surfaces, e.g. Atkinson [3] and Sidi [27] where surfaces that can be mapped to the unit sphere are treated.

The key element of this work is the development of a set of high-order quadrature rules for the numerical integration of the fundamental solution of Stokes flow over a flat surface. To design such a quadrature rule we follow the approach introduced in [1, 19] and further developed in Marin *et al.* [22] for the fundamental solution of the Laplace equation. The idea is to modify the trapezoidal rule by incorporating the singular behavior of the fundamental solution into a small number of correction weights. This modification is performed only locally around the singularity and the number of correction weights determines the accuracy of the new quadrature rule. The linear systems to be solved to obtain the weights are severely ill-conditioned. This necessitates the use of high-precision arithmetics to compute them with sufficient (i.e. machine) precision. Analytical work in one dimension combined with numerical experiments [22] have shed light on how to accelerate the convergence of such weights and, at least partially, alleviate this problem. Once constructed the quadrature rules are easy to implement by using a small number of tabulated correction weights. It should also be emphasized that, besides its simplicity, this method provides a significant increase in accuracy at almost no extra cost since no extra unknowns are introduced. Only a few weights in the quadrature rule are modified.

The type of setup we consider here assumes that the solid boundary is a cross section of a computational domain bounded by periodic boundary conditions, i.e. we impose periodicity in the wall-parallel directions. In the framework of boundary integrals periodicity is imposed by considering that the computational box is replicated in all periodic directions yielding an infinite sum over all periodic images. The formulas for the bi-periodic version of the Stokeslet involving rapidly converging sums in real space and reciprocal space are given in [25]. However, these formulas are only expanded up to expressions which can be numerically approximated and we have further expanded the formulas in order to obtain fully analytical expressions.

This paper is organized as follows. First we describe and formulate mathematically a typical physical problem that involves the present wall treatment. In Section 3 the developed high-order quadrature method for integrating the Stokeslet over a flat surface is presented and validated. We then discuss the techniques used to discretize and integrate the other terms that enter the wall-sphere test case in Section 4. Furthermore, the algebraic system obtained from the discretization of the full mathematical model is analyzed and a memory efficient method is provided. The final Section 5 contains several numerical examples: non-homogenous boundary conditions at the surface of the wall and the wall-sphere problem validated against the analytical expressions for a sphere sedimenting towards one wall and between two parallel walls. Finally conclusions are drawn and a brief outlook is given.

2 Problem description

We consider a viscous fluid in a domain D driven by a body force $\mathbf{b}$. The equations governing the motion of such a flow in the limit of low Reynolds number are the Stokes equations, which in differential form are given as

$$\begin{aligned} \nabla p - \mu \Delta \mathbf{u} &= \mathbf{b} \quad \text{in} \quad D \,, \\ \nabla \cdot \mathbf{u} &= 0 \,, \end{aligned} \tag{1}$$

where $\mathbf{u}$ is the velocity, p is the pressure and μ is the viscosity of the fluid. These equations need to be supplemented with suitable boundary conditions on ∂D. The domain D can be multiply connected, however we shall distinguish between external boundaries that confine the domain, and boundaries fully enclosed within the domain, i.e. internal boundaries.

Using a boundary integral formulation for Stokes flow, the velocity at any point $\mathbf{x}_0 \in \bar{D} = D \cup \partial D$ is given by,

$$\mathbf{u}(\mathbf{x}_0) = \frac{1}{8\pi\mu} \int_{\partial D} \mathbf{G}(\mathbf{x} - \mathbf{x}_0)\mathbf{f}(\mathbf{x}) \mathrm{d}S_{\mathbf{x}} \,, \tag{2}$$

with $\mathbf{f}$ being the force density distribution over the boundary ∂D. The fundamental solution $\mathbf{G}$ will be discussed below.

First, assume that the boundary of the domain, $\partial D = \Gamma$, is fixed in time, with a given boundary condition $\mathbf{u}(\mathbf{x}_0) = \bar{\mathbf{u}}(\mathbf{x}_0)$ on Γ. Eq. (2) can now be solved using $\mathbf{u}(\mathbf{x}_0) = \bar{\mathbf{u}}(\mathbf{x}_0)$ with $\mathbf{x}_0 \in \Gamma$ to obtain the force distribution $\mathbf{f}$ over Γ. Once the distribution of forces $\mathbf{f}$ is known, the velocity can be evaluated at any point in the entire domain using (2).

Imposing a velocity field at the wall surface is common practice in numerical simulations when it suffices to consider approximation models of e.g. walls with orifices, porous walls or suction and blowing walls. Such a model calls for a non-zero velocity component in the wall normal direction. However we could also assume other velocity fields, for example a constant velocity in the wall parallel direction used in simulating two shearing plates.

In addition to the boundary Γ, consider now the presence of immersed solid objects in the flow domain. The surfaces of these objects are treated as internal boundaries. The translational and rotational velocities of these objects are unknown and additional constraints are required to close the coupled system.

Let $\partial D = \Gamma \cup S$, where Γ denotes the solid boundary as previously discussed, and

$$S = \bigcup_{m=1}^{M} S_m,$$

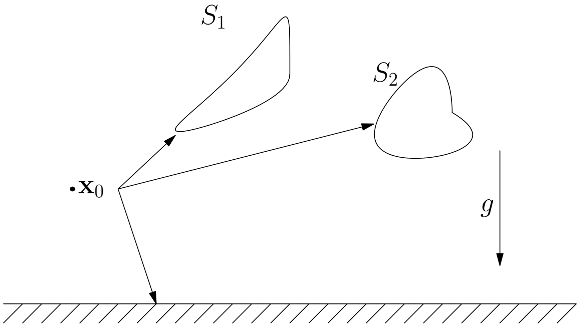

Figure 1: Sketch of $m = 2$ immersed objects sedimenting towards a flat plate. Gravity g is acting in the wall normal z direction. The point $\mathbf{x}_0$ signifies a general point inside the flow domain. (Two-dimensional sketch of a three-dimensional problem)

where S_m is the surface of the m-th immersed body, see illustration in Fig. 1. Imposing the same boundary condition on Γ, $\mathbf{u}(\mathbf{x}_0) = \bar{\mathbf{u}}(\mathbf{x}_0)$, Eq. (2) for $\mathbf{x}_0 \in \Gamma$ yields over ∂D

$$\frac{1}{8\pi\mu}\int_S \mathbf{G}(\mathbf{x}-\mathbf{x}_0)\mathbf{f}_s(\mathbf{x})\mathrm{d}S_{\mathbf{x}} + \frac{1}{8\pi\mu}\int_\Gamma \mathbf{G}(\mathbf{x}-\mathbf{x}_0)\mathbf{f}_w(\mathbf{x})\mathrm{d}\Gamma_{\mathbf{x}} = \bar{\mathbf{u}}(\mathbf{x}_0), \quad \mathbf{x}_0 \in \Gamma \ , \tag{3}$$

where we have now denoted by $\mathbf{f}_w$ the force distribution on the external boundaries or walls, and by $\mathbf{f}_s$ the force distribution on the solid immersed objects.

The approach taken here is to directly discretize the surface of the external boundaries since this allows for more general geometries as well as non-homogenous boundary conditions. However, for one or two flat parallel walls, the method of images could be used. Then, the integral over the external boundaries, Γ, in Eq. (3) vanishes and the Greens function in the first integral would be modified such that the velocity is zero at the walls. However, as mentioned in the introduction, using the method of images for more than one flat wall is computationally very expensive.

Each object performs a rigid body motion, i.e. $\mathbf{u}(\mathbf{x}_0) = \mathbf{V}_m + \mathbf{\Omega}_m \times (\mathbf{x}_0 - \mathbf{x}^c_m)$ for $\mathbf{x}_0 \in S_m$ where $\mathbf{x}^c_m$ is the center of mass of the particle, and $\mathbf{V}_m$ and $\mathbf{\Omega}_m$ represent the translational and rotational velocities, respectively. Requiring a no-slip condition on these surfaces, and using (2) for $\mathbf{x}_0 \in S_m$ yields

$$\frac{1}{8\pi\mu}\int_S \mathbf{G}(\mathbf{x}-\mathbf{x}_0)\mathbf{f}_s(\mathbf{x})\mathrm{d}S_{\mathbf{x}} + \frac{1}{8\pi\mu}\int_\Gamma \mathbf{G}(\mathbf{x}-\mathbf{x}_0)\mathbf{f}_w(\mathbf{x})\mathrm{d}\Gamma_{\mathbf{x}} = \mathbf{V}_m + \mathbf{\Omega}_m \times (\mathbf{x}_0 - \mathbf{x}^c_m) \ . \tag{4}$$

The additional constraints that we need to impose to close the system are that the integrated force and torque over each body equal the externally applied force and torque, i.e.

$$\int_{S_m} \mathbf{f}_s(\mathbf{x})\mathrm{d}S_{\mathbf{x}} = \mathbf{F}_m, \quad \int_{S_m} (\mathbf{x}-\mathbf{x}_c) \times \mathbf{f}_s(\mathbf{x})\mathrm{d}S_{\mathbf{x}} = \mathbf{L}_m \ . \tag{5}$$

If there is a density difference $\Delta\rho$ between the solid objects and the surrounding fluid, $\mathbf{F}_m = \Delta\rho V_m g \mathbf{e}_g$, where V_m is the volume of body m, g is the gravitational constant, assuming that gravity is acting in the $\mathbf{e}_g$ direction. Also when there is no externally applied torque then $\mathbf{L}_m = 0$.

The system of Eqs. (3)-(5), is solved for the force distributions $\mathbf{f}_s$ and $\mathbf{f}_w$ and velocities $\mathbf{V}_m$ and $\mathbf{\Omega}_m$, $m = 1, \dots, M$. Introducing an orthonormal frame $\{\mathbf{b}^1_m, \mathbf{b}^2_m, \mathbf{b}^3_m\}$ fixed to each body, the rigid body rotation of each body can be evaluated by updating this frame together with the location of the center of mass, i.e.

$$\frac{\mathrm{d}\mathbf{x}_m^c}{\mathrm{d}t} = \mathbf{V}_m, \quad \frac{\mathrm{d}\mathbf{b}_m^j}{\mathrm{d}t} = \mathbf{\Omega}_m \times \mathbf{b}_m^j, \; j = 1, 2, 3, \tag{6}$$

for $m = 1, \ldots, M$.

Physical problem under consideration

We will consider domains that are periodic in the x and y direction, with periodic lengths L_x and L_y, respectively. The periodicity is incorporated into the tensor $\mathbf{G}$, which is the fundamental solution of the Stokes equations. The periodic Stokeslet $\mathbf{G}$ can be decomposed into two parts; a free-space contribution and a periodic remainder as

$$\mathbf{G}(\hat{\mathbf{x}}) = \mathbf{G}_0(\hat{\mathbf{x}}) + \mathbf{G}_p(\hat{\mathbf{x}}) \ , \tag{7}$$

where the free-space Stokeslet reads

$$\mathbf{G}_0(\hat{\mathbf{x}}) = \frac{\mathbf{I}}{|\hat{\mathbf{x}}|} + \frac{\hat{\mathbf{x}} \otimes \hat{\mathbf{x}}}{|\hat{\mathbf{x}}|^3}, \quad \text{or} \quad \mathbf{G}_{0,ij}(\mathbf{x}) = \frac{\delta_{ij}}{|\hat{\mathbf{x}}|} + \frac{\hat{x}_i \hat{x}_j}{|\hat{\mathbf{x}}|^3}, \quad i, j = 1, 2, 3. \tag{8}$$

where δ_{ij} is the Kronecker delta and $\hat{\mathbf{x}} = \mathbf{x} - \mathbf{x}_0$. A detailed description of the periodic Stokeslet will be given in Section 2.

The external boundary Γ is taken to be a flat wall at a given z-coordinate, or two parallel flat walls at different z-coordinates. In the numerical examples considered in this manuscript we have one immersed body, namely a sphere. It should, however, be clear from the above how multiple objects can be included into the formulation.

When considering a wall-sphere system, we will non-dimensionalize the equations by taking the characteristic length as the radius, r, of the sphere and the characteristic velocity

$$U_c = \frac{\Delta \rho V g}{8 \pi \mu r}.$$

This allows us to restate the problem in non-dimensional form, and we will now have (dropping the subscript m since there is only one immersed body),

$$\int_S \mathbf{G}(\mathbf{x} - \mathbf{x}_0) \mathbf{f}_s(\mathbf{x}) \mathrm{d}S_{\mathbf{x}} + \int_\Gamma \mathbf{G}(\mathbf{x} - \mathbf{x}_0) \mathbf{f}_w(\mathbf{x}) \mathrm{d}\Gamma_{\mathbf{x}} = 0 \ , \quad \mathbf{x}_0 \in \Gamma \ , \tag{9}$$

where we have assumed $\mathbf{u} = 0$ on Γ, and

$$\int_S \mathbf{G}(\mathbf{x} - \mathbf{x}_0) \mathbf{f}_s(\mathbf{x}) \mathrm{d}S_{\mathbf{x}} + \int_\Gamma \mathbf{G}(\mathbf{x} - \mathbf{x}_0) \mathbf{f}_w(\mathbf{x}) \mathrm{d}\Gamma_{\mathbf{x}} = \mathbf{V} + \mathbf{\Omega} \times (\mathbf{x}_0 - \mathbf{x}^c), \quad \mathbf{x}_0 \in S \ , \tag{10}$$

where $\mathbf{F} = \mathbf{e}_g$ in (5) in this non-dimensional form.

Periodic Boundary conditions

Consider the computational box periodic in x and y with periodic lengths L_x, L_y and free-space in the z direction. For any box $p_1, p_2 \in \mathbb{Z}$ which is a periodic replication of the original computational domain of size $L_x \times L_y$ the origin translates into

$$\mathbf{p} = p_1 \hat{e}_1 L_x + p_2 \hat{e}_2 L_y \ , \tag{11}$$

where $\hat{e}_1$ and $\hat{e}_2$ are the unit vectors in the x and y direction, respectively. Assume a point force located at $\mathbf{x}_0$, then the periodic image of this point in the box p_1, p_2 is given by $\mathbf{X}_\mathbf{p} = \mathbf{x}_0 + \mathbf{p}$. If we intend to compute at a point $\mathbf{x}$ the influence of a point force at $\mathbf{x}_0$ in the domain we need to evaluate the Stokeslet (8) as a function of the relative position $\hat{\mathbf{x}} = \mathbf{x} - \mathbf{x}_0$. Summing up all the contributions from the Stokeslet (8) and its periodic images we obtain

$$\sum_{p_1,p_2\in\mathbb{Z}} \mathbf{G}_0(\hat{\mathbf{x}} + \mathbf{p}) \ .$$

This sum should define the periodic Stokeslet. A direct summation of this sum is however not possible since the free-space Stokeslet $\mathbf{G}_0$ decays as $1/r$ and thus the sum is divergent, see [25]. To make the sum convergent, we assume that all external forces are balanced by a mean pressure gradient.

With this, one can restate the sum as a sum in Fourier space which is convergent, but that converges too slowly for practical purposes. Following the ideas introduced by Ewald in electrostatics [10], Hasimoto [15] was first to derive a decomposition of the periodic Stokeslet in two parts: one sum in real space, including near interactions, and one in Fourier space for the smooth long-range interactions. Here, both sums decay rapidly, and the relative decay of the two sums is controlled by a decomposition parameter. The derivation by Hasimoto was developed for a triply periodic domain in three dimensions.

Pozrikidis [25] has derived a decomposition also for a doubly periodic domain in three dimensions. His decomposition is based on an approach introduced by Beenakker for triply periodic domains [4]. In this derivation, the free space Stokeslet is expressed as $\mathbf{G}_0(\mathbf{x}) = (\boldsymbol{I}\nabla^2 - \nabla\nabla)|\mathbf{x}|$. Now, decompose $\mathbf{G}_0$ into two parts

$$\mathbf{G}_0(\mathbf{x}) = \boldsymbol{\Upsilon}(\mathbf{x}) + \boldsymbol{\Phi}(\mathbf{x}) \ , \tag{12}$$

where

$$\begin{bmatrix}\boldsymbol{\Upsilon}\\ \boldsymbol{\Phi}\end{bmatrix}(\mathbf{x}) = (\boldsymbol{I}\nabla^2 - \nabla\nabla)\begin{bmatrix}|\mathbf{x}|\operatorname{erfc}(\xi|\mathbf{x}|)\\ |\mathbf{x}|\operatorname{erf}(\xi|\mathbf{x}|)\end{bmatrix} \ .$$

Here, $\boldsymbol{\Upsilon}$ contains the singularity at $\mathbf{x} = 0$ and decays rapidly as $|\mathbf{x}|$ increases, while $\boldsymbol{\Phi}$ contains the smooth long-range part. The sum over $\boldsymbol{\Phi}$ in real space is converted into a sum in Fourier space. Here, the decomposition parameter ξ is an arbitrary positive constant with dimension of an inverse length which will eventually control the convergence speed of the emerging sums.

With this, the summation over the Stokeslet becomes

$$\sum_{p_1,p_2\in\mathbb{Z}} \mathbf{G}_0(\hat{\mathbf{x}} + \mathbf{p}) = \sum_{p_1,p_2\in\mathbb{Z}} \boldsymbol{\Upsilon}(\hat{\mathbf{x}} + \mathbf{p}) + \sum_{k_1,k_2\in\mathbb{Z}} \hat{\boldsymbol{\Phi}}(\hat{\mathbf{x}}, \mathbf{k}) \ . \tag{13}$$

Assuming $\hat{\mathbf{x}} \in [-L_x/2, L_x/2) \times [-L_y/2, L_y/2) \times \mathbb{R}$ let us denote

$$\mathbf{S}_r(\hat{\mathbf{x}}) = \sum_{p_1,p_2\in\mathbb{Z}} \boldsymbol{\Upsilon}(\hat{\mathbf{x}} + \mathbf{p}) - \mathbf{G}_0(\hat{\mathbf{x}}) = \boldsymbol{\Upsilon}(\hat{\mathbf{x}}) - \mathbf{G}_0(\hat{\mathbf{x}}) + \sum_{\substack{p_1,\, p_2\, \in\, Z\\ |\mathbf{p}|\neq 0}} \boldsymbol{\Upsilon}(\hat{\mathbf{x}} + \mathbf{p}) \ .$$

The term $\boldsymbol{\Upsilon}(\hat{\mathbf{x}}) - \mathbf{G}_0(\hat{\mathbf{x}})$ has a finite limit at $\hat{\mathbf{x}} = 0$, and $\mathbf{S}_r$ is a smooth function of $\hat{\mathbf{x}}$. Furthermore, introduce

$$\mathbf{S}_F(\hat{\mathbf{x}}, \mathbf{k}) = \sum_{k_1,k_2\in\mathbb{Z}} \hat{\boldsymbol{\Phi}}(\hat{\mathbf{x}}, \mathbf{k}) \ ,$$

and define $\mathbf{G}_p(\hat{\mathbf{x}}) = \mathbf{S}_r(\hat{\mathbf{x}}) + \mathbf{S}_F(\hat{\mathbf{x}})$ where $\mathbf{G}_p(\hat{\mathbf{x}})$ is the smooth periodic remainder as in (7).

In [25] the doubly periodic Stokeslet is derived using a pure Fourier expansion. In order to obtain a well-defined solution, an assumption stating that the pressure gradient balances the external forces across any plane in the periodic directions is used. This assumption is implemented by omitting the zero wave number from the Fourier expansion. As a consequence, the solution will suffer from discontinuities in the derivatives of the velocity. To obtain a Green's function with a continuous stress field, Pozrikidis, [25] suggests a regularization of the periodic Stokeslet which in our case yields a modified periodic remainder,

$$\mathbf{G}_p(\hat{\mathbf{x}}) = \mathbf{S}_r(\hat{\mathbf{x}}) + \mathbf{S}_F(\hat{\mathbf{x}}) - \frac{4\pi}{L_x L_y}\hat{\mathbf{I}}|\hat{x}_3| \ , \tag{14}$$

where $\hat{\mathbf{I}} = \mathrm{diag}(1,1,0)$.

The detailed expressions for the sums $\mathbf{S}_r(\hat{\mathbf{x}})$ and $\mathbf{S}_F(\hat{\mathbf{x}},\mathbf{k})$ are given in Appendix B. In the original reference of Pozrikidis [25], numerical differentiation with respect to the calculations of certain derivatives in the detailed expressions is advocated. In order to avoid unnecessary numerical errors we have derived the analytical expressions, as given in Appendix B.

Since the regularization factor in (14) vanishes at the wall surface and the zero wave number is omitted we obtain for the integral over the wall

$$\int_\Gamma G_{ij}(\mathbf{x}-\mathbf{x}_0)\mathrm{d}\Gamma_{\mathbf{x}} = 0, \quad \forall i,j = 1,\ldots,3, \quad \mathbf{x}_0 \in \Gamma \ . \tag{15}$$

Furthermore Eq. (15) now yields

$$\int_\Gamma G_{ij}(\mathbf{x}-\mathbf{x}_0)(f_w^j(\mathbf{x}) + C_j)\mathrm{d}\Gamma_{\mathbf{x}} \quad = \quad \int_\Gamma G_{ij}(\mathbf{x}-\mathbf{x}_0)f_w^j(\mathbf{x})\mathrm{d}\Gamma_{\mathbf{x}}, \quad \mathbf{x}_0 \in \Gamma \ .$$

This shows that if $\mathbf{f}_w$ satisfies Eq. (3) so does $\mathbf{f}_w + \mathbf{C}$, due to the fact that any constant vector is in the null-space of the integral operator. Hence $\mathbf{f}_w$ will be determined only up to a constant. To remove this ambiguity we require

$$\int_\Gamma f_w^j(\mathbf{x})\mathrm{d}\Gamma_{\mathbf{x}} = 0 \ , \quad j = 1,\ldots,3 \ , \tag{16}$$

which corresponds to a zero average force over the surface of the wall. This extra condition will be imposed as a Lagrangian multiplier as will be further discussed in Section 4. Omitting the condition (16) yields a singular algebraic system.

However if we add to the physical problem a second wall Γ_2 parallel to Γ_1 the extra condition (16) can be weakened. Due to the mutual influence of the two walls the components of the force distribution acting in the wall parallel direction are now determined. This is given by the fact that the regularization term, (14), adds non-zero components to the coupling terms between the two walls in the two periodic directions. In this case the condition (16) reduces to

$$\int_{\Gamma_i} f_{w_i}^3(\mathbf{x})\mathrm{d}\Gamma_{i\mathbf{x}} = 0 \ , \quad i = 1,2 \ , \tag{17}$$

where i denotes either of the walls Γ_1 or Γ_2.

3 A high-order quadrature rule for the Stokeslet

The central contribution of the present work is the development of a high-order quadrature rule to handle the integration of the singular kernel of the Stokes equations over a flat surface Γ, more specifically to evaluate an integral of the type

$$\int_{\Gamma} G_{0,ij}(\mathbf{x}-\mathbf{x}_0) f_j(\mathbf{x}) \mathrm{d}S_{\mathbf{x}} \ , \quad i,j=1,\ldots,3 \ , \quad \mathbf{x}_0 \in \Gamma, \tag{18}$$

where $\mathbf{G}_0$ is the free-space Stokeslet defined as in (8), and $\mathbf{f}$ is some smooth distribution of forces. The kernel $\mathbf{G}_0$ in Eq. (18) is singular at $\mathbf{x}=\mathbf{x}_0$, but the integral is well defined. This is a two-dimensional integral in $x_1,\ x_2$ and the x_3 component in the argument of the Stokeslet is zero.

Here, we will develop a class of *corrected trapezoidal rules* of high orders to evaluate this integral. These quadrature rules use a uniform distribution of quadrature points over the plane, just as the trapezoidal rule, where the weights coincide with the regular trapezoidal rule in all but a small neighborhood around the singularity. We will only be concerned with with quadrature errors due to the singularity. The numerical integration of the smooth periodic remainder $\mathbf{G}_p$ in (7) is done by the regular trapezoidal rule. The sum $\mathbf{G}=\mathbf{G}_0+\mathbf{G}_p$ yields a periodic function and boundary errors for the trapezoidal rule decay exponentially fast.

Let us call Q_h^p a quadrature rule given by the parameter p. The superscript p controls the accuracy of the method and is determined by the number of modified weights. We show numerically that the quadrature rule Q_h^p has $\mathcal{O}(h^{2p+3})$ accuracy, a theoretical analysis is to be found in [22].

Constructing the quadrature rules

In [22] a high-order method for the numerical integration of a singularity of type $1/|\mathbf{x}|$, $\mathbf{x}\in\mathbb{R}^2$ was developed. We will here apply the same guiding principles in order to develop a similar quadrature rule for the integration of the Stokeslet. The main idea used in [22] to design a quadrature rule that integrates $f(\mathbf{x})s(\mathbf{x})$, with $s(\mathbf{x})=1/|\mathbf{x}|$ and $f(\mathbf{x})$ a sufficiently smooth function is to define the *punctured trapezoidal rule* rule as the regular trapezoidal rule excluding the point $|\mathbf{x}|=0$ where the function is singular. This modified trapezoidal rule is well-defined but only first order accurate. This loss of accuracy can be recovered by modifying the quadrature weights *locally* around the singularity. Hence we seek to find correction weights $\omega_{\boldsymbol{\beta}}$ in discretization points $\boldsymbol{\beta}$ only in a close vicinity of the isolated singularity of $s(\mathbf{x})$. In this region which includes the singular point $|\mathbf{x}|=0$, we will have a local correction of the type

$$\sum_{\boldsymbol{\beta}} \omega_{\boldsymbol{\beta}} f(\boldsymbol{\beta} h) \ , \tag{19}$$

where h is the grid size taken constant in all directions. This correction is to be added to the punctured trapezoidal rule. The modified weights of the correction operator depend on the specific singularity.

Although the singularity of the Stokeslet $\mathbf{G}_0$ is of the same order as $1/|\mathbf{x}|$ we cannot directly apply the quadrature rule developed for $1/|\mathbf{x}|$ in [22]. Consider the Stokeslet (8) with the singular part factored out as follows

$$G_{0,ij}(\hat{\mathbf{x}}) = \frac{1}{|\hat{\mathbf{x}}|}\left(\delta_{ij}+\frac{\hat{x}_i\hat{x}_j}{|\hat{\mathbf{x}}|^2}\right) = \frac{\phi_{ij}(\hat{\mathbf{x}})}{|\hat{\mathbf{x}}|} \ , \quad i,j=1,2,3. \tag{20}$$

We note that the function ϕ_{ij} is $O(1)$, but the limit ℓ_{ij} as $|\hat{\mathbf{x}}|\to 0$ is not unique, i.e.

$$\lim_{\mathbf{x}\to\mathbf{x}_0} \frac{\hat{x}_i\hat{x}_j}{|\hat{\mathbf{x}}|^2} = \ell_{ij}(\theta,\varphi), \quad i,j=1,\ldots,3 \ , \tag{21}$$

where (θ, φ) denotes the angles with which we approach the singularity. Due to this non-uniqueness of the limit we cannot factor out $\phi_{ij}(\hat{\mathbf{x}})$ and hence cannot use the quadrature rule as given in [22].

We will, however, follow the same basic idea as in [22] and develop a quadrature rule for the integration of $s(\hat{\mathbf{x}}) = \phi_{ij}(\hat{\mathbf{x}})/|\hat{\mathbf{x}}|$ in the x_1x_2-plane based on the punctured trapezoidal rule and an added local modification. The new quadrature rule designed for $\phi_{ij}(\hat{\mathbf{x}})/|\hat{\mathbf{x}}|$, where $\hat{\mathbf{x}} = \mathbf{x} - \mathbf{x}_0$, will be independent of the shift $\mathbf{x}_0$, therefore in the remaining of the text we shall assume for simplicity that $\mathbf{x}_0 = 0$. Since we now need to embed also ϕ_{ij} into the modified weights the local modification will be different for different components of the Stokeslet. Thus for each component of the Stokeslet we have a new set of quadrature rules.

Since we treat a three-dimensional problem where any point on the flat plate is given as $\mathbf{x} = (x_1, x_2, 0)$ we can reduce the treatment to $\mathbf{x} = (x_1,\ x_2) \in \mathbb{R}^2$ without any loss of information. As we evaluate the Stokeslet for the x_3 component equal to 0 we distinguish three classes of kernels according to which components of the Stokeslet $\phi_{ij}(\mathbf{x})$ in (20) refers to

i) $\phi_{ii}(\mathbf{x}) = 1 + \dfrac{x_i^2}{|\mathbf{x}|^2}$, with $i = 1, 2$ representing the *diagonal* terms of the Stokeslet,

ii) $\phi_{ij}(\mathbf{x}) = \dfrac{x_i x_j}{|\mathbf{x}|^2}$, with $i \neq j = 1, 2$ representing the *off-diagonal* terms of the Stokeslet,

iii) $\phi_{33}(\mathbf{x}) = 1$, representing the diagonal term of the Stokeslet which belongs to the wall normal component.

The remaining components $\phi_{i3} = \phi_{3i}$ for $i = 1, 2$ evaluate to zero. For $\phi_{33}(\mathbf{x}) = 1$, case iii) above, the quadrature rule developed for $1/|\mathbf{x}|$ in [22] applies without any modification. Therefore we shall focus on the first two categories of kernels and refer to case iii) $1/|\mathbf{x}|$ to exemplify the concepts.

The quadrature rule designed here will be applicable to any integrand $s(\mathbf{x})f(\mathbf{x})$ with $s(\mathbf{x}) = \phi_{ij}(\mathbf{x})/|\mathbf{x}|$ and $f(\mathbf{x})$ sufficiently smooth. Consider now the Taylor expansion of the function $f(\mathbf{x})$ which represents $f(\mathbf{x})$ as a sum of high-order monomials that multiply the high-order derivatives of the function in the expansion point. To obtain a higher-order quadrature rule we need to require that it integrates exactly products of $s(\mathbf{x})$ and all the monomials up to a certain order, more precisely that the quadrature rule is exact for each $s(\mathbf{x})\mathbf{x}^{\boldsymbol{\alpha}}$, where $\boldsymbol{\alpha}$ is the degree of the monomial.

In designing the quadrature rule special attention must be given to errors originating from elsewhere in the domain that may hinder a fast, accurate computation of the correction weights. It is known from the Euler-Maclaurin expansion that the order of accuracy of the trapezoidal rule is directly linked to the number of high-order derivatives of the integrand which cancel at the boundaries, see [22] for further details. A complete such cancellation at the boundaries occurs for integrands that are either periodic or compactly supported functions. If we choose a compactly supported function, call it $g(\mathbf{x})$, we can isolate the numerical errors arising from the singularity of $s(\mathbf{x})$ from boundary errors by requesting that the quadrature rule is exact for $s(\mathbf{x})g(\mathbf{x})\mathbf{x}^{\boldsymbol{\alpha}}$ instead of $s(\mathbf{x})\mathbf{x}^{\boldsymbol{\alpha}}$. We shall see that the correction weights obtained through this procedure are ultimately independent of the choice of g.

As a first step we approximate the integral (18) by the punctured trapezoidal rule, T_h^0, where the singular point, $\mathbf{x} = 0$, is skipped in the summation

$$\int_D s(\mathbf{x})g(\mathbf{x})\mathrm{d}\mathbf{x} \approx T_h^0[s \cdot g] = \sum_{|\boldsymbol{\beta}| \neq 0} h^2 s(\boldsymbol{\beta}h)g(\boldsymbol{\beta}h)\ .$$

Here, the integral is over a flat plate, and so $\mathbf{x} \in \mathbb{R}^2$. To first construct a quadrature rule that is exact for $s(\mathbf{x})g(\mathbf{x})\mathbf{x}^{\boldsymbol{\alpha}}$ with $\boldsymbol{\alpha} = 0$, we make the simplest possible modification and introduce a correction weight at the origin, $\omega_0(h)$. We now require that

$$\int_D s(\mathbf{x})g(\mathbf{x})\mathrm{d}x = T_h^0[s \cdot g] + h\omega_0(h)g(0) \ . \tag{22}$$

Here the compactly supported $g(\mathbf{x})$ is introduced to annihilate boundary errors, and $g(0) = 1$. The weight $\omega_0(h)$ depends on g and h according to

$$\omega_0(h) = \frac{1}{hg(0)}\left(\int_D s(\mathbf{x})g(\mathbf{x})\mathrm{d}x - T_h^0[s \cdot g]\right) , \tag{23}$$

and $\omega_0(h) \to \omega_0$ as $h \to 0$. Once the weight has converged it is independent of the grid resolution and also of the function g. How fast the the weight converges depends on the flatness of g at the singularity, see the discussion in [22] and also in Section 3. With a converged weight ω_0 we can define the quadrature rule that integrates $s(\mathbf{x})f(\mathbf{x})$, where $f(\mathbf{x})$ is any smooth function, as

$$Q_h^0[s \cdot f] = T_h^0[s \cdot f] + h\omega_0 f(0) \ . \tag{24}$$

This yields a third order accurate quadrature rule and we shall discuss the specifics for each of the cases i) diagonal and ii) off-diagonal terms in the next sections.

The quadrature rule Q_h^p will be designed requiring that it integrates $s(\mathbf{x})g(\mathbf{x})\mathbf{x}^{\boldsymbol{\alpha}}$ exactly for all $|\boldsymbol{\alpha}|$ such that $|\boldsymbol{\alpha}| \le p$. The monomials which are such that the integral of $s(\mathbf{x})\mathbf{x}^{\boldsymbol{\alpha}}g(\mathbf{x})$ vanishes will be automatically integrated exactly as certain symmetries are preserved by the quadrature rule. These monomials will not be explicitly enforced. Denote the sets of exponents $\boldsymbol{\alpha}$ of the monomials whose exact integration are enforced by $\mathcal{M}_q$, $q \le p$. Furthermore, the sets of discrete points, $\boldsymbol{\beta}$, in which we define correction weights will be denoted by $\mathcal{G}_q^m$, with $m \le q$ and $q \le p$. We construct each set $\mathcal{G}_q^m$ such that

$$s(\boldsymbol{\beta}h) = s(\boldsymbol{\beta}'h) \quad \forall \boldsymbol{\beta}, \boldsymbol{\beta}' \in \mathcal{G}_q^m \ . \tag{25}$$

Hence the symmetries of the singularity are important in this construction. To each set $\mathcal{G}_q^m$, there will be one associated weight ω_q^m.

Since the singular part of $s(\mathbf{x})$, namely $1/|\mathbf{x}|$ is radially symmetric we also require that $g(\mathbf{x})$ shares the same property. The computation of the weights can be expedited by choosing $g(\mathbf{x})$ to be flat around the origin, i.e. have a number of vanishing derivatives at the origin as will be explained in Section 3.

In analogy with (22) we now define the weights ω_q^m as the solution to the linear system of equations for all $\boldsymbol{\alpha} \in \mathcal{M}_q, \ q \le p$,

$$\int s(\mathbf{x})\mathbf{x}^{\boldsymbol{\alpha}}g(\mathbf{x})\mathrm{d}\mathbf{x} = T_h^0[s \cdot \mathbf{x}^{\boldsymbol{\alpha}} \cdot g] + h\sum_{q,m}\sum_{\boldsymbol{\beta}\in\mathcal{G}_q^m} \omega_q^m(h)(\boldsymbol{\beta}h)^{\boldsymbol{\alpha}}g(\boldsymbol{\beta}h) \ . \tag{26}$$

The higher order quadrature rule will be of the form

$$Q_h^p[s \cdot f] = T_h^0[s \cdot f] + A_h^p f \ , \tag{27}$$

where the correction operator is given as

$$A_h^p f = h\sum_{m,q}\omega_q^m \sum_{\boldsymbol{\beta}\in\mathcal{G}_q^m} f(\boldsymbol{\beta}h) \ . \tag{28}$$

For the function $s(\mathbf{x}) = 1/|\mathbf{x}|$ all points that lie at the same distance from the origin satisfy (25) and we can choose $\mathcal{G}_q^m$ to be the set of such points. Since integrands given by odd monomials have vanishing integrals we take monomials of exponent $2\boldsymbol{\alpha}$. At a certain q-level we should consider all monomials with $|\boldsymbol{\alpha}| = q$. We observe that in this case it is enough to take a monomial of exponent (α_1, α_2) since this gives the same computed weight as a monomial of order (α_2, α_1). Details about the quadrature rule can be found in [22], here we provide only the computed weights and corresponding sets in Table A.1. In the following we focus on the different forms the integrand $\phi_{ij}(\mathbf{x})/|\mathbf{x}|$ may take. Since we study separately specific combinations of the indices i, j we drop the subscript of the function ϕ in the subsequent analysis.

Table 1: Table of sets for the diagonal components of the Stokeslet for different values of q, with $q \leq p = 4$. For a quadrature rule Q_h^p, all sets with $q \leq p$ will be included. Order of accuracy is $\mathcal{O}(h^{2p+3})$. Here we consider the diagonal terms $\phi(\mathbf{x}) = 1 + x_1^2/|\mathbf{x}|^2$, for the terms $\phi(\mathbf{x}) = 1 + x_2^2/|\mathbf{x}|^2$ the weights and sets $\mathcal{G}_q^m$ will be swapped.

q	m	$\boldsymbol{\alpha}$	$\mathbf{x}^{2\boldsymbol{\alpha}}$	$\mathcal{G}_q^m$	Associated weight ω_q^m
0	0	(0,0)	1	$(0,0)$	ω_0^0
1	0	(1,0)	x_1^2	$(\pm1, 0)$	ω_1^0
	1	(0,1)	x_2^2	$(0, \pm1)$	ω_1^1
2	0	(2,0)	x_1^4	$(\pm2, 0)$	ω_2^0
	1	(1,1)	$x_1^2 x_2^2$	$(\pm1, \pm1)$	ω_2^1
	2	(0,2)	x_2^4	$(0, \pm2)$	ω_2^2
3	0	(3,0)	x_1^6	$(\pm3, 0)$	ω_3^0
	1	(1,2)	$x_1^2 x_2^4$	$(\pm1, \pm2)$	ω_3^1
	2	(2,1)	$x_1^4 x_2^2$	$(\pm2, \pm1)$	ω_3^2
	3	(0,3)	x_2^6	$(0, \pm3)$	ω_3^3
4	0	(4,0)	x_1^8	$(\pm4, 0)$	ω_4^0
	1	(1,3)	$x_1^2 x_2^6$	$(\pm1, \pm3)$	ω_4^1
	2	(2,2)	$x_1^4 x_2^4$	$(\pm2, \pm2)$	ω_4^2
	3	(3,1)	$x_1^6 x_2^2$	$(\pm3, \pm1)$	ω_4^3
	4	(0,4)	x_2^8	$(0, \pm4)$	ω_4^4
5	0	(5,0)	x_1^{10}	$(\pm5, 0)$	ω_5^0
	1	(1,4)	$x_1^2 x_2^8$	$(\pm1, \pm4)$	ω_5^1
	2	(2,3)	$x_1^4 x_2^6$	$(\pm2, \pm3)$	ω_5^2
	3	(3,2)	$x_1^6 x_2^4$	$(\pm3, \pm2)$	ω_5^3
	4	(4,1)	$x_1^2 x_2^8$	$(\pm1, \pm4)$	ω_5^4
	5	(0,5)	x_2^{10}	$(0, \pm5)$	ω_5^5

Diagonal terms

The integrand $s(\mathbf{x}) = \phi(\mathbf{x})/|\mathbf{x}|$ does not have the same symmetry properties when $\phi(\mathbf{x}) \neq 1$ as discussed for $s(\mathbf{x}) = 1/|\mathbf{x}|$. Therefore we proceed by analyzing the integrand that corresponds to the diagonal terms of the Stokeslet, namely $\phi(\mathbf{x})/|\mathbf{x}|$ where

$$\phi(\mathbf{x}) = 1 + \frac{x_1^2}{|\mathbf{x}|^2} \ .$$

The term $\phi(\mathbf{x}) = 1 + x_2^2/|\mathbf{x}|^2$ exhibits a similar behavior with the sole difference that the system of coordinates is swapped. Note that $\phi(\mathbf{x})$ is symmetric with respect to sign changes but not with respect to index permutations

$$\begin{aligned} \phi(\beta_1 h, \beta_2 h) &\neq \phi(\beta_2 h, \beta_1 h) \ , \\ \phi(\pm\beta_1 h, \pm\beta_2 h) &= \phi(\beta_1 h, \beta_2 h) \ . \end{aligned}$$

This implies that we need to distinguish between points (β_1, β_2) and (β_2, β_1). Consequently we now need to design the quadrature rule to be exact for both monomials of exponent generated by (α_1, α_2) and (α_2, α_1). More precisely we enforce monomials of exponent $2\boldsymbol{\alpha}$ with $\boldsymbol{\alpha} = (q-m, m)$ over sets given as

$$\mathcal{G}_q^m = \{\boldsymbol{\beta} \in \mathbb{Z}^2 \quad s.t. \quad \boldsymbol{\beta} = (\pm(q-m), \pm m)\} \ .$$

We define the sets

$$\mathcal{M}_q = \bigcup_{m \leq q} \{(q-m, m)\}, \qquad \mathcal{L}_q = \bigcup_{m \leq q} \mathcal{G}_q^m .$$

With these sets we compute the modified weights to obtain a quadrature rule of $\mathcal{O}(h^{2p+3})$. In Fig. 2a we illustrate in which points $\boldsymbol{\beta} h$ we modify the weights while in Table 1 we have a description of the sets of points versus the monomials that have to be enforced for an increase in accuracy given by p. The values obtained for the weights are all gathered in Table A.2 in Appendix A.

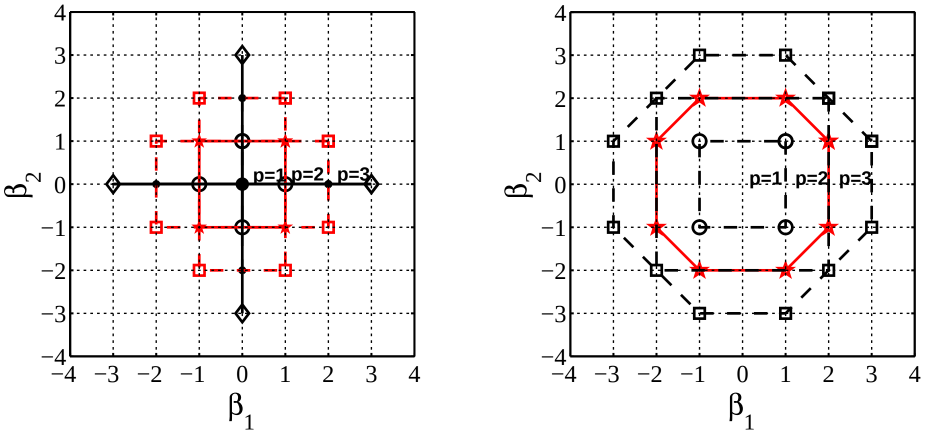

(a) Sets $\mathcal{G}_q^m$ for $G_{0,ii}$ with $i < 3$

(b) Sets $\mathcal{G}_q^m$ for $G_{0,ij}$ with $i \neq j < 3$

Figure 2: Sets of points, $\mathcal{G}_q^m$ surrounding the origin: solid/dashed line connect points belonging to the same set $\mathcal{G}_q^m$, markers of the same type denote all points needed for an increase in accuracy (sets $\mathcal{G}_q^m$ for all m).

The quadrature rule for diagonal terms will then be the same as in (27) with the correction operator

$$A_h^p f = h \sum_{q=0}^{p} \sum_{m=0}^{q} \omega_q^m \sum_{\boldsymbol{\beta} \in \mathcal{G}_q^m} f(\boldsymbol{\beta} h) \ . \tag{29}$$

Whether $\phi(\mathbf{x}) = 1 + x_1^2/|\mathbf{x}|^2$ or $\phi(\mathbf{x}) = 1 + x_2^2/|\mathbf{x}|^2$ we will obtain the same weights mirrored with respect to the x_1 or x_2 axis. The weight that corresponds to (β_1, β_2) computed for $\phi(\mathbf{x}) = x_1^2/|\mathbf{x}|^2$ by enforcing the monomial x_2^2 has the same magnitude as the one for $\phi(\mathbf{x}) = x_2^2/|\mathbf{x}|^2$ in (β_2, β_1). Therefore it is enough to compute one set of such weights and have the corresponding ones by mirroring.

Off-diagonal terms

Regarding integrands given as $\phi(\mathbf{x})/|\mathbf{x}|$ where $\phi(\mathbf{x}) = \dfrac{x_1 x_2}{|\mathbf{x}|^2}$ we notice that no correction is required in order to devise a quadrature rule of $\mathcal{O}(h^3)$, this being automatically satisfied. The integrand is an odd function to be integrated over a symmetric domain which leads to a vanishing integral. Furthermore sets of points where either component x_1 or x_2 evaluates to zero will not be associated with any corrected weight, since the kernel evaluates to zero in such points.

In order to find the sets over which we have the same weight we note that

$$\phi(\beta_1 h, \beta_2 h) = \phi(\beta_2 h, \beta_1 h) \ ,$$

but the integrand is not invariant to sign permutations unless the permutation occurs for both spatial variables, i.e.,

$$\phi(\beta_1 h, \beta_2 h) = \phi(-\beta_1 h, -\beta_2 h) \ .$$

This means that if we embed the kernel into the weights we have the same magnitude of the weight for a certain set of points β_1, β_2 but different signs according to whether $\beta_1\beta_2 > 0$ or $\beta_1\beta_2 < 0$. With this knowledge we make the assumption that all weights corresponding to coordinates generated by β_1, β_2 in the four quadrants of the Cartesian grid are equal in magnitude but of sign given by the product $\beta_1\beta_2$. This assumption simplifies the process of computing the weights.

The sets of discretization points have now for a given p the expression

$$\mathcal{G}_q^m = \{\boldsymbol{\beta} \in \mathbb{Z}^2 \quad s.t. \quad \boldsymbol{\beta} = (\pm(q-m+1), \pm m)\} \ .$$

and

$$\mathcal{M}_q = \bigcup_{m \le [(q+1)/2]} \{(q, m)\} \ , \qquad \mathcal{L}_q = \bigcup_{m \le [(q+1)/2]} \mathcal{G}_q^m \ .$$

Fig. 2b offers a graphical representation of the sets over which the quadrature rule will be modified. In Table 2 we have listed explicitly the sets $\mathcal{G}_q^m$ and the associated monomials $\mathcal{M}_q$. Note that the monomials that have to be enforced over sets $\mathcal{G}_q^m$ are of exponent $2\boldsymbol{\alpha} - (1,1)$. This is justified by the fact that we already have a monomial $x_1 x_2$ incorporated in the integrand. The computed weights can be found in Table A.4. With these weights the correction operator gives a quadrature rule of $\mathcal{O}(h^{2p+3})$.

The quadrature rule for the off-diagonal terms is the same as (27) with the correction operator

$$A_h^p f = h \sum_{q=1}^{p} \sum_{m=1}^{[(q+1)/2]} \omega_q^m \sum_{\boldsymbol{\beta} \in \mathcal{G}_q^m} \operatorname{sgn}(\beta_1 \beta_2) f(\boldsymbol{\beta} h) \ . \tag{30}$$

Computing the weights

To retrieve the corrected weights for the quadrature rule a system as (26) has to be solved. Such a system is severely ill-conditioned. As we decrease h to obtain the weights ω_q^m to

Table 2: Sets of discretization points $\mathcal{G}_q^m$ for the off-diagonal components of the Stokeslet for different values of $q \leq p = 5$. For a quadrature rule Q_h^p, all sets with $q \leq p$ will be included, the order of accuracy is $\mathcal{O}(h^{2p+3})$.

q	m	$\boldsymbol{\alpha}$	$\mathbf{x}^{2\boldsymbol{\alpha}-(1,1)}$	$\mathcal{G}_q^m$	Associated weight ω_q^m
1	1	(1,1)	x_1x_2	$(\pm1,\pm1)$	ω_1^1
2	1	(2,1)	$x_1^3x_2$	$(\pm2,\pm1),\ (\pm1,\pm2)$	ω_2^1
3	2	(2,2)	$x_1^3x_2^3$	$(\pm2,\pm2)$	ω_3^2
	1	(3,1)	$x_1^5x_2$	$(\pm3,\pm1),\ (\pm1,\pm3)$	ω_3^1
4	2	(3,2)	$x_1^5x_2^3$	$(\pm3,\pm2),\ (\pm2,\pm3)$	ω_4^2
	1	(4,1)	$x_1^7x_2$	$(\pm4,\pm1),\ (\pm1,\pm4)$	ω_4^1
5	3	(3,3)	$x_1^5x_2^5$	$(\pm3,\pm3),\ (\pm3,\pm3)$	ω_5^3
	2	(4,2)	$x_1^7x_2^3$	$(\pm4,\pm2),\ (\pm2,\pm4)$	ω_5^2
	1	(5,1)	$x_1^9x_2$	$(\pm5,\pm1),\ (\pm1,\pm5)$	ω_5^1

double precision the condition number increases to such extent that the errors due to ill-conditioning are larger than the gain from the fine resolution. To circumvent this issue we will compute the weights by using a multi-precision library. The choice of the function g can speed up the convergence of the weights. The function $g(\mathbf{x}) = e^{-|\mathbf{x}|^{2k}}$ is radially symmetric and although it is not compactly supported it decays fast enough to be considered as such in numerical computations. For the chosen $g(\mathbf{x}) = e^{-|\mathbf{x}|^{2k}}$ the order of convergence of the weights will be $\mathcal{O}(h^{2k})$. Hence a larger value for k leads to faster convergence of the weights. However a too large value of the parameter k gives a function g which transitions from the value of 1 to zero more rapidly. This implies that higher resolution is needed to obtain a reliable numerical approximation using the trapezoidal rule. Therefore we choose in computations an intermediate value for the parameter k, namely $k = 3$. Nonetheless it is still necessary to solve the system (26) in multi-precision arithmetic but the weights can be obtained by using a reasonably large grid resolution, thus a less ill-conditioned system.

Validation of the quadrature rule

To asses the accuracy of the developed quadrature rule Q_h^p we apply it to

$$I_j(\mathbf{x}_0) = \int_\Gamma G_{ij}(\mathbf{x}-\mathbf{x}_0) f_j(\mathbf{x}) \mathrm{d}\Gamma_{\mathbf{x}} \ , \quad \Gamma = [-1,1]\times[-1,1], \quad \mathbf{x}_0 = 0 \ , \tag{31}$$

with $\mathbf{f} = (\cos(2\pi x) + \cos(4\pi y),\ \cos(4\pi x)\cos(2\pi y),\ \cos(2\pi x))$ and $\mathbf{G}$ as defined in (7). Note that we have chosen a periodic function in order to eliminate boundary errors such that we can observe the high-order treatment of the singularity.

In Fig. 3 we present the convergence rate of a set of quadrature rules Q_h^p with $p = 0, \ldots, 4$. We illustrate only the accuracy of the method as applied to the first component of the above integral, the other components behave in the same manner and the convergence rate for these terms is not displayed here. The expected convergence order is $\mathcal{O}(h^{2p+3})$ and the figure shows the predicted order of accuracy.

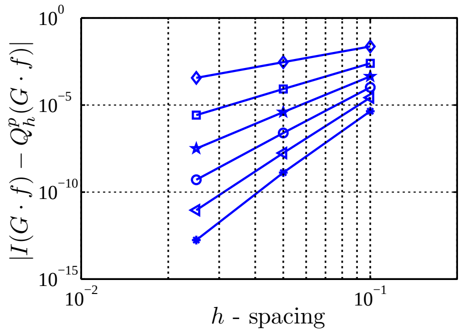

Figure 3: Accuracy results for increasing values of the parameter p: $\diamond$ ($p = 0$), $\square$ ($p = 1$), $\star$ ($p = 2$), $\circ$ ($p = 3$), $\triangle$ ($p = 4$), $*$ ($p = 5$). The convergence order is $\mathcal{O}(h^{2p+3})$. The study is performed for the first component, I_1, in (31).

4 Discretization of the boundary integral equations

In this section we will discuss how to discretize the boundary integral equations given in Section 2, first for the system with only one or two walls and then for the coupled wall-sphere problem. The discretization is performed in the framework of Nyström's method. For the numerical integration, throughout all the examples illustrated here, we use the trapezoidal rule and modifications of the trapezoidal rule that correct for boundary errors and singularities.

Numerical treatment of the wall surface

The wall is discretized on a uniform grid in $x \in [-L_x/2, L_x/2)$ and $y \in [-L_y/2, L_y/2)$ with the same resolution, h_w, in both spatial directions, where L_x, L_y represent the periodic lengths. We omit the last point in the discretization due to the periodic boundary conditions and ultimately have $N_w = N_x N_y$ discretization points over the wall.

Denote by

$$\begin{aligned} I_{ww}^{\mathbf{x}_0}[\mathbf{f}_w] &= \int_\Gamma \mathbf{G}(\mathbf{x}-\mathbf{x}_0)\mathbf{f}_w(\mathbf{x})\mathrm{d}\Gamma_\mathbf{x}, \\ &= \int_\Gamma \mathbf{G}_0(\mathbf{x}-\mathbf{x}_0)\mathbf{f}_w(\mathbf{x})\mathrm{d}\Gamma_\mathbf{x} + \int_\Gamma \mathbf{G}_p(\mathbf{x}-\mathbf{x}_0)\mathbf{f}_w(\mathbf{x})\mathrm{d}\Gamma_\mathbf{x}, \quad \mathbf{x}_0 \in \Gamma . \end{aligned} \tag{32}$$

The first integral containing the free space Stokeslet 8 will be evaluated using the quadrature rule Q_h^p described in Section 3 for all discrete points $\mathbf{x}_0$ in the uniform grid. The quadrature rule will now be centered at the singular points $\mathbf{x} = \mathbf{x}_0$. However it will have the same weights for any $\mathbf{x}_0$ since the quadrature rule is invariant to shifts over the periodic domain. The superscript p determines the accuracy of the method when applied to each component of the tensor $G_{0,ij} f_w^j$ with $i, j = 1, \ldots, 3$. In the following examples we will consider $p = 4$, i.e. the $\mathcal{O}(h^{11})$ quadrature rule. The full periodic Stokeslet $\mathbf{G}_0 + \mathbf{G}_p$ is evaluated over a whole period which means that applying the trapezoidal rule will yield, besides the errors arising from the local integration of the singularity, exponentially decaying boundary errors.

Assume that the unknown discrete three-dimensional distribution of forces over the wall surface $\mathbf{f}_w(x_k, y_l)$ where $k = 1, 2, \ldots N_x$, and $l = 1, 2, \ldots N_y$, has a corresponding discrete vector $f_w = [f_w^1, f_w^2, f_w^3]$. In f_w the unknowns are ordered as

$$f_w^1 = [f_w^1(x_1, y_1), \dots f_w^1(x_1, y_{N_y}), \dots f_w^1(x_{Nx}, y_1), \dots f_w^1(x_{N_x}, y_{Ny})]$$

and similar for f_w^2 and f_w^3. With this ordering the discrete system arising from the integral operator (32) takes the form $I_{ww} f_w$, where I_{ww} is an $3N_w \times 3N_w$ matrix whose structure will be discussed in Section 4.

The fact that the forces f_w are determined only up to a constant, as discussed in Section 2, implies in algebraic terms that the matrix, I_{ww} is singular. It is possible to impose the condition (16) on a full but singular system by including it as a Lagrangian multiplier. This means that we consider an extra variable λ which enforces (16). In a discrete setting we write the integral given by (16) as $C_w f_w = 0$, with C_w being the discrete integral operator (given by the trapezoidal rule which is spectrally accurate for a periodic domain). Now reconsider (2), with the wall being the only boundary, and rewrite the discrete system by imposing the constraint (16) as

$$\begin{aligned} I_{ww} f_w + \lambda C_w^T &= 0 \ , \\ C_w f_w &= 0 \ . \end{aligned}$$

This modification is still necessary as the system is extended to the coupled wall-sphere problem.

Low storage implementation

The numerical simulation of a physical problem stated in terms of boundary integrals requires solely the discretization of the relevant boundaries. Consequently the number of unknowns in a boundary integral formulation is smaller compared to other approaches (finite difference methods, finite element methods). However the matrices corresponding to the discrete algebraic system are dense and as such they need significant amounts of memory to be stored. Since we assume the wall to be non-deformable its position is not time dependent. Therefore we seek to exploit the structure of the underlying wall matrix, I_{ww}, in order to minimize the memory usage.

Let us analyze the integral operator $I_{ww}^{\mathbf{x}_0}[\mathbf{f}_w]$ defined in (32) which generates, for all $\mathbf{x}_0 \in \Gamma$, the matrix I_{ww}. Since G_{ij} is a second order symmetric tensor, $G_{ij} = G_{ji}$ with $i, j = 1, \dots, 3$, we have six distinct blocks that generate the matrix I_{ww} which will be block symmetric. Furthermore recall that the plane Γ spans the whole periodic box thus we integrate a periodic integrand over a whole period and

$$\int_\Gamma G_{ij}(\mathbf{x} - \mathbf{x}_0) \mathrm{d}\Gamma_\mathbf{x} = \int_\Gamma G_{ij}(\mathbf{x} - \overline{\mathbf{x}}_0) \mathrm{d}\Gamma_\mathbf{x} \ , \quad \forall \quad \mathbf{x}_0, \overline{\mathbf{x}}_0 \in \Gamma, \ i, j = 1, \dots, 3 \ . \tag{33}$$

It is therefore enough to discretize the integral operator $I_{ww}^{\mathbf{x}_0}$ which applies to $\mathbf{f}_w$ for a given $\mathbf{x}_0$, say $\mathbf{x}_0 = 0$, and all other evaluations at points $\mathbf{x}_0 \neq 0$ will yield the same result. The emerging matrix block I_{ww} permutes its elements cyclically as $\mathbf{x}_0$ browses the whole plane in a predetermined order. More specifically as $\mathbf{x}_0$ changes its position the corresponding row in the matrix I_{ww} will be a permutation of the previous one as will be further described. The special structure of the matrix I_{ww}, i.e. block-Toeplitz-symmetric with circulant subblocks, implies that the matrix is determined by only three columns. In Fig. 4 we sketch the structure of the matrix by zooming in into one block B although this also holds for all other blocks in the full matrix. In practice this has a great impact on the efficient storage problem since we need to load into memory only the generating vectors and compute each new matrix entry on-site by using the known structure of I_{ww}.

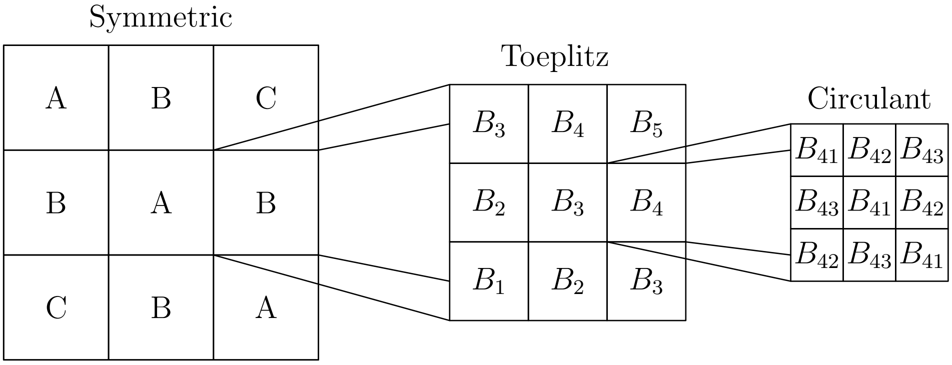

Figure 4: Matrix structure — Block Toeplitz Symmetric with Circulant sub-blocks. The matrix can be regarded as having an hierarchical structure. At the first level the matrix is symmetric, at the second level the blocks have Toeplitz sub-blocks and ultimately each sub-block is a circulant matrix.

Modeling the wall by using only the single layer formulation, more specifically by describing the velocity at the wall solely in terms of the Stokeslet, yields an ill-conditioned problem. The conditioning of the problem does not pose many difficulties in practice since due to the high-order quadrature we can achieve the desired accuracy without too many discrete points over the wall. However we shall briefly discuss the conditioning of the problem and practical approaches.

From Section 2 we know that the block matrix I_{ww} does not have full rank and to close the system we add the extra conditions (16), thus yielding an extended full rank matrix. It is worth noting that the full-rank of the discrete matrix I_{ww} can be easily restored. To do so we are allowed to add the conditions (16) to the integral operator $I^{\mathbf{x}_0}_{ww}[\mathbf{f}_w]$ over the wall. The new modified operator $\tilde{I}^{\mathbf{x}_0}_{ww}[\mathbf{f}_w]$

$$\int_\Gamma \mathbf{G}(\mathbf{x}-\mathbf{x}_0)\mathbf{f}_w(\mathbf{x})\mathrm{d}\Gamma_{\mathbf{x}} + \int_\Gamma \mathbf{f}_w(\mathbf{x})\mathrm{d}\Gamma_{\mathbf{x}} \ . \tag{34}$$

leads to a full rank matrix $\tilde{I}_{ww}$. This is mathematically equivalent to the original formulation since it is coupled to the constraint that the integral over the forces evaluates to zero. It can be numerically observed that the new block $\tilde{I}_{ww}$ has now a condition number $\kappa(\tilde{I}_{ww}) \approx 2\sqrt{N_w}$. This condition number does not pose problems since we can achieve a small numerical error by using a high-order quadrature rule. We have also found that the special structure of the matrix $\tilde{I}_{ww}$ is preserved under inversion. Therefore the inverse matrix of $\tilde{I}_{ww}$ can be easily computed by solving three algebraic systems

$$\tilde{I}_{ww}c_i = e_i \ , \quad i = 1, N_w+1, 2N_w+1 \ , \tag{35}$$

that will return the generating columns c_i of the inverse $\tilde{I}^{-1}_{ww}$. The right-hand side e_i is the base vector which is null everywhere except at i. It has been chosen such that we compute a generating column for each matrix sub-block that corresponds to an element of the tensor G_{ij}, $i,j = 1,\ldots,3$. Since $\tilde{I}_{ww}$ does not require evaluation in each time step, neither does $\tilde{I}^{-1}_{ww}$ which implies that the same efficient storage treatment can be used. In the present context we have used the inverse of the wall matrix $\tilde{I}^{-1}_{ww}$ to reduce the system and solve it using the Schur complement, see [16].

Wall-body coupling

In order to treat numerically the wall-sphere problem we need to discretize and solve the complete system given by (9) when $\mathbf{x}_0 \in \Gamma$ and (10) for $\mathbf{x}_0 \in S$, together with the constraints (5) and (16).

Similar to the definition in (32), the integral operators will be denoted by I, followed by a subscript which specifies the location of the pole $\mathbf{x}_0$ and a second subscript that designates the domain of integration. Previously, we had $I_{ww}^{\mathbf{x}_0}[\mathbf{f}_w]$ as defined in (32), now we introduce also $I_{ws}^{\mathbf{x}_0}[\mathbf{f}_s]$ which is the second integral term in (9) where the pole $\mathbf{x}_0$ is on the wall and the integration is performed over the sphere. With the same type of notation the Eq. (5) involves the terms $I_{ss}^{\mathbf{x}_0}[\mathbf{f}_s]$ and $I_{sw}^{\mathbf{x}_0}[\mathbf{f}_w]$. Hence, $I_{ww}^{\mathbf{x}_0}[\mathbf{f}_w]$ and $I_{ss}^{\mathbf{x}_0}[\mathbf{f}_s]$ have singular integrands.

The evaluation of the operator $I_{ww}^{\mathbf{x}_0}[\mathbf{f}_w]$ has already been discussed in Section 3. For the operator $I_{sw}^{\mathbf{x}_0}[\mathbf{f}_w]$, where the integrand is non-singular, a regular trapezoidal rule can be applied. This is a spectrally accurate quadrature rule since the domain is periodic.

The discretization of the sphere will be performed in spherical coordinates φ, θ, where $\theta \in [0, \pi]$, $\phi \in [0, 2\pi)$, with a spacing of $\Delta_\phi, \Delta_\theta$ giving a total of $N_s = N_\varphi N_\theta$ discretization points on the sphere surface.

To treat the singularity in $I_{ss}^{\mathbf{x}_0}[\mathbf{f}_s]$, we rewrite the integral containing the free-space Stokeslet $\mathbf{G}_0$ using the singularity subtraction method, [24],

$$\begin{aligned}\int_S \mathbf{G}_0(\mathbf{x}-\mathbf{x}_0)\mathbf{f}_s(\mathbf{x})\mathrm{d}S_{\mathbf{x}} = &\int_S \mathbf{G}_0(\mathbf{x}-\mathbf{x}_0)(\mathbf{f}_s(\mathbf{x})-\mathbf{f}_s(\mathbf{x}_0))\mathrm{d}S_{\mathbf{x}} \\ &+ \mathbf{f}_s(\mathbf{x}_0)\int_S \mathbf{G}_0(\mathbf{x}-\mathbf{x}_0)\mathrm{d}S_{\mathbf{x}} \ .\end{aligned} \tag{36}$$

The singular part has been isolated and the first term of the right-hand side is regular and can be evaluated numerically. To this term we apply the trapezoidal rule in spherical coordinates yielding second-order accuracy. The second term can be evaluated analytically, and equals $(16\pi r/3)\mathbf{I}$, with $\mathbf{I}$ being the identity matrix. This integral is invariant to the relative position of $\mathbf{x}_0$ since we can always remap the coordinate system by using a Householder transform as in [3]. The smooth periodic remainder does not pose any numerical difficulties, and it is integrated by using the standard trapezoidal rule.

The integral $I_{ws}^{\mathbf{x}_0}[\mathbf{f}_s]$ for poles $\mathbf{x}_0$ on the wall does not contain any singularities. Applying a standard trapezoidal rule will yield second order accuracy, since the integrand is not periodic in the θ direction. The accuracy in this direction will hence be improved by using boundary corrections as in [2]. A boundary corrected trapezoidal rule of $\mathcal{O}(h^k)$ requires $k-1$ modified weights at each integration boundary and is of the type

$$\int_a^b f\mathrm{d}x \approx T_h^k(f) = T_h(f) + h\sum_{i=1}^{k-1} w_i[f(a+(i-1)h) + f(b-(i-1)h)] \ , \tag{37}$$

where $T_h(f)$ is the regular trapezoidal rule and w_i are modified coefficients tabulated as in [2]. Here we choose a quadrature rule that is $\mathcal{O}(\Delta_\phi^8)$ accurate. This modified quadrature rule falls within the same category as the modified quadrature rule that we have developed for the Stokeslet and leads to a high-order numerical integration with almost no extra cost, since it involves only the adjustment of a few weights.

Advection of the immersed body

Once the full system given by equations (9-10) is solved and the velocities $\mathbf{V}, \mathbf{\Omega}$ are known the sphere can be advected according to (6). This is an ordinary differential equation which is solved by employing a standard second order multi-step scheme

$$\frac{3\mathbf{x}_c^{n+1} - 4\mathbf{x}_c^{n} + \mathbf{x}_c^{n-1}}{2\Delta t} = 2\mathbf{V}^n - \mathbf{V}^{n-1},\ n \geq 1\ , \tag{38}$$

where $\Delta t = t^{n+1} - t^n$ is the time step. In order to initialize the multi-step method the first step is done via a first-order Euler scheme. The rotational velocity can be updated similarly. However it is unnecessary to keep track of the rotational velocity of the sphere since due to its perfectly symmetric geometry the updated position of the sphere is invariant to rotations.

5 Numerical examples

Non-homogeneous boundary conditions

The boundary treatment suggested here allows for any non-homogeneous boundary condition which corresponds to a velocity field with zero net flux in the control volume. We shall now focus on the properties of the numerical treatment of one wall with imposed boundary conditions, however this can be extend to the two-parallel walls problem without any difficulties.

To study the accuracy of the method we impose a smooth boundary condition $\mathbf{u} = (u_1, u_2, u_3) = (0, 0, \sin(2\pi x_1))$ as the right hand side of the Eq. (2) where we take $\Gamma = [-2\ 2]^2$. The wall is not moving and this non-homogeneous boundary condition corresponds to an approximation of a porous wall that allows for velocity inflow/outflow. The velocity field is obtained by first solving the algebraic system emerging from the discretization of (2) which gives the force distribution $\mathbf{f}$ over the wall surface. Once the force distribution is available the velocity field in the entire volume is computed a posteriori by evaluating the same Eq. (2) for points $\mathbf{x}_0$ above or below the wall surface.

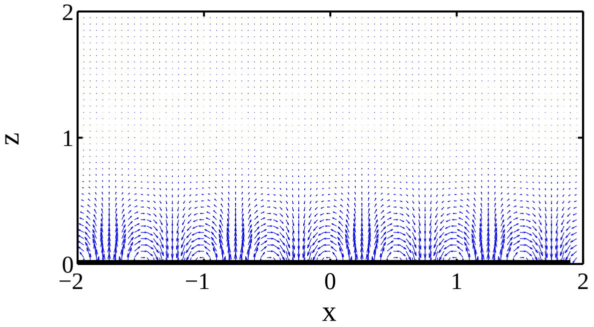

Figure 5: Velocity field u, w in the xz plane. The wall surface is at $z = 0$.

In Fig. 5 we present the generated velocity field in a cross section given by the xz-plane centered in the middle of the domain. The boundary condition was chosen such that it gives rise to vortical structures with one period per unit length. Subsequently we study the accuracy of the velocity field for a number of points per period. To asses the convergence properties we compute the velocity field over two plane sections above the wall Γ situated at $z = 0.3$ and $z = 0.8$. The error, as the solution is refined from a grid with points at equidistant spacing $h_w = 0.4$ to $h_w = 0.2,\ 0.1,\ 0.05$, is evaluated in L_2-norm as defined in (40). From (2) we obtain the force distribution which converges as displayed in Fig. 6a for

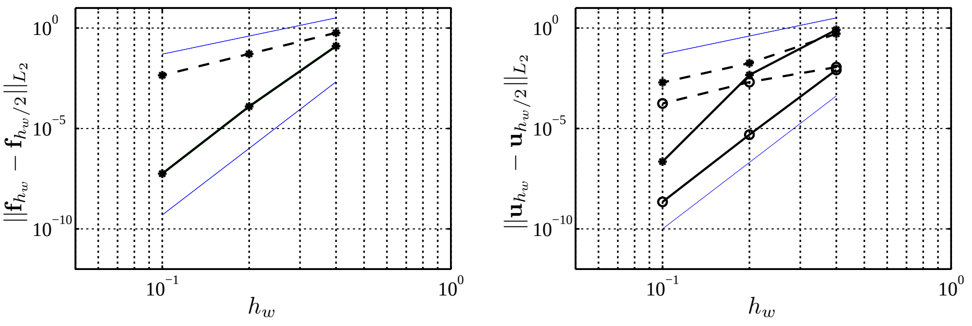

(a) Error versus wall resolution for the distribution of forces over the wall surface.

(b) Error versus wall resolution for cross sectional velocity fields at distance from wall : (∘) — $z = 0.8$; ($*$) — $z = 0.3$.

Figure 6: Convergence rate for two different quadrature rules: (dashed line) — $\mathcal{O}(h^3)$; (continuous line) — $\mathcal{O}(h^{11})$, (thin blue line — expected convergence rate).

two chosen quadrature rules of orders $\mathcal{O}(h^3)$, and $\mathcal{O}(h^{11})$. We observe that for as little as 5 points per period we obtain an error of approximately 10^{-7} with a higher order quadrature rule, i.e. $\mathcal{O}(h^{11})$. Note that using a higher order quadrature rule incurs essentially no extra computational cost since the number of unknowns remains the same thus this method is convenient for numerical implementations.

The errors in the computation of the velocity field originate from two sources: i) the underlying computation of the forces, and ii) the evaluation of the velocity as post-processing. The first source of error was discussed above and is either $\mathcal{O}(h^3)$ or $\mathcal{O}(h^{11})$ while the error arising from the evaluation of the velocity decreases exponentially. We evaluate the velocity field at two different distances away from the wall, $z = 0.3$ and $z = 0.8$. Close to the wall, $z = 0.3$, the error from the post-processing of the velocity field dominates and we notice in Fig. 6b that for large grid sizes the error decreases exponentially. Farther away from the wall, at $z = 0.8$, the dominating error is the one from the computation of the forces. Therefore we retrieve the same convergence order as for the force distribution, and also errors of the same magnitude.

Wall-sphere interaction

The present wall model can be used in conjunction with any kind of bodies immersed in Stokes flow. For validation purposes, however, we impose a no-slip boundary condition at the wall and use the problem of a sphere sedimenting towards a flat plate, for which an analytical expression is available. The equations were discretized as described in Section 4 and the subsequent system solved for the sphere velocity.

Sphere settling onto a plane wall

The sedimentation of a sphere is a classical test case for which an analytical expression is provided by the Stokes law correction as described in Happel and Brenner [14]. The classical theory offers a relationship between the drag force, $\mathbf{F}$, and the sedimentation velocity $\mathbf{U}$ of the sphere, as given by

$$\mathbf{F} = 6\pi\mu r\lambda(H/r)\mathbf{U} \ ,$$

where the function $\lambda(H/r)$ includes the wall effect, assuming an infinite wall. Here, H/r is the distance to the wall measured from the center of the sphere scaled by its radius, r. For free-space problems the Stokes law gives the drag of the sphere as $\mathbf{F}_0 = 8\pi\mu r\mathbf{U}_0$ and we shall use it to present the results in non-dimensional form $\mathbf{F}/\mathbf{F}_0 = 6/8\lambda(H/r)\mathbf{U}/\mathbf{U}_0$.

Since the drag force $\mathbf{F}$ is known (needs to balance the buoyancy force $\Delta\rho V g\mathbf{e_g}$) we can compute $\mathbf{U}$ using the expression for λ from [14]

$$\lambda(\alpha) = \frac{4}{3}\sinh(\alpha)\sum_{n=1}^{\infty}\frac{n(n+1)}{(2n-1)(2n+3)}\left[\frac{2\sinh(2n+1)\alpha + (2n+1)\sinh 2\alpha}{4\sinh^2(n+1/2)\alpha - (2n+1)^2\sinh^2\alpha} - 1\right], \quad (39)$$

with $\alpha = \cosh^{-1}(H/r)$. The series expression for λ converges very quickly and we evaluate it for a set of ratios H/r which we use as the reference solution.

To validate our numerical approach we perform a convergence study for a sphere of radius r and a wall to sphere distance of ratio $H/r = 6$ in a box of periodic size $L_x = L_y = 10r$. We perform a set of consecutive computations and each new simulation is performed on a finer resolution. The difference between two computations is evaluated in L_2-norm for the force distributions and ℓ_2-norm for the velocity components. Assume the solution vector $f \in \mathbb{R}^m$ and the velocity $v \in \mathbb{R}^3$ then

$$|f|^2_{L_2} = \sum_i^m \frac{1}{m}|f(x_i)|^2, \quad |v|^2_{\ell_2} = \sum_i v_i^2, \quad i = 1, \dots, 3. \quad (40)$$

Table 3: Convergence results for the sedimenting sphere at $H/r = 6$ in a box of periodic size $L_x = L_y = 10r$, h corresponds to the spacing on the discretized surface.

Component	Convergence order	Difference	
c	$\log_2 \frac{\lvert c_h - c_{h/2}\rvert}{\lvert c_{h/2} - c_{h/4}\rvert}$	$\lvert c_h - c_{h/2}\rvert$	$\lvert c_{h/2} - c_{h/4}\rvert$
$\mathbf{V}$	2.00	1.9151×10^{-5}	4.7834×10^{-6}
f_s^1	2.82	3.7171×10^{-4}	5.2494×10^{-5}
f_s^2	2.82	3.7171×10^{-4}	5.2494×10^{-5}
f_s^3	2.82	2.3816×10^{-4}	3.3629×10^{-5}
f_w^1	4.24	2.4364×10^{-7}	1.2877×10^{-8}
f_w^2	4.24	2.4364×10^{-7}	1.2877×10^{-8}
f_w^3	3.56	2.0883×10^{-7}	1.7754×10^{-8}

In Table 3 the order of convergence is provided for all the unknowns that do not evaluate to zero for a resolution on the wall $h_w = r, r/2, r/4$ and on the sphere $\Delta_\theta = \Delta_\phi = \pi/10,\ \pi/20, \pi/40$. The second row of the table illustrates how the convergence order is computed. We note that we obtain mixed convergence orders since we solve a coupled system where some of the terms are evaluated with high-order methods while others are discretized with second-order methods.

In our set-up we assume the same periodic length in both spatial directions $L_x = L_y = L$. To study the effect of periodicity, and to validate that our results approach the results for an infinite domain as the periodic box size is increased, we perform a sequence of runs with L/r ranging from 10 to 25, see Fig. 7a. The radius of the sphere is kept fixed while L is varied. The grid sizes used are $h_w = r/2$ and $\Delta_\phi = 2\pi/20$, $\Delta_\theta = \pi/20$.

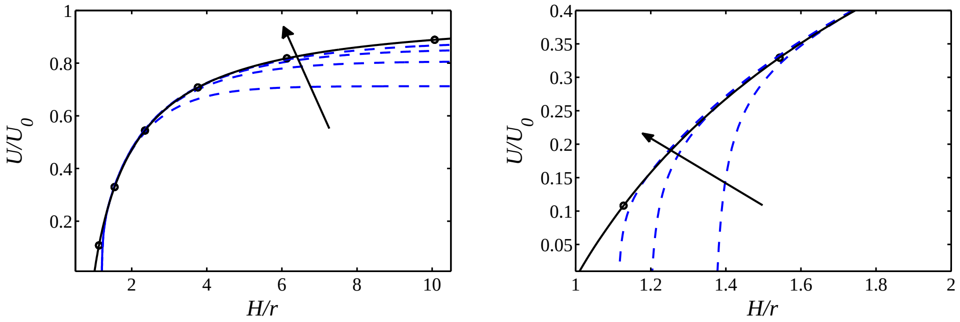

(a) In direction of arrow increasing periodic box with $L/r = 10, 15, 20, 25$.

(b) In direction of arrow increasing resolution on the wall $h_w = r, r/2, r/4$.

Figure 7: Sedimentation velocity $U = |\mathbf{U}|$ normalized by the free-space velocity $U_0 = |\mathbf{U}_0|$ versus wall distance H normalized by the sphere radius r: (solid) analytic solution, (dashed) simulations — sphere resolution is constant.

It is clear that far away from the wall the periodicity has a stronger influence on the drag of the sphere leading to a slower velocity as compared to the unbounded case. However closer to the wall the effect that dominates is the wall influence and the numerical results closely approach the analytical one, also for a small periodic box.

In the near-wall region we notice that the numerical results deviate from the analytical expression. In this case it is an effect of insufficient numerical resolution as the sphere gets very close to the wall. In order to asses the effect of the numerical error from the discretization of the wall we choose a fine resolution on the sphere $\Delta_\theta = \pi/40$ and $\Delta_\phi = 2\pi/40$ and take h_w to browse the values r, $r/2$, $r/4$ as illustrated in Fig. 7b. We notice that as the spacing on the wall decreases the analytical solution is approximated better and better close to the wall. It is worth to remark that we have chosen a resolution rather large as compared to the particle size and still the qualitative behavior is preserved. This indicates that the wall treatment is suitable even for small sized particles and the physical behavior is replicated through simulation irrespective of the particle size.

Extension to two walls

To examine a problem involving two parallel walls we consider once more a sedimenting sphere. A sphere confined in between two walls, on the axis of symmetry, sedimenting due to gravity in a direction parallel to the two walls experiences a translational velocity only in the direction of gravity. The Faxén correction for the drag of a sphere traveling with a velocity U in the wall parallel direction was derived by Faxén in 1923 [11]. Faxén has not provided a general solution for all possible locations of the sphere but only for two particular cases where a sphere is positioned either midway between two walls, or at a quarter of the distance closer to one of the walls. The derivation and a thorough discussion can be found in [14].

Here we consider only the case when the sphere is centered between the two walls since the Faxén solution is given with greater accuracy for this case. Denote the radius of the sphere by r and the distance between the two walls by $\ell = 2H$, with the channel half-width H. The sphere is sedimenting due to gravity in the wall parallel direction, see Fig. 8a. In this case the periodicity is imposed in the same direction as the direction of sedimentation. The drag F of the sphere is given in terms of the ratio r/H and the translational velocity

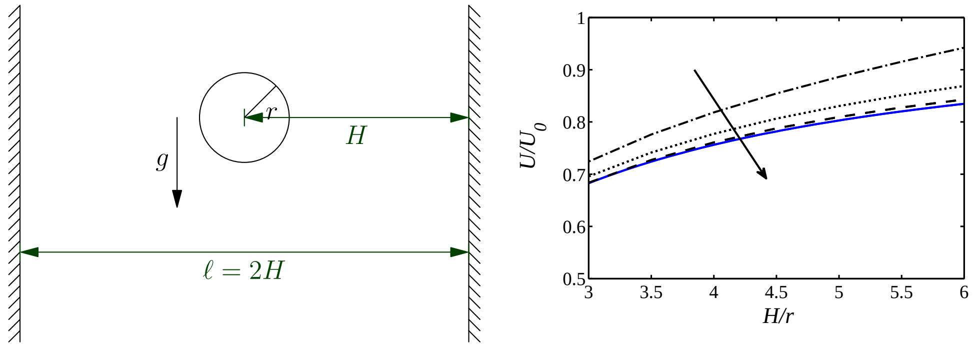

(a) (b)

Figure 8: (a) Sphere positioned midway between the two parallel walls. (b) Sedimentation velocity $U = |\mathbf{U}|$ normalized by the free-space velocity $U_0 = |\mathbf{U}_0|$ versus wall distance H normalized by the sphere radius r: (solid) analytic solution, (dashed) simulations — in the direction of the arrow $L/r = 15, 25, 50$, sphere resolution is constant.

U_F as

$$F = \frac{6\pi\mu r U_F}{1 - 1.004r/H + 0.418(r/H)^3 + 0.21(r/H)^4 - 0.619(r/H)^5}\ , \tag{41}$$

with an error $\mathcal{O}(r/H)^6$, see [14].

In order to check the agreement with the Faxén formula (41) we test for various configurations where the wall to wall distance goes from $\ell = 2H = 3r$ to $\ell = 2H = 12r$. Since the formula (41) is available only with $\mathcal{O}(r/H)^6$ accuracy we cannot use it for comparison of configurations where the sphere to wall distance is too small. The resolution on the sphere is $\Delta_\theta = \pi/20$ and $\Delta_\phi = 2\pi/20$, while on the wall we have $h_w = r/2$. In Fig. 8b we plot the sedimentation velocity normalized by the free-space velocity as a function of the distance from the sphere to the wall normalized by the radius of the sphere. To also investigate the effects of the periodic boundary conditions the simulations are performed using three different periodic box lengths $L_x = L_y = L = 15r, 25r, 50r$. We notice just as in the case of one wall that once the influence of the wall weakens the effect of periodicity takes over and the solution deviates from the analytical solution, predicting higher velocities than the solution provided by Faxén. This differs from the one wall case when the periodic directions were orthogonal to the sedimentation trajectory yielding a simulation curve of lower magnitude than the analytical solution.

6 Conclusions

The present contribution addresses numerical aspects encountered in the simulation of confined Stokes flow. The physical problems considered here are formulated mathematically in the framework of boundary integral equations and discretized using Nyström's method. Specifically, flat bounding walls with periodic boundary conditions in the wall-parallel directions have been considered, and we have extended the work by [25] to obtain analytic expressions for the terms in the rapidly converging sums that define the periodic Stokeslet.

The novel element of the present work is the development of an efficient, high-order numerical treatment of a flat surface by designing quadrature rules that can accurately integrate the singular kernel of the Stokes equations using a uniform distribution of quadrature points. This is accomplished by localized corrections to the trapezoidal rule. Even though the correction weights tabulated in this paper are specific to the wall geometry as well as to the singularity given by the free-space Stokeslet, this work defines a framework for designing quadrature rules also for other geometries and/or singularities.

Discretization by Nyström's method combined with these quadrature rules yields a submatrix associated with each wall which is block Toeplitz symmetric with circulant subblocks. The symmetry properties of such a matrix can be exploited for memory efficient implementations; specifically we show that the matrix can be generated by only three of its columns.

Given a discretization of the wall with a fixed resolution, the accuracy can be increased by applying a higher order quadrature rule, which only requires modifications to the quadrature rule in discretization points in a close neighborhood of the singularity. The accuracy of the quadrature rules has been tested, and the expected orders of convergence (up to 13th order) were obtained. As a discrete system is solved for the force densities at the wall the solution exhibits the same accuracy. This is shown in numerical tests by imposing non-homogeneous boundary conditions at the wall surface. The large gain in accuracy that is obtained as a higher order quadrature rule is used comes almost for free since the resolution of the wall and hence the number of unknowns is fixed.

The wall discretization as coupled to an immersed object has been assessed by studying the classical problem of a sphere sedimenting onto a flat plate, for which analytical solutions are known in the case of an infinite wall. Good agreement between our data and the analytic solution is found as the size of the periodic domain is increased. Similar results were found for the case of a sphere sedimenting between two parallel walls. It is found that the high-order treatment of the walls allows for a rather coarse wall discretization.

The new quadrature rules are attractive for high-order singularity treatment due to their extremely low cost. A natural and very useful continuation of the work presented here is to extend the numerical treatment of a flat plate to that of other geometries such as pipes, spheres or other curvilinear surfaces. Another track to follow is to design quadrature rules for other fundamental solutions of Stokes flow, such as the Stresslet, that appears in so-called double-layer formulations.

As larger problems including many drops or particles in a wall-bounded flow are introduced, a fast summation method will be needed to accelerate the computations that currently scale quadratically with the number of discretization points. The quadrature methods developed here are very well suited to be used in conjunction with fast summation methods, due to their highly localized singularity corrections.

Acknowledgements

O.M. thanks Olof Runborg (KTH NA) and Philipp Schlatter (KTH Mechanics) for valuable suggestions on method and application. Computer time provided by the Swedish National Infrastructure for Computing (SNIC) is gratefully acknowledged.

Appendix A Weights for the correction operator

We provide the tables of the weights for the correction operator A_h^p corresponding to the quadrature rule (27). The weights are available in double precision for the diagonal components in Tables A.2 and A.3 and for the off-diagonal components in Table A.4. We also reproduce the weights for the $1/|\mathbf{x}|$ singularity in Table A.1 from [22].

Table A.1: Modified weights for the $1/|\mathbf{x}|$ singularity in two dimensions.

q	$\mathcal{O}(h^{2q+3})$	Discretization points	Modified weights
0	3	$\mathcal{G}_0^0 = \{(0,0)\}$	$\omega_0^0 = 3.9002649200019564 \times 10^0$
1	5	$\mathcal{G}_0^0 = \{(0,0)\}$	$\omega_0^0 = 3.6714406096247369 \times 10^0$
		$\mathcal{G}_1^0 = \{(\pm1,0),(0,\pm1)\}$	$\omega_1^0 = 5.7206077594304738 \times 10^{-2}$
2	7	$\mathcal{G}_0^0 = \{(0,0)\}$	$\omega_0^0 = 3.6192550095006482 \times 10^0$
		$\mathcal{G}_1^0 = \{(\pm1,0),(0,\pm1)\}$	$\omega_1^0 = 7.0478261675350094 \times 10^{-2}$
		$\mathcal{G}_2^1 = \{(\pm1,\pm1)\}$	$\omega_2^1 = 6.1845239404762928 \times 10^{-3}$
		$\mathcal{G}_2^0 = \{(\pm2,0),(0,\pm2)\}$	$\omega_2^0 = -6.4103079904994854 \times 10^{-3}$
3	9	$\mathcal{G}_0^0 = \{(0,0)\}$	$\omega_0^0 = 3.5956326153661837 \times 10^0$
		$\mathcal{G}_1^0 = \{(\pm1,0),(0,\pm1)\}$	$\omega_1^0 = 7.6498210003072550 \times 10^{-2}$
		$\mathcal{G}_2^1 = \{(\pm1,\pm1)\}$	$\omega_2^1 = 1.0726043096799093 \times 10^{-2}$
		$\mathcal{G}_2^0 = \{(\pm2,0),(0,\pm2)\}$	$\omega_2^0 = -1.0861970941933728 \times 10^{-2}$
		$\mathcal{G}_3^1 = \{(\pm2,\pm1),(\pm1,\pm2)\}$	$\omega_3^1 = -5.6768989454035010 \times 10^{-4}$
		$\mathcal{G}_3^0 = \{(\pm3,0),(0,\pm3)\}$	$\omega_3^0 = 9.3117379008582382 \times 10^{-4}$
4	11	$\mathcal{G}_0^0 = \{(0,0)\}$	$\omega_0^0 = 3.5816901196890991 \times 10^0$
		$\mathcal{G}_1^0 = \{(\pm1,0),(0,\pm1)\}$	$\omega_1^0 = 8.0270822919205118 \times 10^{-2}$
		$\mathcal{G}_2^1 = \{(\pm1,\pm1)\}$	$\omega_2^1 = 1.3733352021301174 \times 10^{-2}$
		$\mathcal{G}_2^0 = \{(\pm2,0),(0,\pm2)\}$	$\omega_2^0 = -1.4045613458587681 \times 10^{-2}$
		$\mathcal{G}_3^1 = \{(\pm2,\pm1),(\pm1,\pm2)\}$	$\omega_3^1 = -1.1741498011806794 \times 10^{-3}$
		$\mathcal{G}_3^0 = \{(\pm3,0),(0,\pm3)\}$	$\omega_3^0 = 1.9899412695107586 \times 10^{-3}$
		$\mathcal{G}_4^2 = \{(\pm2,\pm2)\}$	$\omega_4^2 = 6.2476521748914537 \times 10^{-6}$
		$\mathcal{G}_4^1 = \{(\pm3,\pm1),(\pm1,\pm3)\}$	$\omega_4^1 = 9.6911549656793913 \times 10^{-5}$
		$\mathcal{G}_4^0 = \{(\pm4,\pm0),(0,\pm4)\}$	$\omega_4^0 = -1.5657382234231533 \times 10^{-4}$
5	13	$\mathcal{G}_0^0 = \{(0,0)\}$	$\omega_0^0 = 3.5724020676062076 \times 10^0$
		$\mathcal{G}_1^0 = \{(\pm1,0),(0,\pm1)\}$	$\omega_1^0 = 8.2931084474334645 \times 10^{-2}$
		$\mathcal{G}_2^1 = \{(\pm1,\pm1)\}$	$\omega_2^1 = 1.5807226557430198 \times 10^{-2}$
		$\mathcal{G}_2^0 = \{(\pm2,0),(0,\pm2)\}$	$\omega_2^0 = -1.6446295482375981 \times 10^{-2}$
		$\mathcal{G}_3^1 = \{(\pm2,\pm1),(\pm1,\pm2)\}$	$\omega_3^1 = -1.6998553930113205 \times 10^{-3}$
		$\mathcal{G}_3^0 = \{(\pm3,0),(0,\pm3)\}$	$\omega_3^0 = 2.9905345964354009 \times 10^{-3}$
		$\mathcal{G}_4^2 = \{(\pm2,\pm2)\}$	$\omega_4^2 = 1.5896929239405025 \times 10^{-5}$
		$\mathcal{G}_4^1 = \{(\pm3,\pm1),(\pm1,\pm3)\}$	$\omega_4^1 = 2.4136953002238568 \times 10^{-4}$
		$\mathcal{G}_4^0 = \{(\pm4,\pm0),(0,\pm4)\}$	$\omega_4^0 = -4.0746367252001358 \times 10^{-4}$
		$\mathcal{G}_5^2 = \{(\pm3,\pm2),(\pm2,\pm3)\}$	$\omega_5^2 = -8.0410642204279767 \times 10^{-7}$
		$\mathcal{G}_5^1 = \{(\pm4,\pm1),(\pm1,\pm4)\}$	$\omega_5^1 = -1.7655194334677572 \times 10^{-5}$
		$\mathcal{G}_5^0 = \{(\pm5,\pm0),(0,\pm5)\}$	$\omega_5^0 = 2.8620023884705339 \times 10^{-5}$

Appendix B Doubly periodic Stokeslet

The free space Stokeslet can be expressed as

$$\mathbf{G}_0(\hat{\mathbf{x}}) = (\mathbf{I}\nabla^2 - \nabla\nabla)|\hat{\mathbf{x}}| \ ,$$

with $\hat{\mathbf{x}} = \mathbf{x} - \mathbf{x}_0$. Following Pozrikidis [25] $\mathbf{G}_0$ can be decomposed as

$$\mathbf{G}_0(\hat{\mathbf{x}}) = \boldsymbol{\Upsilon}(\hat{\mathbf{x}}) + \boldsymbol{\Phi}(\hat{\mathbf{x}}) \ , \tag{B.1}$$

Table A.2: Weights for the diagonal components of the Stokeslet for different values of $q \leq 4$. Here we consider G_{11} but the weights for G_{22} can be obtained by swapping the coordinate system, see Table 1.

q	$\mathcal{O}(h^{2q+3})$	Discretization points	Modified weights
0	3	$\mathcal{G}_0^0 = \{(0,0)\}$	$\omega_0^0 = 5.8503973800029342 \times 10^0$
1	5	$\mathcal{G}_0^0 = \{(0,0)\}$	$\omega_0^0 = 5.5071609144371053 \times 10^0$
		$\mathcal{G}_1^0 = \{(\pm 1,0)\}$	$\omega_1^0 = 3.2079800553277232 \times 10^{-2}$
		$\mathcal{G}_1^1 = \{(0,\pm 1)\}$	$\omega_1^1 = 1.3953843222963698 \times 10^{-1}$
2	7	$\mathcal{G}_0^0 = \{(0,0)\}$	$\omega_0^0 = 5.4288825142509724 \times 10^0$
		$\mathcal{G}_1^0 = \{(\pm 1,0)\}$	$\omega_1^0 = 3.9426082424225587 \times 10^{-2}$
		$\mathcal{G}_1^1 = \{(0,\pm 1)\}$	$\omega_1^1 = 1.7200870260182469 \times 10^{-1}$
		$\mathcal{G}_2^0 = \{(\pm 2,0)\}$	$\omega_2^0 = -6.4749634230943083 \times 10^{-3}$
		$\mathcal{G}_2^1 = \{(\pm 1,\pm 1)\}$	$\omega_2^1 = 9.2767859107144393 \times 10^{-3}$
		$\mathcal{G}_2^2 = \{(0,\pm 2)\}$	$\omega_2^2 = -1.2755960548404148 \times 10^{-2}$
3	9	$\mathcal{G}_0^0 = \{(0,0)\}$	$\omega_0^0 = 5.3934489230492755 \times 10^0$
		$\mathcal{G}_1^0 = \{(\pm 1,0)\}$	$\omega_1^0 = 4.4594700242039912 \times 10^{-2}$
		$\mathcal{G}_1^1 = \{(0,\pm 1)\}$	$\omega_1^1 = 1.84899929767177738 \times 10^{-1}$
		$\mathcal{G}_2^0 = \{(\pm 2,0)\}$	$\omega_2^0 = -1.3482758463689264 \times 10^{-2}$
		$\mathcal{G}_2^1 = \{(\pm 1,\pm 1)\}$	$\omega_2^1 = 1.6089064645198640 \times 10^{-2}$
		$\mathcal{G}_2^2 = \{(0,\pm 2)\}$	$\omega_2^2 = -1.9103154362111920 \times 10^{-2}$
		$\mathcal{G}_3^0 = \{(\pm 3,0)\}$	$\omega_3^0 = 9.3102676432729679 \times 10^{-4}$
		$\mathcal{G}_3^1 = \{(\pm 1,\pm 2)\}$	$\omega_3^1 = 7.1081722731558746 \times 10^{-4}$
		$\mathcal{G}_3^2 = \{(\pm 2,\pm 1)\}$	$\omega_3^2 = -2.4138869109366377 \times 10^{-3}$
		$\mathcal{G}_3^3 = \{(0,\pm 3)\}$	$\omega_3^3 = 1.8624946059301746 \times 10^{-3}$
4	11	$\mathcal{G}_0^0 = \{(0,0)\}$	$\omega_0^0 = 5.3725351795336487 \times 10^0$
		$\mathcal{G}_1^0 = \{(\pm 1,0)\}$	$\omega_1^0 = 4.8285272943718170 \times 10^{-2}$
		$\mathcal{G}_1^1 = \{(0,\pm 1)\}$	$\omega_1^1 = 1.9252719581389718 \times 10^{-1}$
		$\mathcal{G}_2^0 = \{(\pm 2,0)\}$	$\omega_2^0 = -1.8965040735392220 \times 10^{-2}$
		$\mathcal{G}_2^1 = \{(\pm 1,\pm 1)\}$	$\omega_2^1 = 2.0600028031951761 \times 10^{-2}$
		$\mathcal{G}_2^2 = \{(0,\pm 2)\}$	$\omega_2^2 = -2.3171799640370824 \times 10^{-2}$
		$\mathcal{G}_3^0 = \{(\pm 3,0)\}$	$\omega_3^0 = 2.3760257513072528 \times 10^{-3}$
		$\mathcal{G}_3^1 = \{(\pm 1,\pm 2)\}$	$\omega_3^1 = 1.2505489384827991 \times 10^{-3}$
		$\mathcal{G}_3^2 = \{(\pm 2,\pm 1)\}$	$\omega_3^2 = -4.7729983420248373 \times 10^{-3}$
		$\mathcal{G}_3^3 = \{(0,\pm 3)\}$	$\omega_3^3 = 3.5937980572250230 \times 10^{-3}$
		$\mathcal{G}_4^0 = \{(\pm 4,0)\}$	$\omega_4^0 = -1.5657413903013782 \times 10^{-4}$
		$\mathcal{G}_4^1 = \{(\pm 1,\pm 3)\}$	$\omega_4^1 = -9.6202937369426739 \times 10^{-5}$
		$\mathcal{G}_4^2 = \{(\pm 2,\pm 2)\}$	$\omega_4^2 = 9.3714782623371805 \times 10^{-6}$
		$\mathcal{G}_4^3 = \{(\pm 3,\pm 1)\}$	$\omega_4^3 = 3.8693758633980847 \times 10^{-4}$
		$\mathcal{G}_4^4 = \{(0,\pm 4)\}$	$\omega_4^4 = -3.1314732799680816 \times 10^{-4}$

where

$$\begin{bmatrix} \boldsymbol{\Upsilon} \\ \boldsymbol{\Phi} \end{bmatrix}(\mathbf{x}) = (\mathbf{I}\nabla^2 - \nabla\nabla) \begin{bmatrix} |\mathbf{x}| \operatorname{erfc}(\xi|\mathbf{x}|) \\ |\mathbf{x}| \operatorname{erf}(\xi|\mathbf{x}|) \end{bmatrix}. \tag{B.2}$$

Table A.3: Weights for the diagonal components of the Stokeslet (continued) for $q = 5$. Here we consider G_{11} but the weights for G_{22} can be obtained by swapping the coordinate system, see Table 1.

q	$\mathcal{O}(h^{2q+3})$	Discretization points	Modified weights
5	13	$\mathcal{G}_0^0 = \{(0,0)\}$	$\omega_0^0 = 5.35860310140931152 \times 10^{0}$
		$\mathcal{G}_1^0 = \{(\pm 1,0)\}$	$\omega_1^0 = 5.09927629110681153 \times 10^{-2}$
		$\mathcal{G}_1^1 = \{(0,\pm 1)\}$	$\omega_1^1 = 1.97800490511935821 \times 10^{-1}$
		$\mathcal{G}_2^0 = \{(\pm 2,0)\}$	$\omega_2^0 = -2.31100073559696708 \times 10^{-2}$
		$\mathcal{G}_2^1 = \{(\pm 1,\pm 1)\}$	$\omega_2^1 = 2.37108398361452974 \times 10^{-2}$
		$\mathcal{G}_2^2 = \{(0,\pm 2)\}$	$\omega_2^2 = -2.62288790911582745 \times 10^{-2}$
		$\mathcal{G}_3^0 = \{(\pm 3,0)\}$	$\omega_3^0 = 3.86019130342424163 \times 10^{-3}$
		$\mathcal{G}_3^1 = \{(\pm 1,\pm 2)\}$	$\omega_3^1 = 1.57939237019213568 \times 10^{-3}$
		$\mathcal{G}_3^2 = \{(\pm 2,\pm 1)\}$	$\omega_3^2 = -6.67895854922609734 \times 10^{-3}$
		$\mathcal{G}_3^3 = \{(0,\pm 3)\}$	$\omega_3^3 = 5.11141248588196129 \times 10^{-3}$
		$\mathcal{G}_4^0 = \{(\pm 4,0)\}$	$\omega_4^0 = -4.78090101298068697 \times 10^{-4}$
		$\mathcal{G}_4^1 = \{(\pm 1,\pm 3)\}$	$\omega_4^1 = -1.79958302040638567 \times 10^{-4}$
		$\mathcal{G}_4^2 = \{(\pm 2,\pm 2)\}$	$\omega_4^2 = 2.38453938591075386 \times 10^{-5}$
		$\mathcal{G}_4^3 = \{(\pm 3,\pm 1)\}$	$\omega_4^3 = 9.04066892107795628 \times 10^{-4}$
		$\mathcal{G}_4^4 = \{(0,\pm 4)\}$	$\omega_4^4 = -7.44300916261972050 \times 10^{-4}$
		$\mathcal{G}_5^0 = \{(\pm 5,0)\}$	$\omega_5^0 = 2.86200232229723715 \times 10^{-5}$
		$\mathcal{G}_5^1 = \{(\pm 1,\pm 4)\}$	$\omega_5^1 = 1.76578650191035792 \times 10^{-5}$
		$\mathcal{G}_5^2 = \{(\pm 2,\pm 3)\}$	$\omega_5^2 = -1.43768888704042014 \times 10^{-5}$
		$\mathcal{G}_5^3 = \{(\pm 3,\pm 2)\}$	$\omega_5^3 = 1.19645696042758084 \times 10^{-5}$
		$\mathcal{G}_5^4 = \{(\pm 4,\pm 1)\}$	$\omega_5^4 = -7.06234480231362978 \times 10^{-5}$
		$\mathcal{G}_5^5 = \{(0,\pm 5)\}$	$\omega_5^5 = 5.72400484311436477 \times 10^{-5}$

Here ξ is an arbitrary positive constant with dimension of an inverse length. The error function is defined as

$$\operatorname{erf}(x) = \frac{2}{\sqrt{\pi}} \int_0^x e^{-t^2} \mathrm{d}t \ ,$$

and the complementary error function as $\operatorname{erfc}(x) = 1 - \operatorname{erf}(x)$.

The idea is to evaluate the periodic sum over $\mathbf{G}_0$ by evaluating the sum over $\boldsymbol{\Upsilon}$ in real space, and the sum over $\boldsymbol{\Phi}$ in Fourier space. The parameter ξ determines the convergence of the two sums and we have used $\xi = \sqrt{\pi}/A$ where $A = L_x L_y$ in the computations. Note that the results are independent of the value of ξ once the sums have converged.

Sum in real space

Let

$$\begin{aligned}\mathbf{S}_r(\hat{\mathbf{x}}) = \sum_{p_1,\, p_2 \,\in\, Z} \boldsymbol{\Upsilon}(\hat{\mathbf{x}} + \mathbf{p}) - \mathbf{G}_0(\hat{\mathbf{x}}) &= (\boldsymbol{\Upsilon}(\hat{\mathbf{x}}) - \mathbf{G}_0(\hat{\mathbf{x}})) + \sum_{\substack{p_1,\, p_2 \,\in\, Z \\ |\mathbf{p}| \neq 0}} \boldsymbol{\Upsilon}(\hat{\mathbf{x}} + \mathbf{p}) \\ &= \widetilde{\boldsymbol{\Upsilon}}(\hat{\mathbf{x}}) + \sum_{\substack{p_1,\, p_2 \,\in\, Z \\ |\mathbf{p}| \neq 0}} \boldsymbol{\Upsilon}(\hat{\mathbf{x}} + \mathbf{p}) \ , \end{aligned} \tag{B.3}$$

Table A.4: Weights for the off-diagonal component G_{12} of the Stokeslet for different values of $q \leq 4$, see correspondence to Table 2.

q	$\mathcal{O}(h^{2q+3})$	Discretization points	Modified weights
1	5	$\mathcal{G}_1^1 = \{(\pm 1, \pm 1)\}$	$\omega_1^1 = 4.1166177317666121 \times 10^{-2}$
2	7	$\mathcal{G}_1^1 = \{(\pm 1, \pm 1)\}$	$\omega_1^1 = 6.6548787549284772 \times 10^{-2}$
		$\mathcal{G}_2^1 = \{(\pm 2, \pm 1)\}$	$\omega_2^1 = -6.3456525579046625 \times 10^{-3}$
3	9	$\mathcal{G}_1^1 = \{(\pm 1, \pm 1)\}$	$\omega_1^1 = 8.2287438803691426 \times 10^{-2}$
		$\mathcal{G}_2^1 = \{(\pm 2, \pm 1)\}$	$\omega_2^1 = -1.2817996961341463 \times 10^{-2}$
		$\mathcal{G}_2^2 = \{(\pm 2, \pm 2)\}$	$\omega_2^2 = 4.4220975418534787 \times 10^{-4}$
		$\mathcal{G}_3^1 = \{(\pm 3, \pm 1)\}$	$\omega_3^1 = 1.3969812237665262 \times 10^{-3}$
4	11	$\mathcal{G}_1^1 = \{(\pm 1, \pm 1)\}$	$\omega_1^1 = 9.2811898832734633 \times 10^{-2}$
		$\mathcal{G}_2^1 = \{(\pm 2, \pm 1)\}$	$\omega_2^1 = -1.8343678532721808 \times 10^{-2}$
		$\mathcal{G}_2^2 = \{(\pm 2, \pm 2)\}$	$\omega_2^2 = 1.1447472391419913 \times 10^{-3}$
		$\mathcal{G}_3^1 = \{(\pm 3, \pm 1)\}$	$\omega_3^1 = 3.4514976628596011 \times 10^{-3}$
		$\mathcal{G}_3^2 = \{(\pm 3, \pm 2)\}$	$\omega_3^2 = -8.7817185619580428 \times 10^{-5}$
		$\mathcal{G}_4^1 = \{(\pm 4, \pm 1)\}$	$\omega_4^1 = -3.1314701130898567 \times 10^{-4}$
5	13	$\mathcal{G}_1^1 = \{(\pm 1, \pm 1)\}$	$\omega_1^1 = 1.00302178953630044 \times 10^{-1}$
		$\mathcal{G}_2^1 = \{(\pm 2, \pm 1)\}$	$\omega_2^1 = -2.29148802528166942 \times 10^{-2}$
		$\mathcal{G}_2^2 = \{(\pm 2, \pm 2)\}$	$\omega_2^2 = 1.95966386197501494 \times 10^{-3}$
		$\mathcal{G}_3^1 = \{(\pm 3, \pm 1)\}$	$\omega_3^1 = 5.69286751251354687 \times 10^{-3}$
		$\mathcal{G}_3^2 = \{(\pm 3, \pm 2)\}$	$\omega_3^2 = -2.74667341901977876 \times 10^{-4}$
		$\mathcal{G}_4^1 = \{(\pm 4, \pm 1)\}$	$\omega_4^1 = -9.19305501089468761 \times 10^{-4}$
		$\mathcal{G}_3^1 = \{(\pm 3, \pm 1)\}$	$\omega_3^1 = 2.13940399318116676 \times 10^{-5}$
		$\mathcal{G}_3^2 = \{(\pm 3, \pm 2)\}$	$\omega_3^2 = 1.68789994258584628 \times 10^{-5}$
		$\mathcal{G}_4^1 = \{(\pm 4, \pm 1)\}$	$\omega_4^1 = 7.15500613660957699 \times 10^{-5}$

denote the sum in real space. From the decomposition in (B.2), we obtain

$$\boldsymbol{\Upsilon}(\hat{\mathbf{x}}) = \frac{C(\xi|\hat{\mathbf{x}}|)}{|\hat{\mathbf{x}}|}\mathbf{I} + \frac{D(\xi|\hat{\mathbf{x}}|)}{|\hat{\mathbf{x}}|^3}\hat{\mathbf{x}}\hat{\mathbf{x}} \ ,$$

where $C(x)$ and $D(x)$ are given by

$$C(x) = \operatorname{erfc}(x) + \frac{2}{\sqrt{\pi}}(2x^2 - 3)xe^{-x^2} \ , \tag{B.4}$$

$$D(x) = \operatorname{erfc}(x) + \frac{2}{\sqrt{\pi}}(1 - 2x^2)xe^{-x^2} \ . \tag{B.5}$$

From the center part of $\boldsymbol{\Upsilon}$ ($\mathbf{p} = 0$) we have subtracted off the free-space Stokeslet. In this way, all parts of $\mathbf{S}_r$ are smooth. The center part is now given by

$$\tilde{\boldsymbol{\Upsilon}}(\hat{\mathbf{x}}) = \frac{\tilde{C}(\xi|\hat{\mathbf{x}}|)}{|\hat{\mathbf{x}}|}\mathbf{I} + \frac{\tilde{D}(\xi|\hat{\mathbf{x}}|)}{|\hat{\mathbf{x}}|^3}\hat{\mathbf{x}}\hat{\mathbf{x}} \ ,$$

with

$$\tilde{C}(x) = -\operatorname{erf}(x) + \frac{2}{\sqrt{\pi}}(2x^2 - 3)xe^{-x^2} \ , \tag{B.6}$$

$$\tilde{D}(x) = -\operatorname{erf}(x) + \frac{2}{\sqrt{\pi}}(1 - 2x^2)xe^{-x^2} \ . \tag{B.7}$$

To define $\widetilde{\mathbf{\Upsilon}}(\hat{\mathbf{x}})$ when $\hat{\mathbf{x}} = 0$ we must use the limits

$$\lim_{|\hat{\mathbf{x}}|\to 0} \frac{\tilde{C}(\xi|\hat{\mathbf{x}}|)}{|\hat{\mathbf{x}}|} = -\frac{8\xi}{\sqrt{\pi}} \ , \quad \lim_{|\hat{\mathbf{x}}|\to 0} \frac{\tilde{D}(\xi|\hat{\mathbf{x}}|)}{|\hat{\mathbf{x}}|} = 0 \ .$$

The sum in real space will decay in a Gaussian manner.

Sum in Fourier space

The sum in Fourier space can be written as

$$\mathbf{S}_F(\hat{\mathbf{x}}) = \sum_{k_1,\, k_2\, \in\, Z} \hat{\mathbf{\Phi}}(\mathbf{k}, \hat{\mathbf{x}}) \ ,$$

where $\hat{\mathbf{\Phi}}(\mathbf{k}, \hat{\mathbf{x}})$ is given in Pozrikidis, [25], as

$$\begin{aligned}\hat{\mathbf{\Phi}}_{jm}(\mathbf{k}, \hat{\mathbf{x}}) =& \frac{4\pi}{A} \sum_{\substack{k_1,\, k_2\, \in\, Z \\ |\mathbf{k}|\, \neq\, 0}} \left(-\delta_{jm}\nabla^2 + \frac{\partial^2}{\partial x_j \partial x_m} \right) \mathbf{S}^{\mathbf{B}}(\mathbf{k}, \hat{\mathbf{x}}) \\ &+ \frac{4\pi}{A} \left[\left(-\delta_{jm}\nabla^2 + \frac{\partial^2}{\partial x_j \partial x_m} \right) (\mathbf{S}^{\mathbf{B}}(\mathbf{k}, \hat{\mathbf{x}}) - \mathbf{S}^{\mathbf{F}}(\mathbf{k}, \hat{\mathbf{x}})) \right]_{|\mathbf{k}|=0} \ .\end{aligned} \quad \text{(B.8)}$$

Here, $A = L_x L_y$, the area of the periodic array and $\mathbf{k} = (k_x, k_y)$, is a two-dimensional wave number vector. The generating functions $\mathbf{S}^{\mathbf{B}}(\mathbf{k}, \hat{\mathbf{x}})$ and $\mathbf{S}^{\mathbf{F}}(\mathbf{k}, \hat{\mathbf{x}})$ are given by

$$\mathbf{S}^{\mathbf{B}}(\mathbf{k}, \hat{\mathbf{x}}) = \frac{1}{\pi\xi^4} \int_{-\infty}^{\infty} \left(\frac{1}{\omega^4} + \frac{1}{4}\frac{1}{\omega^2} + \frac{1}{8} \right) e^{-\frac{1}{4}\omega^2 - i\eta|z| - i\mathbf{k}\cdot\hat{\mathbf{x}}} \mathrm{d}\eta \ , \quad \text{(B.9)}$$

where $\omega = |\mathbf{k} + \eta \boldsymbol{e}_3|/\xi$ and

$$\mathbf{S}^{\mathbf{F}}(\mathbf{k}, \hat{\mathbf{x}}) = \frac{1}{2}\frac{1+\rho}{|\mathbf{k}|^3} e^{-i\mathbf{k}\cdot\hat{\mathbf{x}} - \rho}, \quad \rho = |\mathbf{k}||z| \ . \quad \text{(B.10)}$$

$\mathbf{S}^{\mathbf{F}}(\mathbf{k}, \hat{\mathbf{x}})$ is the generating function we would obtain if we let ξ tend to infinity, corresponding to the case where the summations is only performed in Fourier space.

Partial derivative of the generating functions

To obtain the Fourier part of the periodic Stokeslet, first and second partial derivatives of the generating functions $\mathbf{S}^{\mathbf{B}}(\mathbf{k}, \hat{\mathbf{x}})$ and $\mathbf{S}^{\mathbf{F}}(\mathbf{k}, \hat{\mathbf{x}})$ are required. These are not explicitly given in Pozrikids [25] and will be derived below.

Let $\delta = \xi z$, $\zeta = |\mathbf{k}|/\xi$ and define the integrals

$$I_n(\delta, \zeta) = \int_0^{\infty} \frac{cos(\delta t)}{(\zeta^2 + t^2)^n} e^{-\frac{1}{4}t^2} \mathrm{d}t \ . \quad \text{(B.11)}$$

Then $\mathbf{S}^{\mathbf{B}}$ can be written as $\mathbf{S}^{\mathbf{B}}(\mathbf{k}, \hat{\mathbf{x}}) = \tilde{\mathbf{S}}^{\mathbf{B}}(\mathbf{k}, z) e^{-i\mathbf{k}\cdot\hat{\mathbf{x}}}$ where

$$\tilde{\mathbf{S}}^{\mathbf{B}}(\mathbf{k}, z) = \frac{2}{\pi\xi^3} \left[\frac{1}{8} I_0(\delta, \zeta) + \frac{1}{4} I_1(\delta, \zeta) + I_2(\delta, \zeta) \right] e^{-\frac{1}{4}\zeta^2} \ . \quad \text{(B.12)}$$

Here we note that $\tilde{\mathbf{S}}^{\mathbf{B}}$ is a function of z only and $e^{-i\mathbf{k}\cdot\hat{\mathbf{x}}}$ is a function of x and y only. Hence, only z-derivatives of $\tilde{\mathbf{S}}^{\mathbf{B}}$ are required. Derivatives of $e^{-i\mathbf{k}\cdot\hat{\mathbf{x}}}$ with respect to x and y are straightforward.

The functions I_0, I_1 and I_2 in (B.12) are given by the solution to the integral in (B.11) and are given in [25]. Here we state them in a slightly different form as

$$
\begin{aligned}
I_0 &= \sqrt{\pi} e^{-\alpha^2} \ , \\
I_1 &= -\frac{\pi}{4\zeta} e^{\frac{1}{4}\zeta^2} \tilde{I}_1 \ , \\
I_2 &= \frac{\pi}{8\zeta} e^{\frac{1}{4}\zeta^2} \left[\left(\frac{1}{2} - \frac{1}{\zeta^2} \right) \tilde{I}_1 + \frac{1}{\zeta} \tilde{I}_2 + \frac{2}{\sqrt{\pi}\zeta} \tilde{I}_0 \right] \ ,
\end{aligned}
$$

where we have introduced $\alpha = |\delta|$, $k = |\mathbf{k}|$ and

$$
\begin{aligned}
\tilde{I}_0 &= e^{-(\alpha^2 + \frac{1}{4}\zeta^2)}, \\
\tilde{I}_1 &= -e^{-\zeta\alpha} \{ \operatorname{erf}(\alpha - \frac{1}{2}\zeta) + 1 \} - e^{\zeta\alpha} \operatorname{erfc}(\alpha + \frac{1}{2}\zeta) \ , \\
\tilde{I}_2 &= \alpha \left[e^{-\zeta\alpha} \{ \operatorname{erf}(\alpha - \frac{1}{2}\zeta) + 1 \} - e^{\zeta\alpha} \operatorname{erfc}(\alpha + \frac{1}{2}\zeta) \right] \ ,
\end{aligned}
$$

to simplify the notation. Using the variables introduced above, $\tilde{\mathbf{S}}^{\mathbf{B}}$ can then be recast in the following form

$$
\tilde{\mathbf{S}}^{\mathbf{B}}(\mathbf{k}, z) = \frac{1}{\xi^3} \left[\frac{1}{2\sqrt{\pi}} \left(\frac{1}{2} + \frac{1}{\zeta^2} \right) \tilde{I}_0 - \frac{1}{4\zeta^3} \tilde{I}_1 + \frac{1}{4\zeta^2} \tilde{I}_2 \right] \ .
$$

and the first and second derivative of $\tilde{\mathbf{S}}^{\mathbf{B}}$ with respect to z are

$$
\begin{aligned}
\frac{\partial}{\partial z} \tilde{\mathbf{S}}^{\mathbf{B}} &= \frac{1}{\xi^2} \operatorname{sign}(z) \alpha \left[-\frac{1}{2\sqrt{\pi}} \tilde{I}_0 + \frac{1}{4\zeta} \tilde{I}_1 \right], \\
\frac{\partial^2}{\partial z^2} \tilde{\mathbf{S}}^{\mathbf{B}} &= \frac{1}{\xi} \left[\frac{1}{2\sqrt{\pi}} (2\alpha^2 - 1) \tilde{I}_0 + \frac{1}{4} \left(\frac{1}{\zeta} \tilde{I}_1 + \tilde{I}_2 \right) \right] \ .
\end{aligned}
$$

In order to compute the limit term in (B.8) the first and second partial derivative of $\mathbf{S}^{\mathbf{F}}$, (B.10), are also required. Once again we notice that $\mathbf{S}^{\mathbf{F}}(\mathbf{k}, \hat{\mathbf{x}})$ can be written as a product of two functions, $\mathbf{S}^{\mathbf{F}}(\mathbf{k}, \hat{\mathbf{x}}) = \tilde{\mathbf{S}}^{\mathbf{F}}(\mathbf{k}, z) e^{-i\mathbf{k}\cdot\hat{\mathbf{x}}}$, where $\tilde{\mathbf{S}}^{\mathbf{F}}$, is a function of z only. The z-derivatives of $\tilde{\mathbf{S}}^{\mathbf{F}}$ are

$$
\begin{aligned}
\frac{\partial \tilde{\mathbf{S}}^{\mathbf{F}}}{\partial z} &= -\frac{1}{\xi^2} \operatorname{sign}(z) \frac{\alpha}{2\zeta} e^{-\zeta\alpha} \ , \\
\frac{\partial^2 \tilde{\mathbf{S}}^{\mathbf{F}}}{\partial z^2} &= -\frac{1}{\xi} \frac{1}{2\zeta} (1 - \zeta\alpha) e^{-\zeta\alpha} \ .
\end{aligned}
$$

The limit as $k \to 0$ can be computed and is

$$
\begin{aligned}
\lim_{k \to 0} \frac{\partial^2}{\partial z^2} \left(\mathbf{S}^{\mathbf{B}} - \mathbf{S}^{\mathbf{F}} \right) &= \frac{1}{\xi} \frac{1}{\sqrt{\pi}} \alpha^2 e^{-\alpha^2} + |z| (\operatorname{erf}(\alpha) - 1) \\
&= \frac{1}{\xi} \frac{1}{\sqrt{\pi}} \alpha^2 e^{-\alpha^2} - |z| \operatorname{erfc}(\alpha) \ .
\end{aligned}
$$

All other limits needed in (B.8) vanish as $k \to 0$.

References

[1] J. C. Aguilar. High-order corrected trapezoidal quadrature rules for functions with a logarithmic singularity on a circle. *Int. J. Contemp. Math. Sciences*, 3(23):1133–1140, 2008.

[2] B. K. Alpert. High-order quadratures for integral operators with singular kernels. *J. Comput. Appl. Math.*, 60:367–378, 1995.

[3] K. Atkinson. Quadrature of singular integrands over surfaces. *Electron. T. Numer. Ana.*, 17:133–150, 2004.

[4] C. W. J. Beenakker. Ewald sums of the Rotne-Prager tensor. *J. Chem. Phys.*, 85:1581–1582, 1986.

[5] J. R. Blake. A note on the image system for a Stokeslet in a no-slip boundary. *Proc. Camb. Philos. Soc.*, 70:303–310, 1971.

[6] H. Bruus. *Theoretical Microfluidics.* Oxford University Press, U.S.A., 2007.

[7] H. C. Crenshaw. A New Look at Locomotion in Microorganisms: Rotating and Translating. *Am. Zool.*, 36(6):608–618, 1996.

[8] N. J. De Mestre and W. B. Russel. Low-Reynolds-number translation of a slender cylinder near a plane wall. *J. Eng. Math.*, 9:81–91, 1975.

[9] P. S. Dittrich and A. Manz. Lab-on-a-chip: microfluidics in drug discovery. *Nat. Rev. Drug Discovery*, 5(3):210–218, 2006.

[10] P. P. Ewald. Die Berechnung optischer und elektrostatischer Gitterpotentiale. *Ann. Phys.*, 369(3):253–287, 1921.

[11] H. Faxén. Die Bewegung einer starren Kugel längs der Achse eines mit zäher Flüssigkeit gefüllten Rohres. *Ark. Mat. Astron. Fys.*, 17:1–28, 1923.

[12] S. V. Garimella and C. B. Sobhan. Transport in microchannels – a critical review. *Annu. Rev. Heat Trans.*, 13(13):1–50, 2003.

[13] T. Götz. *Interactions of Fibers and Flow: Asymptotics, Theory and Numerics.* PhD thesis, Universität Kaiserslautern, Germany, 2000.

[14] J. Happel and H. Brenner. *Low Reynolds Number Hydrodynamics.* Kluwer, Dordrecht, The Netherlands, 1983.

[15] H. Hasimoto. On the periodic fundamental solutions of the Stokes equations and their application to viscous flow past a cubic array of spheres. *J. Fluid Mech.*, 5:317–328, 1959.

[16] E. V. Haynsworth. *On the Schur Complement.* Ft. Belvoir, Defense Technical Information Center, 1968.

[17] P. J. A. Janssen and P. D. Anderson. A boundary-integral model for drop deformation between two parallel plates with non-unit viscosity ratio drops. *J. Comput. Phys.*, 227:8807–8819, 2008.

[18] C. Jayageeth, V. I. Sharma, and A. Singh. Dynamics of short fiber suspensions in bounded shear flow. *Int. J. Multiphase Flow*, 35(3):261–269, 2009.

[19] S. Kapur and V. Rokhlin. High-order corrected trapezoidal quadrature rules for singular functions. *SIAM J. Numer. Anal.*, 34(4):1331–1356, 1997.

[20] N. Liron and S. Mochon. Stokes flow for a Stokeslet between two parallel flat plates. *J. Eng. Math.*, 10:287–303, 1976.

[21] N. Liron and Shahar R. Stokes flow due to a Stokeslet in a pipe. *J. Fluid Mech.*, 86:727–744, 1978.

[22] O. Marin, O. Runborg, and A.-K. Tornberg. Corrected trapezoidal rules for a class of singular functions. Paper 1 in this thesis, 2012.

[23] T. Miyazaki and H. Hasimoto. The motion of a small sphere in fluid near a circular hole in a plane wall. *J. Fluid Mech.*, 145:201–221, 1984.

[24] C. Pozrikidis. *Boundary Integral and Singularity Methods for Linearized Viscous Flow.* Cambridge University Press, Cambridge, U.K., 1992.

[25] C. Pozrikidis. Computation of periodic Green's functions of Stokes flow. *J. Eng. Math.*, 30(4):79–96, 1996.

[26] W. B. Russel, E. J. Hinch, L. G. Leal, and G. Tieffenbruck. Rods falling near a vertical wall. *J. Fluid Mech.*, 83:273–287, 1977.

[27] A. Sidi. Application of class $\mathcal{S}$m variable transformations to numerical integration over surfaces of spheres. *J. Comput. Appl. Math.*, 184:475–492, 2005.

[28] M. E. Staben, A. Z. Zinchenko, and R. H. Davis. Motion of a particle between two parallel walls in low-Reynolds number Poiseuille flow. *Phys. Fluids*, 15:1711–1733, 2003.

[29] A.-K. Tornberg and K. Gustavsson. A numerical method for simulations of rigid fiber suspensions. *J. Comput. Phys.*, 215:172–196, 2005.

A fast summation method for fiber simulations

Oana Marin, Katarina Gustavsson, Anna-Karin Tornberg
Linné FLOW Centre, KTH-SCI (NA), SE-100 44 Stockholm, Sweden

Abstract

A numerical method for large scale simulations of fiber suspensions immersed in a Stokesian fluid is presented. The mathematical description is based on a boundary integral formulation with a slender body approximation. Periodic boundary conditions are introduced through the so-called Ewald summation formulas for the fundamental solutions. This decomposes the sum, *i.e.* the matrix-vector product, into one part in real-space and one in Fourier space. The computation of the Fourier space sum is accelerated using a FFT based method, the Spectral Ewald (SE) method, which allows for the use of significantly smaller FFT grids relative to established methods for fast Ewald summation. The real space treatment is based on the Linked Cell List method, and is modified to enable analytical integration for fibers in close vicinity to each other, which ensures better accuracy. By appropriately adjusting the computational load of the sums in the decomposition as the problem scales up, the resulting method is rendered to have a complexity of $\mathcal{O}(N \log N)$, where N is the number of fibers. Provided error bounds offer a straight forward parameter selection. Results from simulations of a few thousand fibers in different configurations are discussed.

1 Introduction

The intriguing physical phenomena surrounding the gravity induced sedimentation of fibers in a Stokesian fluid has been studied in length through experiments [14, 21, 11] and numerical simulations [4, 25, 23, 12]. Due to their elongated shape fibers create clusters, converging into streamers, that sediment at a faster rate than any isolated fiber. The fibers also show a preferred alignment in the direction of gravity. These characteristic features have been seen in both experiments and numerical simulations. To simulate the dynamics of a suspension independent of wall effects periodic boundary conditions are often used to mimic infinite domains. However this introduces periodicity effects which are believed to be minimized for sufficiently large domains, see Butler [4]. Due to the computational cost, the periodic systems simulated so far have been of limited size, and is natural ask whether larger periodic systems, with respect to both domain size and number of fibers, can produce results less influenced by periodicity. To enable larger simulations we have adopted the recently developed Spectral Ewald method by Lindbo and Tornberg [20] to the numerical method of simulating fiber suspensions by Tornberg and Gustavsson [25].

The Stokes equations can be reformulated as boundary integral equations with integrals over the boundaries of the domain. These boundaries are the surfaces of the immersed objects, together with possible external boundaries. In the case of fibers with large aspect ratios, a slender body approximation can be employed to reduce the integral equations from the fiber surfaces to the center lines of the fibers [2, 16, 8]. Assuming the fibers to be slender ellipsoids of length L and cross section radius a, the formulation in [16, 8] is $O(\varepsilon)$ accurate with the slenderness parameter $\varepsilon = a/L$. This is the formulation on which we will base our numerical method.

When discretizing boundary integral equations, the resulting matrix is full due to the slow decay of the Green's function. The dimensionality of the discrete problem has been reduced in our case from three dimensions to one dimension by using the slender body approximation. To further accelerate the calculations, a fast summation method to compute the matrix vector product can be applied. For N_p discretization points, the fast multipole method [10, 26] can evaluate the matrix vector product in $O(N_p)$ operations. We however want to simulate under periodic boundary conditions, and it is natural to consider a method based on the so-called Ewald summation.

Ewald summation was first introduced in the field of electrostatics [7], where the electrostatic potential in each point is evaluated by summing over the contributions from all other points and their associated charges. Periodicity implies that all the charges are to be considered to be periodically replicated, leading to infinite sums. The influence on one particle from another decays slowly, with the inverse of the distance. Summing in three dimensions, the sums are not absolutely convergent, and the assumption of charge neutrality is used to make the sums well defined. To render the sums feasible to compute, Ewald [7] introduced a decomposition which by involving a new scalar parameter ξ splits the short range interactions, to be summed in real space, from the long range interactions which are expressed and summed in Fourier space. The two sums, which can be treated individually, converge at a faster rate and lend themselves to truncation. The convergence speed of each sum depends on ξ, also known as the Ewald parameter. The technique set forth by Ewald has inspired similar decompositions in the field of fluid mechanics for the Stokes equations. Two such decompositions are the one by Hasimoto [13] and later on Beenakker [3], see also [22]. When applied to discretizations of boundary integral equations, the N_p locations for charges in electrostatics are now instead quadrature points used to discretize the boundary integral equations.

The Ewald summation technique is not a fast summation method in itself - each of the two sums have $O(N_p^2)$ complexity, with a large constant, and they become prohibitively expensive to evaluate as N_p grows. In order to create a fast method of better computational complexity, a basic idea is to use the Fast Fourier Transform (FFT) to evaluate the Fourier space sum. The parameter ξ can then be chosen such as to make the real space sum converge faster, and shift more work into the Fourier space sum, which can now be computed more rapidly. With the correct scaling of ξ, an $O(N_p \log N_p)$ method can be attained. FFT-based Ewald summation methods emerged in the field of electrostatics with the widely used Particle Mesh Ewald (PME) [15] and Smooth Particle Mesh Ewald (SPME) [6] methods. Recently, the Spectral Ewald (SE) method was introduced [20]. All these methods have been explored also in the realm of the Stokes equations, *e.g.* PME by Sierou and Brady [24], the SPME by Saintillan *et al.* [23] and SE by Lindbo and Tornberg [19]. The main difference between the methods is that the PME and SPME methods use polynomial interpolation to spread point charges/densities to the grid, and reduction of approximation errors requires an increase of the grid resolution, and hence an increased size of the FFT grid. The FFT grid in the SE method can be chosen as the minimal grid considering only at which mode the Fourier space sum should be truncated. The approximation errors are then separately controlled by the use of suitably scaled Gaussians, and decay spectrally with increased support. As a result, for a given error tolerance, much smaller grids can be used with the SE method than with the other methods, which lowers the memory requirements. The SE method has also been shown to compare favorably to the SPME method in terms of computational effort [20]; here a so-called fast Gaussian gridding algorithm is crucial [9].

In this paper, we build on the formulation for rigid slender fibers in [25, 12]. The force along each fiber is approximated as an expansion in Legendre polynomials, which makes it possible to evaluate analytically the integrals in the formulation in order to calculate the contribution from one fiber to another. This is especially useful when two fibers are close to each other and the integrand becomes nearly singular due to the behavior of the

Green's function, in which case the integral is difficult to evaluate accurately using a numerical quadrature. The Spectral Ewald (SE) method mentioned above, can be applied directly to evaluate the matrix-vector product of the discretized fiber system if the integrals are numerically integrated. In this paper, we modify this method to allow for analytical integration when fibers are close. This modification will enter only into the treatment of the real space sum, and the method for evaluating the Fourier space sum will remain unchanged, as all integrals appearing in this part will have smooth integrands and are suitable for numerical quadrature. The second change to the SE method in this paper, is to extend it from considering a Green's function that is the so-called Stokeslet, to a Green's function that is a combination of the Stokeslet and a so-called Doublet, that appears as the slender body approximation is introduced. New error estimates have been derived for this extended Green's function. An important feature of the SE method is that truncation errors (incurred by truncating the real space and Fourier space sums) decouple from the additional approximation errors introduced by the FFT based procedure. This allows for a systematic parameter selection to meet a certain error tolerance.

By algebraic manipulation of the integral equations and the use of orthogonality of Legendre polynomials, a linear system for the force coefficients in the force expansions is obtained [25, 12]. This reformulation introduces integrals over each fiber, that are evaluated by numerical quadrature after the contributions from all fibers has been accumulated by the use of the SE method. This system is much better conditioned than the original system, and an iterative solver like GMRES typically converges in a moderate number of iterations.

With this, we have achieved a numerical method for fiber simulations, based on a well-conditioned formulation, such that it is much more efficient to use GMRES as compared to a direct solver. Furthermore, the matrix-vector product to be computed in each GMRES iteration is further accelerated by the SE method, which is $O(N \log N)$, where N is the number of fibers. The reduced memory requirements for the SE method makes it feasible to simulate larger systems, *i.e.* more fibers in larger periodic boxes. In our modified SE method, we perform analytical integration over fibers that are close, which avoids quadrature errors. The truncation and approximation errors that are incurred by the SE method can be controlled by appropriate parameter choices.

The outline of the paper is as follows. In Section 2, we introduce the slender-body boundary integral equations for the fiber system without periodicity. In Section 3, Ewald summation for periodic systems is discussed, and the formulation of the fiber system is extended to the periodic case in Section 4, where the fully discretized system is also given. The modified SE method is discussed in Section 5, including error estimates and parameter selection. There are two sections for numerical results. In Section 6, the performance and properties of the modified SE method are discussed, while the actual fiber simulations are presented in Section 7.

2 Fiber-fiber interaction using slender body theory

Owing to their linearity the Stokes equations, as a simplification of the more general Navier-Stokes equations, allow for a reformulation in terms of boundary integral equations. In this framework of boundary integrals the fluid velocity due to the motion of a single fiber can be computed by solving an integral equation stated solely over the fiber surface. Due to the linearity of the equations a large number of fibers mutually influencing each other can be tracked by summing up their individual contributions.

Consider a set of N rigid straight fibers of ellipsoidal shape of length L and cross radius a. If the ellipsoid has a large aspect ratio, *i.e.* $L \gg a$, it can be referred to as a *slender* *body.* For such bodies the governing equations can be reduced by using the slender body theory [2]. The idea is to use asymptotic analysis to match the fiber velocity to the fluid velocity at the virtual boundary of the ellipsoid, a detailed discussion is available in [8]. By reducing the governing equations to the centerline of the slender body we obtain an approximation depending on the slenderness parameter, $\varepsilon = a/L$, of accuracy $\mathcal{O}(\varepsilon)$ as discussed in [25]. The parametrization of each fiber $n = 1, \dots N$ at a time instance t will be given by $\mathbf{x}_n(s,t) = \mathbf{c}_n(t) + s\mathbf{t}_n(t)$ where s is the arclength $s \in [-L/2,\ L/2]$ while $\mathbf{c}_n$ is the center point and $\mathbf{t}_n$ is the orientation vector.

With these considerations the fiber-fiber interaction can be described through the system presented in *e.g.* [25], in terms of two fundamental solutions, the Stokeslet (5) and the dipole (6). The unknown variables in the system are the fiber velocities, *i.e.* translational velocity, $\dot{\mathbf{c}}_n(t)$, and rotational velocity, $\dot{\mathbf{t}}_n(t)$, and also the force densities along the fiber surfaces $\mathbf{f}_n(s,t)$, $s \in [-L/2,\ L/2]$. To avoid a cumbersome notation the explicit reference to the time dependence is omitted when mentioning the force densities, $\mathbf{f}(s,t)$ or velocities, $\dot{\mathbf{c}}_n(t)$, $\dot{\mathbf{t}}_n(t)$, and position vectors $\mathbf{c}_n$, $\mathbf{t}_n$. The equations of fiber motion (see [8, 25]) subject to a background velocity field $\boldsymbol{u}_0$ can be stated in non-dimensional form as

$$d(\dot{\mathbf{c}}_n + s\dot{\mathbf{t}}_n - \boldsymbol{u}_0) = \Lambda_n[\mathbf{f}_n](s) + (\mathbf{I} + \mathbf{t}_n\mathbf{t}_n)\mathbf{K}[\mathbf{f}_n](s) + \sum_{\substack{l=1\\ l\neq n}}^{N} \boldsymbol{\Theta}_{nl}[\mathbf{f}_l](s), \quad n = 1, \dots, N \tag{1}$$

where $d = -\log(e\varepsilon^2)$ and for a fiber of non-dimensional length $\bar{L} = 2$ parametrized as $\mathbf{x}_n(s,t) = \mathbf{c}_n + s\mathbf{t}_n$, $s \in [-1,\ 1]$ we have defined

$$\begin{aligned} \boldsymbol{\Theta}_{nl}[\mathbf{g}](s) &= \int_{-1}^{1} \mathbf{G}(\mathbf{x}_n(s) - \mathbf{x}_l(s'))\mathbf{g}(s')\mathrm{d}s' \\ &= \int_{-1}^{1} \mathbf{G}(\mathbf{c}_n + s\mathbf{t}_n - (\mathbf{c}_l + s'\mathbf{t}_l))\mathbf{g}(s')\mathrm{d}s'. \end{aligned} \tag{2}$$

In (1) we encountered also the operators

$$\Lambda_n[\mathbf{f}](s) = [d(\mathbf{I} + \mathbf{t}_n\mathbf{t}_n) + 2(I - \mathbf{t}_n\mathbf{t}_n)]\mathbf{f}(s), \quad \mathbf{K}[\mathbf{f}](s) = \int_{-1}^{1} \frac{\mathbf{f}(s') - \mathbf{f}(s)}{|s' - s|}\mathrm{d}s'. \tag{3}$$

In the non-dimensionalization the characteristic length has been set to half fiber length, $L/2$, and the timescale has been chosen such that an isolated fiber aligned with gravity sediments half-its length in one non-dimensional time-unit [25]. The integrals in (2) and (3) are defined over an entire fiber length with $s \in [-1,\ 1]$.

To close the system we need to couple it to the additional constraints, given in non-dimensional form

$$\begin{aligned} \mathbf{F}_n &= \int_{-1}^{1} \mathbf{f}_n(s)\mathrm{d}s = \mathbf{g}, \quad \mathbf{g} = (0,\ 0,\ -1)\ , \\ \mathbf{M}_n &= \int_{-1}^{1} s(\mathbf{t}_n \times \mathbf{f}_n(s))\mathrm{d}s = 0\ . \end{aligned}$$

The fundamental solution $\mathbf{G}(\mathbf{x})$ is given as the sum of the Stokeslet $\mathbf{S}(\mathbf{x})$ given by (5) and the dipole $\mathbf{D}(\mathbf{x})$, available in (6), weighted by the slenderness parameter ε as follows

$$\mathbf{G}(\mathbf{x}) = \mathbf{S}(\mathbf{x}) + 2\varepsilon^2\mathbf{D}(\mathbf{x})\ , \tag{4}$$

with the Stokeslet given as

$$\mathbf{S}(\mathbf{x}) = \frac{\mathbf{I}}{|\mathbf{x}|} + \frac{\mathbf{x}\mathbf{x}}{|\mathbf{x}|^3} \ . \tag{5}$$

and the dipole as

$$\mathbf{D}(\mathbf{x}) = \frac{\mathbf{I}}{|\mathbf{x}|^3} - 3\frac{\mathbf{x}\mathbf{x}}{|\mathbf{x}|^5} \ . \tag{6}$$

By applying a set of vector calculus operations to the underlying equations the system in (1) can be further manipulated such that the forces $\mathbf{f}_n(s)$ are decoupled from the velocities $\dot{\mathbf{c}}_n$ and $\dot{\mathbf{t}}_n$. To avoid redundancy we refer the reader to a description of these steps in [25]. Such a reformulation of the mathematical model leads to a discrete system with better conditioning properties. It is this formulation that we work with in the following sections.

Since the operator $\mathbf{K}[\mathbf{f}]$ from (3) simplifies under Legendre polynomials as commented in [25] we express the densities $\mathbf{f}_n(s)$ distributed along the fiber length as an expansion in terms of R Legendre polynomials, $P_q(s)$, $q = 0, \ldots, R$, *i.e.*

$$\mathbf{f}_n^R(s) = \frac{1}{2}\mathbf{F}_n + \sum_{q=1}^{R} \mathbf{a}_n^q P_q(s) = \frac{1}{2}\mathbf{F}_n + \tilde{\mathbf{f}}_n^R(s) \ . \tag{7}$$

The full expression of the polynomials $P_q(s)$, $q = 1, \ldots, 8$, can be found in Appendix C. With this expansion the fiber system can be written as

$$\begin{aligned}
\mathbf{a}_n^1 \quad + \quad & D_1 \mathbf{t}_n \mathbf{t}_n \int_{-1}^{1} \sum_{\substack{l=1 \\ l\neq n}}^{N} \mathbf{\Theta}_{nl}[\tilde{\mathbf{f}}_l^R](s) P_1(s) \mathrm{d}s = \\
& \frac{3}{2}(\mathbf{M}_n \times \mathbf{t}_n) - \frac{1}{2} D_1 \mathbf{t}_n \mathbf{t}_n \int_{-1}^{1} \sum_{\substack{l=1 \\ l\neq n}}^{N} \mathbf{\Theta}_{nl}[\mathbf{F}_l](s) P_1(s) \mathrm{d}s \ , \qquad (8) \\
\mathbf{a}_n^q \quad + \quad & \gamma_q [I - E_q \mathbf{t}_n \mathbf{t}_n] \int_{-1}^{1} \sum_{\substack{l=1 \\ l\neq n}}^{N} \mathbf{\Theta}_{nl}[\tilde{\mathbf{f}}_l^R](s) P_q(s) \mathrm{d}s = \\
& -\frac{1}{2}\gamma_q [I - E_q \mathbf{t}_n \mathbf{t}_n] \int_{-1}^{1} \sum_{\substack{l=1 \\ l\neq n}}^{N} \mathbf{\Theta}_{nl}[\mathbf{F}_l](s) P_q(s) \mathrm{d}s \ .
\end{aligned}$$

for $n = 1, \ldots, N$, $q = 2, \ldots, R$. The operator $\mathbf{\Theta}_{nl}$ is defined in (2) and the remaining quantities are given by

$$\gamma_q = \frac{2q+1}{2(2+d-\lambda_q)}, \quad D_1 = \frac{3}{4}\frac{1}{d-\lambda_1}, \quad E_q = \frac{d-2-\lambda_q}{2(d-\lambda_q)} \ .$$

In this compact form of the system the operator $\mathbf{\Theta}_{nl}$ as in (2) is applied to the force expansion in Legendre polynomials $\tilde{\mathbf{f}}_n^R$ of coefficients $\mathbf{a}_l^q$. On the right hand side of the system however $\mathbf{\Theta}_{nl}$ is applied to the constant vector $\mathbf{F}_l$. Consequently the system (8) is a linear system in the unknowns $\mathbf{a}_l^q$ of size $(3NR)^2$.

The temporal argument has been suppressed only to relieve the notation, however this system is to be solved at every time instance $t = \bar{t}$ for the current configuration. By solving (8) we compute the coefficients $\mathbf{a}_l^q$ at $t = \bar{t}$ to obtain the force distribution over each fiber

$\mathbf{f}_n(s)$ according to the expansion (7). With the computed force distribution the fiber velocity at time $t = \bar{t}$ can be retrieved as

$$\begin{aligned}
\dot{\mathbf{c}}_n &= \frac{1}{2d}\Lambda_n \mathbf{F}_n + \frac{1}{2d}\int_{-1}^{1}\sum_{\substack{l=1\\ l\neq n}}^{N} \boldsymbol{\Theta}_{nl}[\mathbf{f}_l^R](s)P_0(s)\mathrm{d}s \ , \\
\dot{\mathbf{t}}_n &= \frac{3}{2}\mathbf{M}_n \times \mathbf{t}_n + \frac{3}{2d}(I - \mathbf{t}_n\mathbf{t}_n)\int_{-1}^{1}\sum_{\substack{l=1\\ l\neq n}}^{N} \boldsymbol{\Theta}_{nl}[\mathbf{f}_l^R](s)P_1(s)\mathrm{d}s \ , \quad n = 1,\dots N
\end{aligned} \tag{9}$$

These 2 × N ordinary differential equations provide the translational and rotational velocities for each fiber, hence the updated position and direction vectors, *i.e.* $\mathbf{c}_n$ and $\mathbf{t}_n$ respectively.

3 Periodicity

We shall discuss how to impose periodic boundary conditions in the boundary integral framework using an Ewald summation method. To do so we start from the simple example of a collection of point particles, after which we shall regard the added difficulties of fiber suspensions. Consider first the Stokeslet S as given in (5). The influence onto the fluid at a point $\mathbf{x}_n$ due to a set of particles at positions $\mathbf{x}_l$ with force strengths $\mathbf{q}_l$, $l = 1, \dots, N_p$ is given as

$$\mathbf{u}_S(\mathbf{x}_n) = \sum_{\substack{l=1\\ l\neq n}}^{N_p} \mathbf{S}(\mathbf{x}_n - \mathbf{x}_l)\mathbf{q}_l, \tag{10}$$

Assume now periodicity, *i.e.* periodically repeated point forces, which for (10) translates into an infinite sum over all periodic images. If we consider periodic lengths of B_1, B_2 and B_3 in the three directions and a shift $\mathbf{p} = p_1 B_1 \mathbf{e}_1 + p_2 B_2 \mathbf{e}_2 + p_3 B_3 \mathbf{e}_3$ with $p_i \in \mathbb{Z},\ i = 1, \dots, 3$ the contribution of all particles will be instead

$$\mathbf{u}_S(\mathbf{x}_n) = \sum_{\mathbf{p}}{}' \sum_{l=1}^{N_p} \mathbf{S}(\mathbf{x}_n - \mathbf{x}_l + \mathbf{p})\mathbf{q}_l \ , \tag{11}$$

where the prime superscript over the sum over $\mathbf{p}$ indicates that the term $l = n$ for $\mathbf{p} = 0$ is excluded from the sum. With this the primary cell $\Omega = [0,\ B_1) \times [0,\ B_2) \times [0,\ B_3)$ is periodically replicated in all three spatial directions.

This sum is not absolutely convergent and certain assumptions are needed to make it well defined. The basic principle is to split the sum in two terms which are to be evaluated separately and in the splitting process remove the divergent part by assuming that there is a mean pressure gradient balancing the applied forces such that the integrated velocity over the domain is zero. One term will contain the singularity of the kernel and is to be computed in the real space, while the remaining term is smooth and can be evaluated in Fourier space. A few different decompositions are available in the literature, see Beenakker [3], Hasimoto [13], or for a better overview Pozrikidis [22]. We use here the decomposition suggested by Hasimoto [13] since this formulation has been shown in [19] to converge faster than the Beenakker formulation [3]. According to Hasimoto's decomposition the velocity at a point $\mathbf{x}_n$ in the interior of a periodic domain due to a set of point forces at $\mathbf{x}_l$, with strengths $\mathbf{q}_l$ can be written as

$$\mathbf{u}_S(\mathbf{x}_n) = \sum_{l=1}^{N_p} {\sum_{\mathbf{p}}}' \Gamma_S(\xi, \mathbf{x}_n - \mathbf{x}_l + \mathbf{p})\mathbf{q}_l + \frac{1}{V}\sum_{l=1}^{N_p}\sum_{\mathbf{k}\neq 0} \Phi_S(\xi, \mathbf{k})\mathrm{e}^{-i\mathbf{k}\cdot(\mathbf{x}_n - \mathbf{x}_l)}\mathbf{q}_l - \frac{4\xi}{\sqrt{\pi}}\mathbf{q}_n \ . \quad (12)$$

The parameter ξ introduced here is a decomposition parameter that controls the convergence of the two sums, and although each component in (12) depends on ξ the total sum is independent of it.

The real space sum component Γ_S in (12) is defined as

$$\Gamma_S(\xi, \mathbf{x}) \quad = \quad C(\xi r)\frac{\mathbf{I}}{r} + D(\xi r)\frac{\hat{\mathbf{x}}\hat{\mathbf{x}}}{r} \ , \quad (13)$$

where we used the notation $\hat{\mathbf{x}} = \mathbf{x}/|\mathbf{x}|$, $r = |\mathbf{x}|$ and

$$C(\xi r) = \operatorname{erfc}(\xi r) - \frac{2\xi r}{\sqrt{\pi}}e^{-\xi^2 r^2}, \quad D(\xi r) = \operatorname{erfc}(\xi r) + \frac{2\xi r}{\sqrt{\pi}}e^{-\xi^2 r^2} \ .$$

With the wavenumber $\mathbf{k} = \{2\pi(k_1/B_1,\ k_2/B_2,\ k_3/B_3),\ k_{i=1,\ldots,3} \in \mathbb{Z}\}$ and $k = |\mathbf{k}|$ the Fourier space term Φ_S in (12) is defined as

$$\Phi_S(\xi, \mathbf{k}) \quad = \quad B(\xi, \mathbf{k})e^{-k^2/4\xi^2} \ , \quad (14)$$

where

$$B(\xi, \mathbf{k}) = 8\pi\left(1 + \frac{k^2}{4\xi^2}\right)\frac{1}{k^4}(k^2\mathbf{I} - \mathbf{k}\mathbf{k}) \ . \quad (15)$$

Note that in Fourier space the divergent part which has been removed corresponds to the zero-th wave number, and is equivalent to imposing the condition $\int_\Omega \mathbf{u} = 0$. The real space sum has a prime as superscript which is used to indicate that the term $n = l, \mathbf{p} = 0$ is excluded from the sum in accordance with (11). The original term has however been split into two parts and the part of it that is included in the Fourier sum needs to be removed. This is achieved by the last single term in (12) that is commonly referred to as the self interaction and can be evaluated from

$$\lim_{|\mathbf{x}|\to 0}\left(\Gamma_S(\xi, \mathbf{x}) - \mathbf{S}(\mathbf{x})\right) = -\frac{4\xi}{\sqrt{\pi}}\mathbf{I} \ . \quad (16)$$

The sums in (12) decay at an exponential rate as it can be seen from their expressions and can be truncated as will be discussed in Sec.5.

Periodic dipole

The fiber-fiber interaction system in (8) involves two fundamental solutions: the Stokeslet (5) and the dipole (6). The periodic Stokeslet is treated using the Hasimoto decomposition and thus it is natural to derive the corresponding decomposition for the dipole. The dipole (6) stems from the Stokeslet (5) according to

$$\mathbf{D}(\mathbf{x}) = \frac{1}{2}\Delta\mathbf{S}(\mathbf{x}).$$

The same relationship will hold in the periodic framework and the periodic dipole arising from the Hasimoto formulation will have a similar expression as in (12) with the real space sum component $\Gamma_S(\xi, \mathbf{x})$ replaced by $\Gamma_D(\xi, \mathbf{x})$, the Fourier space sum component $\Phi_S(\xi, \mathbf{k})$ substituted by $\Phi_D(\xi, \mathbf{k})$ and a self interaction term to be computed as in (16). To retrieve the real space sum component Γ_D we proceed by computing the Laplacian of the corresponding Stokeslet component $\Gamma_S(\xi, \mathbf{x})$ and obtain

$$\Gamma_D(\xi, \mathbf{x}) \quad = \quad \frac{\mathbf{I}}{r^3} C(\xi r) - 3\frac{\hat{\mathbf{x}}\hat{\mathbf{x}}}{r^3} D(\xi r) \tag{17}$$

with

$$\begin{aligned} C(\xi r) &= \operatorname{erfc}(\xi r) + \frac{2}{\sqrt{\pi}}(-2\xi^5 r^5 + 4\xi^3 r^3 + \xi r)\mathrm{e}^{-\xi^2 r^2} \\ D(\xi r) &= \operatorname{erfc}(\xi r) - \frac{2}{3\sqrt{\pi}}(2\xi^5 r^5 - 2\xi^3 r^3 - 3\xi r)\mathrm{e}^{-\xi^2 r^2} \end{aligned}$$

The self interaction term is, in correspondence with (16), evaluated by taking the limit

$$\lim_{|\mathbf{x}|\to 0} \Big(\Gamma_D(\xi, \mathbf{x}) - \mathbf{D}(\mathbf{x}) \Big) = \frac{20\xi^3}{3\sqrt{\pi}} \mathbf{I} \ .$$

Similarly, to obtain the Fourier sum component $\Phi_D(\xi, \mathbf{k})$ it suffices to compute the Laplacian of the Fourier space part of the periodic Stokeslet. This computation however is less cumbersome since the spatial variable $\mathbf{x}$ appears only in the $\mathrm{e}^{-i\mathbf{x}\cdot\mathbf{k}}$ term. This yields a largely unchanged expression for $\Phi_D(\xi, \mathbf{k})$ with only a $-k^2/2$ extra factor, *i.e.*

$$\Phi_D(\xi, \mathbf{k}) = \frac{-k^2}{2} B(\xi, \mathbf{k}) e^{-k^2/4\xi^2} \ , \tag{18}$$

where $B(\xi, \mathbf{k})$ is the same as in (15). Hence the periodic sum for the dipole is given by

$$\begin{aligned} \mathbf{u}_D(\mathbf{x}_n) \quad = \quad & \sum_{l=1}^{N_p} \sum_{\mathbf{p}}{}' \Gamma_D(\xi, \mathbf{x}_n - \mathbf{x}_l + \mathbf{p})\mathbf{q}_l + \\ & \frac{1}{V} \sum_{l=1}^{N_p} \sum_{\mathbf{k}\neq 0} \Phi_D(\xi, \mathbf{k}) \mathrm{e}^{-i\mathbf{k}\cdot(\mathbf{x}_n - \mathbf{x}_l)} \mathbf{q}_l + \frac{20\xi^3}{3\sqrt{\pi}} \mathbf{q}_n \ . \end{aligned} \tag{19}$$

with Γ_D and Φ_D given by (17), and (18) respectively.

Fiber system kernel

To model the fiber suspension as given by (8) we need to integrate the kernel $\mathbf{G}(\mathbf{x}) = \mathbf{S}(\mathbf{x}) + 2\varepsilon^2 \mathbf{D}(\mathbf{x})$ defined for a free space problem in (4). In accordance to the sum (11) for the periodic Stokeslet we state the entire periodic kernel as

$$\mathbf{u}(\mathbf{x}_n) = \sum_{\mathbf{p}}{}' \sum_{l=1}^{N_p} \mathbf{G}(\mathbf{x}_n - \mathbf{x}_l + \mathbf{p})\mathbf{q}_l \ , \tag{20}$$

Since the periodic equivalent of the kernel $\mathbf{G}$ involves the periodic expressions of the Stokeslet and the dipole the sum in (20) has the decomposition

$$\mathbf{u}(\mathbf{x}_n) = \sum_{l=1}^{N_p} \sum_{\mathbf{p}}{}' \Gamma(\xi, \mathbf{x}_n - \mathbf{x}_l + \mathbf{p})\mathbf{q}_l + \frac{1}{V} \sum_{l=1}^{N_p} \sum_{\mathbf{k}\neq 0} \Phi(\xi, \mathbf{x}_n - \mathbf{x}_l, \mathbf{k}) \mathrm{e}^{-i\mathbf{k}\cdot(\mathbf{x}_n - \mathbf{x}_l)} \mathbf{q}_l + C_\xi \mathbf{q}_n \ , \tag{21}$$

where

$$\begin{aligned}\Gamma(\xi,\mathbf{x}) &= \Gamma_S(\xi,\mathbf{x}) + 2\varepsilon^2\Gamma_D(\xi,\mathbf{x}) \ , &(22)\\ \Phi(\xi,\mathbf{k}) &= \Phi_S(\xi,\mathbf{k}) + 2\varepsilon^2\Phi_D(\xi,\mathbf{k}) \ , &(23)\\ C_\xi &= \frac{-4\xi}{\sqrt{\pi}} + 2\varepsilon^2\frac{20\xi^3}{3\sqrt{\pi}} \ , &(24)\end{aligned}$$

with $\Gamma_S(\xi,\mathbf{x})$ as in (13), $\Gamma_D(\xi,\mathbf{x})$ as in (17), $\Phi_S(\xi,\mathbf{x})$ as in (14) and $\Phi_D(\xi,\mathbf{x})$ as in (18).

Equivalently by setting $\tilde{\Gamma}(\xi,\mathbf{x}) = \Gamma(\xi,\mathbf{x}) - \mathbf{G}(\mathbf{x})$ we can write (21) as

$$\begin{aligned}\mathbf{u}(\mathbf{x}_n) &= \sum_{\mathbf{p}}\left(\sum_{\substack{l=1\\l\neq n}}^{N_p}\mathbf{G}(\xi,\mathbf{x}_n-\mathbf{x}_l+\mathbf{p})\mathbf{q}_l + \sum_{l=1}^{N_p}\tilde{\Gamma}(\xi,\mathbf{x}_n-\mathbf{x}_l+\mathbf{p})\mathbf{q}_l\right) + \\ &\quad \frac{1}{V}\sum_{l=1}^{N_p}\sum_{\mathbf{k}\neq 0}\Phi(\xi,\mathbf{k})\mathrm{e}^{-i\mathbf{k}\cdot(\mathbf{x}_n-\mathbf{x}_l)}\mathbf{q}_l \ . &(25)\end{aligned}$$

The term $\mathbf{p}=0$, $l=n$ is included in the sum over $\tilde{\Gamma}(\xi,\mathbf{x})$ and for this term the limit value as $|\mathbf{x}|\to 0$ should be used. This limit value is the limit computed earlier for the self-interaction term, $\lim_{|\mathbf{x}|\to 0}\tilde{\Gamma}(\xi,\mathbf{x}) = \lim_{|\mathbf{x}|\to 0}\Gamma(\xi,\mathbf{x}) - \mathbf{G}(\mathbf{x}) = C_\xi$ where C_ξ as in (24).

4 The simulation of a periodic fiber suspension

Periodic fiber suspension model

Consider a suspension of N fibers within a domain $\Omega = [0,\ B_1)\times[0,\ B_2)\times[0,\ B_3)$ subject to periodic boundary conditions. Let us introduce the operator

$$\mathbf{\Theta}^{\mathbf{p}}_{nl}[\mathbf{g}](s) = \int_{-1}^{1}\mathbf{G}(\mathbf{x}_n(s)-\mathbf{x}_l(s')+\mathbf{p})\mathbf{g}(s')\mathrm{d}s' \ , \quad l=1,\ldots,N \ , \tag{26}$$

and note that for $\mathbf{p}=0$ this expression coincides with $\mathbf{\Theta}_{nl}$ as defined in (2).

To introduce periodicity as in the fiber system (8) we need to extend the sum over the fibers by adding all periodic images of all fibers, including the fiber itself. We introduce the notation

$$A_n[\{\mathbf{g}_l\}_{l=1}^N](s) = \sum_{\substack{l=1\\l\neq n}}^{N}\mathbf{\Theta}_{nl}[\mathbf{g}_l](s) + \sum_{\mathbf{p}\neq 0}\sum_{l=1}^{N}\mathbf{\Theta}^{\mathbf{p}}_{nl}[\mathbf{g}_l](s) = {\sum_{\mathbf{p}}}'\sum_{l=1}^{N}\mathbf{\Theta}^{\mathbf{p}}_{nl}[\mathbf{g}_l](s) \ , \tag{27}$$

where the prime superscript over the sum over $\mathbf{p}$ means that the term $l=n$ for $\mathbf{p}=0$ is excluded from the sum.

If we use the decomposition in (25) the entire term A_n can now be written as

$$\begin{aligned}A_n[\{\mathbf{g}_l\}_{l=1}^N](s) &= \sum_{\mathbf{p}}\Bigg(\sum_{\substack{l=1\\l\neq n}}^{N}\int_{-1}^{1}\mathbf{G}(\mathbf{x}_n(s)-\mathbf{x}_l(s')+\mathbf{p})\mathbf{g}_l(s')\mathrm{d}s' &(28)\\ &\quad +\sum_{l=1}^{N}\int_{-1}^{1}\tilde{\Gamma}(\xi,\mathbf{x}_n(s)-\mathbf{x}_l(s')+\mathbf{p})\mathbf{g}_l(s')\mathrm{d}s'\Bigg)\\ &\quad +\frac{1}{V}\sum_{l=1}^{N}\sum_{\mathbf{k}\neq 0}\int_{-1}^{1}\Phi(\xi,\mathbf{k})\mathrm{e}^{-i\mathbf{k}\cdot(\mathbf{x}_n-\mathbf{x}_l)}\mathbf{g}_l(s')\mathrm{d}s'\end{aligned}$$

with $\tilde{\Gamma}(\xi,\mathbf{x}) = \Gamma(\xi,\mathbf{x}) - \mathbf{G}(\mathbf{x})$, and $\lim_{|\mathbf{x}|\to 0} \tilde{\Gamma}(\xi,\mathbf{x}) = C_\xi$ as given in (4) and (23)–(24).

To restate the fiber system in (8) we use the operator A_n and have for $n = 1,\dots,N$,

$$
\begin{aligned}
\mathbf{a}_n^1 \quad + \quad & D_1 \mathbf{t}_n \mathbf{t}_n \int_{-1}^{1} A_n[\{\tilde{\mathbf{f}}_l^R\}_{l=1}^N](s) P_1(s) \mathrm{d}s = \\
& \frac{3}{2}(\mathbf{M}_n \times \mathbf{t}_n) - \frac{1}{2} D_1 \mathbf{t}_n \mathbf{t}_n \int_{-1}^{1} A_n[\{\mathbf{F}_l\}_{l=1}^N](s) P_1(s) \mathrm{d}s \ , \\
\mathbf{a}_n^q \quad + \quad & \gamma_q [I - E_q \mathbf{t}_n \mathbf{t}_n] \int_{-1}^{1} A_n[\{\tilde{\mathbf{f}}_l^R\}_{l=1}^N](s) P_q(s) \mathrm{d}s = \\
& -\frac{1}{2} \gamma_q [I - E_q \mathbf{t}_n \mathbf{t}_n] \int_{-1}^{1} A_n[\{\mathbf{F}_l\}_{l=1}^N](s) P_q(s) \mathrm{d}s \ .
\end{aligned}
\tag{29}
$$

The system is linear in $\mathbf{a}_l^q$, $q = 1,\dots,R$, the coefficients in the expansion of the force densities $\mathbf{f}_n$ in Legendre polynomials (7). In [25] the system was stated in a form that illustrates how to construct explicitly the matrix of the system. Here however it is stated in a form that is convenient for computing directly the matrix-vector product. This is suitable when using an iterative method, such as GMRES. This avoids the memory cost associated with the full (non-sparse) matrix and allows for the use of a fast summation method to accelerate the computations, such as the fast Ewald method discussed in this paper.

The velocities $\dot{\mathbf{c}}_n$ and $\dot{\mathbf{t}}_n$ given in (9), can be expressed in the periodic setup in terms of the operator A_n as

$$
\begin{aligned}
\dot{\mathbf{c}}_n &= \frac{1}{2d} \Lambda_n \mathbf{F}_n + \frac{1}{2d} \int_{-1}^{1} A_n[\{\mathbf{f}_l^R\}_{l=1}^N](s) P_0(s) \mathrm{d}s \ , \\
\dot{\mathbf{t}}_n &= \frac{3}{2} \mathbf{M}_n \times \mathbf{t}_n + \frac{3}{2d} (I - \mathbf{t}_n \mathbf{t}_n) \int_{-1}^{1} A_n[\{\mathbf{f}_l^R\}_{l=1}^N](s) P_1(s) \mathrm{d}s \ , n = 1,\dots,N \ .
\end{aligned}
\tag{30}
$$

With the velocities obtained from (30) the fiber positions can be updated through a straight forward first order differential equation.

Numerical discretization

The real space term $\Gamma(\xi,\mathbf{x}) = \mathbf{G}(\mathbf{x}) + \tilde{\Gamma}(\xi,\mathbf{x})$ decays exponentially fast as $|\mathbf{x}|$ increases, at a rate that depends on ξ. Given a parameter ξ one can determine at which point $|\mathbf{x}| = r_c$ the real space sum can be truncated for a given error tolerance. The contribution from other fibers farther away than a distance r_c will be neglected, as discussed in Sec.5. For the moment let us simply assume that for each fiber n with $n = 1,\dots,N$ there exists a set of fibers in a neighborhood of n, $\mathcal{N}(n)$, including the fiber itself, which should be included in the real space sum.

Note here that a fiber n may be closer to a periodic image of a fiber l than to the fiber l itself. In this case there is a $\mathbf{p} = p_1 B_1 \mathbf{e}_1 + p_2 B_2 \mathbf{e}_2 + p_3 B_3 \mathbf{e}_3$ with $p_i \in \{-1, 0, 1\}$, $i = 1,\dots,3$ such that

$$|\mathbf{c}_n - \mathbf{c}_l + \mathbf{p}| < |\mathbf{c}_n - \mathbf{c}_l| \ .$$

We denote this $\mathbf{p}$ by $\mathbf{p}_c(n,l)$, if there is no such $\mathbf{p}$ then $\mathbf{p}_c(n,l) = 0$. We assume here that the cut-off radius is small enough such that at most one periodic image of any fiber l is to be included in the real space sum.

Returning now to the integral terms building up (28) we must evaluate them either analytically or numerically. Analytical integration is preferable to a numerical quadrature especially when two fibers are very close to each other, *i.e.* $|\mathbf{x}_n(s) - \mathbf{x}_l(s')| \to 0$ for some s, s', since in this case the kernel $\mathbf{G}$ becomes nearly singular. As described in [25] the inner integrals in the expression of A_n in (28) can be evaluated analytically

$$I_l^q(\mathbf{x}) = \int_{-1}^{1} \mathbf{G}(\mathbf{x} - \mathbf{x}_l(s'))P_q(s')\mathrm{d}s'. \tag{31}$$

Regarding the first integral term in (28) as applied to $\tilde{\mathbf{f}}_l^R(s)$ given in (7) we can express it as

$$\begin{aligned} \int_{-1}^{1} \mathbf{G}(\mathbf{x}_n(s) - \mathbf{x}_l(s') + \mathbf{p})\tilde{\mathbf{f}}_l^R(s')\mathrm{d}s' &= \sum_{q=1}^{R} \int_{-1}^{1} \mathbf{G}(\mathbf{x}_n(s) - \mathbf{x}_l(s') + \mathbf{p})P_q(s')\mathrm{d}s'\mathbf{a}_l^q \\ &= \sum_{q=1}^{R} I_l^q(\mathbf{x}_n(s))\mathbf{a}_l^q \ . \end{aligned} \tag{32}$$

Both terms $\tilde{\Gamma}(\xi, \mathbf{x})$ and $\Phi(\xi, \mathbf{x})$ in (28) are smooth and thus suitable for numerical integration. For the numerical integration we use a three point composite Gaussian rule, where each fiber is divided in N_q intervals of 3 discrete points each, amounting to a total of $Q = 3 \times N_q$ integration points in the quadrature rule. The weights associated to each discrete point s_j will be denoted here by w_j.

The discrete operator corresponding to A_n defined in (28) will be here denoted by $\bar{A}_n$. The operator $A_n[\{\mathbf{g}_l\}_{l=1}^N](s)$ is to be found in the system (29) on both the right hand side as applied to the expansion $\{\tilde{\mathbf{f}}_l^R\}_{l=1}^N$ and the left hand side applied to $\{\mathbf{F}_l\}_{l=1}^N$. To avoid any puzzling notation we expand explicitly both terms and to start with $A_n[\{\tilde{\mathbf{f}}_l^R\}_{l=1}^N](s)$

$$\begin{aligned} \bar{A}_n[\{\tilde{\mathbf{f}}_l^R\}_{l=1}^N](s_i) \; = \; & \sum_{\substack{l \in \mathcal{N}(n) \\ l \neq n}}^{N} \sum_{q=1}^{R} I_l^q(\mathbf{x}_n(s_i) + \mathbf{p}_c(n,l))\mathbf{a}_l^q \; + \\ & \sum_{l \in \mathcal{N}(n)}^{N} \sum_{j=1}^{Q} \tilde{\Gamma}(\xi, \mathbf{x}_n(s_i) - \mathbf{x}_l(s_j) + \mathbf{p}_c(n,l)) w_j \tilde{\mathbf{f}}_l^R(s_j) \; + \\ & \frac{1}{V} \sum_{l=1}^{N} \sum_{\mathbf{k} \neq 0} \sum_{j=1}^{Q} \Phi(\xi, \mathbf{k}) \mathrm{e}^{-i\mathbf{k}\cdot(\mathbf{x}_n(s_i) - \mathbf{x}_l(s_j))} w_j \tilde{\mathbf{f}}_l^R(s_j) \end{aligned} \tag{33}$$

For $l = n$ and $j = i$ the limit value of $\tilde{\Gamma}$ must be used as discussed below equation (25). For the term for $A_n[\{\mathbf{F}_l\}_{l=1}^N](s)$ we note that $\mathbf{F}_l$ is now a constant vector independent of s leading to

$$\begin{aligned} \bar{A}_n[\{\mathbf{F}_l\}_{l=1}^N](s_i) \; = \; & \sum_{\substack{l \in \mathcal{N}(n) \\ l \neq n}}^{N} I_l^q(\mathbf{x}_n(s_i) + \mathbf{p}_c(n,l))\mathbf{F}_l \; + \\ & \sum_{l \in \mathcal{N}(n)}^{N} \sum_{j=1}^{Q} \tilde{\Gamma}(\xi, \mathbf{x}_n(s_i) - \mathbf{x}_l(s_j) + \mathbf{p}_c(n,l)) w_j \mathbf{F}_l \; + \\ & \frac{1}{V} \sum_{l=1}^{N} \sum_{\mathbf{k} \neq 0} \sum_{j=1}^{Q} \Phi(\xi, \mathbf{k}) \mathrm{e}^{-i\mathbf{k}\cdot(\mathbf{x}_n(s_i) - \mathbf{x}_l(s_j))} w_j \mathbf{F}_l \ . \end{aligned} \tag{34}$$

In (29) the operators $A_n[\cdot](s)$ on both sides of the system are to be integrated once more over the entire fiber. This outer integral is evaluated numerically using the same composite Gaussian method as used for the smooth $\tilde{\Gamma}(\xi, \mathbf{x})$ and $\Phi(\xi, \mathbf{x})$. The entire discrete system now reads

$$\begin{aligned}
\mathbf{a}_n^1 \quad &+ \quad D_1 \mathbf{t}_n \mathbf{t}_n \sum_{i=1}^{Q} \bar{A}_n[\{\tilde{\mathbf{f}}_l^R\}_{l=1}^N](s_i) w_i P_1(s_i) = \\
&\frac{3}{2}(\mathbf{M}_n \times \mathbf{t}_n) - \frac{1}{2} D_1 \mathbf{t}_n \mathbf{t}_n \sum_{i=1}^{Q} \bar{A}_n[\{\mathbf{F}_l\}_{l=1}^N](s_i) w_i P_1(s_i), \qquad (35) \\
\mathbf{a}_n^q \quad &+ \quad \gamma_q [I - E_q \mathbf{t}_n \mathbf{t}_n] \sum_{i=1}^{Q} \bar{A}_n[\{\tilde{\mathbf{f}}_l^R\}_{l=1}^N](s_i) w_i P_q(s_i) = \\
&-\frac{1}{2}\gamma_q [I - E_q \mathbf{t}_n \mathbf{t}_n] \sum_{i=1}^{Q} \bar{A}_n[\{\mathbf{F}_l\}_{l=1}^N](s_i) w_i P_q(s_i) \ ,
\end{aligned}$$

for $l = 1, \ldots, N$, $q = 1, \ldots, R$.

The discrete problem as currently stated can be evaluated by means of a fast summation method to obtain an expression of the left hand side as a function of the unknowns $\mathbf{a}_l^q$. This can be then solved for the coefficients $\mathbf{a}_l^q$ using an iterative method. With the newly obtained coefficients $\mathbf{a}_l^q$ the forces $\mathbf{f}_l$ can be retrieved from the expansion (7). Subsequently velocities $\dot{\mathbf{c}}_n$ and $\dot{\mathbf{t}}_n$ in (9) provide the updated position and orientation vectors at the new time instance. Their evaluation involves one more fast Ewald summation as it it to be done for (35) however now applied to the force expansion $\mathbf{f}_l^R$. The advection will be performed using a second order multi-step method, here we take BDF2/EXT2 [17], also employed in [25].

5 Fast summation method

In numerical computations both infinite sums in (21) must be truncated. Assume that the computational domain we work in is $\Omega = [0,\ B_1) \times [0,\ B_2) \times [0,\ B_3)$. The parameter ξ affects both the accuracy and the efficiency. The computational cost of evaluating the Fourier space sum can balance the cost of the real space sum for a carefully picked ξ. Also for a chosen ξ the truncation can be performed such that the method is of a certain accuracy δ. To start with we perform an error analysis as in [19] to asses the loss of accuracy due to truncation. The error analysis is performed in euclidean norm for a particle positioned at $\mathbf{x}_n$. For the Stokeslet it has been shown that if the real space sum is truncated at a certain cut-off $|\mathbf{x} + \mathbf{p}| = r_c$ then the truncation error is

$$\begin{aligned}
\left| \sum_{\mathbf{p}} \Gamma_S(\xi, \mathbf{x} + \mathbf{p}) \mathbf{f} - \sum_{|\mathbf{x}+\mathbf{p}| \le r_c} \Gamma_S(\xi, \mathbf{x} + \mathbf{p}) \mathbf{f} \right| \quad &\le \quad \sum_{|\mathbf{x}+\mathbf{p}| > r_c} ||\Gamma_S(\xi, \mathbf{x} + \mathbf{p}) \mathbf{f}||_2 \\
&\le \quad E_R^S(\xi, r_c) ||\mathbf{f}||_2 \ ,
\end{aligned}$$

and $E_R^S(\xi, r_c)$ can be estimated as

$$E_R^S(\xi, r_c) \le (12\pi + 16\sqrt{\pi} r_c \xi) \frac{1}{\xi^2} e^{-\xi^2 r_c^2} \ . \qquad (36)$$

Similarly for the Fourier space sum it was obtained that the truncation error at a certain k_∞ is

$$\left|\sum_{\mathbf{k}} |\Phi_S(\xi,\mathbf{k})\mathbf{f} - \sum_{|\mathbf{k}|\leq k_\infty} |\Phi_S(\xi,\mathbf{k})\mathbf{f}\right| \leq \sum_{|\bar{\mathbf{k}}|>k_\infty} ||\Phi_S(\xi,\mathbf{k})\mathbf{f}||_2 \leq E_F^S(\xi,k_\infty)||\mathbf{f}||_2$$

where for $\mathbf{k} = 2\pi\bar{\mathbf{k}}$ with $\bar{\mathbf{k}} = (k_1/B_1,\ k_2/B_2,\ k_3/B_3)$ and $k_i \in \mathbb{Z}, i = 1,\ldots,N$ and $k_\infty = |\bar{\mathbf{k}}|$

$$E_F^S(\xi,k_\infty) \leq (2\sqrt{\pi}k_\infty + 3\xi)\frac{2}{\sqrt{\pi}}e^{-k_\infty^2(\pi/\xi)^2}.$$

For the dipole we have obtained similar error estimates

$$E_R^D(\xi,r_c) \quad \leq \quad (16\sqrt{\pi}r_c^3\xi^3 + 48\sqrt{\pi}r_c\xi + 40\pi)\mathrm{e}^{-\xi^2 r_c^2}\ , \tag{37}$$

and for the Fourier space component

$$E_F^D(\xi,k_\infty) \quad \leq \quad 8\pi\left(\frac{5\sqrt{\pi}}{4a^3} + \frac{5k_\infty}{4a^2} + \frac{k_\infty^3}{2}\right)\mathrm{e}^{-a^2k_\infty^2}\ , \quad a = \frac{\pi}{\xi}\ . \tag{38}$$

the full derivation can be found in Appendix A.

These bounds provide an estimate according to which we can truncate the real space sum and the Fourier space sum at a cut-off r_c, and k_∞ respectively. For a fixed ξ the computational complexity of the real space sum is $\mathcal{O}(N^2)$, and the same holds for the Fourier space sum, however this can be expedited as will be further discussed.

Real space sum treatment

To start with we discuss the case of a system of N_p particles uniformly distributed within a volume V, *i.e.* the number density $\rho = N_p/V$ can be assumed to be constant in any subvolume. The real space sum has a total computational complexity of $\mathcal{O}(N_p^2)$ due to the $N_p(N_p-1)/2$ pairwise interactions. The error estimates for the real space sum truncation for both the Stokeslet (36) and the dipole (37) decay exponentially in r_c at a rate controlled by the parameter ξ. It can be seen that the sum is properly decayed, *i.e.* below an accuracy threshold δ, for a certain value of the product ξr_c. Thus if a sufficiently large ξ is chosen it follows that r_c can have a magnitude smaller than the length of the domain. Consequently if r_c is small we do not need to compute the pairwise interactions in the entire volume but solely inside a sphere of radius r_c centered at the source particle. The aim is then to identify for each individual particle the neighbors that need to be included in the computation, and to store them in a list.

A naive approach to obtain the list of neighbors specific to each particle would be to compute all inter-particle distances. However this operation would already be $\mathcal{O}(N_p^2)$ and should therefore be avoided. An algorithm widely used to reduce the number of interactions which are to be computed is the Linked Cell List (LCL) [1]. The main idea is to create a neighbor list by diving the entire computational domain into boxes and subsequently establishing a box-particle correspondence list. It suffices then for each particle to compute the contribution of the neighboring particles lying in the immediate sub-boxes, *e.g.* if we deal with a three-dimensional problem we have to consider besides the current sub-box 26 additional sub-boxes. Identifying what particles belong to certain boxes is a logical operation which is much cheaper than computing distances. However for this approach to bring any gain it is clear that the computational domain must be split in more than

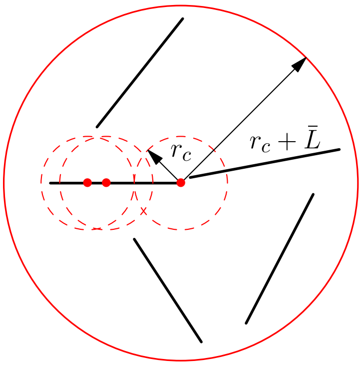

Figure 1: Diagram of a fiber configuration. The real space sum is sufficiently decayed at a certain cut-off r_c. A fiber may be only partially inside the sphere of radius r_c. To accommodate the analytical integration we consider in the computation of the real space sum a cut-off $r_c^* = r_c + \bar{L}$, where $\bar{L}$ is one fiber length.

3 sub-boxes in each direction. Assuming that within this sub-volume lie N_{LCL} particles then the number of pairwise interactions that needs to be taken into account decreases to $N_p(N_{LCL} - 1)/2$. If every sub-box has a side of length b then $N_{LCL} \approx 27\rho b^3$ (we have 27 boxes each of volume b^3). This algorithm is essentially $\mathcal{O}(N_p)$ if N_{LCL} is preserved constant as N_p increases.

The number of elements in the neighbor list can be further reduced by filtering the list of N_{LCL} particles to exclude everything that does not lie inside the sphere of radius r_c. This gives a lower number of neighboring particles $N_c \approx 4\pi/3\rho r_c^3$, with $r_c \approx b$, $r_c \leq b$.

Reverting to the fiber suspension model no modification to the above algorithm is required if we decide to integrate numerically all the terms in (8). For the numerical integration the fact that a fiber may not be included entirely inside the sphere of radius r_c, as illustrated in Fig. 2b imposes no restrictions since numerical integration is a discrete process. However since we intend to use analytical integration as the fibers get close to each other we need to maintain the continuous representation of the fiber. To avoid inconsistencies we find r_c for which the real space sum is properly decayed and in practice use $r_c^* = r_c + \bar{L}$, where $\bar{L}$ is one fiber length ($\bar{L} = 2$ in our non-dimensional setting). This choice is based on an analysis of the most extreme cases that can occur, one such example is provided in Fig. 1. It is however clear from Fig. 1 that some of the fibers within a sphere of radius r_c^* do not contribute to the final result since they do not intersect at any instance the sphere of radius r_c. Therefore we can filter once more the neighbor list of the current fiber. The filtering in this case requires the computation of fiber to fiber distances which relies on minimizing a quadratic. This is far more expensive than the computation of particle-to-particle distances and should be employed only as a last step. To sum up the algorithm described so far for truncating the real space sum we order the steps in Alg.5.

With the newly created neighbor lists we compute the real space sum by adding the contribution to the fiber n of all $l \in \mathcal{N}(n)$ as indicated in the sums (33)-(34).

Fourier space sum treatment

When considering the Fourier space sums in (33)-(34) it is natural to think of applying the Fast Fourier Transform to lower the computational complexity of $\mathcal{O}(N^2)$. Several FFT-based Ewald summation algorithms of $\mathcal{O}(N \log N)$ complexity emerged in the field

Algorithm 1 Real space sum treatment — algorithm for generating neighbor lists

```
[1] Choose $r_c$ and set $r_c^* = r_c + \bar{L}$, then compute $q_i = floor(\bar{B}_i/r_c^*)$ the number of boxes in each $\bar{B}_i$ direction ($i = 1, \ldots, 3$). The Linked Cell List has now $q_i$ boxes of side length $b = B_i/q_i \geq r_c^*$ (in practice we take $B_i/q_i$ constant in all directions to assure a splitting of the domain into cubic boxes).
[2] Section the domain in boxes of side length $b$, see Fig. 2a.
[3] Pad the computational domain with cubic boxes of side $b$ to assure that all closest periodic images are included in the domain.
[4] For the midpoint of each fiber $l$ identify the box it belongs to (this is a logical operation). Create for each fiber a neighbor list $\mathcal{N}(l)$ of all other fibers whose midpoints lie in the current box and also in the adjacent boxes, i.e. the cube of side $3b$.
[5] Refine the neighbor list $\mathcal{N}(l)$ by eliminating all fibers whose midpoints are at a distance larger than $r_c^*$ away, see Fig. 2b.
[6] Refine once more $\mathcal{N}(l)$ by computing the fiber-fiber distance and retaining only the ones at less than $r_c$ away from the current fiber.
```

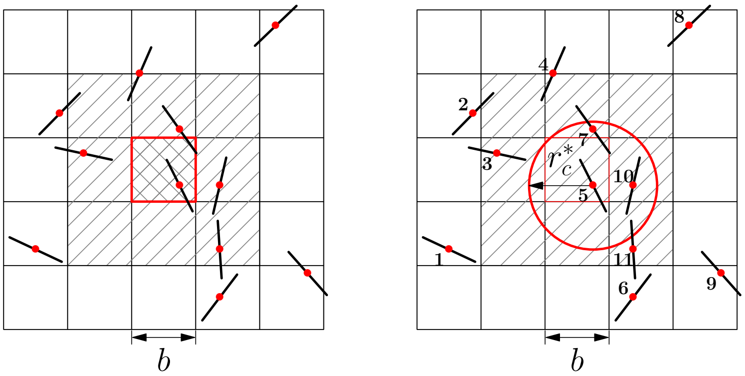

(a) Linked cell list

(b) Neighbor list for fiber No.5 (List includes fibers No.7,10 but not fiber No.11)

Figure 2: Linked cell list division of the computational domain ($r_c^* = r_c + \bar{L}$).

of molecular dynamics: Particle Mesh Ewald (PME) [15] or the Smooth PME (SPME) [6], followed by the Spectral Ewald (SE) [19]. The main idea of FFT-based method is to grid the computational volume and interpolate using B-splines (SPME) or spread using Gaussians (SE) the point forces onto the grid. This enables the use of FFTs to compute the Fourier space sum. As noted in [20] the accuracy of the interpolation onto the grid using B-splines as in the SPME method has a polynomial convergence order, while as the use of Gaussians as in the SE method exhibits spectral accuracy. This main difference between the two approaches yields that for similar accuracy requirements the SE method is more memory efficient than the SPME method, *i.e.* much smaller grid sizes can be used in the FFTs . To this end we employ the SE method [19] to compute the Fourier space sums in (33)-(34).

Following the derivation in [19] express the Fourier sum (28) as

$$\frac{1}{V}\sum_{n}\sum_{\mathbf{k}\neq 0}\Phi(\xi,\mathbf{k})\mathbf{f}_n \mathrm{e}^{-i\mathbf{x}\cdot\mathbf{k}} = \int_{\Omega}\widetilde{H}(x)\left(\frac{2\xi^2}{\pi\eta}\right)^{3/2}\mathrm{e}^{-2\xi^2|\mathbf{x}-\mathbf{x}_l|_*^2/\eta}\mathrm{d}\mathbf{x}\ . \tag{39}$$

where $|\cdot|_*$ denotes the closest periodic image and $\widetilde{H}$ is the inverse transform of $\widehat{\widetilde{H}}$ given by

$$\widehat{\widetilde{H}}_k = (1-\varepsilon^2k^2)B(\xi,\mathbf{k})\mathrm{e}^{-(1-\eta)k^2/4\xi^2}\widehat{H}_k\ , \tag{40}$$

Here $\widehat{H}$ is the Fourier transform of H provided as

$$H = \sum_{n}\mathbf{f}_n\left(\frac{2\xi^2}{\pi\eta}\right)^{3/2}\mathrm{e}^{-2\xi^2|\mathbf{x}-\mathbf{x}_n|_*^2/\eta}\ , \tag{41}$$

with $|\cdot|_*$ being the distance to closest periodic image.

Assume the entire domain $\Omega = [0,\ B_1) \times [0,\ B_2) \times [0,\ B_3)$ is discretized in $M_g^0 \cdot B_1 \times M_g^0 \cdot\ B_2 \times M_g^0 \cdot B_3$, points with $M_g^0 = 1/h$. The only free parameter in (41) is η which controls the shape of the Gaussians $e^{-2\xi^2|\mathbf{x}-\mathbf{x}_n|_*^2/\eta}$. If we consider the width of a Gaussian after truncation to be w then for a set of P discrete points in the support of the Gaussian at a spacing h away from each other we have $w = Ph/2$. If now, as explained in [19], we take the width to correspond to m standard deviations $w = \sigma m$, $\sigma^2 = \eta/4\xi^2$, we obtain that

$$\eta = \left(\frac{Ph\xi}{m}\right)^2$$

It remains then to choose a set of three parameters: M_g^0, which controls the truncation of the sum, P, the number of points in the support of a Gaussian and m, giving the shape of the Gaussian, and by that the level of the Gaussian at the truncation point. In Algorithm 5 we provide only the steps to evaluate the Fourier sums in (33)–(34) using FFTs, for details the reader is referred to [19].

In the truncation error estimate we used $\bar{\mathbf{k}}$ where $\mathbf{k} = 2\pi\bar{\mathbf{k}}$ and

$$\bar{\mathbf{k}} = (k_1/B_1,\ k_2/B_2,\ k_3/B_3)$$

and truncated the sum at $|\bar{k}| = k_\infty$. A uniform Fourier grid with $M_g^0 \cdot B_1 \times M_g^0 \cdot B_2 \times M_g^0 \cdot B_3$ (M_g^0 odd points) yields the wave numbers $k_i = \{-(M_g^0-1)/2, \ldots, 0, \ldots, (M_g^0-1)/2\}$, $i = 1, \ldots, 3$, hence $M_g^0 = 2k_\infty + 1$ and is to be chosen according to the discussion in Section 5.

Algorithm 2 Algorithm for fast computation of Fourier space sum

```
[1] Construct a uniform grid over the domain $\Omega = [0,\ B_1) \times [0,\ B_2) \times [0,\ B_3)$ and evaluate $H$ using (41) for $\eta = (P\xi h/m)^2$. For this a fast Gaussian gridding algorithm [9] is used.
[2] Use a three-dimensional FFT to evaluate $\widehat{H}$.
[3] Compute $\widehat{\widehat{H}}$ using (40).
[4] Use a inverse FFT to retrieve $\widetilde{H}$.
[5] Evaluate (39) using the trapezoidal rule, yielding spectral accuracy due to the periodicity of the integrand. This again yields sums over Gaussians which calls once more for the fast Gaussian gridding algorithm.
```

A simple operation count gives the following complexity of the algorithm, with $M_g^3 = {M_g^0}^3 V$

$$\underbrace{\mathcal{O}(NP^3)}_{Eq.(41)} + \underbrace{\mathcal{O}({M_g}^3 \log {M_g}^3)}_{FFT+IFFT} + \underbrace{\mathcal{O}({M_g}^3)}_{Eq.(40)} + \underbrace{\mathcal{O}(NP^3)}_{Eq.(39)}$$

This algorithm however has to be combined with the real space sum treatment which is $\mathcal{O}(N)$ only under certain conditions. As a consequence by combing the two algorithms as it will be discussed in Section 5 the complexity will ultimately be $\mathcal{O}(N \log N)$.

Parameter choice

The main difficulty in using a fast Ewald method lies in choosing the parameters in such way that both issues of accuracy and efficiency are satisfactorily addressed. Any simulation requires as input data N - the number of fibers, V - the volume of the computational domain, and δ - the desired accuracy. The decomposition parameter, ξ, affects both accuracy and efficiency thus intertwining the two aspects. Let us start by considering the truncation errors. For a certain ξ and a certain tolerance δ we need to find $r_c = r_c(\xi, \delta)$ and $M_g^0 = M_g^0(\xi, \delta)$ at which the tails of the two sums are below the threshold δ, *e.g.*

$$E_R(\xi, r_c) \leq \delta, \quad E_F(\xi, k_\infty) \leq \delta$$

Since the entire FFT grid used in the Fourier space sum scales with M_g^0 it is sufficient to study how the truncation error relates to M_g^0.

Regarding the efficiency let us denote by T the execution time for either the real space sum or the Fourier space one and consider also the dependency on the number of particles N and the volume V. To optimize for efficiency we aim to find ξ that solves the minimization problem

$$\min_{\xi}[T_F(r_c(\xi, \delta), N, V) + T_R(M_g^0(\xi, \delta), N, V)].$$

This minimization problem however depends on a large number of parameters such as N, V, r_c but also on the construction of the neighbor lists, the cost of the analytical integration *etc.* The volume V was also mentioned here as having an impact on the computational complexity however the volume enters the complexity problem only implicitly through the density of fibers which is $\rho = N/V$. If the optimal ξ is known for a given set-up N, V, δ it is

Table 1: Dependency of r_c on ξ for the total kernel, $r_c = f_{r_c}(\xi, \delta) = a(\delta) \cdot \xi^{-b(\delta)}$.

δ	10^{-4}	10^{-6}	10^{-8}	10^{-10}	10^{-12}	10^{-14}
a	3.74	4.305	4.805	5.259	5.679	6.071
b	1.051	1.03	1.019	1.013	1.009	1.007

possible, based on theoretical considerations, to obtain a guideline for the choice of ξ valid for any other configuration. For fiber suspensions however additional hinders are introduced by the construction of neighbor fiber lists. It is therefore advisable to seek empirically the optimal ξ for efficiency by browsing a number of parameters, details in Section 5. As it will be noted the values of optimal ξ are however not so different from the guidelines we obtain through the theoretical analysis on the simple Ewald summation problem for particles.

Accuracy

In the field of molecular dynamics it is possible to derive sharp error estimates in RMS norm which are invertible expressions in terms of ξ, see [20] following [18]. This estimate is however statistical, meaning that it is valid only for randomly distributed data. Not only that a fiber does not fall within this category, being rather a set of particles aligned segment-wise, but the fiber suspensions lead to cluster formations. As a consequence we compute the error in euclidean norm on a per-particle basis and from hereon obtain the truncation errors (36)-(38) for both the Stokeslet and the dipole. Based on these estimates we seek to find the connection between ξ and r_c for a given δ and proceed by sketching contour plots of $E_R(\xi, r_c) \leq \delta$ for a set of $\delta = 10^{-4},\ 10^{-6},\ 10^{-8},\ 10^{-10},\ 10^{-12},\ 10^{-14}$ which are likely to be used in practice, here

$$E_R(\xi, r_c) \quad = \quad E_R^S(\xi, p_\infty) + 2\varepsilon^2 E_R^D(\xi, r_c)\ , \tag{42}$$

$$E_F(\xi, k_\infty) \quad = \quad E_F^S(\xi, k_\infty) + 2\varepsilon^2 E_F^D(\xi, k_\infty)\ , \tag{43}$$

with $E_R^S(\xi, r_c)$ as in (36) and $E_F^S(\xi, k_\infty)$ as in (37); $E_R^D(\xi, r_c)$ as in (37) and $E_F^D(\xi, k_\infty)$ as in (38). For the purpose of our study we settle for a value of the slenderness parameter $\varepsilon = 10^{-2}$ and provide rules for the parameter choice tailored to the entire kernel $\mathbf{G} = \mathbf{S} + 2\varepsilon^2\mathbf{D}$. Nonetheless we supply in Appendix B similar results differentiating between the Stokeslet and the dipole.

From Fig. 3a we notice that the dependency of r_c on ξ follows a power law, $r_c = a\xi^{-b}$. For each δ we perform a curve fitting to find the parameters. The rules for retrieving r_c corresponding to a certain ξ at a fixed δ are available in Table 1.

Table 2: Dependency of M_g^0 on ξ for the total kernel, $M_g^0 = f_M(\xi, \delta) = a(\delta) \cdot \xi + b(\delta)$.

δ	10^{-4}	10^{-6}	10^{-8}	10^{-10}	10^{-12}	10^{-14}
a	2.629	2.987	3.284	3.557	3.81	4.048
b	-0.6498	-0.4762	-0.222	-0.0446	0.0849	0.1848

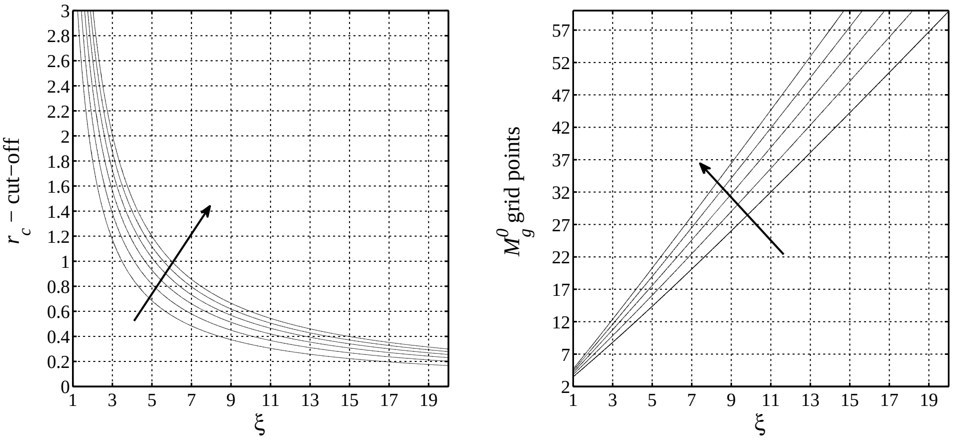

(a) Parameter choice for r_c as a function of ξ according to the estimate (42).

(b) Parameter choice for M_g^0 as a function of ξ according to the estimate (43).

Figure 3: Isolines representing the relation between ξ and M_g^0, ξ and r_c respectively, for various accuracies, in the direction of the arrow $\delta = 10^{-4},\ 10^{-6},\ 10^{-8},\ 10^{-10},\ 10^{-12},\ 10^{-14}$.

The Fourier space sum is to be truncated at k_∞ as suggested by (43). However the computation of the Fourier sum uses $M_g^0 = 2k_\infty + 1$ and for this reason we formulate the relations using M_g^0 instead. We follow the same steps and observe in Fig. 3b that M_g^0 scales almost linearly with ξ, *i.e.* $M_g^0 = a\xi + b$. Once again by curve fitting for each δ we obtain the laws in Table 2. Note that in practice we need to round off the values of M_g^0 given in Table 2 since M_g^0 yields the number of grid points in Fourier space, and should be an integer. The laws obtained here allow us to go back and forth from ξ to r_c and M_g^0 for the kernel $\mathbf{G}$ in the system (29).

The accuracy of the Fourier space sum evaluation depends also on P, the number of discrete points in the support of a Gaussian. Besides the inherent truncation errors the procedure applied here incurs also discretization errors emerging from the numerical integration over the gridded domain, *i.e.* equation (39). This has been discussed in [19], however for the purpose of the current work we recall only the guiding error estimate $4e^{-P^2\pi^2/(2m^2)} + \mathrm{erfc}(m/\sqrt{2})$ for the numerical integration of the Gaussian by the trapezoidal rule. The first term, $4e^{-P^2\pi^2/(2m^2)}$, corresponds to how well the Gaussians are resolved on the grid, while the second term, $\mathrm{erfc}(m/\sqrt{2})$, arises from the fact that the Gaussian is truncated at a level $\mathrm{e}^{-m^2/2}$. It is optimal then to choose the parameters P and m such that the two terms balance. Knowing that the complementary error function is bounded by a Gaussian for positive values of the argument we obtain a relationship between P and m as in [20]. The parameter m can then be chosen as a function of P through the relation $m(P) = C\sqrt{\pi P}$ with a $C = 0.98$ observed in practice. For a precise study regarding the values P should take to achieve a certain accuracy δ we choose a sufficiently large M_g^0 for which the truncation errors are negligible and perform a study of the error decay. This study will be performed on $N_p = 100$ point particles uniformly distributed in the unit cube but for the entire kernel $\mathbf{G} = \mathbf{S} + 2\varepsilon^2\mathbf{D}$. Here we settle for a slenderness parameter of $\varepsilon = 10^{-2}$, which is the one used all throughout the simulations performed in the present work. In Fig. 4 we illustrate the behavior of the error computed in max-norm increasing values of P for a set of $\xi = 2, \ldots, 10$ with $m = 0.98\sqrt{\pi P}$, see Algorithm 5. We notice a small increasing demand on the number of points P for larger values of ξ, but note the expected exponential decay of the error.

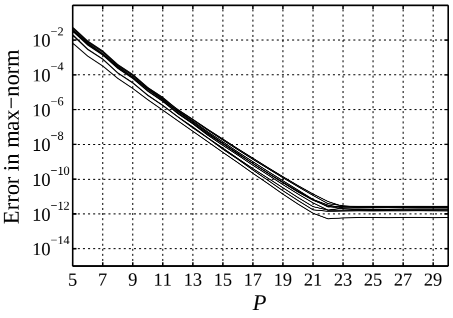

Figure 4: Decay of the error for increasing number of points P in the support of the Gaussian. The number of grid points in the FFT grid is chosen such that $\delta = 10^{-16}$ for a set of increasing $\xi = 2, \dots, 10$.

Efficiency

For efficiency r_c and M_g^0 should be chosen such that the real space sum and the Fourier sum are well balanced and this is controlled through the parameter ξ. Reconsidering the Fourier space sum $(\mathcal{O}(NP^3) + \mathcal{O}({M_g}^3 \log {M_g}^3) + \mathcal{O}({M_g}^3) + \mathcal{O}(NP^3)$, with $M_g^3 = {M_g^0}^3 V)$ we note that the free parameter P is fixed for a certain accuracy δ and $M_g^0(\xi, \delta)$. The Fourier space sum would be essentially $\mathcal{O}(N)$ if the grid size M_g^3 were not connected to the real space sum cut-off r_c through ξ. The real space sum however is only conditionally $\mathcal{O}(N)$, *i.e.* if r_c is chosen such that each particle has an approximately constant number of neighbors as N increases. Since r_c and M_g^0 are intertwined through ξ (and also δ) it leads to the fact that ${M_g}^3$, *i.e.* the total size of the FFT grid, grows approximately proportional with N. This argument can be followed by studying the relationship between r_c, ξ and M_g^0. In essence if the real space sum is $\mathcal{O}(N)$ the Fourier sum is of complexity $\mathcal{O}(N \log N)$ rather than $\mathcal{O}({M_g}^3 \log {M_g}^3)$.

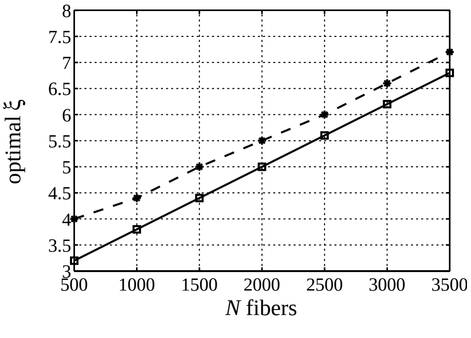

Figure 5: Optimal ξ for a set of N fibers in a constant volume, $V = 36 \times 36 \times 36$: $(*)$ accuracy $\delta = 10^{-4}$, $(\square)$ accuracy $\delta = 10^{-8}$.

Based on the previous error analysis it is straightforward to choose M_g^0 and r_c for a given ξ and δ. To find an optimal ξ which minimizes the computational cost it suffices theoretically to find one ξ^* which optimizes one configuration N_*, Ω_*, δ and based on this compute ξ which optimizes N, Ω, δ. We distinguish two cases depending on whether the density number $\rho = N/V$ grows at constant volume or the density number is constant at increasing volume. Here we study the case of increasing density at constant volume V_*, yielding an increasing number of fibers $N > N_*$.

Example

[1] Assume ξ_* optimal for a simulation of N_* fibers in a volume V_* at an accuracy δ, $\rho_* = N_*/V_*$.

[2] Compute $r_c^0 = f_{r_c}(\xi_*, \delta)$ according to Table 1.

[3] Knowing that the real space sum is $\mathcal{O}(N)$ if $N_c = 4\pi/3\rho_* r_c^3$, is preserved constant compute the new $r_c = \sqrt[3]{\rho_*/\rho}\; r_c^0$, with $\rho = N/V_*$.

[4] Compute a new $\xi = f_{r_c}^{-1}(r_c, \delta)$ again from Table 1.

[5] The FFT grid spacing will then be $M_g^0 = f_M(\xi, \delta)$ from Table 2.

For the new simulation of N fibers in the same volume V_* the optimal parameters are ξ, M_g^0, r_c. A similar example can be worked out for a fixed r_c and a volume growing with N, which would leave the density ρ unchanged.

In our case however $r_c^* = r_c + \bar{L}$ and this is further refined to exclude fibers at a distance larger than r_c. This does not leave us with a tractable formula for N_c as in the previous example. On top of the two Ewald sums we introduced a set of analytical integrations $\mathcal{O}(N)$, and there is also an overhead from the outer numerical integration, also $\mathcal{O}(N)$. These increase the computational cost which leads to a small shift in the values of the optimal ξ that we obtain from the theoretical guideline. To observe this we perform an analysis on a per simulation basis, advocated also by [24], and compare the optimal parameters with the ones from the approach in the example above.

The search for the optimal ξ for a given input data N at a fixed volume V is detailed below

[1] Identify the simulation input data: N number of fibers, $\Omega = [0,\ B_1) \times [0,\ B_2) \times [0,\ B_3)$ the domain, δ desired accuracy.

[2] Choose ξ_0 such that $r_c * < \min(B_1,\ B_2,\ B_3)/3$.

[3] Perform a set of simulation for $\xi = \xi_i$, $i = 1, \ldots, p$, and $\xi_0 < \xi_1 < \ldots \xi_p$.

[4] Find $\xi = \min_i(t(N, \xi_i))$, where $t(N, \xi_i)$ is the computational time for a simulation with N fibers at a ξ_i.

We choose a domain $\Omega = [0,\ B)^3$, $B = 36$, large enough such that a few values of r_c can be browsed. To keep in mind that we operate in practice with $r_c^* = r_c + \bar{L}$ and since one fiber length is $\bar{L} = 2$ we shall have rather large values for the cut-off r_c^*. Other parameters in the simulations are the ones fixed for a certain accuracy $P = 8$ for $\delta = 10^{-4}$, $P = 16$ for $\delta = 10^{-8}$, and $m = 0.98\sqrt{\pi P}$ as advised in Section 5. The forces over the fibers are expanded in Legendre polynomials of up to $R = 5$. For the numerical integration in (35) we perform a 3-point Gaussian integration segment-wise, thus having a sixth order method. In this case we choose 3×6 discretization points.

In Fig. 5 we provide the optimal ξ for a given N corresponding to an accuracy of $\delta = 10^{-4}$, and $\delta = 10^{-8}$ respectively. As a general guideline we provide the corresponding values of r_c and M_g^0 for $\delta = 10^{-4}$. The total number of points in the FFT grid is $(M_g^0 \cdot B)^3$, $B = 36$. In Table 3 we reproduce the parameter values which optimize the computational costs as they are obtained from the simulations, while in Table 4 we present the expected parameter values according to the analysis in the example previously given. It can be noticed that the quantitative difference is small.

Table 3: Scaling for different simulation configurations in a domain $\Omega = [0,\ B)^3$, with $B = 36$ for $\delta = 10^{-4}$.

N - fibers	ξ	r_c	M_g^0
500	4	2.8712	10
1000	4.4	2.7881	11
1500	5	2.6891	12
2000	5.5	2.6234	14
2500	6.0	2.5689	15
3000	6.6	2.5147	17
3500	7.2	2.4697	18

Table 4: Expected scaling according to the theory in a domain $\Omega = [0,\ B)^3$, with $B = 36$ for $\delta = 10^{-4}$.

N - fibers	ξ	r_c	M_g^0
500	4	2.8712	10
1000	4.9835	2.6915	12
1500	5.6674	2.6040	14
2000	6.2088	2.5488	16
2500	6.6641	2.5095	17
3000	7.0609	2.4794	18
3500	7.4146	2.4554	19

6 Numerical results

Two main aspects were stressed all throughout the analysis of the Spectral Ewald method as applied to a suspension of fibers, namely accuracy and computational complexity. In Section 5 we have established a straightforward way of choosing the parameters to satisfy the accuracy requirement and further on in Section 5 we determined how to choose ξ for efficiency. To solve the system (35) stated in matrix-vector form we use the fast summation method in conjunction with an iterative method, here we consider GMRES to be the method of choice.

In the fiber simulation there will be errors introduced also by the expansion of the forces in R Legendre polynomials, as well as discretization errors from numerical quadrature. In this section we want to evaluate the performance of the Spectral Ewald method. Therefore we keep the discretized system fixed and as a reference solution consider one computed with very strict error tolerances in the the Ewald method. We first consider a system of $N = 100$ fibers in $\Omega = [0,\ B)^3$, $B = 15$ discretized as in (35) with $R = 5$ and $3 \times N_q$, $N_q = 16$ discrete points on each fiber. The system (35) is solved to compute force coefficients $\mathbf{a}_l^q$, $q = 1, \ldots, R$ and hence the forces $\mathbf{f}_l(s)$, $l = 1, \ldots, N$. Given these forces the left hand side of (35) is computed with parameters in the Ewald method adjusted to different accuracy requirements. Since the real space sum treatment is partially analytical and partially numerical we cannot track the error decay by choosing a fix ξ and browsing r_c. We can however choose a fix r_c and control the decay in error of the real space sum by changing ξ, and from here on M_g^0. For this purpose we have chosen a smaller volume for our simulation since the number of points in the FFT grid will grow more with ξ as we increase the accuracy. The cut-off radius r_c is maintained at a fixed value while ξ and M_g^0 are changed according to Table 1-2. The accuracy results in max-norm for a set of parameters corresponding to various $\delta = 10^{-4},\ 10^{-6},\ 10^{-8},\ 10^{-10},\ 10^{-12}$ starting from $r_c^* = r_c + \bar{L} = 5$ are reproduced, together with the exact parameters that have been used, in Table 5.

Table 5: Error of the method for various parameter choices. The cut-off radius is fixed at $r_c^* = 5$. The computational domain is $\Omega = [0,\ B)^3$ with $B = 15$.

Tolerance δ	ξ	$M_g^0 \cdot B$	P	Obtained accuracy
10^{-4}	1.2334	45	8	3.0505×10^{-5}
10^{-6}	1.4200	60	12	2.2963×10^{-7}
10^{-8}	1.5877	75	16	3.5234×10^{-9}
10^{-10}	1.7404	90	19	1.1021×10^{-11}
10^{-12}	1.8823	105	23	3.0069×10^{-13}

We expect the computational complexity to scale as $\mathcal{O}(N \log N)$. To check this we analyze the same set of runs as for the efficiency tests presented in Fig. 5. Assume now that the computational time $t(N)$ is a function $t(N) = \beta N \log(N)$. We plot in Fig. 6 the quantity $t(N)/\log(N)$ and note that indeed there is a linear dependence on N as expected. We note a difference in slope between the two simulation sets. This could be foreseen since the two sets of runs are performed for two different accuracies. For each accuracy we have used a different number of points P in the support of the Gaussians in the Fourier space sum. Reverting back to the operations count for the Fourier space sum we note that there is a constant P^3 in the $\mathcal{O}(N)$ term which is partly the reason for the difference in slope visible in Fig. 6.

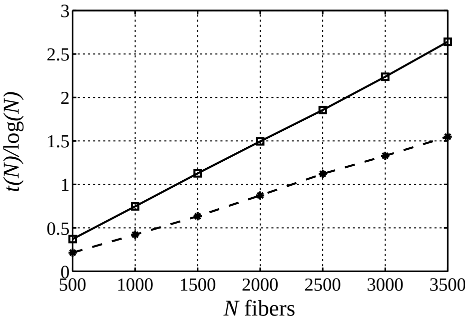

Figure 6: Complexity of the algorithm represented as $t(N)/\log(N)$ versus N for an optimal ξ: $(*)$ accuracy $\delta = 10^{-4}$, $(\Box)$ accuracy $\delta = 10^{-8}$.

The error analysis has been performed on a per particle basis . Thus it is necessary to assess how summing up a large number of fibers influences the error. To this end we consider a set of fibers $N = 500, \ldots, 3500$ in a domain $\Omega = [0,\ B)^3$, $B = 36$ for fixed parameters $r_c = 3$ and a fiber discretization in $3 \times N_q$, $N_q = 6$ points. To assess the errors as they would arise from a distribution of fibers, which has a different homogeneity properties than a distribution of particles, we used a pre-computed solution of the system (35) as the initial data for the Ewald summation. The other parameters ξ and M_g^0 are adjusted according to the imposed accuracy $\delta = 10^{-4}$, $\delta = 10^{-8}$ respectively. The error, computed in max-norm using a reference solution of $\delta = 10^{-12}$, is illustrated in Fig. 7. The computational error lies below the threshold imposed by δ however an apparent increase as N grows can be noticed.

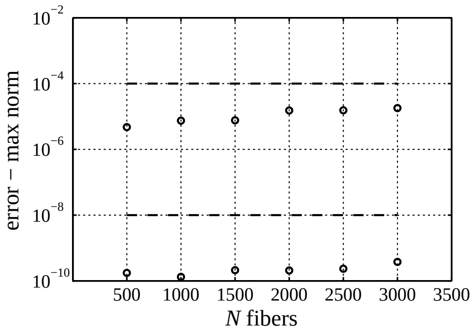

Figure 7: Accuracy for increasing number of N fibers at an imposed accuracy of 10^{-4}, and 10^{-8} respectively.

7 Fiber simulations

Background

Numerical simulations of fiber suspensions in periodic domains have been studied previously, see *e.g.* [4, 23, 25, 12], the review article by Guazzelli and Hinch [11], and references therein. Many characteristic features of a sedimenting fiber suspension, such as the formation of coherent regions known as flocs and streamers, and the preferential alignment of fibers in the direction of gravity can be accurately captured using numerical simulations, as careful comparisons with existing experimental data certify [14, 21].

Whereas in a laboratory the physical domain is always bounded, in simulations one has the possibility to choose periodic boundary conditions as a means to consider an *infinite* suspension, hence to eliminate wall effects. Nonetheless periodic boundary conditions may have a non-negligible influence on the sedimentation process, and certain quantities and phenomena show a dependency on the chosen size of the simulation domain. In particular the sedimentation velocity turns out to be sensitive as discussed by Butler *et al.* [4]. Similar observations were made by Saintillan *et al.* [23] who performed a set of numerical simulations with up to 512 fibers at a volume fraction of $nl^3 = 0.05$ using the SPME method. Further numerical experiments by Gustavsson and Tornberg [12] also noted the influence of the domain width/height in simulations of up to $N = 800$ fibers.

In this section we present results from numerical simulations of fiber suspensions in a periodic setting performed using the Spectral Ewald method. Compared to previous simulations, the present implementation of the Spectral Ewald method has made it possible to perform simulations in larger periodic domains with substantially more fibers than previously feasible. It is thus the aim of the present study to examine the capabilities of the newly developed numerical method and to supplement the aforementioned results by studying larger periodic domains and more fibers. The results we report here are for systems with up to $N = 3840$ fibers in domains that have either a square or a rectangular cross section. A summary of the various simulation cases is given in Table 6. All simulations are performed in a dilute regime at a volume fraction of fibers of $nl^3 = 0.05$. The non-dimensional fiber length is $\bar{L} = 2$. The algebraic solver used in this case was GMRES, which lead to convergence rates of $10 - 30$ iterations in each timestep. The parameters chosen for the fiber discretization and time-step are according to the accuracy tests in [25]. The parameters in the Ewald summation are chosen according to the discussion in Section 5. All simulations

Table 6: Summary of performed simulations. The numerical parameters are chosen to correspond to an error tolerance, $\delta = 10^{-4}$, according to the discussion in Section 5 as $\xi = 6.5194$, $r_c* = 2.5124$ and $M_g^0 = 16$, and timestep $\Delta_t = 0.1$.

Case	Size of periodic cell	Number of fibers	nl^3
1	$24 \times 24 \times 40$	1152	0.05
2	$24 \times 24 \times 80$	2304	0.05
3	$24 \times 24 \times 120$	3456	0.05
4	$80 \times 8 \times 40$	1280	0.05
5	$80 \times 8 \times 80$	2560	0.05
6	$80 \times 8 \times 120$	3840	0.05

start from a random configuration of fibers, and the dynamics of the system is recorded up to at least time $t = 300$ for all cases.

Averaged quantities

Statistical quantities such as the mean sedimentation velocity and mean square orientation, where averages are taken over all fibers, are often used to describe key characteristics of a sedimenting suspension. Previous numerical simulations, *e.g.* [4, 23, 12], showed that the sedimentation velocity is in general not affected by the height of the domain for a constant concentration as long as the dimensions of the domain in the horizontal directions are kept fixed. In Fig. 8 we present and compare the mean sedimentation velocity for all six runs listed in Table 6. The sedimentation velocity displays the same qualitative behavior in all cases, *i.e.* both for a domain with a square cross section, Fig. 8a, and for a domain with a rectangular cross section, Fig. 8b. In the latter cases, for a domain of height H larger than 80, a region of nearly constant sedimentation velocity is apparent between $t = 60$ and 80, which does not appear in the other cases. Inspection of the instantaneous fields shows that this feature is due to the building up of strong vertical streamers and the disappearance of swirling motion in the spatially extended domain. This will be discussed further below in Section 7, where we also see that although the sedimentation rate is qualitatively similar for all cases the structure of the sedimenting fiber suspension is different depending on the cross section of the domain.

As noted in Saintillan *et al.* [23] reaching a steady state of the average sedimentation velocity is not achievable in a comparable period of time as the number of fibers in the system increases; in the present cases the velocity continues to increase throughout the duration of the simulation. The transient state of the orientation dynamics is however shorter, as shown in Fig. 9 by means of the fluctuations of the fiber orientations. For the case of a square cross section, the statistical steady state is reached at approximately $t = 150$, see Fig. 9a, while for rectangular cross section domains the transient state ends at approximately $t = 200$, see Fig. 9b.

There is a correlation between the instance when the streamers form and the onset of the steady state of the orientation dynamics. At a first stage clusters form starting from a random distribution of fibers. These clusters accumulate and coalesce to form streamers. Eventually, the streamers extend through the entire height of the periodic domain and have a sedimentation velocity higher than that of isolated fibers. The streamer velocity then increases further as the densification process continues. Within a streamer fibers have less freedom to flip due to the fact that they are constrained by other fibers that occupy

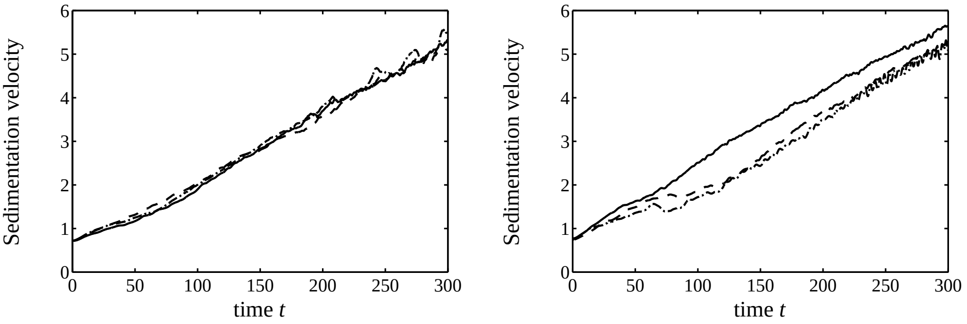

(a) Runs 1-3, square cross section. (b) Runs 4-6, rectangular cross section.

Figure 8: Comparison of the average fiber sedimentation velocity in absolute value as a function of time for simulations in domains with different cross sections and different heights, $H = 40$ (solid), $H = 80$ (dashed) and $H = 120$ (dashed-dotted line).

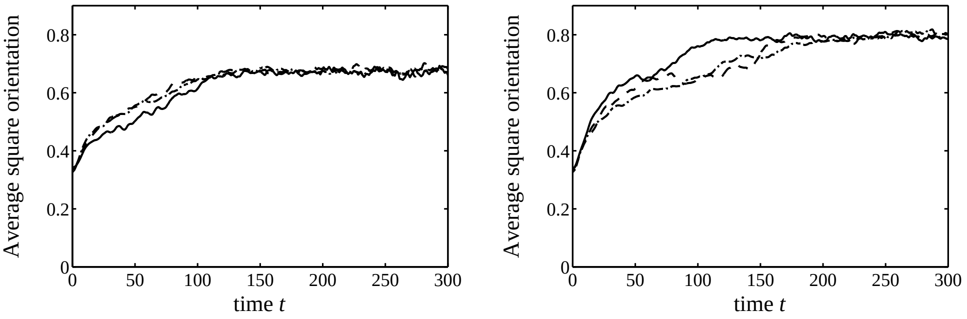

(a) Runs 1-3, square cross section. (b) Runs 4-6, rectangular cross section.

Figure 9: Comparison of the average square orientation of fibers as a function of time for simulations in domains with different cross sections and different heights, H. $H = 40$ (solid), $H = 80$ (dashed) and $H = 120$ (dashed-dotted line).

the surrounding space. Thus a steady orientation distribution can be reached before the densification process is completed. According to [23] the time at which the sedimentation velocity reaches a plateau is also a function of the periodic cell aspect ratio.

The above argumentation is supported also by an analysis of the preferred fiber orientations. Therefore, we now discuss probability density functions (pdfs) of the angles between the fiber long-axis and the horizontal plane obtained from our simulations. The obvious definition of such an angle is to take the inner product between the orientation unit vector $\mathbf{t}$ and the vertical z-direction, $\sin\theta = (t_x, t_y, t_z) \cdot (0,0,1) = t_z$, $\theta \in [-\pi/2, \pi/2]$. However, in experiments it turns out that the determination of θ is prone to considerable numerical inaccuracies caused by the measurement technique (see *e.g.* the discussion by Herzhaft and Guazelli [14]). Therefore, another measure has been proposed and used, namely the angle ϕ between the horizontal plane and the two-dimensional projected image of a fiber on a fixed vertical plane, formally $\tan\phi = t_z/t_x$. In the following, both ϕ and θ are shown for three different cases using our numerical method. Note that our definition of θ is such that $\theta = 0$ corresponds to a fiber with a horizontal alignment, whereas Herzhaft and Guazelli

[14] define θ with respect to the vertical direction (*i.e.* $\cos\theta = t_z$).

In the following we plot estimates for the probability density function pdf for both $|\theta|$ and $|\phi|$. For this purpose, a histogram using 80 equidistant bins has been computed for all fibers, which is then scaled to unit area,

$$\int_0^{\pi/2} \mathrm{pdf}(|\phi|)\,\mathrm{d}\,\phi \;=1 \quad \text{and} \quad \int_0^{\pi/2} \mathrm{pdf}(|\theta|)\,\mathrm{d}\,\theta \;=1.$$

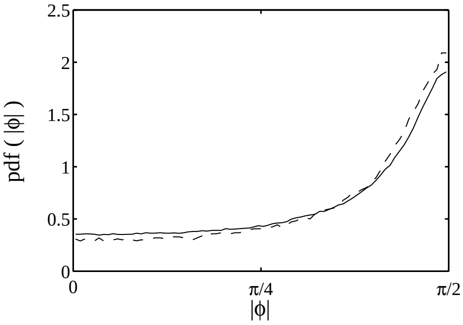

Figure 10: Probability density function (pdf) of the projected angle ϕ for square cross section. (solid) our data for the statistically stationary state (averaged $t = 300-380$), (dashed) SPME data by Saintillan *et al.* [23].

To validate our results with literature data, we present in Fig. 10 a comparison of the pdf for ϕ with the SPME simulations by Saintillan *et al.* [23]. To this end, we simulated the case with square horizontal cross cut, in a domain $10\times10\times80$ with matched fiber density. After reaching the steady state, we obtain very good agreement with [23], both in terms of the qualitative shape and the quantitative behavior for all angles. We can therefore conclude that our method captures the relevant aspects of the fiber dynamics.

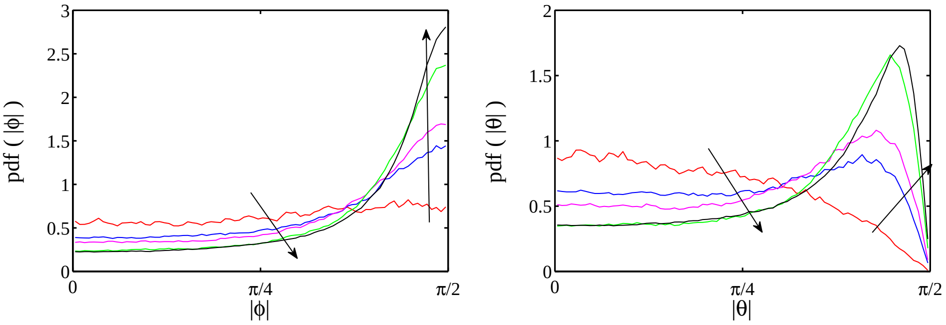

Figure 11: Probability density function (pdf) of the projected angles ϕ and θ for square cross section of size $24\times24\times120$. Averaging time in direction of arrow: $t = 0-10$, $20-50$, $50-80$, $120-150$, $300-380$.

Still in a square cross cut domain, but with considerably larger horizontal domain extent of size 24×24 and height $H = 120$ we show the transient behavior of the pdfs in Fig. 11. The final distribution corresponds to the statistically stationary state, and is averaged from

$t = 300-380$. At time $t = 0$, the fibers are initialized with random position and orientation. Therefore, the angle ϕ averaged up to $t = 10$ features a nearly uniform distribution with approximate value $2/\pi$. However, the angle θ for the same average closely follows the distribution $\cos|\theta|$ due to the spherical coordinates. For later times, both angles show a considerable increase of the probability close to $\pi/2$. As opposed to the experiments by Herzhaft and Guazelli [14] in our data the maximum is reached exactly at $\phi = \pi/2$. Furthermore, their secondary (flat) maximum near zero is not reproduced in our data. For this particular configuration, the probability for $\phi = \pi/2$ is increased by a factor of 4.4 compared to the uniform distribution. The angle θ in principle shows the same behavior for increasing time; the maximum however is not located at $\pi/2$ but rather at $\theta \approx 1.44$.

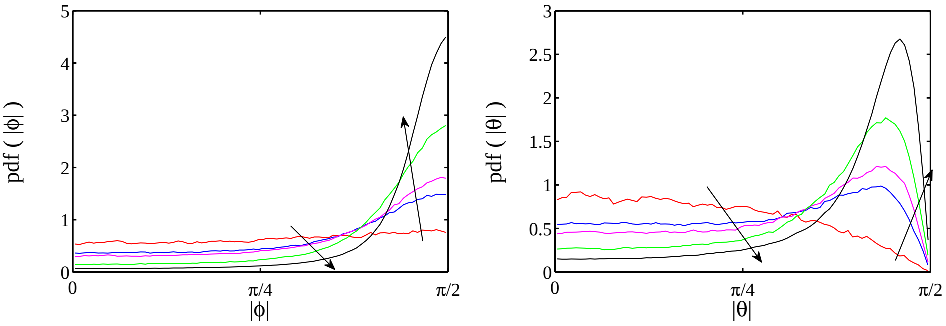

Figure 12: Probability density function (pdf) of the projected angles ϕ and θ for rectangular layout of size $80 \times 8 \times 120$. Averaging time in direction of arrow: $t = 0-10$, $20-50$, $50-80$, $120-150$, $300-420$.

The rectangular cross section shows the same qualitative behavior as the square cross section as documented in Fig. 12; starting with a uniform distribution of the angles ϕ, the peak values at $\pi/2$ is increased gradually. In the stationary state, a 7-fold increase compared to the uniform distribution is reached which is nearly twice than for the square cross section (Fig. 11) with the same fiber density. In particular, the probabilities for lower angles are very low indicating that almost all fibers are oriented towards the vertical settling direction. This behavior can be explained by the increased migration of the fibers into the streamers. The pdf of θ is very similar to the square cross-cut case, but also shows an 1.5-fold increase of the peak value at $\theta \approx 1.44$.

Dynamics and fiber density

One of the most interesting phenomena pertaining to sedimenting fiber suspensions is the formation of vertical streamers. Most computational studies using periodic boundary conditions note the formation of only one streamer, [4, 23, 12], while as in experiments, see *e.g.* Metzger *et al.* [21], the presence of more than one vertical streamer is reported.

In an attempt to observe more than one streamer with periodic boundary conditions, Saintillan *et al.* [23] considered a sedimenting suspension in a domain with rectangular cross section of dimensions $80 \times 8 \times 16$ (stated in terms of our non-dimensionalization). A number of simulations was performed using different random initial distributions. The authors observed one, two and in rare cases even three streamers, all of them separated by wide regions of clear fluid. They conclude that there is a strong dependence of the initial streamer formation on the initial fiber distribution. Since their domain is comparably short in the direction of gravity, the fibers appear to be trapped in the strong shear between the streamers and the void regions set up early in the time evolution. Recent stability analysis performed by Zhang [27] following a study on spheroidal particles [5], shows however that in the stationary Stokes flow regime there cannot be more than one sustained streamer, at least when an infinite flow domain is considered.

Using the same cross section and fiber density as in Saintillan *et al.* [23] but with a considerably longer domain in the direction of gravity, the behavior of the suspension was observed to change, and no more than one large streamer was seen to develop for any of the runs 4–6. In Figs. 13a to 13c we show the fiber configuration at different time instances for the longest domain, $H = 120$. During the transient regime, *i.e.* before a clear streamer develops, the fibers move in a rather chaotic manner. Regions of fibers with high downward velocity are randomly interspersed with regions of lower velocity and regions of upward moving fibers, see Fig. 13a. After the initial transient up to the final instances of the simulations, see Figs. 13b–13c, one wide, dense streamer with enclosed smaller clusters is located in the middle of the domain. On both sides of the streamer regions with lower fiber density are observed to move in the opposite direction. At $t = 100$, see Fig. 13b, large-scale swirling motions are still visible which by $t = 300$ have decayed significantly, see Fig. 13c.

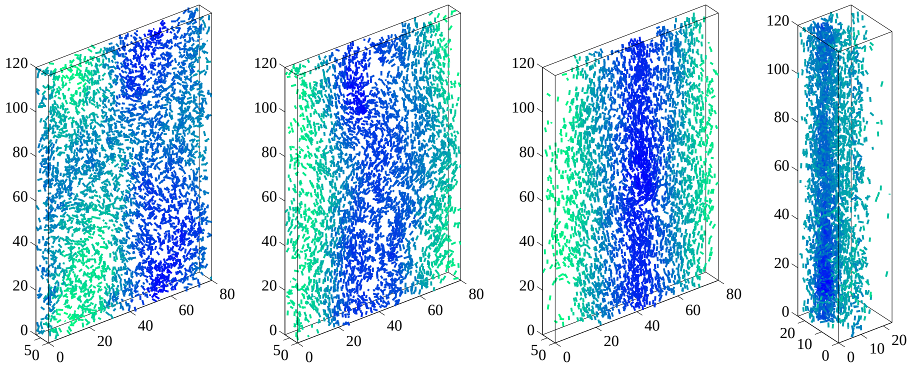

(a) Run 6, $t = 10$ (b) Run 6, $t = 100$ (c) Run 6, $t = 300$ (d) Run 3, $t = 300$

Figure 13: Fiber configuration at different time instances during the sedimentation process. Fibers with blue-dark green colors are moving downwards, and with light green colors upwards. Note the difference in suspension structure at time $t = 300$ using different cross sections (runs 3 and 6).

Comparing the final configuration of the large-scale structure of the streamer between the two cross sections, Figs. 13c and 13d, we note in the latter case the presence of one very distinct, circular and dense streamer and a surrounding region with clear fluid with only some fibers moving upwards; approximately 93% of all fibers are found inside the streamer with a downward velocity. In the case of the rectangular cross section the streamer is not circular, and its boundaries are less sharp. The region outside the streamer has a significant amount of upwards-moving fibers (about 33% of all fibers).

This difference is further highlighted in Figs. 14 and 15 which show the vertically averaged fiber density in the two configurations. The density is computed by a standard binning procedure with bin size 0.5×0.5. We distinguish three different situations: i) the initial fiber configuration (averaged between $t = 0 - 10$), the transient phase ($t = 50 - 80$) and the stationary state ($t > 300$). In both cross sections the density in the core region of the streamer is continuing to increase as time progresses. When the stationary state is reached, the maximum density of the streamer is substantially higher in the case with square cross section (reaching up to a value of 0.8) as opposed to the ones with rectangular cross section (reaching 0.18). In both cases, the core region has a diameter of about 10 units; for run 3 (square cross section) a circular shape is obtained whereas for run 6 (rectangular cross section) a two-dimensional shape is reached. To what extent the diameter and shape of the streamer depends on the box dimensions will be the subject of further studies. Note that high density circular streamers have also been observed in domains with square cross sections of smaller size than used here. In [12], a periodic domain with a square size 8×8 lead to a qualitatively similar density distribution as illustrated in Fig. 15. Hence, an interesting question is whether the size of the streamer core region scales with the domain size, or whether a finite diameter will be reached at some point. The results here would indicate that a diameter of around 10 could be expected.

For the rectangular cross sections, comparing with the results by Saintillian *et al.* [23] there is a notable difference in the way fibers fill out the entire periodic domain, even though the fiber density is the same. Whereas these authors observe distinct regions of essentially clear fluid, in our case the fibers are localizing in the streamers, but no extended regions without fibers appear as illustrated in Fig. 14. In the case of square cross section (Fig. 15) essentially all fibers are trapped in the streamer (93% of all fibers as mentioned above).

To study the micro-structure of the suspension we show in Fig. 16 a number of fiber trajectories in an xz projection pertaining to the stationary state ($t = 300 - 310$). In the case of the square cross section we only included trajectories inside the region $y = 18 - 22$ due to the circular shape of the streamer; for the rectangular case y is a homogeneous direction and thus the whole span could be included. For both cross sections we observe a dense core with strong negative vertical velocity in the streamer of approximately the same diameter, however as discussed above much denser in the case of square cross section. The fiber trajectories are very straight in the center region for both cases. Similarly, the region opposite of the streamer (*i.e.* half the domain width shifted due to the periodic boundary conditions) is also dominated by straight, upward-directed trajectories. These are however only visible in sufficient numbers for the case of the rectangular domain (Fig. 16a) where a third of the particles is not located in the streamer. The interface between these two regions is dominated by fiber trajectories that are curling up with a much smaller length scale than the height of the domain. Such a motion can be seen in both cases (*i.e.* rectangular and square cross section), however the structure is different. It is expected that the magnitude of the shear and the overall geometry (2D or circular) is relevant in determining the exact behavior of this region. Further studies, in particular in terms of understanding the exact fiber dynamics (*e.g.* tumbling motion), but also in terms of analytical models of the interface region, are clearly necessary to fully understand this phenomenon.

8 Conclusions

A detailed description and discussion has been provided for a new efficient method designed to simulate large fiber suspensions in periodic domains. The fibers are immersed in a Stokesian fluid and are assumed to be rigid and slender, *i.e.* with a large aspect ratio. The mathematical model that describes the fiber-fiber interaction is based on a boundary integral formulation which uses the slender body theory and has been reformulated and discretized in a manner that yields good conditioning properties of the discrete system [25].

Periodicity has been introduced through an Ewald summation method, decomposing

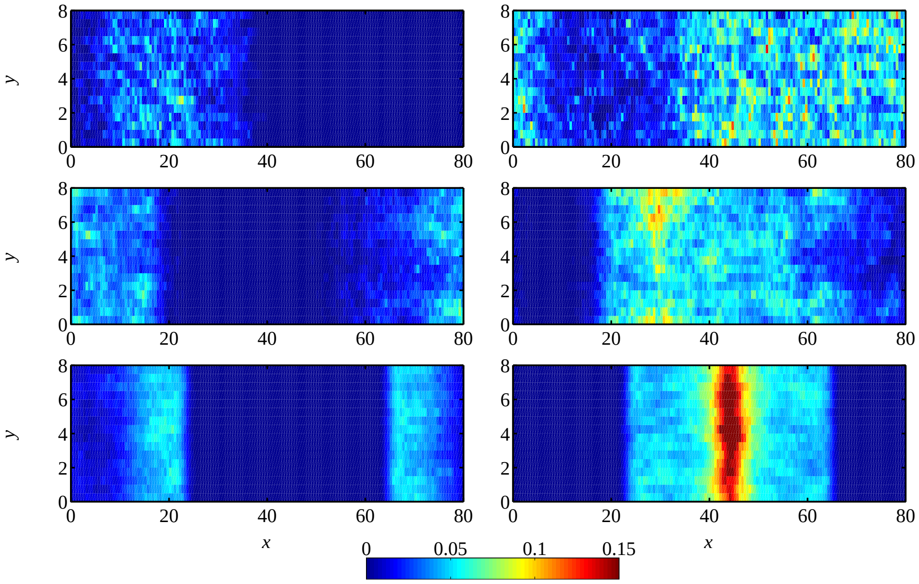

Figure 14: Fiber density in a xy view averaged over the z-direction and over different time spans, 0–10, 50–80, 300–420. Left: Density of fibers moving in the direction opposite to gravity. Right: Density of fibers moving in the direction of gravity. Domain with rectangular cross section and height $H = 120$, run 6.

the periodic Green's function into two sums, one treated in real space and one computed in Fourier space. The two sums converge at a rate controlled by the decomposition parameter ξ and can thus be truncated at cut-offs which are interconnected through the decomposition parameter and determined by accuracy requirements. The decomposition we used for the Stokeslet is due to Hasimoto [13] and had to be derived here for the dipole which is also present in the current fiber suspension model.

The computations in Fourier space were accelerated by a FFT based method, the Spectral Ewald (SE) method [19], now extended also to the dipole. By the use of suitably scaled Gaussians, approximation errors decay exponentially and are controlled independent of the size of the FFT grid. The FFT grid in the SE method can hence be chosen as the minimal grid considering only at which mode the Fourier sum should be truncated. This lowers the memory requirements as compared to other established methods such as the Smooth Particle Mesh Ewald (SPME) method, and allows for the simulation of larger systems.

The real space treatment is based on a Linked Cell List, and is modified to allow for analytical integration for better accuracy as fibers get close to each other. The real space treatment is $O(N)$ as the system scales up, if the average number of fibers within the interaction list of each fiber is preserved constant as N grows. This is accomplished by adjusting the decomposition parameter ξ as needed, thereby intertwining the costs of the two sums, yielding an algorithm of a total complexity of $\mathcal{O}(N \log N)$, where N is the number of fibers.

A difficult issue in using a fast Ewald summation method is the choice of parameters such that both efficiency and accuracy issues are optimally addressed. Using the error estimates in [19] supplemented by our own error estimates for the dipole we propose a straightforward method of choosing the parameters for the method to satisfy accuracy requirements, given

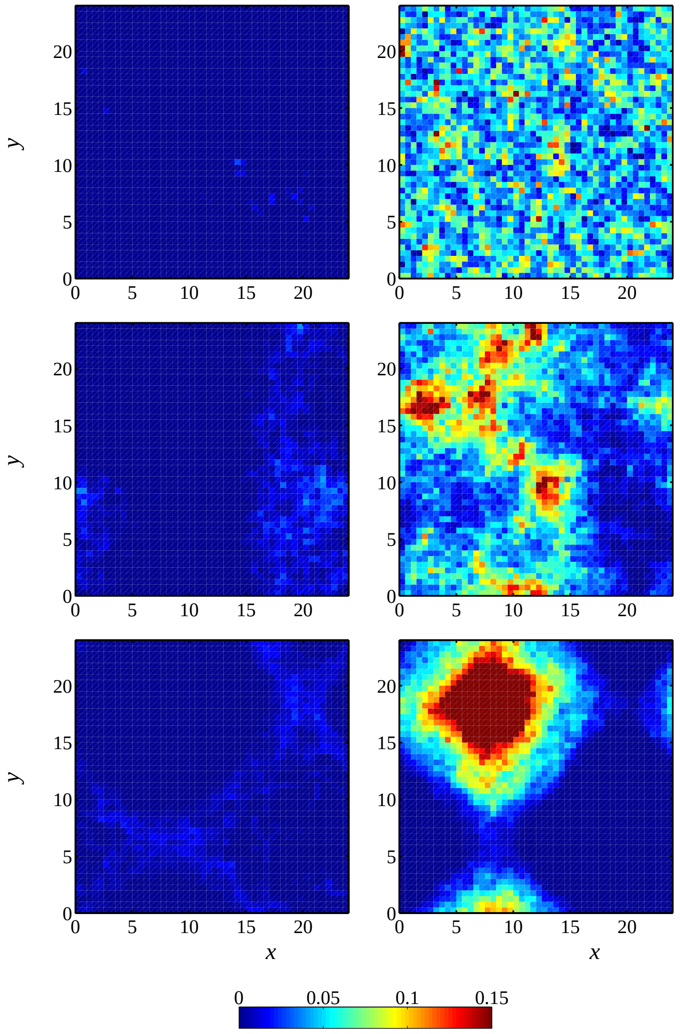

Figure 15: Fiber density in a xy view averaged over the z-direction and over different time spans, 0–10, 50–80, 300–380. Left: Density of fibers moving in the direction opposite to gravity. Right: Density of fibers moving in the direction of gravity. Domain with square cross section and height $H = 120$, run 3.

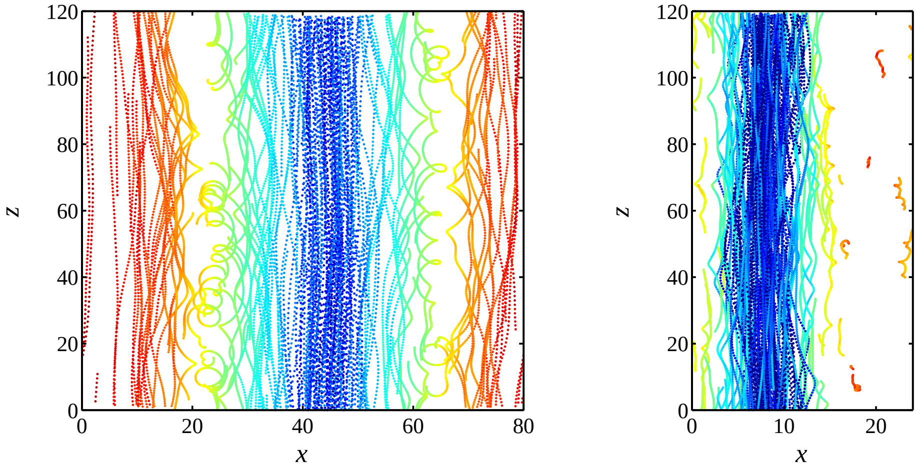

(a) Rectangular cross section, run 6.

(b) Square cross section, run 3.

Figure 16: Fiber trajectories in a xz-view for 100 arbitrary fibers during time interval $t = 300 - 310$. For (a) the full y-extent is shown, whereas for (b) only $y = 18 - 22$ is included. The color indicates the vertical fiber velocity, ranging from negative (blue) to positive (red).

the decomposition parameter ξ. The choice of ξ affects the efficiency and is discussed based on numerical results. We provide numerical results that confirm the expected accuracy and computational complexity.

To validate the method we perform a number of simulations of a sedimenting fiber suspension. Taking advantage of the fact that the newly developed method has made it possible to use larger periodic domains and a substantially larger amount of fibers than previously simulated, we performed a set of simulations comparable to those in [23, 12] in terms of aspect ratio, but within larger periodic domains. The effective concentration of fibers was fixed to $nl^3 = 0.05$ and the number of fibers range from 1152 up to 3840.

Comparisons of our results to previous simulations show that we reproduce correctly characteristic features of a sedimenting suspension, like cluster and streamer formation, enhanced sedimentation velocity and alignment of the fibers in the direction of gravity. Furthermore results from periodic domains of square cross sections are in agreement with previously reported findings. Domains with a rectangular cross section display different structures of the fiber suspension with streamers that do not localize in a circular fashion. There are no regions of clear fluid separating the streamer from the upward moving fibers and the fibers are distributed in the entire periodic domain during the simulation. At a micro-scale there are small recirculation zones in the suspension where fibers undergo a swirling motion.

The simulations performed here were meant to show that the method developed can be used for large scale simulations. At the same time we aimed to make way for new insights in the behavior of fiber suspensions as larger and larger domains can be simulated. As a next step a systematic study involving many simulations for different configurations and fiber densities will be performed with a parallelized implementation of the method presented in this paper.

Appendix A Truncation error for the dipole

We seek bounds on both terms Γ_D and Φ_D and besides the triangle inequality we use

$$\operatorname{erfc}(x) \leq e^{-x^2},\ x \geq 0 \ .$$

Now for the real space sum we start by estimating

$$\begin{aligned} ||\Gamma_D(\xi,\mathbf{x})\mathbf{f}||_2 &\leq |C(\xi r)|\frac{1}{r^3}||\mathbf{f}||_2 + |D(\xi r)|\frac{3r^2}{r^5}||\mathbf{f}||_2 \\ &\leq \frac{4\operatorname{erfc}(\xi r)}{r^3}||\mathbf{f}||_2 + \left|\frac{2}{\sqrt{\pi}}(4\xi^5r^5 + 6\xi^3r^3 + 4\xi r)\right|\frac{\mathrm{e}^{-\xi^2r^2}}{r^3}||\mathbf{f}||_2 \\ &\leq \left(4 + \frac{2}{\sqrt{\pi}}(4\xi^5r^5 + 6\xi^3r^3 + 4\xi r)\right)\frac{\mathrm{e}^{-\xi^2r^2}}{r^3}||\mathbf{f}||_2 \end{aligned} \tag{A.1}$$

need We proceed to bound the sum over all periodic boxes

$$\sum_{|\mathbf{x}+\mathbf{p}|\geq r_c} ||\Gamma_D(\xi,\mathbf{x}+\mathbf{p})\mathbf{f}||_2 \leq E_R^D(\xi,r_c)||\mathbf{f}||_2 \tag{A.2}$$

Given that from (A.1) we notice that Γ_D decays in a radially symmetric fashion we can proceed by restating the sum above as an integral in the radial direction. To avoid unnecessary cluttering of the text we drop the term $||\mathbf{f}||_2$ in the remaining of error estimate analysis to recover it once we are ready to state the final result. We then have

$$\begin{aligned} E_R^D(\xi,r_c) &\leq \int_{r_c}^{\infty} 4\pi r^2\left(4 + \frac{2}{\sqrt{\pi}}(4\xi^5r^5 + 6\xi^3r^3 + 4\xi r)\right)\frac{\mathrm{e}^{-\xi^2r^2}}{r^3}\mathrm{d}r \\ &\leq 4\pi\Gamma(0,\xi^2r^2)\Big|_{r_c}^{\infty} + 8\sqrt{\pi}\int_{r_c}^{\infty}(4\xi^5r^5 + 6\xi^3r^3 + 4\xi r)\frac{\mathrm{e}^{-\xi^2r^2}}{r}\mathrm{d}r \end{aligned} \tag{A.3}$$

Using here

$$\int_{r_c}^{\infty} r^2\mathrm{e}^{-ar^2}\mathrm{d}r = \frac{1}{2}\left(\frac{r}{a}\mathrm{e}^{-ar^2} - \frac{\sqrt{\pi}\operatorname{erfc}(\sqrt{a}r)}{2a\sqrt{a}}\right)\Big|_{r_c}^{\infty} \leq \left(\frac{\sqrt{\pi}}{4a\sqrt{a}} + \frac{r_c}{2a}\right)\mathrm{e}^{-ar_c^2} \tag{A.4}$$

and

$$\int_{r_c}^{\infty} r^4\mathrm{e}^{-ar^2}\mathrm{d}r = -\left(\frac{3r}{4a^2} + \frac{r^3}{2a}\right)\mathrm{e}^{-ar^2}\Big|_{r_c}^{\infty} + \frac{3\sqrt{\pi}\operatorname{erf} r\sqrt{a}}{8\sqrt{a}^5}\Big|_{r_c}^{\infty} \leq \left(\frac{3r_c}{4a^2} + \frac{r_c^3}{2a} + \frac{3\sqrt{\pi}}{8\sqrt{a}^5}\right)\mathrm{e}^{-ar_c^2} \tag{A.5}$$

Let us now take each integral term in (A.3) individually and using (A.4) and (A.5)

$$\left|32\sqrt{\pi}\xi^5\int_{r_c}^{\infty} r^4\mathrm{e}^{-\xi^2r^2}\mathrm{d}r\right| \leq (24\sqrt{\pi}r_c\xi + 16\sqrt{\pi}r_c^3\xi^3 + 12\pi)\mathrm{e}^{-\xi^2r_c^2} \tag{A.6}$$

The next integral term

$$\left|48\sqrt{\pi}\xi^3\int_{r_c}^{\infty} r^2\mathrm{e}^{-\xi^2r^2}\mathrm{d}r\right| \leq 48\sqrt{\pi}\xi^3\left(\frac{\sqrt{\pi}}{4\xi^3} - \frac{r_c}{2\xi^2}\right)\mathrm{e}^{-\xi^2r_c^2} \leq (12\pi + 24\sqrt{\pi}\xi r_c)\mathrm{e}^{-\xi^2r_c^2}$$

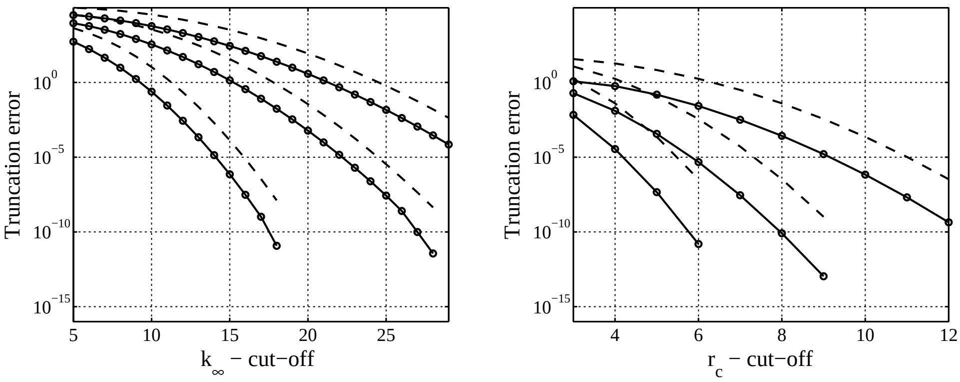

(a) Truncation error for the Fourier space vs. number of layers for $\xi = 10, 15, 20$

(b) Truncation error for the real space vs. number of layers for $\xi = 0.4, 0.6, 0.8$

Figure A.1: Truncation error estimates for $N = 1$: (–) error estimate; (-o-) computed sum.

And lastly

$$\left| 8\sqrt{\pi} \int_{r_c}^{\infty} 4\xi r \frac{\mathrm{e}^{-\xi^2 r^2}}{r} \mathrm{d}r \right| \quad \leq \quad 16\pi\,\mathrm{erfc}(\xi r) \leq 16\pi \mathrm{e}^{-\xi^2 r_c^2} \tag{A.7}$$

Summing up now the terms (A.6)–(A.7)

$$E_R^D(\xi, r_c) \quad \leq \quad (16\sqrt{\pi} r_c^3 \xi^3 + 48\sqrt{\pi} r_c \xi + 40\pi)\mathrm{e}^{-\xi^2 r_c^2} \tag{A.8}$$

For the Fourier space sum consider first the change of variables $\mathbf{k} = 2\pi\bar{\mathbf{k}}$ and $\bar{\mathbf{k}} = (k_1/B_1,\ k_2/B_2,\ k_3/B_3)$ and estimate the following truncation error

$$\sum_{|\bar{\mathbf{k}}| > k_\infty} ||\Phi_D(\xi, \bar{\mathbf{k}})\mathbf{f}||_2 \leq E_F^D(\xi, \bar{\mathbf{k}})\mathbf{f}||_2$$

and by integrating only in the radial direction

$$\begin{aligned} E_F^D(\xi, \bar{\mathbf{k}}) \quad & \leq \quad \int_{|\bar{\mathbf{k}}| > k_\infty} 8\pi \left(1 + \frac{4\pi^2 k^2}{4\xi^2}\right) e^{-4\pi^2 k^2 / 4\xi^2} \mathrm{d}k \\ & \leq \quad 8\pi \int_{k_\infty}^{\infty} k^2 \left(1 + \frac{\pi^2 k^2}{\xi^2}\right) e^{-\pi^2 k^2/\xi^2} \mathrm{d}k \\ & \leq \quad 8\pi \left(\int_{k_\infty}^{\infty} k^2 e^{-\pi^2 k^2 \xi^2} \mathrm{d}k + \int_{k_\infty}^{\infty} \frac{\pi^2 k^4}{\xi^2} e^{-\pi^2 k^2/\xi^2} \mathrm{d}k \right) \end{aligned} \tag{A.9}$$

Denote $a = \frac{\pi}{\xi}$ and continue to evaluate the above integrals

$$\begin{aligned} E_F^D(\xi,\bar{\mathbf{k}}) &\leq 8\pi\left(\int\limits_{k_\infty}^{\infty} k^2 e^{-a^2k^2}\mathrm{d}k + \int_{k_\infty}^{\infty} a^2k^4e^{-a^2k^2}\mathrm{d}k\right) \\ &\leq 8\pi\left(\left(\frac{\sqrt{\pi}}{4a^3}+\frac{k_\infty}{2a^2}\right)\mathrm{e}^{-a^2k_\infty^2} + a^2\left(\frac{3k_\infty}{4a^4}+\frac{k_\infty^3}{2a^2}+\frac{3\sqrt{\pi}}{8\sqrt{a}^5}\right)\mathrm{e}^{-a^2k_\infty^2}\right) \\ &\leq 8\pi\left(\frac{5\sqrt{\pi}}{4a^3}+\frac{5k_\infty}{4a^2}+\frac{k_\infty^3}{2}\right)\mathrm{e}^{-a^2k_\infty^2} \end{aligned} \qquad \text{(A.10)}$$

These error estimates are functions of both ξ and the cut-off r_c in real space and k_∞ in Fourier space. To asses whether these estimates are valid we compare them with the corresponding truncated sums for an increasing number of periodic layers and a fixed ξ, see Fig A.1a,A.1b. Although the estimates are not very sharp they offer good guidelines for the parameter choice as they are used in Sec.5.

Appendix B Parameter dependency for the Stokeslet and the dipole

In Fig. B.1a for the Stokeslet and Fig. B.1b for the dipole we draw contour plots for the dependency between r_c and ξ. This dependency is quantified in Table B.1 for the Stokeslet and Table B.2 for the dipole.

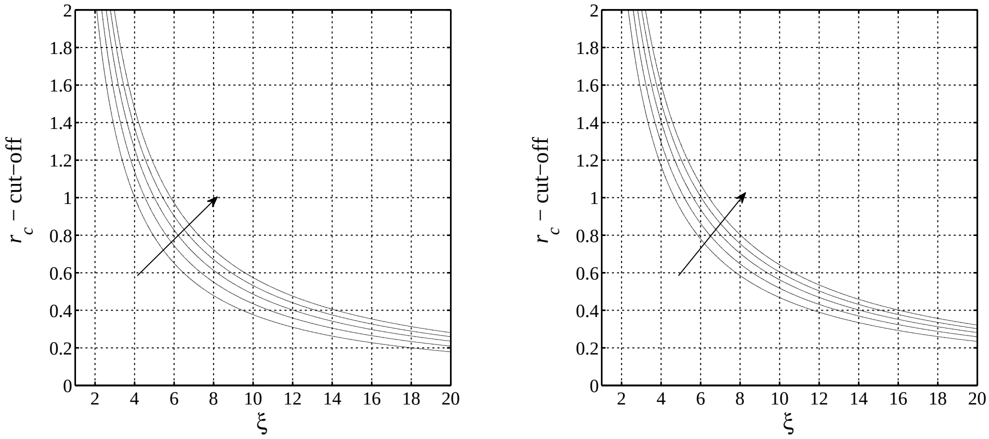

(a) Parameter choice for Stokeslet

(b) Parameter choice for dipole

Figure B.1: Isolines representing the relation between ξ and r_c for various accuracies, in the direction of the arrow $\delta = 10^{-6},\ 10^{-8},\ 10^{-10},\ 10^{-12},\ 10^{-14}$.

Similarly in Fig. B.2a for the Stokeslet and Fig. B.2b for the dipole we represent contour plots for the dependency between M and ξ. Table B.3 for the Stokeslet and Table B.4 for the dipole gather the rules to be used for choosing parameters for a given tolerance δ.

Table B.1: Dependency of r_c on ξ for the Stokeslet

δ	10^{-6}	10^{-8}	10^{-10}	10^{-12}	10^{-14}
a	4.359	4.867	5.326	5.746	6.138
b	1.062	1.048	1.04	1.033	1.029

Table B.2: Dependency of r_c on ξ for the dipole

δ	10^{-6}	10^{-8}	10^{-10}	10^{-12}	10^{-14}
a	4.677	5.173	5.621	6.034	6.417
b	0.9997	0.9997	0.9997	0.9996	0.9996

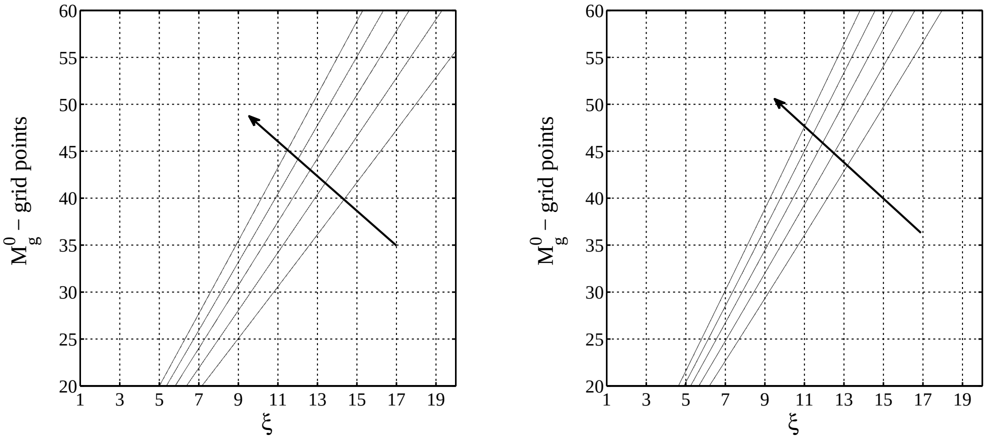

(a) Parameter choice for Stokeslet

(b) Parameter choice for dipole

Figure B.2: Isolines representing the relation between ξ and M for various accuracies, in the direction of the arrow $\delta = 10^{-6},\ 10^{-8},\ 10^{-10},\ 10^{-12},\ 10^{-14}$.

Table B.3: Dependency of M on ξ for the Stokeslet

δ	10^{-6}	10^{-8}	10^{-10}	10^{-12}	10^{-14}
a	2.798	3.109	3.392	3.654	3.899
b	-0.2066	-0.03486	0.1918	0.3123	0.3992

Appendix C Legendre polynomials expansion

The Legendre polynomials are given by the following recursion formula

$$P_k(x) = 2^{-k} \sum_{n=0}^{[k/2]} (-1)^n \binom{k}{n} \binom{2k-2n}{k} x^{k-2n}, \quad k = 0, 1, 2, \ldots$$

Table B.4: Dependency of M on ξ for the dipole

δ	10^{-6}	10^{-8}	10^{-10}	10^{-12}	10^{-14}
a	3.439	3.697	3.939	4.169	4.388
b	-1.677	-1.258	-0.9502	-0.7266	-0.571

$$\begin{aligned}
P_0(x) &= 1\\
P_1(x) &= x\\
P_2(x) &= (3x^2 - 1)/2\\
P_3(x) &= (5x^3 - 3x)/2\\
P_4(x) &= (35x^4 - 30x^2 + 3)/8\\
P_5(x) &= (63x^5 - 70x^3 + 15x)/8\\
P_6(x) &= (231x^6 - 315x^4 + 105x^2 - 5)/16\\
P_7(x) &= (429x^7 - 693x^5 + 315x^3 - 35x)/16\\
P_8(x) &= (6435x^8 - 12012x^6 + 6930x^4 - 1260x^2 + 35)/128
\end{aligned}$$

References

[1] M. P. Allen and D. J. Tildesley. *Computer Simulation of Liquids.* Clarendon Press, New York, U.S.A., 1989.

[2] G. K. Batchelor. Slender-body theory for particles of arbitrary cross-section in Stokes flow. *J. Fluid Mech.*, 44:419–440, 1970.

[3] C. W. J. Beenakker. Ewald sums of the Rotne-Prager tensor. *J. Chem. Phys.*, 85:1581–1582, 1986.

[4] J. E. Butler and E. S. G. Shaqfeh. Dynamic simulations of the inhomogeneous sedimentation of rigid fibres. *J. Fluid Mech.*, 468:205–237, 2002.

[5] A. A. Dahlkild. Finite wavelength selection for the linear instability of a suspension of settling spheroids. *J. Fluid Mech.*, 689:183–202, 2011.

[6] U. Essmann, L. Perera, M. L. Berkowitz, T. Darden, H. Lee, and L. G. Pedersen. A smooth particle mesh Ewald method. *J. Chem. Phys.*, 103(19):8577–8593, 1995.

[7] P. P. Ewald. Die Berechnung optischer und elektrostatischer Gitterpotentiale. *Ann. Phys.*, 369(3):253–287, 1921.

[8] T. Götz. *Interactions of Fibers and Flow: Asymptotics, Theory and Numerics.* PhD thesis, Universität Kaiserslautern, Germany, 2000.

[9] L. Greengard and J. Y. Lee. Accelerating the nonuniform fast Fourier transform. *SIAM Rev.*, 46(3):443–454, 2004.

[10] L. Greengard and V. Rokhlin. A fast algorithm for particle simulations. *J. Comput. Phys.*, 73:325–348, 1987.

[11] É. Guazzelli and E. J. Hinch. Fluctuations and instability in sedimentation. *Annu. Rev. Fluid Mech.*, 43:97–116, 2011.

[12] K. Gustavsson and A.-K. Tornberg. Gravity induced sedimentation of slender fibers. *Phys. Fluids*, 21(123301), 2009.

[13] H. Hasimoto. On the periodic fundamental solutions of the Stokes equations and their application to viscous flow past a cubic array of spheres. *J. Fluid Mech.*, 5:317–328, 1959.

[14] B. Herzhaft and É. Guazzelli. Experimental study of the sedimentation of dilute and semi-dilute suspensions of fibres. *J. Fluid Mech.*, 384:133–158, 1999.

[15] R. W. Hockney and J. W. Eastwood. *Computer Simulation Using Particles.* Taylor & Francis, New York, U.S.A, 1988.

[16] R. E. Johnson. An improved slender-body theory for Stokes flow. *J. Fluid Mech.*, 99:411–431, 1980.

[17] G. E. Karniadakis, M. Israeli, and S. A. Orszag. High-order splitting methods for the incompressible Navier–Stokes equations. *J. Comput. Phys.*, 97(2):414–443, 1991.

[18] J. Kolafa and J. W. Perram. Cutoff errors in the Ewald summation formulae for point charge systems. *Mol. Simul.*, 9(5):351–368, 1992.

[19] D. Lindbo and A.-K. Tornberg. Spectrally accurate fast summation for periodic Stokes potentials. *J. Comput. Phys.*, 229(23):8994–9010, 2010.

[20] D. Lindbo and A.-K. Tornberg. Spectral accuracy in fast Ewald-based methods for particle simulations. *J. Comput. Phys.*, 230(24):8744–8761, 2011.

[21] B. Metzger, J. E. Butler, and É. Guazelli. Experimental investigation of the instability of a sedimenting suspension of fibres. *J. Fluid Mech.*, 575:307–332, 2007.

[22] C. Pozrikidis. Computation of periodic Green's functions of Stokes flow. *J. Eng. Math.*, 30(4):79–96, 1996.

[23] D. Saintillan, E. Darve, and E. S. G. Shaqfeh. A smooth particle-mesh Ewald algorithm for Stokes suspension simulations: The sedimentation of fibers. *Phys. Fluids*, 17(033301), 2005.

[24] A. Sierou and J. F. Brady. Accelerated Stokesian Dynamics simulations. *J. Fluid Mech.*, 448:115–146, 2001.

[25] A.-K. Tornberg and K. Gustavsson. A numerical method for simulations of rigid fiber suspensions. *J. Comput. Phys.*, 215:172–196, 2005.

[26] H. Wang, T. Lei, J. Huang, and Z. Yao. A parallel fast multipole accelerated integral equation scheme for 3D Stokes equations. *Int. J. Num. Meth. Eng.*, 70:812–839, 2007.

[27] F. Zhang. *Eulerian Numerical Study of the Sedimentation of Fibre Suspensions.* Licentiate thesis, KTH Mechanics, Royal Institute of Technology, Sweden, 2012.

A new fast converging decomposition for the periodic Stresslet

Oana Marin
Linné FLOW Centre, KTH-SCI (NA), SE-100 44 Stockholm, Sweden

Abstract

A fundamental solution of the Stokes equations, the Stresslet, is periodized here through a new decomposition. An alternative to the previously derived decomposition by Bennakker is developed by starting from the periodic kernels of the Laplace equation and Stokes equations. The Hasimoto decomposition for the periodic Stokeslet (fundamental solution of the Stokes equations) is extended to the kernel of the Laplace equation. Based on these periodized solutions a new expression for the periodic Stresslet is obtained. This novel decomposition exhibits faster decaying properties while maintaining the same structure as the Beenakker decomposition. Numerical tests show that the sums stemming from the new decomposition yield a result which is approximately two orders of magnitude more accurate than the one computed using the Beenakker decomposition for the same truncation cut-offs. The advantage of this new decomposition is that it can replace the one by Beenakker without any additional modifications yielding either better accuracy or alternatively smaller cut-offs of the two sums expediting the computations. Error estimates in RMS norm, which are necessary guidelines in choosing the truncation parameters, are also derived for the new decomposition.

1 Introduction

The boundary integral method is a suitable mathematical modeling tool for a wide range of applications such as wave scattering [20], particle simulations [2], fiber suspensions [22]. The Stokes equations, which are the focus of the present work, can be restated as a boundary integral equation through which the velocity is expressed in terms of a kernel, *e.g.* Stokeslet or Stresslet, convolved with a set of force densities acting at the surface of either bounding walls or immersed objects. The core advantage of models based on boundary integrals formulations is that they lead to numerical discretizations over surfaces of lower dimensionality, *e.g.* instead of discretizing an entire volume it suffices to discretize the boundaries present in the problem at hand.The benefits brought by such formulation do not always come cheaply though, especially when periodic boundary conditions are considered. Various simulations involving the periodic kernels of the Stokes equations have been performed, *i.e.* the periodic Stokeslet used by [16, 21] or periodic Stresslet [15, 3, 7].

Periodicity in the context of boundary integrals has to be reinterpreted by the reader familiar mainly with grid based methods. It is thus understood by periodicity that any physical phenomena that occurs in the computational cell repeats itself identically in all other self similar cells that add to build up the entire physical space. To treat this in the context of *e.g.* electrostatics one ends up having to evaluate infinite sums, which are not absolutely convergent. To alleviate the aforementioned mathematical difficulty the eponymous Ewald [6] suggested to split the short range interactions which are to be treated in the real space from the long range interactions which are dealt with in Fourier space and additionally impose a physical constraint on the problem at hand. To do so he introduced a screening function γ depending on a parameter ξ, also known as the Ewald parameter, and through this function he performs two complementary convolutions in real and reciprocal space. Many other attempts at finding faster converging decompositions have been made, *e.g.* [11] lists an entire range of choices for the Laplace equation, however the Ewald scheme remains the most popular due to the exponential decay of both sums in the split. The technique has been reproduced in many other scientific areas such as fluid dynamics [19], and an application emerging from this field is also the focus of the present work. For the singularity which gives the velocity field due to a point source, *i.e.* Stokeslet, there have been two alternative formulations widely used, *i.e.* Hasimoto [9] and Beenakker [1], though others have been suggested [19]. The difference between the formulations arises from either the use of a different screening function, or the means of derivation. According to [13] the Hasimoto formulation exhibits faster decaying properties than the one by Beenakker, and this becomes non-negligible as the system scales up. For the fundamental solution of the stress tensor, Stresslet, the decomposition for treating periodicity has been based on the Beenakker formulation [7]. Since both the real and the Fourier space sum that enter the decomposition have a computational complexity of $\mathcal{O}(N^2)$, where N is the number of particles it is imperative to seek improvements of this method. One straightforward way of speeding up the computations is to involve a fast summation method, *e.g.* Smooth Particle Mesh Ewald (SPME) [5], or Spectral Ewald (SE) [13]. These methods build on a certain decomposition and by conveniently truncating the real space and the Fourier space sum the computational complexity reduces to $\mathcal{O}(N \log N)$. However the decay of the decomposition plays an important role even if a fast summation method is considered.

The fundamental solution of the stress tensor, *i.e.* the Stresslet, has been periodized so far by using the Beenakker decomposition, and has been used as such in [15, 3]. In the present work, as a substitute to the Beenakker formulation, an alternative decomposition of the Stresslet is being derived which will exhibit faster decaying properties. Given that the Hasimoto decomposition has been noted to converge at a faster rate than the Beenakker splitting scheme for the fundamental solution of the Stokeslet it seems plausible to assume that the same will hold for the Stresslet. The reason for the faster decay will be shown in this paper. The Beenakker solution has been derived by using a set of vector operations applied to $r = |\mathbf{r}_i - \mathbf{r}_j|$ the distance between two particles at positions $\mathbf{r}_i$, $\mathbf{r}_j$. The Hasimoto derivation on the other hand could be derived following the screening technique introduced by Ewald to obtain the fundamental solution of the Stokeslet. It is cumbersome to follow the very same approach as Hasimoto since the Stresslet is a third order tensor. The procedure here is based on the observation that the fundamental solution of the pressure in the Stokes equations can be also obtained as the gradient of the kernel of the Laplace equation. Since the stress tensor can be expressed in terms of the pressure and the gradient of the velocity a formula can be established to write the Stresslet solely as a function of the kernels of the Stokes and Laplace equations. Thereon we are able to work out a derivation for a new expression of the periodic Stresslet using the already periodized Stokeslet. Since the Hasimoto's decomposition of the periodic Stokeslet is used here we were prompted to derive the corresponding decomposition for the kernel of the Laplace equation. The resulting expression proves to be a faster decaying summation formula for the periodic Stresslet. To validate our result we compare it with the Beenakker solution and note that if the sums are truncated at the same cut-off the new decomposition yields a result approximately two orders of magnitude more accurate than the Beenakker solution. Since the structure of the new decomposition is similar to the one provided by Beenakker it is very easy to use in practice in any of the already developed codes and profit from the gain in accuracy at no extra cost. For completeness we close by providing error estimates for the newly derived converging sum, accompanied by a brief discussion on how to choose the cut-off parameters as a function of the splitting parameter ξ. As a side note a different derivation was obtained using the Ewald decomposition for the Laplace kernel, however the symmetry of the terms does not match those of the Beenakker formulation, although the decay of the sums is similar to the one of the new decomposition. This result is provided in the Appendix.

2 Mathematical background

There are many physical phenomena in the field of fluid dynamics characterized by dominating viscous effects [18, 8]. These applications are often numerically simulated within a volume Ω using the Stokes equations

$$\begin{aligned} \nabla p - \mu \Delta \mathbf{u} &= \mathbf{f} \ , \quad \text{in} \quad \Omega \ , \\ \nabla \cdot \mathbf{u} &= 0 \ . \end{aligned} \tag{1}$$

where $\mathbf{u}$ represents the velocity field, p the pressure and $\mathbf{f}$ a volume force.

If the problem at hand involves a large set of particles it is more convenient to discretize the equations using boundary integrals instead of a grid based method. In a boundary integral formulation it is sufficient to track all the present boundaries rather than the entire volume. There are various mathematical models used for describing the surfaces of the immersed objects, however here we focus on the double layer formulation used in *e.g.* drop deformation studies [23].

Assume we intend to determine the velocity $\mathbf{u}$ at a point $\mathbf{x}_0$ due to an immersed object of surface given by a set of points $\mathbf{x} \in S$. The double layer formulation for the velocity is then expressed in terms of the kernel of the stress tensor as

$$u_l(\mathbf{x}_i) = \frac{1}{8\pi} \int_S T_{0,lmp}(\mathbf{x}_j - \mathbf{x}_i) f_m(\mathbf{x}_j) n_p(\mathbf{x}_j) \mathrm{d}S_{\mathbf{x}}, \quad \mathbf{x}_0 \in S \ , \tag{2}$$

with $\mathbf{f}$ being the force densities over the object surface, $\mathbf{n}$ the unit normal vector and the fundamental solution of the stress tensor, *i.e.* Stresslet, given by

$$T_{0,lmp}(\mathbf{x}) = -6 \frac{x_l x_m x_p}{|\mathbf{x}|^5} \ . \tag{3}$$

For simplicity of the argument we shall consider that we deal only with points particles $\mathbf{x}_i$, $i = 1, \ldots, N$, which is of course what would arise from a discretization of the surface S once we employ a numerical quadrature to evaluate (2). If however the computational domain, $\Omega = [0, L)^3$ is subject to periodic boundary conditions all the periodic images of all points have to be summed up. For any point $\mathbf{x}$ on the surface S the periodic image is given by $\mathbf{x} + \tau(\mathbf{p})$ with $\tau(\mathbf{p}) = p_1 L\mathbf{e}_1 + p_2 L\mathbf{e}_2 + p_3 L\mathbf{e}_3$, $\mathbf{p} \in \mathbb{Z}^3$, yielding

$$u_l(\mathbf{x}_i) = \frac{1}{8\pi} \sum_{\mathbf{p} \in \mathbb{Z}^3}{}' \sum_j T_{0,lmp}(\mathbf{x}_j - \mathbf{x}_i + \tau(\mathbf{p})) f_m(\mathbf{x}_j) n_p(\mathbf{x}_j) \ , \quad i = 1, \ldots, N \ . \tag{4}$$

where the prime over the sum over $\mathbf{p}$ stands for skipping the singular point $i = j$ for $|\mathbf{p}| = 0$.

In the present form this sum is only conditionally convergent and typically an additional physical constraint has to be imposed. In the case of the Stresslet this condition comes in rather implicitly, as opposed to the case of the Laplace equation, as will be explained. To expedite the truncation of the sum an extra step has to be taken, *i.e.* the short range interactions, which remain to be summed in real space, are split from the long range interactions to be summed in Fourier space, thus obtaining two fast converging sums. To the author's knowledge the only derivation available in the literature [3], [7], [15] is the one based on Beenakker's decomposition. According to Beenakker we can split the sum in (4) as follows

$$u_l^T(\mathbf{x}_i) = u_l^{T,r}(\mathbf{x}_i) + u_l^{T,F}(\mathbf{x}_i) \ . \tag{5}$$

The Fourier space sum is given in terms of the wavenumber $\mathbf{k} \in 2\pi\boldsymbol{\kappa}/L,\ \boldsymbol{\kappa} \in \mathbb{Z}^3$ and $k = |\mathbf{k}|$ as

$$u_l^{T,F}(\mathbf{x}_i) = -\frac{1}{V}\sum_{\mathbf{k}\neq 0}\sum_j \Phi_{lmp}(\xi,\mathbf{k})S_{mp}(\mathbf{x}_j)i\mathrm{e}^{-i\mathbf{k}\cdot(\mathbf{x}_i-\mathbf{x}_j)}\ , \tag{6}$$

with $S_{mp}(\mathbf{x}) = f_m(\mathbf{x})n_p(\mathbf{x})$, V the volume of the domain Ω and

$$\Phi_{lmp}(\xi,\mathbf{k}) = 8\pi\Big[-\frac{2}{k^4}k_lk_mk_p + \frac{1}{k^2}(\delta_{mp}k_l + \delta_{lp}k_m + \delta_{lm}k_p)\Big]\Big(1 + \frac{k^2}{4\xi^2} + \frac{k^4}{8\xi^4}\Big)\mathrm{e}^{-k^2/4\xi^2}.$$

It is natural to skip the wavenumber $\mathbf{k} = 0$ since the limit as $\mathbf{k} \to 0$ is zero.

With the same notation for S_{mp} the real space sum is given as

$$u_l^{T,r}(\mathbf{x}_i) = \sum_{\mathbf{p}\in\mathbb{Z}^3}{}^{\prime}\sum_j \Gamma_{lmp}(\xi,\mathbf{x}_j - \mathbf{x}_i + \tau(\mathbf{p}))S_{mp}(\mathbf{x}_j)\ , \tag{7}$$

with

$$\Gamma_{lmp}(\xi,\mathbf{x}) = C(\xi,|\mathbf{x}|)\hat{x}_l\hat{x}_m\hat{x}_p + D(\xi,|\mathbf{x}|)(\delta_{lm}\hat{x}_p + \delta_{lp}\hat{x}_m + \delta_{mp}\hat{x}_l)\ ,$$

where $\hat{\mathbf{x}} = \mathbf{x}/|\mathbf{x}|$ and for $r = |\mathbf{x}|$

$$\begin{aligned} C(\xi,r) &= -\frac{6}{r^2}\operatorname{erfc}(\xi r) + \Big(-\frac{12\xi}{r\sqrt{\pi}} - \frac{8\xi^3 r}{\sqrt{\pi}} + \frac{16\xi^5r^3}{\sqrt{\pi}}\Big)\mathrm{e}^{-\xi^2r^2} \\ D(\xi,r) &= \frac{8\xi^3}{\sqrt{\pi}}(2 - \xi^2r^2)\mathrm{e}^{-\xi^2r^2}\ . \end{aligned}$$

This decomposition has good convergence properties and proved itself to be useful in various applications [15], [7]. However in the sections to follow we develop a faster converging decomposition which will be compared to the currently stated expressions for the periodic Stresslet.

3 Periodic Stresslet

To start with we note that the stress tensor can be expressed as a function of the pressure p and the velocity $\mathbf{u}$ as

$$\tau = -p + \nabla\mathbf{u} + \nabla\mathbf{u}^T\ .$$

The same expression can be applied to obtain the Stresslet given as in (3) in terms of the fundamental solutions $\mathbf{G}$, also known as the Stokeslet, and pressure $\mathbf{\Pi}$, more details in [18]. With

$$G_{lm}(\mathbf{x}) = \frac{1}{|\mathbf{x}|}\delta_{lm} + \frac{x_lx_m}{|\mathbf{x}|^3}\ , \tag{8}$$

and

$$\Pi_l(\mathbf{x}) = -2\frac{x_l}{|\mathbf{x}|}\ . \tag{9}$$

By noticing now that $\mathbf{\Pi} = -2\nabla\frac{1}{r}$ we can express the pressure as a function of the fundamental solution of the Laplace equation

$$\Pi_m(\mathbf{x}) = -2\frac{\partial L(\mathbf{x})}{\partial x_m}\ ,$$

where we denoted by L the fundamental solution of the Laplace operator, *i.e.* $L(\mathbf{x}) = 1/|\mathbf{x}|$, also known as the harmonic Green's function. We can therefore express the Stresslet in terms of the kernels of the Stokes and Laplace equations

$$T_{lmp}(\mathbf{x}) = 2\frac{\partial L(\mathbf{x})}{\partial x_m}\delta_{lp} + \frac{\partial G_{lm}(\mathbf{x})}{\partial x_p} + \frac{\partial G_{mp}(\mathbf{x})}{\partial x_l} = -6\frac{x_l x_m x_p}{|\mathbf{x}|^5} \ . \tag{10}$$

To this end we also verified that using the above formulation we can retrieve the Stresslet as stated in (3).

As expression (10) was applied to the Stokeslet and the harmonic Green's function it can also be applied to their periodic corresponding expressions to obtain the periodic Stresslet. First we list the Hasimoto decomposition of the Stokeslet. The Hasimoto split has been noted to yield superior convergence properties, albeit slight, [13], for the fundamental solution of the Stokes equations. Hasimoto used a technique similar to Ewald's to split the short range interactions from the long range ones. In the field of electrostatics Ewald [6] used a screening function $\gamma(\xi, r) = \mathrm{e}^{-\xi^2 r^2}$, a suitable choice for the periodic kernel of the Laplace equation, to yield two sums of exponential decay in both real and Fourier space. The Hasimoto decomposition [9], [10] is however based on a different screening function $\gamma(\xi, r) = \mathrm{e}^{-\xi^2 r^2}(5/2 - \xi^2 r^2)$ that is suitable to the tensorial nature of the Stokeslet. Based on these two decompositions we suggest a novel approach to generate a decomposition for the Stresslet which exhibits faster decay as will be seen in Section 4. However the formulas obtained using the Ewald decomposition of the harmonic Green's function, provided for completeness in Appendix B, do not share the same symmetry of terms as the Beenakker decomposition provided above. To alleviate this we have re-derived the decomposition of the Laplace periodic kernel starting from the very same screening function as Hasimoto used in deriving the decomposition of the Stokeslet. These formulas have a similar structure as the Beenakker decomposition, with the main difference that the polynomials that enter the sums are of lower degree and as will be shown lead to faster convergence of both sums (in real and Fourier space).

Hasimoto decomposition for the Stokeslet

The velocity field of the Stokes flow at a point $\mathbf{x}_i$ due to a set of N particles positioned at $\mathbf{x}_j$ exerting a force $\mathbf{f}(\mathbf{x}_j)$, $j = 1, \dots, N$ onto the fluid is given as

$$\mathbf{u}(\mathbf{x}_i) = \sum_{j=1}^{N} \mathbf{G}(\mathbf{x}_i - \mathbf{x}_j)\mathbf{f}(\mathbf{x}_j) \ ,$$

where $\mathbf{G}$ is the Stokeslet given in (8). Here we use $\mathbf{f}(\mathbf{x}_j)$ to denote the force at a particle position $\mathbf{x}_j$ to avoid index confusions as we switch to indicial notation. However it should be noted that $\mathbf{f}$ differs in magnitude from one particle position to another. Even more $\mathbf{f}(\mathbf{x}_j)$ are here only discrete point values.

If periodic boundary conditions are imposed the summation over all periodic images has to be included

$$\mathbf{u}_S(\mathbf{x}_i) = \sum_{\mathbf{p}}{}' \sum_{j=1}^{N} \mathbf{G}(\mathbf{x}_i - \mathbf{x}_j + \mathbf{p})\mathbf{f}(\mathbf{x}_j) \ ,$$

where the prime over the sum over $\mathbf{p}$ indicates that the singular point $i = j$ for $|\mathbf{p}| = 0$ has been omitted.

To be able to evaluate this conditionally convergent sum Hasimoto [9] introduced the following decomposition

$$\mathbf{u}_S(\mathbf{x}_i) = \mathbf{u}_S^r(\mathbf{x}_i) + u_S^F(\mathbf{x}_i) + \mathbf{u}_{self}(\mathbf{x}_i) \ , \tag{11}$$

with

$$\mathbf{u}_S^r(\mathbf{x}_i) = \sum_{j=1}^{N} \sum_{\mathbf{p}}{}^{\prime} \boldsymbol{\Gamma}_S(\xi, \mathbf{x}_j - \mathbf{x}_i + \mathbf{p})\mathbf{f}(\mathbf{x}_j) \ , \tag{12}$$

Here $\boldsymbol{\Gamma}_S$, the component that sums up to give the real space sum in the split, is defined as

$$\boldsymbol{\Gamma}_S(\xi, \mathbf{x}) = C(\xi r)\frac{\mathbf{I}}{r} + D(\xi r)\frac{\hat{\mathbf{x}}\hat{\mathbf{x}}}{r} \ ,$$

where $\hat{\mathbf{x}} = \mathbf{x}/|\mathbf{x}|$, $r = |\mathbf{x}|$ and

$$C(\xi r) = \operatorname{erfc}(\xi r) - \frac{2\xi r}{\sqrt{\pi}} e^{-\xi^2 r^2}, \quad D(\xi r) = \operatorname{erfc}(\xi r) + \frac{2\xi r}{\sqrt{\pi}} e^{-\xi^2 r^2} \ .$$

The self contribution term $\mathbf{u}_{self}(\mathbf{x}_i) = -4\xi/\sqrt{\pi}\mathbf{f}(\mathbf{x}_i)$, is computed from

$$\lim_{|\mathbf{x}| \to 0} (\boldsymbol{\Gamma}_S(\mathbf{x}) - \mathbf{G}(\mathbf{x})) = -\frac{4\xi}{\sqrt{\pi}} \ . \tag{13}$$

The Fourier sum is given for wave numbers $\mathbf{k} \in 2\pi\boldsymbol{\kappa}/L,\ \boldsymbol{\kappa} \in \mathbb{Z}^3,\ k = |\mathbf{k}|$ as

$$\mathbf{u}_S^F(\mathbf{x}_i) = \frac{1}{V} \sum_{j=1}^{N} \sum_{\mathbf{k} \neq 0} \boldsymbol{\Phi}_S(\xi, \mathbf{k}) \mathrm{e}^{-i\mathbf{k}\cdot(\mathbf{x}_j - \mathbf{x}_i)} \mathbf{f}(\mathbf{x}_j) \ , \tag{14}$$

where

$$\boldsymbol{\Phi}_S(\xi, \mathbf{k}) = B(\xi, \mathbf{k}) e^{-k^2/4\xi^2} \ ,$$

and

$$B(\xi, \mathbf{k}) = 8\pi \left(1 + \frac{k^2}{4\xi^2}\right) \frac{1}{k^4} (k^2 \mathbf{I} - \mathbf{k}\mathbf{k}) \ . \tag{15}$$

The zero wave number $\mathbf{k} = 0$ is omitted in the Fourier space sum, however it yields the total force in the domain $\mathbf{F} = \sum_j \mathbf{f}(\mathbf{x}_j)$ which is demanded to balance the pressure gradient within the periodic cell Ω.

Hasimoto decomposition for the kernel of the Laplace equation

The solution of the Laplace equation at a point $\mathbf{x}_i$ due to a set of N point particles positioned at $\mathbf{x}_j$ of charges $f(\mathbf{x}_j)$, $j = 1, \ldots, N$ is given as

$$u(\mathbf{x}_i) = \frac{1}{4\pi} \sum_{j=1}^{N} L(\mathbf{x}_i - \mathbf{x}_j) f(\mathbf{x}_j) \ ,$$

where L is the kernel of the Laplace equation, $L = 1/|\mathbf{x}|$.

Consider a periodic domain $\Omega = [0,\ L)^3$. In the periodic setup this prompts for the inclusion of all periodic images $\mathbf{x} + \tau(\mathbf{p})$ with $\tau(\mathbf{p}) = p_1 L\mathbf{e}_1 + p_2 L\mathbf{e}_2 + p_3 L\mathbf{e}_3$ where $p_i \in \mathbb{Z},\ i = 1, \ldots, 3$ and leads to solving a problem of the type

$$-\Delta u_L(\mathbf{x}) = 4\pi \sum_{j=1}^{N} \sigma^j(\mathbf{x}), \quad \sigma^j(\mathbf{x}_i) = \sum_{\mathbf{p} \in \mathbb{Z}^3} f(\mathbf{x}_j) \delta(\mathbf{x}_i - \mathbf{x}_j + \tau(\mathbf{p})) \ . \tag{16}$$

From here the expression for the harmonic Green's function in a periodic domain is

$$u_L(\mathbf{x}_i) = \frac{1}{4\pi} \sum_{j=1}^{N} \sum_{\mathbf{p}\in\mathbb{Z}^3} \frac{f(\mathbf{x}_j)}{|\mathbf{x}_i - \mathbf{x}_j + \tau(\mathbf{p})|} \ ,$$

which is a conditionally convergent sum with a slow decay.

Let us now introduce a screening function $\gamma(\xi, \mathbf{x})$ to split the source term in (16) as

$$\sigma^j(\mathbf{x}) = \sigma^j(\mathbf{x}) - (\sigma^j * \gamma)(\mathbf{x}) + (\sigma^j * \gamma)(\mathbf{x}) \ . \tag{17}$$

The decomposition in (17) leads to a component $\sigma^{j,R}(\xi, \mathbf{x}) = \sigma^j(\mathbf{x}) - (\sigma^j * \gamma)(\mathbf{x})$ to be evaluated in real space and $\sigma^{j,F}(\xi, \mathbf{x}) = (\sigma^j * \gamma)(\mathbf{x})$ to be evaluated in Fourier space. By the linearity of the Laplace operator the two problems can be solved separately

$$-\Delta u_L^{j,R}(\mathbf{x}) \quad = \quad 4\pi\sigma^{j,R}(\mathbf{x}) \ , \tag{18}$$

$$-\Delta u_L^{j,F}(\mathbf{x}) \quad = \quad 4\pi\sigma^{j,F}(\mathbf{x}) \ . \tag{19}$$

To retrieve the full solution of the Laplace problem subject to periodic boundary conditions it remains to sum up $u_L(\mathbf{x}) = \sum_j u_L^{j,R}(\mathbf{x}) + u_L^{j,F}(\mathbf{x})$. So far the screening function has not been specified since the above treatment holds for any screening function such that $\gamma(\xi, 0) = 1$, $\gamma(\xi, |\mathbf{x}| \to \infty) \to 0$ and also $|\gamma(\xi, \mathbf{x})|_{L_2} = 1$. Here we shall use the function that yields the Hasimoto decomposition of the periodic Stokeslet provided in Section 3, *i.e.* $\gamma = \mathrm{e}^{-\xi^2 r^2}(5/2 - \xi^2 r^2)$.

The real space sum can be evaluated directly by computing the convolution

$$\begin{aligned} u_L^{j,R}(\mathbf{x}) \quad &= \quad \int_{\mathbb{R}^3} \frac{f(\mathbf{x}_j)}{|\mathbf{y}-\mathbf{x}_j|} \sum_{\mathbf{p}\in\mathbb{Z}^3} (\delta(\mathbf{y}-\mathbf{x}_j+\tau(\mathbf{p})) - \gamma(\mathbf{y}-\mathbf{x}_j+\tau(\mathbf{p})))\mathrm{d}\mathbf{y} \\ &= \quad f(\mathbf{x}_j) \sum_{\mathbf{p}\in\mathbb{Z}^3} \left(\frac{\mathrm{erfc}(\xi|\mathbf{x}-\mathbf{x}_j+\mathbf{p}|)}{|\mathbf{x}-\mathbf{x}_j+\mathbf{p}|} - \frac{2\xi}{\sqrt{\pi}} \mathrm{e}^{-\xi^2|\mathbf{x}-\mathbf{x}_j+\mathbf{p}|^2} \right), \quad \mathbf{x} \neq \mathbf{x}_j \ . \end{aligned}$$

To obtain the solution of the second Laplace problem (19) in the frequency domain we write

$$-\Delta u_L^{j,F}(\mathbf{x}) = \sum_{\mathbf{k}} k^2 \hat{u}^{j,F}(\mathbf{k}) e^{i\mathbf{k}\cdot(\mathbf{x}-\mathbf{x}_j)} \ . \tag{20}$$

Using the Poisson summation we express the right hand side of $-\Delta u_L^{j,F}(\mathbf{x}) = 4\pi\sigma^{j,F}(\mathbf{x})$ as being

$$\begin{aligned} \sigma^{j,F}(\mathbf{x}) \quad &= \quad \sum_{\mathbf{p}\in\mathbb{Z}^3} f_j \gamma(\mathbf{x}-\mathbf{x}_j+\mathbf{p}) = \frac{f(\mathbf{x}_j)}{V} \sum_{\mathbf{k}} \hat{\gamma}(\mathbf{k}) e^{i\mathbf{k}\cdot(\mathbf{x}-\mathbf{x}_j)} \\ &= \quad \frac{f(\mathbf{x}_j)}{V} \sum_{\mathbf{k}} \left(1 + \frac{k^2}{4\xi^2}\right) e^{-k^2/4\xi^2} e^{i\mathbf{k}\cdot(\mathbf{x}-\mathbf{x}_j)} \ , \end{aligned} \tag{21}$$

since $\hat{\gamma}(\mathbf{k}) = \left(1 + \frac{k^2}{4\xi^2}\right) e^{-k^2/4\xi^2}$.

From both (20) and (21) we obtain

$$u_L^{j,F}(\mathbf{x}) = \frac{4\pi f(\mathbf{x}_j)}{V} \sum_{\mathbf{k}} \frac{1}{k^2} \left(1 + \frac{k^2}{4\xi^2}\right) e^{-k^2/4\xi^2} e^{i\mathbf{k}(\mathbf{x}-\mathbf{x}_j)} \ . \tag{22}$$

Summing up over all point particles j we have the final expression for the potential in a periodic setup.

$$u_L(\mathbf{x}_i) = u_L^r(\mathbf{x}_i) + u_L^F(\mathbf{x}_i) + u_{self}(\mathbf{x}_i) \ . \tag{23}$$

The real space sum is given as

$$u_L^r(\mathbf{x}_i) = \sum_{j=1}^{N} \sum_{\mathbf{p}}{}' \Gamma_L(\xi, \mathbf{x}_j - \mathbf{x}_i + \mathbf{p}) f(\mathbf{x}_j) \ , \tag{24}$$

with

$$\Gamma_L(\xi, \mathbf{x}) = \frac{\mathrm{erfc}(\xi r)}{r} - \frac{2\xi}{\sqrt{\pi}} \mathrm{e}^{-\xi^2 r^2} \ . \tag{25}$$

The prime superscript over the real space sum indicates that the term $\mathbf{p} = 0, \ i = j$ is being skipped. To account for this term we compute in the limit $\mathbf{x}_j - \mathbf{x}_i \to 0$ obtaining the self interaction $u_{self}(\mathbf{x}_i) = -4\xi/\sqrt{\pi} f(\mathbf{x}_i)$ from

$$\lim_{|\mathbf{x}| \to 0} (\Gamma_L(\mathbf{x}) - L(\mathbf{x})) = \lim_{|\mathbf{x}| \to 0} \left(\frac{\mathrm{erfc}(\xi |\mathbf{x}|)}{|\mathbf{x}|} - \frac{2\xi}{\sqrt{\pi}} \mathrm{e}^{-\xi^2 |\mathbf{x}|^2} - \frac{1}{|\mathbf{x}|} \right) = -\frac{4\xi}{\sqrt{\pi}} \ .$$

The Fourier space sum is given in terms of the wavenumber $\mathbf{k} \in 2\pi \boldsymbol{\kappa}/L, \ \boldsymbol{\kappa} \in \mathbb{Z}^3$ and $k = |\mathbf{k}|$

$$u_L^F(\mathbf{x}_i) = \frac{4\pi}{V} \sum_{\mathbf{k} \neq 0} \Phi_L(\xi, \mathbf{k}) \sum_{j=1}^{N} e^{-i\mathbf{k} \cdot (\mathbf{x}_j - \mathbf{x}_i)} f(\mathbf{x}_j) \ , \tag{26}$$

with

$$\Phi_L(\xi, \mathbf{k}) = A(\xi, \mathbf{k}) e^{-k^2/4\xi^2} \ ,$$

where $A(\xi, \mathbf{k}) = \dfrac{1}{k^2} \left(1 + \dfrac{k^2}{4\xi^2} \right)$.

To remove the ambiguity brought by the fact that the solution to a Laplace equation is determined only up to a constant the requirement $\sum_i f(\mathbf{x}_i) = 0$ is imposed. This allows for skipping the $\mathbf{k} = 0$ term in the Fourier space sum. In the field of electrostatics this constraint is equivalent to requiring that the system is charge neutral.

Alternative formulation for the Stresslet

To express the velocity in terms of the periodic Stresslet we can assume to be having a formulation just as the one in (5), *i.e.*

$$u_l^T(\mathbf{x}_i) = u_l^{T,r}(\mathbf{x}_i) + u_l^{T,F}(\mathbf{x}_i) \ . \tag{27}$$

The same notations as in the description of the Beenakker decomposition are used in the following, *i.e.* $S_{mp}(\mathbf{x}) = f_m(\mathbf{x}) n_p(\mathbf{x})$, with $\mathbf{n}$ being the normal vector, $\mathbf{f}$ the point force.

The Fourier sum is in terms of the wavenumber $\mathbf{k} \in 2\pi \boldsymbol{\kappa}/L, \ \boldsymbol{\kappa} \in \mathbb{Z}^3$, $k = |\mathbf{k}|$

$$u_l^{T,F}(\mathbf{x}_i) = -\frac{1}{V} \sum_{j=1}^{N} \sum_{\mathbf{k} \neq 0} \Phi_{lmp}(\xi, \mathbf{k}) i \mathrm{e}^{-i\mathbf{k} \cdot (\mathbf{x}_i - \mathbf{x}_j)} S_{mp}(\mathbf{x}_j) \ , \tag{28}$$

The amplification factor Φ_{lmp} in the Fourier space sum can be obtained by substituting the expressions of the Fourier space sums of the Laplace (26) and Stokes (14) periodic kernels in (10) leading to

$$\begin{aligned}\Phi_{lmp}(\xi,\mathbf{k}) &= (2k_m\delta_{lp}A(\xi,\mathbf{k})) + k_pB_{lm}(\xi,\mathbf{k}) + k_lB_{mp}(\xi,\mathbf{k}))\mathrm{e}^{-k^2/4\xi^2} \\ &= 8\pi\Big(1+\frac{k^2}{4\xi^2}\Big)\Big(-\frac{2}{k^4}k_lk_mk_p + \frac{1}{k^2}(k_l\delta_{mp}+k_p\delta_{lm}+k_m\delta_{lp})\Big)\mathrm{e}^{-k^2/4\xi^2}\end{aligned}$$

Note that here we removed the $-i$ factor which was already included in the full sum (27).

Omitting the zero wave number in the Fourier space is not problematic since the limit as $\mathbf{k}\to 0$ is zero. However skipping the $\mathbf{k}=0$ term in the case of the Stokeslet implies that the mean pressure gradient balances the forces in the computational cell. Through a proper derivation of the Stokes equations in Fourier space as in [17] it is obtained that this bears no changes for the Stokeslet in a periodic setup, however the pressure gains a non-periodic component. Following [19] we have that the non-periodic component satisfies

$$\frac{\partial\Pi_l}{\partial x_m} = \frac{8\pi}{V}\delta_{lm} ,$$

from where we obtain the non-periodic component of the pressure which will be carried over to the total Stresslet

$$\Pi^0_m(\mathbf{x}) = \frac{8\pi}{V}x_m . \tag{29}$$

The real space sum of the periodic Stresslet is computed analogously to the Fourier one, by replacing in (10) the real space terms given by the formulas in (25) and (13) leading to

$$u_l^{T,r}(\mathbf{x}_i) = \sum_{j=1}^{N}\sum_{\mathbf{p}}{}' \,\Gamma_{lmp}(\xi,\mathbf{x}_j-\mathbf{x}_i+\mathbf{p})S_{mp}(\mathbf{x}_j) , \tag{30}$$

with

$$\Gamma_{lmp}(\xi,\mathbf{x}) = C(\xi,|\mathbf{x}|)\hat{x}_l\hat{x}_m\hat{x}_p + D(\xi,|\mathbf{x}|)(\delta_{lm}\hat{x}_p+\delta_{mp}\hat{x}_l+\delta_{lp}\hat{x}_m) , \tag{31}$$

where $\hat{\mathbf{x}} = \mathbf{x}/|\mathbf{x}|$ and for $r=|\mathbf{x}|$

$$\begin{aligned}C(\xi,r) &= -\frac{6}{r^2}\,\mathrm{erfc}(\xi r) + \Big(-\frac{12\xi}{r\sqrt{\pi}} - \frac{8\xi^3 r}{\sqrt{\pi}}\Big)\mathrm{e}^{-\xi^2r^2} \\ D(\xi,r) &= \frac{4\xi^3}{\sqrt{\pi}}\mathrm{e}^{-\xi^2r^2} .\end{aligned}$$

The self interaction term is not present in this formulation, such as it is not in Beenakker's expressions, since

$$\lim_{|\mathbf{x}|\to 0}(\mathbf{\Gamma}(\mathbf{x}) - \mathbf{T}(\mathbf{x})) = 0 . \tag{32}$$

To restate the entire Stresslet including the non-periodic term we have

$$\begin{aligned}u_l(\mathbf{x}_i) &= \tilde{u}_l(\mathbf{x}_i) + \sum_{j=1}^{N}\sum_{\mathbf{p}}{}' \,\Gamma_{lmp}(\xi,\mathbf{x}_j-\mathbf{x}_i+\mathbf{p})S_{mp}(\mathbf{x}_j) \\ &\quad -\frac{1}{V}\sum_{j=1}^{N}\sum_{\mathbf{k}\neq 0}\Phi_{lmp}(\xi,\mathbf{k})i\mathrm{e}^{-i\mathbf{k}\cdot(\mathbf{x}_i-\mathbf{x}_j)}S_{mp}(\mathbf{x}_j) ,\end{aligned} \tag{33}$$

where the first term $\tilde{u}_l$ arises form the non-periodic component of the pressure (29) and is given by

$$\tilde{u}_l(\mathbf{x}_i) = \sum_{j=1}^{N} -\frac{8\pi}{V}r_m\delta_{lp}S_{mp}(\mathbf{x}_j), \quad \mathbf{r} = \mathbf{x}_i - \mathbf{x}_j . \tag{34}$$

This is consistent with the formulas provided by [24, 25].

4 Comparison with Beenakker formulation

The periodic Stresslet can be used in practice by either the Beenakker decomposition (5) or the Hasimoto decomposition (27) derived here, albeit the decay of the sums is faster in the latter case as we intend to show here. We refer to as *layers* in real space to the number of **p** integers over which we need to sum. Correspondingly the layers in Fourier space are the wave-numbers **k**. To compute either of the sums in the decomposition a number of *layers* has to be considered, after which the truncation can be performed with a satisfactory error tolerance.

The Fourier space sum and the real space sum in either of the decompositions are intertwined through the splitting parameter ξ, however the addition of these two components is independent of ξ. The splitting parameter affects at which cut-off the sums can be truncated to yield an end result with error tolerance δ. Examining the terms in (27) it can be seen that the real space sum converges faster with increasing ξ while the decay of the Fourier space sum is inversely proportional to ξ. Since both sums have a computational complexity of $\mathcal{O}(N^2)$ it is of interest to find the particular ξ which gives a good computational balance between the two sums. Assume that both sums are truncated at a tolerance δ, then since both sums are just as computationally expensive it is advisable to find ξ such that the cost is balanced, *i.e.* the truncation is performed after including the same number of layers in both sums. In Fig. 4 it is illustrated for $\delta = 10^{-8}$ at what value of ξ the Fourier sum and real space sum are balanced for both decompositions Beenakker, and Hasimoto respectively.

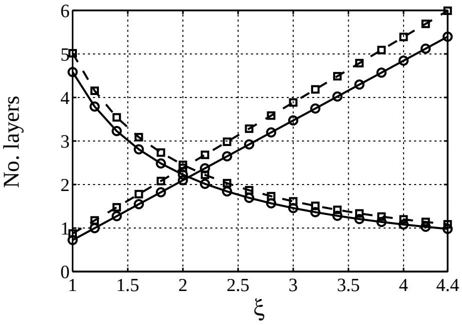

Figure 1: Optimal ξ that balances the real space sum vs. the Fourier space sum. (○) Hasimoto decomposition, (□) Beenkakker decomposition, (solid) real space sum, (dashed) Fourier space sum.

Looking at the expressions of the periodic Stresslet based on the Beenakker decomposition (5) and the Hasimoto decomposition (27) we note that both have the same structure containing sums with exponential decay. However the difference between them lies in the order of the polynomials that multiply the exponentials. In short by analyzing *e.g.* the real space sum (7) and (30) it can be observed that both sums are given by terms of the type $P(\xi, r)\mathrm{e}^{-\xi^2 r^2}$, this of course is the case if we keep in mind that the complementary error function can be approximated by a Gaussian. The difference between the real space sum in the two decompositions, *i.e.* (7), (30) respectively, lies in the order of the polynomial $P(\xi, r)$. In the Beenakker decomposition this polynomial has a leading order of two degrees higher than the one generating the components of the Hasimoto real space sum (30). Both sums can be truncated as soon as $P(\xi, r)\mathrm{e}^{-\xi^2 r^2}$ has decayed under a certain threshold, *i.e.* for ξr sufficiently large. However the exponential decay of $\mathrm{e}^{-\xi^2 r^2}$ is counterbalanced by the polynomial $P(\xi, r)$ which grows with increasing ξr, and thus the leading order of the polynomial has also an impact on the decay of the sum. Nonetheless the polynomial grows with ξr at a slower rate than the decay of the Gaussian. To assess this numerically both real space sums are computed for a set of fixed values of ξ as illustrated in Fig. 2a. The numerical test in Fig. 2a is performed in RMS norm on a set of $N = 20$ randomly distributed particles. The gain in accuracy for the real space sum is of approximately two orders of magnitude higher for the Hasimoto decomposition compared to the Beenakker formulation if both sums are truncated at the same cut-off. Alternatively it can be considered that the truncation can be performed after at a lower cut-off in the case of the Hasimoto decomposition.

Regarding the Fourier space sums we note the same behavior in the relative decay of the Beenakker Fourier space sum versus the Hasimoto Fourier space sum. Without further ado in Fig. 2b is illustrated comparatively the relative decay of the Fourier component in the two decompositions. In Fig. 4 we illustrate the total error at $\xi = 2$ which is the approximate value that balances the two sums for an accuracy of $\delta = 10^{-8}$ and we note a relative difference in the total error of almost two orders of magnitude.

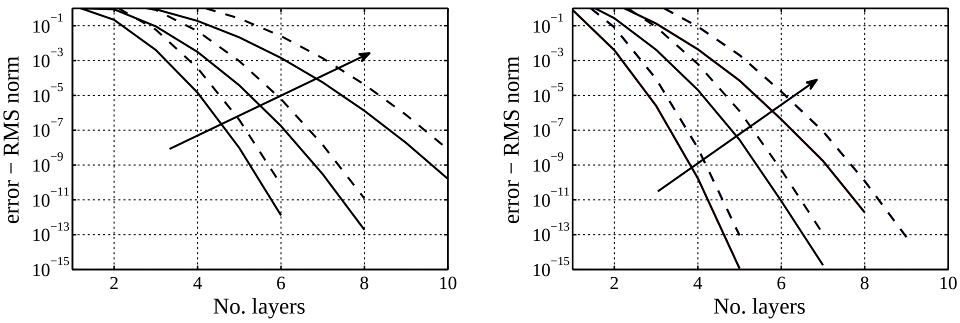

(a) Real space sum error: (solid) Hasimoto decomposition, (dashed) Beenakker decomposition, in direction of the arrow $\xi = 0.5,\ 0.7,\ 0.9$.

(b) Fourier space sum error: (solid) Hasimoto decomposition, (dashed) Beenakker decomposition, in direction of the arrow $\xi = 3,\ 4,\ 5$.

Figure 2: Error in RMS norm for a system of $N = 20$ randomly generated point particles in a domain $[0,\ 1)^3$.

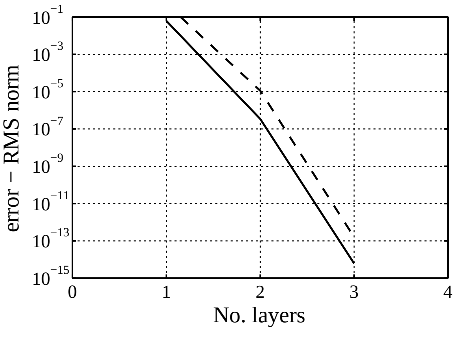

Figure 3: Total error at $\xi = 2$: (solid) Hasimoto decomposition, (dashed) Beenkakker decomposition.

5 Error estimates

The choice of the parameter ξ affects the decay of both the Fourier space sum and real space sum as discussed in Section 4. If the sums in the decomposition are summed directly without any further efficient treatment such as a fast summation method [14, 5] the parameter ξ is to be chosen such that the real space sum is truncated at the same level as the Fourier space one. However in practice as larger and larger systems are considered the involvement of a fast summation method is imperative. In this case proper error estimators are essential to provide a straight-forward means of choosing ξ and further-on the truncation cut-offs.

Most approaches for estimating the truncation error have been initially developed for systems of particles in the field of molecular dynamics. Due to the work of Kolafa *et al.* [12] very sharp error estimates in RMS-norm have been obtained using a statistical approach. These estimates however are valid only for random systems where the contributions from other particles are assumed to be uncorrelated. Alternatively upper bounds can be computed by making less limited assumptions on the homogeneity of the particles distribution [13]. The physical problems where the periodic Stresslet comes into use pertain mainly to the field of multi-phase flows where the Stresslet is being integrated over surfaces of immersed objects, *e.g.* [15]. The points stemming from the corresponding discrete problem are not strongly inhomogeneous, however for the choice of parameters it is preferable to have sharp estimates that are then adjusted to the degree of inhomogeneity rather than overestimating right from the start. Another advantage of a root mean square error estimate is that the scaling with the system size, *i.e.* N the number of particles, is decoupled from the actual estimate. To this end the path followed in the present work is the one set forth by Kolafa *et al.* [12] with the note of caution that real problems may lead to larger errors that need to be accounted for.

Real space sum error estimate

Let us define the real space sum component of the Hasimoto decomposition (27) to be given as

$$u_l(\mathbf{x}_i) = \sum_{j=1}^{N} \sum_{\mathbf{p}}{}' \, \Gamma_{lmp}(\xi, \mathbf{x}_j - \mathbf{x}_i + \mathbf{p}) S_{mp}(\mathbf{x}_j) \ , \tag{35}$$

where $S_{mp}(\mathbf{x}) = f_m(\mathbf{x}) n_p(\mathbf{x})$, with $\mathbf{n}$ being the normal vector, $\mathbf{f}$ the point force and with Γ_{lmp} as in (30). The root mean square error of the variable $\mathbf{u}$ with respect to the exact solution $\tilde{\mathbf{u}}$ is defined as

$$\Delta\mathbf{u} = \sqrt{\frac{1}{N}\sum_{i=1}^{N}(\mathbf{u}(\mathbf{x}_i) - \tilde{\mathbf{u}}(\mathbf{x}_i))} = \sqrt{\frac{1}{N}\sum_{i=1}^{N}(\Delta\mathbf{u}(\mathbf{x}_i))^2} \ . \tag{36}$$

By making the ansatz that the error for one particle at position $\mathbf{x}_i$ originates from all other particles and is proportional to the force densities $\mathbf{f}$ and the normals to the surface $\mathbf{n}$ we can write

$$\Delta\mathbf{u}(\mathbf{x}_i) = \sum_{\substack{j=1 \\ j\neq i}}^{N} \chi_{lmp}(\xi, \mathbf{x}_j - \mathbf{x}_i) S_{mp}(\mathbf{x}_j) \ , \tag{37}$$

with

$$\chi_{lmp}(\mathbf{x}) = \sum_{|\mathbf{x}+\mathbf{p}|>r_c} \Gamma_{lmp}(\xi, \mathbf{x}+\mathbf{p}) \ . \tag{38}$$

Following Kolafa et. al. [12] and Deserno et. al. [4] the average over all configurations, using the angular brackets notation, can be written

$$< \Delta\mathbf{u}(\mathbf{x}_i)^2 >= \sum_{\substack{j=1\\j\neq i}}^{N}\sum_{\substack{k=1\\k\neq i}}^{N} \chi_{lmp}(\xi, \mathbf{x}_j - \mathbf{x}_i) S_{mp}(\mathbf{x}_j) \chi_{lmp}(\xi, \mathbf{x}_k - \mathbf{x}_i) S_{mp}(\mathbf{x}_k) \ . \tag{39}$$

By expanding the terms in (39) and assuming that contributions from different particles are uncorrelated, *i.e.* $< \Gamma_{lmp}(\xi, \mathbf{x}_j - \mathbf{x}_i) \cdot \Gamma_{lmp}(\xi, \mathbf{x}_k - \mathbf{x}_i) >= \delta_{jk}\Gamma^2$, where $\Gamma^2 = \sum\limits_{j,l,m=1,3} \Gamma^2_{lmp}$ is given by the tensor dot product. With the same notation for the tensor dot product $S^2 = \sum\limits_{m,p=1,3} S^2_{mp}$ and $\chi^2 = \sum\limits_{|\mathbf{x}+\mathbf{p}|>r_c} \Gamma^2$ we obtain the error

$$< \Delta\mathbf{u}(\mathbf{x}_i)^2 >= \chi^2 S^2 \ . \tag{40}$$

Deserno et. al [4] reasons that based on the law of large numbers the error is ultimately given by

$$\Delta\mathbf{u} \approx \frac{\chi S^2}{\sqrt{N}} \tag{41}$$

It remains thus to evaluate χ^2 which is to be done in two steps. First the sum over $\mathbf{p}$ is to be approximated by an integral, which in a second step is computed in spherical coordinates. Thus we have

$$\begin{aligned}
\chi^2_{lmp} &= \sum_{|\mathbf{x}+p|>r_c} \sum_{j=1}^{3}\sum_{l=1}^{3}\sum_{m=1}^{3} \Gamma^2_{lmp}(\xi, \mathbf{x}+\mathbf{p}) \\
&\approx \int_{r_c}^{\infty}\int_{0}^{\pi}\int_{0}^{2\pi} \sum_{j=1}^{3}\sum_{l=1}^{3}\sum_{m=1}^{3} \Gamma^2_{lmp}(\mathbf{x}) \sin(\theta) r^2 \mathrm{d}\phi \mathrm{d}\theta \mathrm{d}r \ ,
\end{aligned}$$

with

$$\Gamma^2_{lmp}(\xi, \mathbf{x}) = [C(\xi, |\mathbf{x}|)\hat{x}_j\hat{x}_l\hat{x}_m + D(\xi, |\mathbf{x}|)(\delta_{jl}\hat{x}_m + \delta_{lm}\hat{x}_j + \delta_{mj}\hat{x}_l)]^2 \ ,$$

where

$$\begin{aligned}
C(\xi, r) &= -\frac{6}{r^2}\operatorname{erfc}(\xi r) + \left(-\frac{12\xi}{r\sqrt{\pi}} - \frac{8\xi^3 r}{\sqrt{\pi}} \right) \mathrm{e}^{-\xi^2 r^2} \\
D(\xi, r) &= \frac{4\xi^3}{\sqrt{\pi}} \mathrm{e}^{-\xi^2 r^2} \ .
\end{aligned}$$

Using the commutativity of the integral with the summation we need to evaluate terms of the type

$$\int_{r_c}^{\infty}\int_{0}^{\pi}\int_{0}^{2\pi} \Gamma^2_{lmp}(\xi, r\sin\theta\cos\phi, r\sin\theta\sin\phi, r\cos\theta) \sin(\theta) r^2 \mathrm{d}\phi \mathrm{d}\theta \mathrm{d}r \ .$$

If the complementary error function $\operatorname{erfc}(\xi r)$ is approximated by $\mathrm{e}^{-\xi^2 r^2}/\sqrt{\pi}\xi r$ for positive arguments then Γ_{lmp} becomes the product of a rational polynomial with a Gaussian. In consequence the term $\mathrm{e}^{-\xi^2 r^2}$ which does not have any angular dependence can be neglected while computing the inner integrals and reintroduced only upon integrating from r_c to ∞. Since we need to consider configuration averages each of the integrals in the angular direction should be averaged, thus the integral over the angle θ is to be divided by the area of the integral, *i.e.* π, while the integral over ϕ is divided by a factor 2π. The end result is a polynomial $P(\xi, r)$ multiplying $\mathrm{e}^{-2\xi^2 r^2}$. Such terms can be integrated according to the formula

$$\int\limits_{r_c}^{\infty} f(r)\mathrm{e}^{-Br^2}\mathrm{d}r \approx \frac{e^{-Br_c^2} f(r_c)}{2Br_c} \; , \tag{42}$$

valid for $B > 0$ and any function f which fulfills $\mathrm{d}[f(r)/2Br]/\mathrm{d}r \ll f(r)$ for $r \geq r_c$.

Although not complicated in nature but rather tedious the computations were performed using the MATLAB Symbolic Toolbox to obtain

$$\begin{aligned} \chi^2 \quad = \quad & \frac{2\mathrm{e}^{-2\xi^2 r_c^2}}{\pi^2 \xi^4 r_c^5}(16\xi^8 r_c^8 - 48\xi^8 r_c^7 + 60\xi^8 r_c^6 + 48\xi^6 r_c^6 \qquad (43) \\ & -72\xi^6 r_c^5 + 60\xi^4 r_c^4 - 36\xi^4 r_c^3 + 36\xi^2 r_c^2 + 9) \; . \end{aligned}$$

To obtain a more accurate comparison of the Hasimoto decomposition with the Beenakker formulation the same steps were applied to the Beenakker real space sum (7) obtaining

$$\begin{aligned} \chi^2 \quad = \quad & \frac{2\mathrm{e}^{-2\xi^2 r_c^2}}{\pi^2 \xi^4 r_c^5}(64\xi^{12} r_c^{12} - 192\xi^{12} r_c^{11} + 240\xi^{12} r_c^{10} - 64\xi^{10} r_c^{10} + 480\xi^{10} r_c^9 \\ & -960\xi^1 0 r_c^8 - 80\xi^8 r_c^8 - 48\xi^8 r_c^7 + 960\xi^8 r_c^6 - 216\xi^6 r_c^5 \\ & +60\xi^4 r_c^4 - 144\xi^4 r_c^3 + 36\xi^2 rc^2 + 9)) \; . \end{aligned} \tag{44}$$

In Fig. 4a we compare the decay of the error in RMS-norm for the real space sum with the computed error estimate for Hasimoto decomposition, while as in Fig. 4b we provide the corresponding results for the Beenakker decomposition.

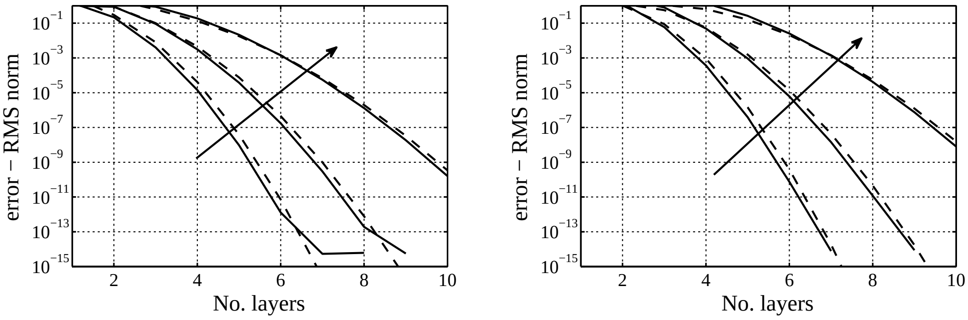

(a) Real space sum error (Hasimoto decomposition), in the direction of the arrow $\xi = 0.5,\ 0.7,\ 0.9$.

(b) Real space sum error (Beenakker decomposition), in the direction of the arrow $\xi = 0.5,\ 0.7,\ 0.9$.

Figure 4: Decay of the solution: $(*)$ – computed error in RMS norm; $(\circ)$ – error estimate.

Fourier space sum error estimate

The Fourier space sum can be analyzed similarly according to Kolafa et. al. [12], however in our case this leads to an error estimate that overestimates the solution severely. The decay of the Fourier space sum depends on the wavenumber $\mathbf{k}$ and the splitting parameter ξ, however the expression of the sum includes also the term $i\mathrm{e}^{-i\mathbf{k}\cdot\mathbf{x}}$ which ties in with the particle configuration. Let us consider the Fourier space sum of the Hasimoto decomposition where the wavenumbers $\mathbf{k} = 2\pi/L\mathbf{k}$ with $\mathbf{k} \in \mathbb{Z}^3$ are normalized, *i.e.* $\hat{\mathbf{k}} = \mathbf{k}/|\mathbf{k}|$

$$u_l(\mathbf{x}_i) = -\frac{1}{V}\sum_{\mathbf{k}\neq 0}\Phi_{lmp}(\xi,\mathbf{k})\sum_{j=1}^{N} S_{mp}(\mathbf{x}_j) i\mathrm{e}^{-i\mathbf{k}\cdot(\mathbf{x}_j-\mathbf{x}_i)} \ , \tag{45}$$

where $S_{mp}(\mathbf{x}) = f_m(\mathbf{x})n_p(\mathbf{x})$, with $\mathbf{n}$ being the normal vector and $\mathbf{f}$ the point force. If we consider that the wavenumbers $\mathbf{k}$ are normalized, *i.e.* $\hat{\mathbf{k}} = \mathbf{k}/|\mathbf{k}|$, we can write

$$\Phi_{lmp}(\xi,\mathbf{x},\mathbf{k}) = \frac{8\pi}{k}\left(1+\frac{k^2}{4\xi^2}\right)\Big(-2\hat{k}_l\hat{k}_m\hat{k}_p + (\hat{k}_l\delta_{mp} + \hat{k}_p\delta_{lm} + \hat{k}_m\delta_{lp})\Big)\mathrm{e}^{-k^2/4\xi^2} \ . \tag{46}$$

With the same approach as for the real space sum and by using the Euler formula $i\mathrm{e}^{-i\mathbf{k}\cdot(\mathbf{x}_j-\mathbf{x}_i)} = \sin(\mathbf{k}\cdot\mathbf{x})$ we have

$$\begin{aligned}
\chi^2_{lmp} &= \sum_{|\mathbf{k}+\mathbf{p}|>k_c}\sum_{j=1}^{3}\sum_{l=1}^{3}\sum_{m=1}^{3}\Phi^2_{lmp}(\xi,\mathbf{k}+\mathbf{p})\sin(\mathbf{k}\cdot\mathbf{x})^2 \\
&\approx \int_{k_c}^{\infty}\int_{0}^{\pi}\int_{0}^{2\pi}\sum_{j=1}^{3}\sum_{l=1}^{3}\sum_{m=1}^{3}\Phi^2_{lmp}(\xi,\mathbf{k})\sin(\mathbf{k}\cdot\mathbf{x})^2\sin(\theta)k^2\mathrm{d}\phi\mathrm{d}\theta\mathrm{d}k \ .
\end{aligned}$$

The idea used by Kolafa is to consider the angle between $\mathbf{k}$ and $\mathbf{r}$ given as $\mathbf{k}\cdot\mathbf{x} = 2\pi kr/L\cos\theta$ and take θ to be the same as the angle used in the transformation of the wavenumber $\mathbf{k}$ in spherical coordinates, in other words to assume that the vector $\mathbf{x}$ is the very same as the third coordinate of the wavenumber $\mathbf{k}$. This leads to a change of variables $\cos\theta \to z$ and $\sin\theta\mathrm{d}\theta \to \mathrm{d}z$.

Let us denote the tensorial part of (46) by

$$A_{lmp} = -2\hat{k}_l\hat{k}_m\hat{k}_p + \hat{k}_l\delta_{mp} + \hat{k}_p\delta_{lm} + \hat{k}_m\delta_{lp} \ .$$

For the inner integrals we obtain then

$$\sum_{j=1}^{3}\sum_{l=1}^{3}\sum_{m=1}^{3}\int_{0}^{2\pi}\int_{-1}^{1}A^2_{lmp}\sin(2\pi kzr/L)^2\mathrm{d}z\mathrm{d}\phi = \frac{28\pi kr/L - 7\sin(4\pi kr/L)}{8\pi kr/L} \leq 14 \ . \tag{47}$$

The answer obtained which depends on a sine wave cannot be integrated over k without further assumptions. The very same assumptions made by Kolafa for the electrostatics problem are not possible here. We can however assume that since $x - \sin(x) < 2x$ the integral in (47) can be easily computed. Integrating further over k from k_c to infinity gives

$$\chi^2 = \frac{14(\pi^2k_c^2+\xi^2)^2}{\pi^3k_c\xi^2}\mathrm{e}^{-2\pi^2k_c^2/\xi^2} \ . \tag{48}$$

Similarly for the Beenakker decomposition we obtain

$$\chi^2 = \frac{28(2\pi^4k_c^4+\pi^2k_c^2\xi^2+\xi^4)^2}{\pi^3k_c\xi^6}\mathrm{e}^{-2\pi^2k_c^2/\xi^2} \ . \tag{49}$$

In Fig. 4a we compare the decay in error in RMS-norm for the Fourier space sum with the computed error estimate for the Hasimoto decomposition, while as in Fig. 4b we provide the corresponding results for the Beenakker decomposition.

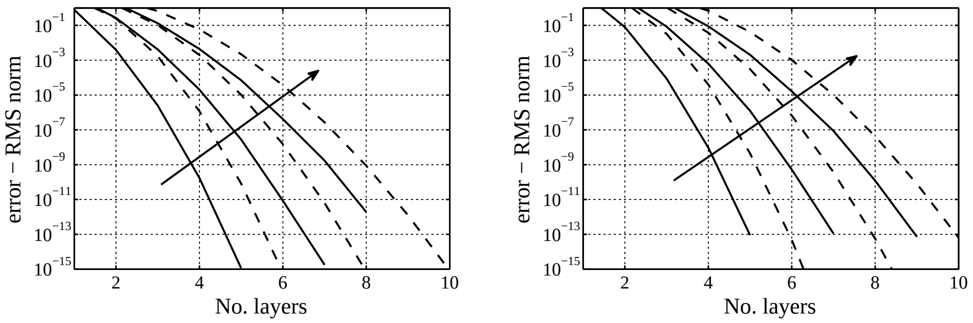

(a) Fourier sum error (Hasimoto decomposition), in direction of the arrow $\xi = 3,\ 4,\ 5$.

(b) Fourier sum error (Beenakker decomposition), in direction of the arrow $\xi = 3,\ 4,\ 5$.

Figure 5: Decay of the solution: (solid) – computed error in RMS norm; (dashed) – error estimate.

6 Choice of truncation parameters

For any decomposition of a periodic kernel the most important question that arises when using it in a simulation is how to choose the cut-offs r_c for the real space sum and k_c for the Fourier space sum for a given ξ. Reversely and of equal significance it is important to be able to identify what ξ gives cut-offs for which the computational cost of the method is well balanced. The error estimates derived in Section5 are the mathematical tool to use when seeking to identify the optimal parameters.

The error for the real space sum is given as

$$\Delta \mathbf{u} \approx \frac{\chi S^2}{\sqrt{N}} \ , \tag{50}$$

where $\chi = P(\xi, r_c)\mathrm{e}^{-2\xi^2 r_c^2}$ with P being a polynomial that depends on the decomposition. The rather extensive expression of $P(\xi, r_c)$ can be reduced in practice to the leading order term, *i.e.* for the Hasimoto decomposition (43) can be used in the form

$$\chi \approx \sqrt{\frac{32\xi^8 r_c^8 \mathrm{e}^{-2\xi^2 r_c^2}}{\pi^2 \xi^4 r_c^5}} \approx \frac{4\sqrt{2}\xi^2 r_c^{3/2} \mathrm{e}^{-\xi^2 r_c^2}}{\pi} \tag{51}$$

If the computations are to be performed with an accuracy δ for a given ξ then the real space sum has to be truncated at a level δ which means that the equation $\chi \approx \delta$ has to be solved to yield the desired r_c. Note that the total error scales with the number of particles and this also has to be taken into consideration when requesting a total error tolerance to be met.

A similar type of reasoning can be applied to the Fourier space sum truncation estimate to obtain for a given ξ the cut-off k_c.

7 Conclusions

As an alternative to the Beenakker decomposition, which was widely used for treating the kernel of the stress tensor in a periodic framework, a new decomposition that yields faster decaying sums was derived. The new splitting scheme was pursued motivated by the observation that the Hasimoto decomposition of the Stokeslet (fundamental solution of the Stokes equations) has a faster convergence than the Beenakker decomposition.

The stress tensor can be expressed in terms of the pressure and the gradient of the velocity. Noting that the pressure can be expressed in terms of the fundamental solution of the Laplace equation a formula that provides the kernel of the stress tensor in terms of the kernels of the Stokes and Laplace equations is established. The very same formula can be applied to the periodized kernels of both Laplace and Stokes to attain the periodic Stresslet. To assure that the periodic Stresslet obtained in the aforementioned fashion has a symmetric structure we have derived a decomposition of the periodic kernel of the Laplace equation that corresponds to the Hasimoto decomposition for the Stokeslet. The new expression for the periodic Stresslet is compared to the pre-existing one due to Beenakker and a faster decay of the sums is being noted. The truncation error at the truncation cut-off is of two orders of magnitude lower for the new decomposition. This implies that by using the decomposition derived here either a gain in accuracy is obtained or alternatively the truncation can be performed at lower cut-offs.

The derivation was supplemented by error estimates in RMS norm which offer a guideline in choosing the truncation cut-offs for both the Fourier space and the real space sum.

Acknowledgements

Ludvig af Klinteberg is gratefully acknowledged for providing a code of an initial implementation of the Beenakker formulation.

Appendix A Ewald decomposition for Laplace

If we express the split of the sum due to N electrostatic potentials as

$$u(\mathbf{x}_i) = \sum_{j=1}^{N} {\sum_{\mathbf{p}}}' \Gamma_L(\xi, \mathbf{x}_j - \mathbf{x}_i + \mathbf{p}) f_j + \frac{1}{V} \sum_{j=1}^{N} \sum_{\mathbf{k}\neq 0} \Phi_L(\xi, \mathbf{k}) \mathrm{e}^{-i\mathbf{k}\cdot(\mathbf{x}_j - \mathbf{x}_i)} f_j + u_{self}(\mathbf{x}_i) \ , \tag{A.1}$$

where now $u_{self}(\mathbf{x}_i) = -2\xi/\sqrt{\pi} f_i$ and

$$\Phi_L(\xi, \mathbf{k}) = A(k) e^{-k^2/4\xi^2} \ , \quad A(k) = \frac{1}{k^2} \ , \tag{A.2}$$

and

$$\Gamma_L(\xi, \mathbf{x}) = \frac{\mathrm{erfc}(\xi r)}{r} \ . \tag{A.3}$$

Appendix B Hasimoto-Ewald mixed decomposition for Laplace

Using the Ewald decomposition (A.1) instead of the Hasimoto based one (23) a different decomposition of the Stresslet can be obtained

$$\begin{aligned} u_l(\mathbf{x}_i) \quad = \quad & \sum_{j=1}^{N} {\sum_{\mathbf{p}}}' \Gamma_{lmp}(\xi, \mathbf{x}_j - \mathbf{x}_i + \mathbf{p}) S_{mp}(\mathbf{x}_j) && \text{(B.1)} \\ & - \frac{1}{V} \sum_{j=1}^{N} \sum_{\mathbf{k}\neq 0} \Phi_{lmp}(\xi, \mathbf{k}) i \mathrm{e}^{-i\mathbf{k}\cdot(\mathbf{x}_i - \mathbf{x}_j)} S_{mp}(\mathbf{x}_j) \ , \end{aligned}$$

The real space sum is given by terms

$$\begin{aligned}\Gamma_{lmp}(\mathbf{x}) &= -\frac{6\,\mathrm{erfc}(\xi r)}{r^5}x_l x_m x_p \\ &+\Big(-\frac{12\xi}{\sqrt{\pi}r^4}x_l x_m x_p - \frac{8\xi^3}{\sqrt{\pi}r^2}x_l x_m x_p + \frac{4\xi^3(x_l\delta_{mp} + x_p\delta_{lm})}{\sqrt{\pi}}\Big)\mathrm{e}^{-\xi^2 r^2}\end{aligned} \qquad \text{(B.2)}$$

Analogously for the Fourier space sum we obtain by substituting the expressions of Φ_S and Φ_L the amplification factor

$$\Phi_{lmp}(\xi, \mathbf{k}) = (2k_m\delta_{jm}A(\xi, \mathbf{k})) + k_p B_{jl}(\xi, \mathbf{k}) + k_l B_{lm}(\xi, \mathbf{k})) \qquad \text{(B.3)}$$

with $A(\xi, \mathbf{k}))$ as in (A.2) and $B(\xi, \mathbf{k})$ as in (15). This decomposition does not share the same symmetry as the Beenakker formulation (5), however both the real space sum and Fourier space sum decay at a rate similar to the one of the newly derived Hasimoto decomposition (27).

References

[1] C. W. J. Beenakker. Ewald sums of the Rotne-Prager tensor. *J. Chem. Phys.*, 85:1581–1582, 1986.

[2] J. F. Brady and G. Bossis. Stokesian dynamics. *Annu. Rev. Fluid Mech.*, 20:111–157, 1988.

[3] F. R. Cunha and M. Loewenberg. A study of emulsion expansion by a boundary integral method. *Mech. Res. Commun.*, 30(6):639–649, 2003.

[4] M. Deserno and C. Holm. How to mesh up Ewald sums. II. an accurate error estimate for the particle-particle-particle-mesh algorithm. *J. Chem. Phys.*, 109(18):7694–7701, 1998.

[5] U. Essmann, L. Perera, M. L. Berkowitz, T. Darden, H. Lee, and L. G. Pedersen. A smooth particle mesh Ewald method. *J. Chem. Phys.*, 103(19):8577–8593, 1995.

[6] P. P. Ewald. Die Berechnung optischer und elektrostatischer Gitterpotentiale. *Ann. Phys.*, 369(3):253–287, 1921.

[7] X.-J. Fan, N. Phan-Thien, and R. Zheng. Completed double layer boundary element method for periodic suspensions. *Z. Angew. Math. Phys.*, 49:167–193, 1998.

[8] J. Happel and H. Brenner. *Low Reynolds Number Hydrodynamics.* Kluwer, Dordrecht, The Netherlands, 1983.

[9] H. Hasimoto. On the periodic fundamental solutions of the Stokes equations and their application to viscous flow past a cubic array of spheres. *J. Fluid Mech.*, 5:317–328, 1959.

[10] J. P. Hernández-Ortiz, J. J. de Pablo, and M. D. Graham. Fast computation of many-particle hydrodynamic and electrostatic interactions in a confined geometry. *Phys. Rev. Lett.*, 98(140602), 2007.

[11] D. M. Heyes and F. von Swol. The electrostatic potential and field in the surface region of lamina and semi infinite point charge lattices. *J. Chem. Phys.*, 75(10):5051–5058, 1981.

[12] J. Kolafa and J. W. Perram. Cutoff errors in the Ewald summation formulae for point charge systems. *Mol. Simul.*, 9(5):351–368, 1992.

[13] D. Lindbo and A.-K. Tornberg. Spectrally accurate fast summation for periodic Stokes potentials. *J. Comput. Phys.*, 229(23):8994–9010, 2010.

[14] D. Lindbo and A.-K. Tornberg. Spectral accuracy in fast Ewald-based methods for particle simulations. *J. Comput. Phys.*, 230(24):8744–8761, 2011.

[15] M. Loewenberg and E. J. Hinch. Numerical simulation of a concentrated emulsion in shear flow. *J. Fluid Mech.*, 321:395–419, 1996.

[16] O. Marin, K. Gustavsson, and A.-K. Tornberg. A highly accurate boundary treatment for confined Stokes flow. *Comput. Fluids*, 66:215–230, 2012.

[17] C. Pozrikidis. Computation of periodic Green's functions of Stokes flow. *J. Eng. Math.*, 30(4):79–96, 1996.

[18] C. Pozrikidis. *Introduction to Theoretical and Computational Fluid Dynamics*. Oxford University Press, Oxford, U.K., 1996.

[19] C. Pozrikidis. Orbiting motion of a freely suspended spheroid near a plane wall. *J. Fluid Mech.*, 541:105–114, 2005.

[20] F. J. Rizzo, D. J. Shippy, and M. Rezayat. A boundary integral equation method for radiation and scattering of elastic waves in three dimensions. *Int. J. Num. Meth. Eng.*, 21(1):115–129, 1985.

[21] D. Saintillan, E. Darve, and E. S. G. Shaqfeh. A smooth particle-mesh Ewald algorithm for Stokes suspension simulations: The sedimentation of fibers. *Phys. Fluids*, 17(033301), 2005.

[22] A.-K. Tornberg and K. Gustavsson. A numerical method for simulations of rigid fiber suspensions. *J. Comput. Phys.*, 215:172–196, 2005.

[23] L. C. Wrobel, D. Soares Jr., and C. L. Das Bhaumik. Drop deformation in Stokes flow through converging channels. *Eng. Anal. Bound. Elem.*, 33(7):993–1000, 2009.

[24] H. Zhao, A. H. G. Isfahani, L. N. Olson, and J. B. Freund. A spectral boundary integral method for flowing blood cells. *J. Comput. Phys.*, 229:3726–3744, 2010.

[25] A. A. Zick and G. M. Homsy. Stokes flow through periodic arrays of spheres. *J. Fluid Mech.*, 115:13–26, 1982.

A quadrature rule for the singular kernels of Laplace and Stokes equations over a class of parameterizable surfaces

Oana Marin
Linné FLOW Centre, KTH-SCI (NA), SE-100 44 Stockholm, Sweden

Abstract

A third order accurate corrected trapezoidal is developed to integrate numerically the singular kernels of Laplace and Stokes equations over a class of parameterizable surfaces with special focus on cylindrical surfaces. The corrected trapezoidal rule has so far been applied to flat surfaces on equidistant grids for the kernels of Laplace and Stokes. Corrected trapezoidal rules are based on the standard trapezoidal rule where the singular point, which is assumed to be a discretization point, is omitted. To account for the omitted point corrected weights are computed which are applied locally in a vicinity of, and at, the singular point. For general surfaces the weights depend on the position of the singular point on the surface leading to specific weights for each grid point. However we identify a special class of manifolds for which universal weights, independent of the position relative to the surface, can be computed. We select from this class of surfaces the model problem of a cylinder for which we explicitly develop and validate quadrature rules for both the kernel of Stokes and Laplace equations. This quadrature rule can be applied to simulations of pipe flows in conjunction with *e.g.* particle suspensions, fiber suspensions, swimming micro-organisms. Here we validate the obtained quadrature rule by computing the drag on a spheroidal particle positioned on the inner axis of a cylinder.

1 Introduction

Numerous mathematical models in the fields of electrostatics (Laplace equation) [13], fluid mechanics (Stokes equations) [18], electromagnetics (Helmholtz equation) [14] rely upon integral equations. To name a few of the advantages of an integral equation formulation: suitable for free-space problems since they can be stated over the surfaces of relevant boundaries, computationally efficient since they reduce the dimensionality of a problem (three-dimensional problems are reduced to two-dimensional problems stated over surfaces), easily extensible to many-body problems through superposition of solutions. However the drawback is that the kernels of these equations, the Green's functions, are typically singular functions which are not easily integrable numerically to high accuracy, and the associated discrete system yields upon numerical treatment dense and in certain cases ill-conditioned matrices.

To evaluate numerically boundary integrals the collocation method is mostly used [15], by which the solution is enforced to be valid at a set of grid points. From the collocation method emerges: the boundary element method [20] and Nyström's method [7]. In the boundary element method the solution is represented as a linear combination of basis functions defined over the underlying surface. To this end the surface is meshed using *e.g.* triangular elements. Nyström's method however solves the integral equation at the grid points, which are the same as the collocation points. Typically Nyström's method is used in conjunction with parameterizable surfaces. Although the boundary element method has a higher degree of flexibility in handling integration over irregular surfaces, the Nyström's method has the advantage that it may yield matrices with a homogeneous structure [16]. Using the Nyström's method the problem of integrating a singular kernel becomes geometry dependent. For the integration of the kernel of the Laplace equation over the surface of a spheroidal object, Atkinson [4] used mappings to the unit sphere to eliminate the singularity of the kernel prior to using a numerical integration scheme. To increase the order of accuracy of the integration Sidi [24] introduced a class of transformations to periodize the integrand such that the trapezoidal rule may achieve high accuracy. A hybrid approach to handling the singularity is the singularity removal technique [18] by which the integral is split into two integrals; one singular but integrable analytically and one non-singular and integrable numerically.

The numerical integration of singular kernels can be performed by starting with a known quadrature rule, *e.g.* the trapezoidal rule where we skip the singular point, referred to as the punctured trapezoidal rule. To account for the omitted singular point one has to compute modified weights which are applied in a vicinity of and at the singular points where standard techniques cannot be used. These modified weights can be computed as in [17, 2] for a specific kernel and the specific surface over which the numerical integration is to be performed. This type of approach has been used to integrate the kernel of the Laplace equation in three dimensions [2], or the two-dimensional kernel over a circle [1]. Similarly the kernel of the Stokes equations has been integrated over a flat plate [16].

The present work is based on the same method of designing a modified trapezoidal rule for the Laplace kernel [17] and the Stokes kernel [16] over a flat surface. We extend the principles used in the aforementioned articles to integrate the kernels of Laplace and Stokes over smooth parameterizable surfaces. In both [17, 16] analytical integration was used to obtain the modified correction weights. This procedure is however not possible in the case of a curvilinear surface since the analytical integrals are too difficult to compute. Alternatively we use repeated Richardson extrapolation to obtain the corrected weights from a low order punctured trapezoidal rule used to approximate the singular integrals. Although the quadrature rules designed in [17, 16] are high order, as high as $\mathcal{O}(h^{13})$ a curvilinear surface imposes a higher degree of difficulty and the present work is restricted to obtaining rules of only $\mathcal{O}(h^3)$. As mentioned earlier a weight computed through the techniques in [17, 16] is not independent of the position of the singularity on the surface, as is the case of a curvilinear surface. As will be shown it is not straightforward to obtain an universal modified weight unless the surface has certain symmetry properties. This translates mathematically into the requirement of having a parametrization of the surface which is periodic in all spatial directions. To this end we establish a class of surfaces for which it is possible to obtain universal modified weights.

Although Nyström's method seems cumbersome since it requires different integration techniques according to which kernel and what type of surface is to be integrated, it has the great advantage of yielding, under certain circumstances, matrices with a specific ordered structure, *e.g.* symmetric block-Toeplitz with circulant sub-blocks [16]. This is increasingly interesting when we deal with large problems since, as mentioned earlier, boundary integral methods lead to discrete systems given by non-sparse matrices which are difficult to store in memory. If the structure of the matrix is known before-hand then the matrix can be stored by using only a small set of matrix generators which lowers the burden on the memory in computer implementations. The kernels of Laplace and Stokes equations in three dimensions on which we shall focus here are determined by distances between points in the domain of integration. These distances will display a certain pattern under a homogeneous discretization of the surface if the surface has a level of isotropy, *e.g.* flat surface or cylindrical and spheroidal surface. The matrix arising from the discretization will then contain entries which repeat themselves, and we shall refer to such a matrix as a Toeplitz-like matrix. Such a matrix can be stored efficiently in the memory since it is generated by a small number of columns, *i.e.* three columns for a flat surface [16], also three columns but stemming from a different structure for the case of a periodically replicated cylinder as we shall see in the present work. These matrices may also lead to efficient algebraic treatments by using the FFT transforms as it will be briefly discussed in the this manuscript.

Keeping in mind these considerations on the advantages of the Nyström's method in conjunction with a corrected trapezoidal rule we explicitly develop here a third order method for the kernels of Laplace and Stokes for a cylindrical surface. The quadrature rules are then tested numerically and the matrix structure arising from the discretization is investigated. The special interest taken in the discretization of a cylinder is justified by the numerous pipe flow simulations which are so far performed using the boundary element method [21, 22]. To make way to applications we validate the quadrature rules developed here on the classical problem of the drag on a sedimenting sphere positioned at the axis of a cylinder, cylinder which is periodically replicated in the axial direction. Comparisons with a known asymptotic solution for an infinite cylinder are performed and convergence is obtained with increasing periodic lengths in the axial direction.

Section 2 of this manuscript sets the mathematical background necessary for developing a corrected trapezoidal rule for a curvilinear surface. The techniques introduced here for computing modified weights are tested on a general surface. In Section 2 it is established which class of surfaces allow for a weight independent of the position of the singularity on the surface. One of the surfaces in this class is that of a cylinder periodic in the axial direction. In Section 3 we develop quadrature rules for the kernels of Laplace and Stokes over the surface of a cylinder. In Section 4 the quadrature rule for the Stokeslet is validated numerically. The physical problem of a sphere sedimenting along the inner axis of a cylinder is compared to known analytic solutions. A discussion on the advantages of the developed quadrature rule follows in Section 5. The manuscript is then concluded with some final remarks on possible future developments.

2 Theoretical considerations — simply corrected trapezoidal rule

Corrected trapezoidal rules for singular functions have been studied for a long time, some of the most cited works surrounding this topic are probably the articles by [23, 3]. The principles of integrating the three-dimensional kernels of the Laplace equation and the Stokes equations over flat surfaces using such quadrature rules were introduced in [17], [16] respectively. Prior to this the corrected trapezoidal rule was applied in a two-dimensional framework to the kernel of the Laplace equation over a circle [1]. Here we extend the previous work in [17, 16] to parameterizable surfaces. To this end we outline how to obtain a simply corrected trapezoidal rule for a general surface. The correction weight depends on the position of the singularity on the surface. Thus we seek to identify a class of surfaces that yield a universal weight independent of position.

Numerical integration of singularities over parametrized surfaces

Consider a set of points $\mathbf{x}$ in a square domain $D = [0,\ a_1] \times [0,\ a_2]$ and a parameterizable surface S given by points $\mathbf{y} = \gamma(\mathbf{x})$, through a vector valued smooth function γ. Assume we intend to evaluate numerically over S the following integral

$$\int\limits_S s(\mathbf{y}-\mathbf{y}_0) f(\mathbf{y}) \mathrm{d}S_{\mathbf{y}} \ , \tag{1}$$

where $f(\mathbf{y})$ is a smooth function $\mathbf{y}_0$ a point on the surface of S, *i.e.* $\mathbf{y}_0 = \gamma(\mathbf{x}_0)$, and $s(\mathbf{y}-\mathbf{y}_0)$ is a singular but integrable function ($\mathbf{y} = \mathbf{y}_0$ singular point). This is in fact a convolution, $(s * f)(\mathbf{y}_0)$, which with the parameterization γ becomes $(s * f)(\gamma(\mathbf{x}_0))$. Therefore we can express the integral over the surface S in terms of an integral over the square domain D as

$$\int\limits_S s(\mathbf{y}-\mathbf{y}_0)f(\mathbf{y})\mathrm{d}S_{\mathbf{y}} = \int\limits_D s \circ (\gamma(\mathbf{x}) - \gamma(\mathbf{x}_0))(f \circ \gamma)(\mathbf{x})\left|\frac{\partial \gamma}{\partial x_1} \times \frac{\partial \gamma}{\partial x_2}\right|\mathrm{d}D_{\mathbf{x}} \ , \tag{2}$$

where $|\frac{\partial \gamma}{\partial x_1} \times \frac{\partial \gamma}{\partial x_2}|$ is the surface element associated with the change of variables. Further notations are however necessary to render the text legible. By analyzing the integrand in (2) we note that if we assume that $|\frac{\partial \gamma}{\partial x_1} \times \frac{\partial \gamma}{\partial x_2}|$ is a smooth function then the entire term $(f \circ \gamma)(\mathbf{x})|\frac{\partial \gamma}{\partial x_1} \times \frac{\partial \gamma}{\partial x_2}|$ is smooth and we introduce the notation

$$\psi(\mathbf{x}) = (f \circ \gamma)(\mathbf{x})\left|\frac{\partial \gamma}{\partial x_1} \times \frac{\partial \gamma}{\partial x_2}\right| \ .$$

With one additional notation, $\gamma_{\mathbf{x}_0}(\mathbf{x}) = \gamma(\mathbf{x}) - \gamma(\mathbf{x}_0)$, for the shift of the function γ by $\gamma(\mathbf{x}_0)$ we are left with evaluating integrals of the type

$$\int\limits_S s(\mathbf{y}-\mathbf{y}_0)f(\mathbf{y})\mathrm{d}S_{\mathbf{y}} = \int\limits_D (s \circ \gamma_{\mathbf{x}_0})(\mathbf{x})\psi(\mathbf{x})\mathrm{d}D_{\mathbf{x}} \ . \tag{3}$$

In the present work we consider the singular function s to be either the kernel of the Laplace equation, *i.e.*

$$L(\hat{\mathbf{y}}) = \frac{1}{|\hat{\mathbf{y}}|}, \quad \hat{\mathbf{y}} = \mathbf{y} - \mathbf{y}_0 \ , \tag{4}$$

or the Stokeslet, the kernel of the Stokes equations, $\mathbf{G}$, given in vector notation as

$$\mathbf{G}(\hat{\mathbf{y}}) = \frac{\mathbf{I}}{|\hat{\mathbf{y}}|} + \frac{\hat{\mathbf{y}}\hat{\mathbf{y}}}{|\hat{\mathbf{y}}|^3}, \quad \hat{\mathbf{y}} = \mathbf{y} - \mathbf{y}_0 \ , \tag{5}$$

where $\mathbf{I}$ is the identity tensor and $\hat{\mathbf{y}}\hat{\mathbf{y}}$ the dyadic product. Note that the kernel of the Stokes equations is in fact a second order tensor as opposed to the kernel of the Laplace equation. Thus the integrals over the kernel $\mathbf{G}$ are applied to vector valued functions $\mathbf{f}$ yielding a vector. The operation of evaluating integrals over $\mathbf{Gf}$ reduces to evaluating an integral over each component of the product $G_{ij}f_j$. We shall however suppress the vector notation in the theoretical part and pick it up once we discuss the specifics of the kernel $\mathbf{G}$. Unless mentioned explicitly which of the kernels is being discussed then the singularity s refers here to either of them.

The multidimensional trapezoidal rule applied to a smooth function γ over a square domain $D = [0,\ a_1] \times [0,\ a_2]$ can be regarded as a tensor product of one-dimensional rules leading to

$$\int_D f(\mathbf{x})\mathrm{d}\mathbf{x} \approx T_{\underline{h}}[\gamma] = \sum_{i=0}^{N}\sum_{j=0}^{M} \mathcal{W}_i(h_1)\mathcal{W}_j(h_2)\gamma(ih,_1 jh_2) \ , \tag{6}$$

where $h_1 = a_1/N,\ h_2 = a_2/M,\ \underline{h} = (h_1, h_2)$ and the weights are, similarly to the one-dimensional trapezoidal rule, given by the vector $\mathcal{W}(h) = [h/2,\ h, \ldots, h,\ h/2]$. Over a surface S parametrized as $\mathbf{y} = \gamma(\mathbf{x})$ with $\mathbf{x} \in D = [0,\ a_1] \times [0,\ a_2]$ the trapezoidal rule applied to a function $f \circ \gamma$ reads

$$T_{\underline{h}}[f \circ \gamma] \quad = \quad \sum_{i=0}^{N}\sum_{j=0}^{M} \mathcal{W}_i(h_1)\mathcal{W}_j(h_2)f(\gamma(ih_1, jh_2)) \ . \tag{7}$$

If we intend to apply the trapezoidal rule to the integral in equation (3), assuming that $\mathbf{x}_0$ is a grid point, then we cannot use $\mathbf{x}_0$ in the discretization. Therefore we introduce the so-called *punctured trapezoidal rule*, $T^0_{\underline{h}}$, which omits this point. Let us assume that $\mathbf{x}_0 = (i'h_1, j'h_2)$ and define

$$T^0_{\underline{h}}[(s \circ \gamma_{\mathbf{x}_0}) \cdot \psi] \quad = \quad \sum_{\substack{i=0 \\ i \neq i'}}^{N} \sum_{\substack{j=0 \\ j \neq j'}}^{M} \mathcal{W}_i(h_1)\mathcal{W}_j(h_2) s(\gamma_{\mathbf{x}_0}(ih_1, jh_2))\psi(ih_1, jh_2) \; . \tag{8}$$

Here we consider that singular points are inner to the domain, and since the integration is in fact performed over the domain D we need to have in the discrete setup that $\mathbf{x}_0 = (i'h_1, j'h_2)$ with $0 \ll i' \ll N$, $0 \ll j' \ll M$. The *punctured* trapezoidal rule has lower order convergence than the standard trapezoidal rule as mentioned in [17]. Let us make the following ansatz on the difference between the analytical integral and the punctured trapezoidal rule where the point $\mathbf{x}_0$ is skipped

$$\int_D (s \circ \gamma_{\mathbf{x}_0})(\mathbf{x})\psi(\mathbf{x}) \mathrm{d}D_{\mathbf{x}} - T^0_{\underline{h}}[(s \circ \gamma_{\mathbf{x}_0}) \cdot \psi] = \omega_0(\underline{h}) a(\gamma(\underline{h}))\psi(\mathbf{x}_0), \quad \mathbf{y}_0 = \gamma(\mathbf{x}_0) \; , \tag{9}$$

where $\omega_0(\underline{h})$ is a modified weight which accounts for the skipped point $\mathbf{x}_0$ and $a(\gamma(\underline{h}))$ is a correction factor which depends on the order of the singularity and on the parametrization of S. With $a(\gamma(\underline{h}))$ properly chosen, the weight $\omega_0(\underline{h})$ will converge to a value independent of the grid size, *i.e.* as $\underline{h} \to 0$ the weights converge to a limiting value $\omega_0(\underline{h}) \to \omega_0$. With the converged weight ω_0 let us now define $A^0_{\underline{h}}$ applied to a function ψ as being

$$A^0_{\underline{h}}[\psi] = a(\gamma(\underline{h}))\omega_0\psi(\mathbf{x}_0) \; , \tag{10}$$

and we shall further refer to $A^0_{\underline{h}}$ as a correction operator. With this correction operator we can devise a modified quadrature rule which is of higher order than the punctured trapezoidal rule, *i.e.*

$$Q^0_{\underline{h}}[(s \circ \gamma_{\mathbf{x}_0}) \cdot \psi] = T^0_{\underline{h}}[(s \circ \gamma_{\mathbf{x}_0}) \cdot \psi] + A^0_{\underline{h}}[\psi] \; , \tag{11}$$

where $T^0_{\underline{h}}$ is the punctured trapezoidal rule (8). The error of the quadrature rule $Q^0_{\underline{h}}$ will be proportional to $a(\gamma(\underline{h}))$. This is commented on in Section 2 and assessed through numerical experiments, formal proofs however could be obtained following [17].

The correction factor $a(\gamma(\underline{h}))$ depends on the parametrization of the surface and will be discussed in the next subsection. If $a(\gamma(\underline{h}))$ is carefully chosen, the weight $\omega_0(\underline{h})$ converges to ω_0 independent of the grid size. Since $a(\gamma(\underline{h}))$ is known a priori it remains to determine how to compute the converged weights $\omega_0(\underline{h}) \to \omega_0$.

Development of a quadrature rule over a parametrized surface

Assume we want to develop a quadrature rule (11) which approximates numerically the integral (3) with order $\mathcal{O}(h^3)$, $h = \max(h_1, h_2)$. The rule will be designed in fact for the right hand side of (3) for integrands $\psi(\mathbf{x})$. For the parametrization γ is sufficient to demand to be continuously differentiable such that we can perform the change of variables in (3). Here we consider that it is sufficient to require that $f \in C^4(\mathbb{R})$ since we aim to obtain a low order rule $\mathcal{O}(h^3)$, however rigorous proofs may tighten the requirements on the regularity of f. To devise a quadrature rule of the type (11) we seek to obtain a weight ω_0 which depends only on the singularity $s(\mathbf{y})$. The classical approach [10] is to compute a set of weights to be exact for the Taylor expansion of ψ. Thus as more and more monomials are considered in the Taylor expansion of ψ proportionally more weights have to be computed to obtain a correction of higher and higher order. The present work is restricted to a low order correction and thus it is sufficient to consider the monomial of degree 0, *i.e.* a constant.

Therefore we take a function $g(\mathbf{x}) \equiv 1$ to compute $\omega_0(\underline{h})$ corresponding to equation (10) such that

$$a(\gamma(\underline{h}))\omega_0(\underline{h})g(\mathbf{x}_0) = \int\limits_D (s \circ \gamma_{\mathbf{x}_0})(\mathbf{x})g(\mathbf{x})\mathrm{d}D_{\mathbf{x}} - T^0_{\underline{h}}[(s \circ \gamma_{\mathbf{x}_0}) \cdot g] \; . \tag{12}$$

From here as $\underline{h} \to 0$ we can obtain $\omega_0(\underline{h}) \to \omega_0$ to be used by the correction operator.

A few theoretical prerequisites are however necessary. The trapezoidal rule applied to a smooth function is second order accurate unless the integrand is periodic, integrated over a full period, or compactly supported. This is an immediate consequence of the Euler-Maclaurin expansion, see Appendix A. From the Euler-Maclaurin expansion we also note that the error in the approximation of an integral by the trapezoidal rule is determined by the boundary errors and the regularity of the integrand. The integrand of (12) is singular at $\mathbf{x}_0$ but integrable and of sufficiently high regularity away from the singularity. We assume that the singularity is always interior to the domain such that there is no interference with the boundary errors.

To correct the errors emerging from the boundaries two approaches can be followed

i) introduce boundary corrections, [2, 3]

ii) use compactly supported functions, [17, 16]

In higher dimensions we can use boundary corrections as provided by Alpert [3] for the one-dimensional case. Since the multi-dimensional trapezoidal rule is a tensor product of one-dimensional rules we can apply the boundary correction only in directions where the integrand is non-compactly supported, or non-periodic since the approximation error in these directions will not cancel as given by the Euler-Maclaurin formula. Boundary corrections can thus be implemented by simply replacing the weights $\mathcal{W}$ in expression (8) by the correction weights $\mathcal{W}^c$ in Appendix B, equation (B.3). Since we aim for rules that are $\mathcal{O}(h^3)$ accurate it is necessary to choose boundary corrections of at least $\mathcal{O}(h^3)$. In Appendix B we list correction weights needed to obtain boundary errors of $\mathcal{O}(h^8)$. Using boundary corrections we can obtain ω_0, ($\omega_0(\underline{h}) \to \omega_0$) from (12) using a function $g(\mathbf{x}) = 1$.

If the second approach of involving compactly supported functions is chosen to derive the weight ω_0 we can follow the work in [17] where it is suggested to pick $g(\mathbf{x}) = \mathrm{e}^{-|\mathbf{x}|^{2k}}$ to fulfill (12). This choice of g is not a compactly supported function in the true mathematical sense since it decays asymptotically to zero, but can be considered as such in numerical calculations if g is properly decayed at the boundaries of the domain and can thus be truncated. The decay of the function g is faster for increasing values of k, but too high values are not recommended since the function g becomes very sharp leading to poor approximations using the punctured trapezoidal rule. Here we settle for a value of $k = 4$. The correction operator acts locally only in a vicinity of the singularity where $g(0) = 1$ and the property of the function of being compactly supported is needed only to eliminate the boundary errors.

Both approaches yield the same result for the converged weight ω_0. The approach taken here is tailored to the cylindrical surface we consider and we take compactly supported functions only in the non-periodic direction as will be explained.

The work of Aguilar and Chen [2] which uses boundary corrections lacks theoretical results. However, Marin et al. [17] supplements this in the framework of compactly supported functions applied to kernels over flat surfaces. The main result in [17], *i.e.* Theorem 4, states that a rule of the type (11) is $\mathcal{O}(h^3)$ accurate for the kernel of the Laplace equation over a surface parametrized as $\gamma(\mathbf{x}) = (x_1, x_2, 0)$. This theorem is stated for $\underline{h} = (h_1, h_2)$ with $h_1 = h_2 = h$ and $a(\gamma(\underline{h})) = h$. As we attempt to extend this result to more general surfaces where $\gamma(\mathbf{x})$ is not necessarily the plane $O_{x_1}O_{x_2}$ we note that this choice of $a(\gamma(\underline{h}))$ is insufficient for surfaces with a given curvature. Numerical experiments show that if $\underline{h} = (h_1, h_2)$ is taken such that $h_1 = \lambda h_2$ the weights become more and more sensitive to the discretization, *i.e.* their convergence is not uniform, as the ratio λ deviates from unity, *i.e.* either $\lambda \ll 1$ or $\lambda \gg 1$. However this is not the case if for a parametrization γ we take $a(\gamma(\underline{h})) = |\gamma(\underline{h})|_2$, where $|\cdot|_2$ is the Euclidean norm. This expression of $a(\gamma(\underline{h}))$ connects to the form of the singularity s which, for both kernels of Stokes and Laplace equations, has a denominator given as $|\mathbf{x}|$, and also incorporates the curvature of the surface S through the parametrization γ. In this way the dependency on the discretization is embedded in $a(\gamma(\underline{h}))$ and the weight ω_0 converges as expected even in cases such as $h_1 = \lambda h_2$ with $\lambda \ll 1$ or $\lambda \gg 1$. With this choice of $a(\gamma(\underline{h}))$ we have for a flat surface discretized on a uniform grid the correction factor $a(\gamma(\underline{h})) = |\gamma(\underline{h})|_2 = h\sqrt{2}$ as opposed to $a(h) = h$ as stated in [17]. This minor difference implies that the $\sqrt{2}$ factor was instead incorporated in the correction weight ω_0 showing that our choice is consistent with the choice $a(h) = h$ in [17] for the considered cases.

The work performed in [17] and [16] relied on computing the integral in (12) analytically. However for parametrized surfaces the integrals become more cumbersome to compute and a different approach must be taken. The computation of the converged ω_0 will be performed here entirely numerically in multi-precision arithmetic. We consider to have obtained a fully converged weight if ω_0 is correct to a relative error 10^{-16}, which is sufficient for practical purposes.

The present work is limited to considerations that emerge only from numerical experiments and the theory in [17] will not be reiterated. The major difference of our endeavor compared to [17] is that the trapezoidal rule is now applied to functions $s(\gamma(\mathbf{x}))$ in the coordinate system given by the points $\mathbf{x}$ and the spacing over the surface at hand is not required to be equidistant in all directions.

Modified weights for general parametrized surfaces

Consider a second relation of the type (12) now for $\underline{h}/2$

$$a(\gamma(\underline{h}/2))\omega_0(\underline{h}/2)g(0) = \int\limits_D (s \circ \gamma_{\mathbf{x}_0})(\mathbf{x})g(\mathbf{x})\mathrm{d}D_{\mathbf{x}} - T^0_{\underline{h}/2}[(s \circ \gamma_{\mathbf{x}_0}) \cdot g] \ . \tag{13}$$

We can ignore the $g(0)$ term since $g(0) = 1$ regardless of which treatment of the boundary errors is used. By subtracting equation (12) from (13) we can eliminate the analytic integral

$$a(\gamma(\underline{h}/2))\omega_0(\underline{h}/2) - a(\gamma(\underline{h}))\omega_0(\underline{h}) = T^0_{\underline{h}}[(s \circ \gamma_{\mathbf{x}_0}) \cdot g] - T^0_{\underline{h}/2}[(s \circ \gamma_{\mathbf{x}_0}) \cdot g] \ . \tag{14}$$

In [17] it is noted that if the weights $\omega(\underline{h})$ are computed using compactly supported functions $\mathrm{e}^{-|\mathbf{x}|^{2k}}$ they converge to ω_0 at a rate that depends on k . Also in the case of boundary corrections the convergence rate of the weights depends on the order of accuracy of the corrections. The same convergence rate may not be achieved over parameterizable curves. In fact for the rules we have developed here over a cylindrical surface the convergence of the weights was only second order.

We further assume that $\omega_0(\underline{h}) \to \omega_0$ with $\mathcal{O}(h^\eta)$. If $\omega_0(\underline{h}) \to \omega_0$ with $\mathcal{O}(h^\eta)$ the error expansion can be written as

$$\omega_0 = \omega_0(\underline{h}) + Kh^\eta \ , \tag{15}$$

where $h = \max(h_1, h_2)$. Consider now equation (15) multiplied by $a(\gamma(\underline{h}/2))$ and upon rewriting (15) for $\underline{h}/2$ multiplied by $a(\gamma(\underline{h}/2))$ we obtain from subtracting the two

$$(a(\gamma(\underline{h}/2)) - a(\gamma(\underline{h})))\omega_0 = a(\gamma(\underline{h}/2))\omega_0(\underline{h}/2) - a(\gamma(\underline{h}))\omega_0(\underline{h}) + (a(\gamma(\underline{h}/2)) - a(\gamma(\underline{h})))Kh^\eta \ .$$

We can now establish an expression for the weights which is independent of the analytic integral in equation (12), *i.e.*

$$\omega_0 = \frac{a(\gamma(\underline{h}/2))\omega_0(\underline{h}/2) - a(\gamma(\underline{h}))\omega_0(\underline{h})}{(a(\gamma(\underline{h}/2)) - a(\gamma)(\underline{h})))} + Kh^\eta \ . \tag{16}$$

The numerator of (16) is in fact the left hand side of the expression in (14) and gives an approximation of order $\mathcal{O}(h^\eta)$ for the weights

$$\tilde{\omega}_0(\underline{h}) = \frac{T^0_{\underline{h}}[(s \circ \gamma_{\mathbf{x}_0}) \cdot g] - T^0_{\underline{h}/2}[(s \circ \gamma_{\mathbf{x}_0}) \cdot g]}{(a(\gamma(\underline{h}/2)) - a(\gamma(\underline{h})))} + Kh^\eta \ . \tag{17}$$

The approximation (17) of $\tilde{\omega}_0(\underline{h})$ converges to ω_0 with $\mathcal{O}(h^\eta)$. This may be a rather slow convergence which can be expedited using repeated standard Richardson extrapolation. Starting from $n = \eta$ the Richardson extrapolations yields

$$\omega_0 = \frac{2^n \tilde{\omega}_0(\underline{h}/2) - \tilde{\omega}_0(\underline{h})}{2^{n-1} - 1} + Kh^{n+1}. \tag{18}$$

Once a converged ω_0 is obtained, *i.e.* ω_0 accurate with 16 decimals, we can use the quadrature rule in (11) to evaluate numerically kernels s over surfaces given by a parametrization γ.

Using some of the prerequisites and notations provided in this section we can sum up the method of developing a corrected trapezoidal rule for a singular function over a parametrized surface.

Proposition 1. To evaluate numerically for interior points $\mathbf{y}_0 = \gamma(\mathbf{x}_0)$ an integral of the type

$$\int\limits_S s(\mathbf{y} - \mathbf{y}_0) f(\mathbf{y}) \mathrm{d}S_{\mathbf{y}} = \int\limits_D (s \circ \gamma_{\mathbf{x}_0})(\mathbf{x}) \psi(\mathbf{x}) \mathrm{d}D_{\mathbf{x}} \ , \tag{19}$$

we can devise a quadrature rule

$$Q^0_{\underline{h}}[(s \circ \gamma_{\mathbf{x}_0}) \cdot \psi] = T^0_{\underline{h}}[(s \circ \gamma_{\mathbf{x}_0}) \cdot \psi] + a(\gamma(\underline{h}))\omega_0 \psi(\mathbf{x}_0) \ , \quad a(\gamma(\underline{h})) = |\gamma(\underline{h})|_2 \ .$$

The weights ω_0 can be obtained as $\omega_0(\underline{h}) \to \omega_0$ using

$$\tilde{\omega}_0(\underline{h}) = \frac{T^0_{\underline{h}}[(s \circ \gamma_{\mathbf{x}_0}) \cdot g] - T^0_{\underline{h}/2}[(s \circ \gamma_{\mathbf{x}_0}) \cdot g]}{(a(\gamma(\underline{h}/2)) - a(\gamma(\underline{h})))} + Kh^\eta \ , \tag{20}$$

for a smooth function g such that $g(0) \equiv 1$. The function g is chosen such that either g compactly supported on D, or $g \equiv 1$ on D and boundary corrections at the end of the domain are used according to the expressions in Appendix B.

The quadrature rule has a convergence order proportional to $a(\gamma(\underline{h}))^3$. By Taylor expanding $a(\gamma(\underline{h}))$ in terms of $\underline{h}$ we obtain a convergence order which depends on $h = \max(h_1, h_2)$.

The statements above were made following the theoretical analysis in [17]. For the cylindrical surface regarded here we shall see that we have $\mathcal{O}(h^3)$.

Parametrized surfaces that allow for a universal weight independent of the position of the singularity

We assumed so far that $\gamma(\mathbf{x}_0)$ which will give a weight ω_0. For this weight to be independent of the position on the surface of S given through the parametrization γ the integral in (12) must be invariant to shifts $\mathbf{x}_0$.

Consider a domain D and for $\mathbf{x} \in D$ define the surface S given by points $\gamma(\mathbf{x})$. For a singular function $s(\gamma(\mathbf{x}) - \gamma(\mathbf{x}_0))$, where s is the kernel of the Laplace equation, to be integrated over a surface S we can obtain a weight ω_0 invariant to the position of $\mathbf{x}_0$ to construct a quadrature rule (11) if there exists a function $\tilde{\gamma}$ such that

$$|\gamma(\mathbf{x}) - \gamma(\mathbf{x}_0)|_2^2 = \tilde{\gamma}(\mathbf{x} - \mathbf{x}_0) \ , \tag{21}$$

where $|\cdot|_2$ is the Euclidean norm and $\tilde{\gamma}$ smooth and periodic over D. Then the weight ω_0 corresponds to $\tilde{\gamma}$ in (21) and is independent of $\mathbf{x}_0$. The integral (3) for s the Laplace kernel can be approximated by a quadrature rule $Q^0_{\underline{h}}[(s \circ \gamma_{\mathbf{x}_0}) \cdot \psi]$ as

$$\int\limits_D (s \circ \gamma_{\mathbf{x}_0})(\mathbf{x})\psi(\mathbf{x})\mathrm{d}D_{\mathbf{x}} \approx Q^0_{\underline{h}}[(s \circ \gamma_{\mathbf{x}_0}) \cdot \psi] = T^0_{\underline{h}}[(s \circ \gamma_{\mathbf{x}_0}) \cdot \psi] + \omega_0 a(\gamma(\underline{h}))\psi(\mathbf{x}_0) \ . \tag{22}$$

For the Stokeslet however the tensorial nature of the denominator, given by the dyadic product $\hat{\mathbf{y}}\hat{\mathbf{y}}$ with $\hat{\mathbf{y}} = \gamma(\mathbf{x}) - \gamma(\mathbf{x}_0)$, leads to an additional requirement

$$\gamma(\mathbf{x}) - \gamma(\mathbf{x}_0) = \sum_i \lambda_i(\mathbf{x}_0)\tilde{\gamma}_i(\mathbf{x} - \mathbf{x}_0) \ , \tag{23}$$

with $\tilde{\gamma}_i$ smooth and periodic over D and λ_i only continuous since it is to be evaluated at discrete points $\mathbf{x}_0$. A quadrature can be constructed in this form such that there is one ω_i corresponding to products of $\tilde{\gamma}_i$ scaled by $\tilde{\gamma}$ from (21). This will be further explained on the specific structure of the Stokeslet in Section 3. If both (21) and (23) are fulfilled then the integral (3) for s the Stokeslet can be approximated by a quadrature rule $Q^0_{\underline{h}}[(s \circ \gamma_{\mathbf{x}_0}) \cdot \psi]$ as

$$Q^0_{\underline{h}}[(s \circ \gamma_{\mathbf{x}_0}) \cdot \psi] = T^0_{\underline{h}}[(s \circ \gamma_{\mathbf{x}_0}) \cdot \psi] + \left(\sum_i \lambda_i(\mathbf{x}_0)\omega_i(\underline{h})\right) a(\gamma(\underline{h}))\psi(\mathbf{x}_0) \ . \tag{24}$$

Both requirements (21) and (23) are quite strong thus they are not met by many surfaces. This does not mean however that a weight cannot be obtained, but it merely implies that ω_0 depends on the point $\gamma(\mathbf{x}_0)$.

3 Quadrature rules over a cylindrical surface

Consider the surface of a cylinder parametrized as $\gamma(x_1,\ x_2) = (\rho\cos x_1, \rho\sin x_1, x_2)$, with ρ the radius of the circular cross-section of the cylinder, $x_1 \in [0, 2\pi)$ and x_2 the coordinate in the axial direction. In fact the cylinder can be regarded as a mapping defined on the square domain $D = [0,\ 2\pi) \times [0, a_2)$. Since the cylinder radius is a constant we take $\rho = 1$ for simplicity of the presentation. Let us define $\mathbf{x} = (x_1, x_2)$ and $\mathbf{x}_0 = (x_1^0, x_2^0)$ then the difference of points on the surface $\mathbf{y} - \mathbf{y}_0 = \gamma(\mathbf{x}) - \gamma(\mathbf{x}_0)$ is given by

$$\begin{aligned} y_1 - y_0^1 &= \cos x_1 - \cos x_1^0 = (1 - \cos(x_1 - x_1^0))\cos x_1^0 + \sin(x_1 - x_1^0)\sin x_1^0 \ , \\ y_2 - y_0^2 &= \sin x_1 - \sin x_1^0 = \sin(x_1 - x_1^0)\cos x_1^0 - (1 - \cos(x_1 - x_1^0))\sin x_1^0 \ , \\ y_3 - y_0^3 &= x_2 - x_2^0 \ , \end{aligned} \tag{25}$$

From (25) we have that $\tilde{\gamma}(\mathbf{x}-\mathbf{x}_0) = |\gamma(\mathbf{x}) - \gamma(\mathbf{x}_0)|_2^2 = 2 - 2\cos(x_1 - x_1^0) + (x_2 - x_2^0)^2$. We can see that the surface given by γ is of the type (21) if we impose periodic boundary conditions in the axial direction x_2.

The requirement (23) where γ is the parameterization in cylindrical coordinates reads

$$\gamma(\mathbf{x}) - \gamma(\mathbf{x}_0) = \sum_{i=1}^{2} \lambda_i(\mathbf{x}_0)\tilde{\gamma}_i(\mathbf{x}-\mathbf{x}_0)\ , \tag{26}$$

where

$$\begin{aligned}
\lambda_1(\mathbf{x}) &= [\cos x_1, \cos x_1, 0]\ ,\\
\lambda_2(\mathbf{x}) &= [\sin x_1, -\sin x_1, 1]\ ,\\
\tilde{\gamma}_1(\mathbf{x}) &= [1-\cos x_1, \sin x_1, 0]\ ,\\
\tilde{\gamma}_2(\mathbf{x}) &= [\sin x_1, 1-\cos x_1, x_2]\ .
\end{aligned}$$

This shows that the condition in (23) is fulfilled for the parametrization in cylindrical coordinates and will be described in Section 3 how is to be used.

The change of variables γ yields a surface element $|\frac{\partial\gamma}{\partial x_1} \times \frac{\partial\gamma}{\partial x_2}| = \rho$ and since we assume $\rho = 1$ it means that $\psi(\mathbf{x}) = f(\gamma(\mathbf{x}))|\frac{\partial\gamma}{\partial x_1} \times \frac{\partial\gamma}{\partial x_2}|$ will simply be the function f defined in cylindrical coordinates.

For a discretization over the cylindrical surface with h_{x_1} in the angular direction and h_{x_2} in the axial direction the correction factor of the quadrature rule of type (11) becomes

$$a(\gamma(\underline{h})) = |\gamma(\underline{h})|_2 = \sqrt{2 - 2\cos(h_{x_1}) + h_{x_2}^2}, \quad \underline{h} = \max(h_{x_1}, h_{x_2})\ . \tag{27}$$

Since the convergence order of the quadrature (11) is proportional to $a(\gamma(\underline{h}))^3$ we Taylor expand $\cos(x) = 1 - x^2/2 + h.o.t.$. This leads to $a(\gamma(\underline{h})) \approx \sqrt{h_{x_1}^2 + h_{x_2}^2}$, from where the method is of order $\mathcal{O}(h^3)$ with $h = \max(h_{x_1}, h_{x_2})$.

Quadrature rule for the singular kernel of the Laplace equation

Consider the singular kernel of the Laplace equation as in (4) to be integrated over a cylindrical surface periodic in the axial direction with period $T = a_2$. With the expansion in cylindrical coordinates in (25), $\rho = 1$ the radius of a circular cross-section of the cylinder, $\mathbf{x} \in [0, 2\pi) \times [0,\ a_2]$, the kernel of the Laplace equation becomes

$$(L \circ \gamma_{\mathbf{x}_0})(\mathbf{x}) = \frac{1}{|\tilde{\gamma}(\mathbf{x}-\mathbf{x}_0)|} = \frac{1}{\sqrt{2 - 2\cos(x_1 - x_1^0) + (x_2 - x_2^0)^2}}\ ,$$

where γ is the parametrization in cylindrical coordinates. In this form the integral is independent of the position of $\gamma(\mathbf{x}_0)$ if we impose periodicity in the axial direction. Thus it is possible to obtain a universal weight ω_0 which solves

$$\int_D (L \circ \gamma_{\mathbf{x}_0})(\mathbf{x})\psi(\mathbf{x})\mathrm{d}D_{\mathbf{x}} = T_{\underline{h}}^0[(L \circ \gamma_{\mathbf{x}_0}) \cdot \psi] + a(\gamma(\underline{h}))\psi(\mathbf{x}_0)\omega_0\ , \tag{28}$$

where $D = [0,\ 2\pi] \times [0,\ a_2]$ and $a(\underline{h}) = \sqrt{2 - 2\cos(h_{x_1}) + h_{x_2}^2}$.

In Listing 1 we provide the Matlab code for computing the weights tailored to the Laplace kernel over a cylinder in multi-precision arithmetic with repeated Richardson extrapolation.

Table 1: Weights computed for various discretizations h_{x_1}, h_{x_2}.

ω_0	h_{x_1}/h_{x_2}
1.541926823103929	π
2.534308571196347	$\pi/2$
2.692229466234622	$\pi/4$

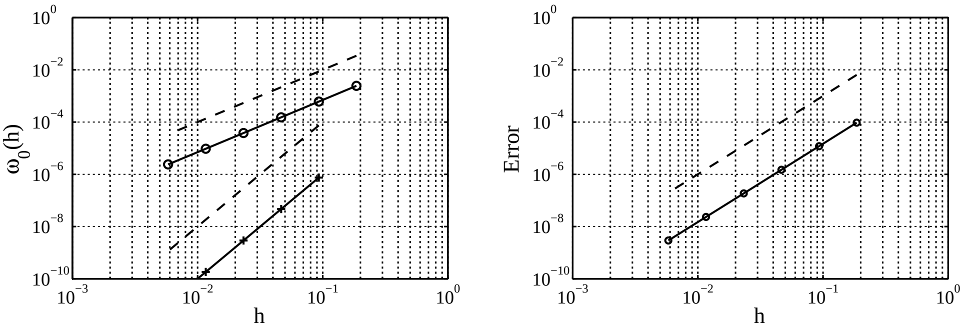

(a) Convergence of the weights ($\mathcal{O}(h^2)$), (solid ∘) error weights ω_0, (dashed) expected convergence order ($\mathcal{O}(h^2)$), (solid +) error weights ω_0 after one Richardson extrapolation ($\mathcal{O}(h^4)$).

(b) Convergence of the quadrature rule ($\mathcal{O}(h^3)$), (solid) error quadrature $Q^0_{\underline{h}}$, (dashed) expected convergence order.

Figure 1: Convergence of the weights and quadrature rule for the integration of the Laplace kernel over a cylinder discretized with $h_{x_1}/h_{x_2} = \pi$. The convergence is illustrated for $h = \max(h_{x_1}, h_{x_2})$.

To reduce boundary errors we use an exponential $\mathrm{e}^{-|x_2|^{2k}}$ defined only in the axial direction. Since in the angular direction the integrand is periodic boundary errors in this direction depend only on the regularity of the integrand. In this case the weights converge as $\omega_0 = \omega_0(h) + K_1 h^2 + K_2 h^4 + \ldots$ and Richardson extrapolation can be used for even orders of accuracy, *i.e.* the expression in (18) is used for $n = 2,\ 4, \ldots$.

For a few different ratios of the grid size in the angular and axial direction of the cylinder we compute the weight ω_0 and obtain the values listed in Table 1. From this table we choose the first ratio and check the convergence of the weights, Fig. 1a, and also the convergence of the first Richardson extrapolation to certify that indeed odd orders are skipped. The convergence of the quadrature rule stemming from the obtained ω_0 is illustrated in Fig. 1b. The accuracy test was performed at a single point $\mathbf{x}_0$ for a function $f(\gamma(\mathbf{x})) = \cos x_1$ using boundary corrections to eliminate boundary errors. A full convergence test where periodicity is considered will be performed for the more intricate kernel of the Stokes equations in Section 4.

Quadrature rule for the singular kernel of the Stokes equation

Consider now the same set-up of a cylinder expressed in cylindrical coordinates and the kernel of the Stokes equations (5). For points $\mathbf{x} = (x_1, x_2) \in D = [0,\ 2\pi) \times [0,\ a_2]$ and the parametrization γ in cylindrical coordinates we shall use at times $\mathbf{y}$, where $\mathbf{y} = \gamma(\mathbf{x})$, to simplify the notations. We note that the Stokeslet has one component which is similar to the kernel of the Laplace equation (4) and a tensorial component. It can thus be split into

$$\mathbf{G}(\hat{\mathbf{y}}) = L(\hat{\mathbf{y}})\mathbf{I} + \mathbf{\Gamma}(\hat{\mathbf{y}}), \quad \hat{\mathbf{y}} = \mathbf{y} - \mathbf{y}_0 \ , \tag{29}$$

where $\mathbf{I}$ is the identity matrix and the tensorial part denoted $\mathbf{\Gamma}$ is in index notation

$$\Gamma_{ij}(\hat{\mathbf{y}}) = \frac{\hat{y}_i \hat{y}_j}{|\hat{\mathbf{y}}|^3} \ . \tag{30}$$

We seek to devise a quadrature rule $Q^0_{\underline{h}}[(\mathbf{G} \circ \gamma_{\mathbf{x}_0}) \cdot \boldsymbol{\psi}]$ to integrate numerically

$$\int\limits_S \mathbf{G}(\mathbf{y} - \mathbf{y}_0)\mathbf{f}(\mathbf{y})\mathrm{d}S_{\mathbf{y}} = \int\limits_D (\mathbf{G} \circ \gamma_{\mathbf{x}_0})(\mathbf{x})\boldsymbol{\psi}(\mathbf{x})\mathrm{d}D_{\mathbf{x}} \ , \tag{31}$$

where $\boldsymbol{\psi}(\mathbf{x}) = \mathbf{f}(\gamma(\mathbf{x}))$, keeping in mind that the change of variables yields no surface element since we set $\rho = 1$.

The first component of $\mathbf{G}$ in (29) can be integrated in the very same way it has been previously done for the Laplace kernel and the quadrature rule can be written as

$$Q^0_{\underline{h}}[(\mathbf{G} \circ \gamma_{\mathbf{x}_0}) \cdot \boldsymbol{\psi}] = Q^0_{\underline{h}}[(L \circ \gamma_{\mathbf{x}_0}) \cdot \boldsymbol{\psi}]\mathbf{I} + Q^0_{\underline{h}}[(\mathbf{\Gamma} \circ \gamma_{\mathbf{x}_0}) \cdot \boldsymbol{\psi}] \ ,$$

with $Q^0_{\underline{h}}[(\mathbf{\Gamma} \circ \gamma_{\mathbf{x}_0}) \cdot \boldsymbol{\psi}]$ given as

$$Q^0_{\underline{h}}[(\mathbf{\Gamma} \circ \gamma_{\mathbf{x}_0}) \cdot \boldsymbol{\psi}] = \begin{pmatrix} Q^0_{\underline{h}}[(\Gamma_{11} \circ \gamma_{\mathbf{x}_0}) \cdot \psi_1] + Q^0_{\underline{h}}[(\Gamma_{12} \circ \gamma_{\mathbf{x}_0}) \cdot \psi_2] + Q^0_{\underline{h}}[(\Gamma_{13} \circ \gamma_{\mathbf{x}_0}) \cdot \psi_3] \\ Q^0_{\underline{h}}[(\Gamma_{21} \circ \gamma_{\mathbf{x}_0}) \cdot \psi_1] + Q^0_{\underline{h}}[(\Gamma_{22} \circ \gamma_{\mathbf{x}_0}) \cdot \psi_2] + Q^0_{\underline{h}}[(\Gamma_{23} \circ \gamma_{\mathbf{x}_0}) \cdot \psi_3] \\ Q^0_{\underline{h}}[(\Gamma_{31} \circ \gamma_{\mathbf{x}_0}) \cdot \psi_1] + Q^0_{\underline{h}}[(\Gamma_{32} \circ \gamma_{\mathbf{x}_0}) \cdot \psi_2] + Q^0_{\underline{h}}[(\Gamma_{33} \circ \gamma_{\mathbf{x}_0}) \cdot \psi_3] \end{pmatrix} \ .$$

Let us analyze all the components of the tensorial part in cylindrical coordinates for $\hat{\mathbf{y}} = \gamma(\mathbf{x}) - \gamma(\mathbf{x}_0)$. To denote the components of the vector valued functions λ_i and $\tilde{\gamma}_i$ we introduce a superscript and to simplify the expressions arising from the split (26) we define

$$\chi_j(\mathbf{x}; \mathbf{x}_0) = \sum_{i=1}^{2} \lambda_i^j(\mathbf{x}_0)\tilde{\gamma}_i^j(\mathbf{x} - \mathbf{x}_0) \ .$$

With this notation the tensorial components become

$$\begin{aligned} \Gamma_{11}(\hat{\mathbf{y}}) &= \frac{\hat{y}_1\hat{y}_1}{|\hat{\mathbf{y}}|^3} = \frac{[\chi_1(\mathbf{x}; \mathbf{x}_0)]^2}{\sqrt{\tilde{\gamma}(\mathbf{x} - \mathbf{x}_0)}^3} \\ \Gamma_{22}(\hat{\mathbf{y}}) &= \frac{\hat{y}_2\hat{y}_2}{|\hat{\mathbf{y}}|^3} = \frac{[\chi_2(\mathbf{x}; \mathbf{x}_0)]^2}{\sqrt{\tilde{\gamma}(\mathbf{x} - \mathbf{x}_0)}^3} \\ \Gamma_{12}(\hat{\mathbf{y}}) &= \frac{\hat{y}_1\hat{y}_2}{|\hat{\mathbf{y}}|^3} = \frac{[\chi_1(\mathbf{x}; \mathbf{x}_0)][\chi_2(\mathbf{x}; \mathbf{x}_0)]}{\sqrt{\tilde{\gamma}(\mathbf{x} - \mathbf{x}_0)}^3} \\ \Gamma_{33}(\hat{\mathbf{y}}) &= \frac{\hat{y}_3\hat{y}_3}{|\hat{\mathbf{y}}|^3} = \frac{[\chi_3(\mathbf{x}; \mathbf{x}_0)]^2}{\sqrt{\tilde{\gamma}(\mathbf{x} - \mathbf{x}_0)}^3} \ . \end{aligned}$$

With the expressions from the equations (25) we can reconstruct all the tensorial components, *e.g.* Γ_{11} has a numerator given as

$$\begin{aligned} [\chi_1(\mathbf{x}; \mathbf{x}_0)]^2 &= (\lambda_1^1(\mathbf{x}_0)\tilde{\gamma}_1^1(\mathbf{x} - \mathbf{x}_0))^2 + (\lambda_2^1(\mathbf{x}_0)\tilde{\gamma}_2^1(\mathbf{x} - \mathbf{x}_0))^2 \\ &\quad + 2\lambda_1^1(\mathbf{x}_0)\tilde{\gamma}_1^1(\mathbf{x} - \mathbf{x}_0)\lambda_2^1(\mathbf{x}_0)\tilde{\gamma}_2^1(\mathbf{x} - \mathbf{x}_0) \ . \end{aligned}$$

By replacing the expressions for λ_i, $\tilde{\gamma}_i$ and computing the limit as $\mathbf{x} \to \mathbf{x}_0$ we note that the first and last terms in the expansion vanish

$$\lim_{\mathbf{x}\to\mathbf{x}_0} \frac{(1-\cos(x_1-x_1^0))^2\cos^2 x_1^0}{\sqrt{2-2\cos(x_1-x_1^0)+(x_2-x_2^0)^2}^3} = 0 \ , \qquad (32)$$
$$\lim_{\mathbf{x}\to\mathbf{x}_0} \frac{2(1-\cos(x_1-x_1^0))\sin(x_1-x_1^0)\sin x_1^0\cos x_1^0}{\sqrt{2-2\cos(x_1-x_1^0)+(x_2-x_2^0)^2}^3} = 0 \ .$$

we can thus disregard them since they do not yield non-zero weights. We are then left to compute a modified weight ω_c corresponding to $[\tilde{\gamma}_2^1(\mathbf{x}-\mathbf{x}_0)]^2[\lambda_2^1(\mathbf{x}_0)]^2$. In fact the constant $[\lambda_2^1(\mathbf{x}_0)]^2$ can be omitted in the process of computing the modified weight and reintroduced as a multiplicator in the correction operator.

The computation of the weight ω_c that corresponds to the integral

$$\int_D \frac{[\lambda_2^1(\mathbf{x}_0)\tilde{\gamma}_2^1(\mathbf{x}-\mathbf{x}_0)]^2}{\sqrt{\tilde{\gamma}(\mathbf{x}-\mathbf{x}_0)}^3}\mathrm{d}D_{\mathbf{x}} = \int_0^{2\pi}\int_0^{a_2} \frac{\sin^2(x_1-x_1^0)}{\sqrt{2-2\cos(x_1-x_1^0)+(x_2-x_2^0)^2}^3}\mathrm{d}x_1\mathrm{d}x_2 \ ,$$

is available in the Matlab code provided in Listing 1 in the Appendix of this manuscript. With the new weight ω_c we can define a quadrature rule for the first tensorial component of the Stokeslet

$$Q_{\underline{h}}^0[(\Gamma_{11}\circ\gamma_{\mathbf{x}_0})\cdot\psi_1] = T_{\underline{h}}^0[(\Gamma_{11}\circ\gamma_{\mathbf{x}_0})\cdot\psi_1] + a(\gamma(\underline{h}))\psi_1(\mathbf{x}_0)\omega_c\sin^2 x_1^0 \ . \qquad (33)$$

By performing a similar analysis for all other terms we obtain for the second diagonal term of the Stokeslet

$$Q_{\underline{h}}^0[(\Gamma_{22}\circ\gamma_{\mathbf{x}_0})\cdot\psi_2] = T_{\underline{h}}^0[(\Gamma_{22}\circ\gamma_{\mathbf{x}_0})\cdot\psi_2] + a(\gamma(\underline{h}))\psi_2(\mathbf{x}_0)\omega_c\cos^2 x_1^0 \ . \qquad (34)$$

Note that the same weight ω_c is obtained since the other terms vanish similarly to (32). The only off-diagonal terms of the Stokeslet that receive one more modified weight are the ones involving both radial directions thus

$$Q_{\underline{h}}^0[(\Gamma_{12}\circ\gamma_{\mathbf{x}_0})\cdot\psi_2] = T_{\underline{h}}^0[(\Gamma_{12}\circ\gamma_{\mathbf{x}_0})\cdot\psi_2] - a(\gamma(\underline{h}))\psi_2(\mathbf{x}_0))\omega_c\cos x_1^0\sin x_1^0 \ . \qquad (35)$$

For the last term of the Stokeslet we need to compute a different modified weight ω_z corresponding to the integral

$$\int_D \frac{[\lambda_2^3(\mathbf{x}_0)\tilde{\gamma}_2^3(\mathbf{x}-\mathbf{x}_0)]^2}{\sqrt{\tilde{\gamma}(\mathbf{x}-\mathbf{x}_0)}^3}\mathrm{d}D_{\mathbf{x}} = \int_0^{2\pi}\int_0^{a_2} \frac{(x_2-x_2^0)^2}{\sqrt{2-2\cos(x_1-x_1^0)+(x_2-x_2^0)^2}^3}\mathrm{d}x_1\mathrm{d}x_2 \ ,$$

the terms $\lambda_1^3\tilde{\gamma}_1^3 = 0$ therefore they are not included in the above integral. For the tensorial component Γ_{33} we obtain a quadrature rule

$$Q_{\underline{h}}^0[(\Gamma_{33}\circ\gamma_{\mathbf{x}_0})\cdot\psi_3] = T_{\underline{h}}^0[(\Gamma_{33}\circ\gamma_{\mathbf{x}_0})\cdot\psi_3] + a(\gamma(\underline{h}))\psi_3(\mathbf{x}_0)\omega_z \ . \qquad (36)$$

The terms Γ_{23}, Γ_{23} were not discussed but it can be easily verified by taking the limit just as in (32) that they yield weights which are zero. To sum up we developed a third order quadrature rule for the kernel of the Stokes equations over the surface of a cylinder. The quadrature rule reads

$$Q_{\underline{h}}^0[(\mathbf{G}\circ\gamma_{\mathbf{x}_0})\cdot\boldsymbol{\psi}] \ = \ T_{\underline{h}}^0[(\mathbf{G}\circ\gamma_{\mathbf{x}_0})\cdot\boldsymbol{\psi}] + A_{\underline{h}}^0[\boldsymbol{\psi}] \qquad (37)$$

Table 2: Weights computed for various discretizations h_{x_1}, h_{x_2}, for the Stokeslet over a cylindrical surface.

ω_0	ω_c	ω_z	h_{x_1}/h_{x_2}
1.541926823103929	1.905780916041877	-0.363854092648452	π
2.534308571196347	1.685701948440279	0.848606622756068	$\pi/2$
2.692229466234622	1.127178590303698	1.565050875926132	$\pi/4$

with

$$A^0_{\underline{h}}[\boldsymbol{\psi}] = a(\gamma(\underline{h})) \begin{pmatrix} \omega_0 + \omega_c \sin^2 x_1^0 & -\omega_c \cos x_1^0 \sin x_1^0 & 0 \\ -\omega_c \cos x_1^0 \sin x_1^0 & \omega_0 + \omega_c \sin^2 x_1^0 & 0 \\ 0 & 0 & \omega_0 + \omega_z \end{pmatrix} \begin{pmatrix} \psi_1(\mathbf{x}_0) \\ \psi_2(\mathbf{x}_0) \\ \psi_3(\mathbf{x}_0) \end{pmatrix} ,$$

where $a(\underline{h}) = \sqrt{2 - 2\cos(h_{x_1}) + h_{x_2}^2}$ and $\mathbf{x}_0 = (x_1^0, x_2^0)$. The weights ω_0, ω_c, ω_z depend on the relative discretization on the cylindrical surface and are tabulated for various ratios h_{x_1}/h_{x_2} in Table 2.

4 Numerical results for the quadrature rule for a Stokeslet

To assess the accuracy of the obtained quadrature rules on a physically relevant problem we consider the Stokes equations expressed over a cylindrical surface periodic in the axial direction. It is sufficient to regard only the Stokeslet since it involves more intricate expressions and incorporates also the singularity of the Laplace kernel as previously noted. To introduce periodicity we must note that the periodic Stokeslet has different expressions according to whether the problem is periodic in one direction, *e.g.* axial direction, or two or more directions [19]. Although it may seem suitable to impose periodicity only in the axial direction there is no significant computational gain in doing so. The periodicity in all three directions however has been heavily employed [16], [9], [25]. Since the application we aim to address here concerns internal pipe flows we can consider a cylinder in a fully periodic setting, in which the periodic length in the radial direction of the cylinder is taken to be sufficiently large.

Convergence of the quadrature rule over a cylinder periodically replicated in the axial direction

Consider a periodic domain $\Omega = [0, L_x) \times [0, L_y) \times [0, L_z)$ and a set of N particles at positions $\mathbf{y}_i$ where $i = 1, \ldots, N$. The particles considered here will be the discrete points on the surface of the cylinder. If this computational domain is now periodically replicated in every direction then the velocity at a point $\mathbf{y}$ would be determined not only by the presence of the particles immersed in the current domain Ω but also their periodic images. For a particle at position $\mathbf{y}$ the periodic image is given by $\mathbf{y} + \tau(\mathbf{p})$ with $\tau(\mathbf{p}) = p_1 L_x \mathbf{e}_1 + p_2 L_y \mathbf{e}_2 + p_3 L_z \mathbf{e}_3$ where $p_i \in \mathbb{Z},\ i = 1, \ldots, 3$. Summing up all the contributions from the Stokeslet (5) and its periodic images we obtain

$$\mathbf{G}_p(\mathbf{y} - \mathbf{y}_0) = \sum_{\mathbf{p} \in \mathbb{Z}^3}{}' \, \mathbf{G}(\mathbf{y} - \mathbf{y}_0 + \tau(\mathbf{p})) \ , \tag{38}$$

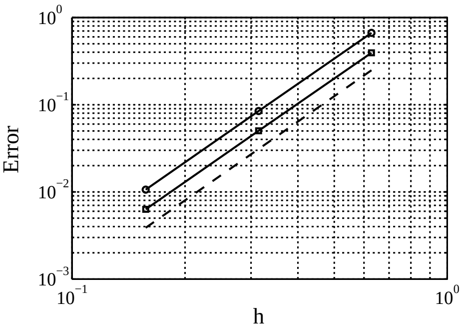

Figure 2: Convergence of the quadrature rule ($\mathcal{O}(h^3)$) with $h = \max(h_{x_1},\ h_{x_2})$, (solid) error quadrature $Q^0_{\underline{h}}$, (dashed) expected convergence order, ($\circ$) resolution $h_{x_1}/h_{x_2} = \pi/2$, ($\square$) resolution $h_{x_1}/h_{x_2} = \pi$.

where the prime stands for skipping the singular point $\mathbf{y} = \mathbf{y}_0$ for $\mathbf{p} = 0$. This sum defines the periodic Stokeslet $\mathbf{G}_p$. A direct summation is however not possible since the free-space Stokeslet $\mathbf{G}$ decays as $1/r$, $r = |\mathbf{y} - \mathbf{y}_0|$ and thus the sum is not absolutely convergent. To circumvent this an extra physical constraint is imposed on the problem, *i.e.* mean zero velocity within the domain, and to render the sum in (38) quickly convergent it is decomposed in a suitable fashion. The long range interactions are summed in Fourier space while only the short range interactions are to be summed up in real space by introducing a splitting parameter ξ which determines how to differentiate between long/short range interactions. This technique is known in the literature as an Ewald type decomposition, named after Ewald who introduced the idea in the field of electrostatics. Two splitting schemes stemmed in the field of fluid dynamics to treat the periodic Stokeslet, the Beenakker decomposition [5] and the Hasimoto decomposition [12].

Without further ado the periodic Stokeslet can be split as

$$\mathbf{G}_p(\mathbf{y} - \mathbf{y}_0) = \mathbf{G}(\mathbf{y} - \mathbf{y}_0) + \tilde{\Upsilon}(\mathbf{y} + \mathbf{p}, \xi) + \sum_{\substack{\mathbf{p} \in \mathbb{Z}^3 \\ |\mathbf{p}| \neq 0}} \Upsilon(\mathbf{y} + \mathbf{p}, \xi) + \frac{1}{V} \sum_{\substack{\mathbf{k} \in \mathbb{Z}^3 \\ |\mathbf{k}| \neq 0}} \Phi(\mathbf{y} - \mathbf{y}_0, \xi, \mathbf{k}) \ . \quad (39)$$

where $\mathbf{k}$ is the wavenumber given as $\mathbf{k} = \{2\pi(k_1/L_x,\ k_2/L_y,\ k_3/L_z),\ k_{i=1,\ldots,3} \in \mathbb{Z}\}$ and $V = L_x L_y L_z$. The last component in (39) is to be evaluated in Fourier space, while all other terms are evaluated in the real space. The expressions for $\tilde{\Upsilon}$, Υ and Φ can be found in Appendix C as given by the Hasimoto decomposition. If we write the periodic Stokeslet as in (39) we separate the singular term $\mathbf{G}$ from the remaining smooth terms. The singular term will be numerically integrated with the presently developed quadrature rule while the periodic remainder can be safely evaluated using the classical trapezoidal rule.

To assess the accuracy of the developed method we consider a periodic domain $\Omega = [0,\ a_1) \times [0,\ a_2) \times [0,\ a_3)$ with $a_1 = 10\rho$, $a_2 = 4\rho$, $a_3 = 10\rho$, where $\rho = 1$ is the radius of the cylinder. And evaluate the integral over the cylinder expressed through the parametrization γ in cylindrical coordinates

$$\mathbf{u}(\mathbf{x}_0) = \int_D (\mathbf{G} \circ \gamma_{\mathbf{x}_0})(\mathbf{x}) \boldsymbol{\psi}(\mathbf{x}) \mathrm{d}D_{\mathbf{x}} \ , \quad (40)$$

where $D = [0,\ 2\pi] \times [0,\ a_2]$, $\mathbf{x} = (x_1, x_2)$ and $\gamma(\mathbf{x}) = (\cos x_1, \sin x_1, x_2)$. The smooth integrand is chosen to $\boldsymbol{\psi}(\mathbf{x}) = \mathbf{f}(\gamma(\mathbf{x})) = [x_2, \cos(2\pi/a_1 x_1), \sin(2\pi/a_1 x_1)]$ since $\mathbf{f}$ must be periodic over the domain of integration such that the trapezoidal rule does not yield boundary errors. In Fig.4 we present the convergence results in L_2 norm for the computed velocity $\mathbf{u}$ evaluated using the quadrature rule (37). For completeness we perform two convergence tests corresponding to the resolutions $h_{x_1}/h_{x_2} = \pi$ and $h_{x_1}/h_{x_2} = 2\pi$.

Sphere immersed in Stokes flow sedimenting along the inner axis of a cylinder

The quadrature rule developed for the Stokeslet over a cylindrical surface (37) is validated against a physical problem. The test case is that of a sphere settling due to gravity in a cylinder in the Stokes flow regime. A schematic of the setup is given in Fig. 3. The radii of the sphere and cylinder are denoted by r_s and ρ, respectively.

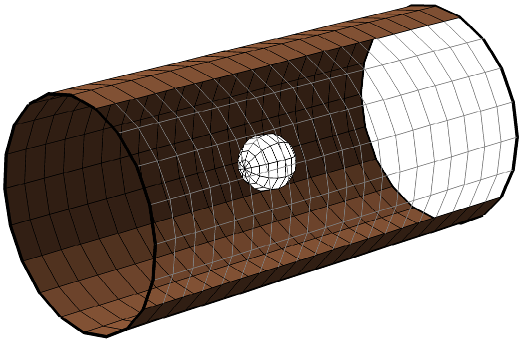

Figure 3: Schematic of a sphere settling in a cylinder. The gravity is acting in the axial x_2 direction.

The drag on a spherical particle sedimenting along the inner axis of a cylinder has been studied analytically through asymptotic expansions and can be found in the textbook by Happel & Brenner [11]. The drag force F is thus related to the (steady) settling velocity U,

$$F = \frac{6\pi\mu U r_S}{1 - 2.1042(r_s/\rho) + 2.08658(r_s/\rho)^3} \ , \tag{41}$$

with the fluid kinematic viscosity μ.

Our numerical discretization assumes periodic boundary conditions in the axial direction; with a period of L_z. The cylinder is embedded in a cube of size $(8\rho)^2 \times L_z$. The spherical particle is discretized in spherical coordinates (r_s, α, θ) using the singularity subtraction method to treat the singularity of the Stokeslet. This is a classic approach more throughly described in [16].

As a first step we assess the resolution necessary to obtain a settling velocity independent of the discretization over the spherical and cylindrical surfaces. We consider the relative change of the settling velocity as a function of the grid refinement, and investigate it independently for the sphere and cylinder mesh. This is done starting from a chosen ratio of $h_{x_1}/h_{x_2} = \pi/2$ over the cylinder. As shown in Fig. 4a, a resolution of $N_{x_2} = N_{x_1} = 20$ is sufficient on the cylinder. The necessary number of grid points on the sphere to attain a settling velocity independent of the grid is $N_\alpha = N_\theta = 20$.

The comparison with the analytical expression (41) is illustrated in Fig. 4b. The equation (41) is derived for a sphere settling in an infinite cylinder, whereas our numerical results are obtained in a periodic cylinder of length L_z. Therefore, it is expected that L_z will have an influence on the final U, converging to the analytical result for large L_z. We consider two cases, $r_s/\rho = 0.2$ and $r_s/\rho = 0.1$. Indeed the analytical result is reproduced by our simulation in both cases. For the sphere of radius $r_s = 0.2\rho$ independence of L_z is reached for $L_z > 12$, whereas for the sphere with $r_s = 0.1\rho$ a much shorter L_z is required. This is consistent with the more localized effect on the flow field in the small sphere case, *i.e.* $r_s = 0.1\rho$.

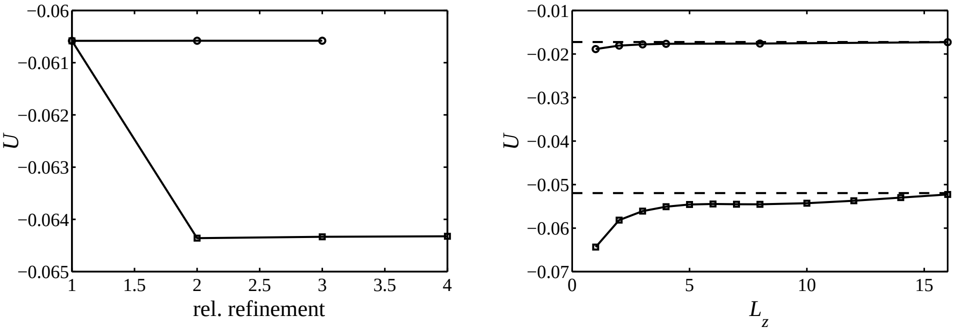

(a) Grid refinement for radius ratio $r_s/\rho = 0.2$ relative to the base resolution of the cylinder $N_{x_2} = N_{x_1} = 20$ with length $L_z = 4$ (○), and of the sphere $N_\alpha = N_\theta = 10$ (□).

(b) Variation of the axial length of the cylinder for two sphere sizes, $r_s/\rho = 0.2$ (□) and $r_s/\rho = 0.1$ (○). Resolution as in the second refinement step. Dashed lines: analytical expression (41).

Figure 4: Settling velocity of a sphere with radius r_s in a cylinder with radius ρ.

5 Advantages of using a discretization based on a corrected trapezoidal rule

It is clear that one great advantage of using a corrected trapezoidal rule is that it is straightforward to implement. Moreover, under certain circumstances, the matrices that stem from such a discretization have special properties that lead to efficient algebraic treatments or are inexpensive to store in the memory.

Consider the problem of solving for an imposed boundary condition on $\mathbf{u}$ the integral

$$\mathbf{u}(\mathbf{x}_0) = \int_D (\mathbf{G} \circ \gamma_{\mathbf{x}_0})(\mathbf{x})\boldsymbol{\psi}(\mathbf{x})\mathrm{d}D_{\mathbf{x}} \ , \quad \mathbf{x} = (x_1, x_2),\ \mathbf{x}_0 = (x_1^0, x_2^0) \ , \tag{42}$$

where $D = [0,\ 2\pi] \times [0,\ a_2]$ and $\gamma(\mathbf{x}) = (\cos x_1, \sin x_1, x_2)$ and $\gamma_{\mathbf{x}_0}(\mathbf{x}) = \gamma(\mathbf{x}) - \gamma(\mathbf{x}_0)$.

Assume we use the quadrature rule (37) and for each $\mathbf{x}_0$ let us define the discrete operator

$$I_c^{\mathbf{x}_0}[(\mathbf{G} \circ \gamma_{\mathbf{x}_0}) \cdot \boldsymbol{\psi}] = Q_{\underline{h}}^0[(\mathbf{G} \circ \gamma_{\mathbf{x}_0}) \cdot \boldsymbol{\psi}] \ . \tag{43}$$

The matrix of the system, let us call it I_c will be determined by $I_c^{\mathbf{x}_0}$ for each $\mathbf{x}_0 = (x_1^0, x_2^0)$ on the surface of the cylinder expressed in cylindrical coordinates. Assume a certain ordering of the unknowns with respect to the discrete points. Let us say the unwrapping of the discrete f_{ij}^k with $k = 1, \ldots, 3$ is performed first in the angular direction in points (x_{1i}, x_2), then the axial direction in points (x_1, z_j) and lastly in the direction k corresponding to the spatial direction. The matrix I_c will then be a hierarchical matrix with three levels of symmetry, see Fig. 5. Starting from top to bottom and by noting that G_{ij} is a second order symmetric tensor, $G_{ij} = G_{ji}$ with $i, j = 1, \ldots, 3$, we have six distinct blocks that generate

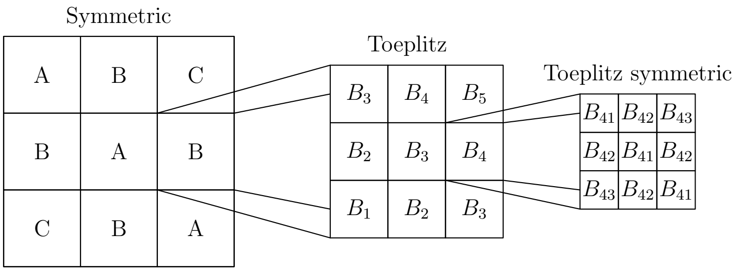

Figure 5: Matrix structure — Block Toeplitz Symmetric with Toeplitz symmetric sub-blocks. The matrix can be regarded as having an hierarchical structure. At the first level the matrix is symmetric, at the second level the blocks have Toeplitz sub-blocks and ultimately each sub-block is also Toeplitz symmetric matrix.

the matrix I_c, *i.e.* I_c is block symmetric. Furthermore recall that the cylinder spans the entire periodic domain and is also periodic in the angular direction $x_1 \in [0, 2\pi)$ thus we integrate a periodic integrand over an entire period and

$$\int_D (\mathbf{G} \circ \gamma_{\mathbf{x}_0})(\mathbf{x})\boldsymbol{\psi}(\mathbf{x})\mathrm{d}D_{\mathbf{x}} = \int_D (\mathbf{G} \circ \gamma_{\overline{\mathbf{x}}})(\mathbf{x})\boldsymbol{\psi}(\mathbf{x})\mathrm{d}D_{\mathbf{x}}\ , \quad \forall \quad \mathbf{x}_0, \overline{\mathbf{x}}_0 \in D\ . \tag{44}$$

It is therefore enough to discretize the integral operator $I_c^{\mathbf{x}_0}$ which applies to $\mathbf{f}$ for a given $\mathbf{x}_0$, say $\mathbf{x}_0 = 0$, and all other evaluations at points $\mathbf{x}_0 \neq 0$ will yield the same result.

In Fig. 5 we sketch the structure of the matrix by zooming in into one block B although this also holds for all other blocks in the full matrix. The special structure of the matrix I_c is block-Toeplitz-symmetric with Toeplitz symmetric sub-blocks, which implies that the matrix is determined by only three columns. In practice this has a great impact on the efficient storage problem since we need to load into memory only the generating vectors and compute each new matrix entry on-site by using the known structure of I_c. Note the difference between this matrix and the one emerging from the discretization of a flat wall [16] which has circulant sub-blocks instead of Toeplitz symmetric.

These type of matrices are also suitable for efficient algebraic treatments. The matrix vector product where the matrix is circulant of size $N \times N$ can be computed using FFTs with $\mathcal{O}(N \log N)$ operations as opposed to $\mathcal{O}(N^2)$ when the matrix has no structure, see [8]. If the matrix is of Toeplitz form it can be embedded in a circulant matrix of size $2N \times 2N$ leading once again to more efficient matrix vector product computations.

6 Conclusions and outlook

In this note we have extended the set of applications of modified quadrature rules for singular functions based on a corrected trapezoidal rule to a class of parameterizable surfaces. Corrected trapezoidal rules are based on the punctured trapezoidal rule, which omits the singular grid point, to which we add a correction operator acting in a vicinity, and at, the singular point. The correction operator is constructed by computing a weight which depends on the singularity and the surface over which numerical integration is performed. On general curvilinear surfaces such a weight depends on the position of the singular point on the surface. However a certain class of parameterizable surfaces admits a universal weight, independent of the relative position on the surface. From this class we selected the surface of a cylinder for which we devised explicitly third order quadrature rules for the kernels of

Laplace and Stokes. The quadrature rules were validated through numerical examples and we also discussed the advantages brought by this approach to numerical integration. These rules are suitable for surfaces with a high degree of regularity since they yield Toeplitz-like matrices. Such matrices are generated by a small number of matrix entries, thus can be stored in memory in an efficient fashion, and lead also to efficient algebraic computations using FFTs.

The weights computed with this quadrature rule should depend only on the curvature of the surface. Further studies should be performed on the simple case of a cylinder to assess how to decouple the cylinder radius from the weights. In the present work we have settled for a radius equal to unity, result which should be generalized to various radii. The present study is limited to the third order case, where only one weight is needed. It is however of interest to inquire how to develop higher order methods for surfaces with a high degree of isotropy such as the cylinder or the sphere.

Acknowledgments

Anna-Karin Tornberg is gratefully acknowledged for her comments surrounding this manuscript.

MATLAB code

In Listing 1 we reproduce the MATLAB code which uses the Symbolic Toolbox for computing a modified weight for a cylinder of radius equal to unity. The spacing in the radial direction of the cylinder is h_{x_1} and in the axial direction h_{x_2}. Important here is the ratio between the spacing in the two directions and not the length of the cylinder. In this case we have $h_{x_2} = 2h_{x_1}/\pi$.

If a different surface is considered instead of the cylinder lines no. 26 and 32–37 in the code must be modified to consider the function $1/r$ as a function of the new coordinates.

Listing 1: MATLAB code for the $1/r$ singularity over a cylinder

```
 1  % Compute weights for singularity on a cylinder surface
 2  % Geometry
 3  circ   = 2*pi;       % circumference 2pi
 4  Lz     = 4;             % length of cylinder in axial direction
 5
 6  % Number of points on cylinder surface
 7  Nx1  = 20;         % azimuthal direction
 8  Nx2  = 20;         % axial direction
 9
10  % Grid spacing (numerically)
11  hx1  = circ/Nx1;
12  hx2  = Lz/Nx2;
13
14  % Main loop for Richardson extrapolation (5 refinements)
15  for i=1:7
16      disp(sprintf('Richardson␣extrapolation,␣step␣%i',i))
17
18      % Generate grid (symbol tool box)
19      hx1 =  sym(circ/Nx1);
20      hx2 =  sym(Lz/Nx2);
21
22      x1  = -circ/2:hx1:circ/2-hx1;
23      x2  = -Lz/2:hx2:Lz/2;
24
25      % Define r
```

```
    r = sqrt(kron(ones(1,Nx2+1),(cos(x1')-cos(0)).^2 + ...
         (sin(x1')-sin(0)).^2) + kron(x2.^2,ones(Nx1,1)) );

    % Set r(0,0)=1 to avoid singularity
    r(Nx1/2+1,Nx2/2+1) = sym(1);

    % Construct phi for w0, wc and wz, repsectively
    phi_1 =   kron(exp(-x2.^8),ones(Nx1,1));
    phi_2 = ( kron(ones(1,Nx2+1),sin(x1').^2).* ...
              kron(exp(-x2.^8),ones(Nx1,1)) )./r.^2;
    phi_3 = ( kron(ones(1,Nx2+1),ones(Nx1,1)).* ...
              kron(exp(-x2.^8).*x2.^2,ones(Nx1,1)) )./r.^2;

    % Set phi(0,0)=0 to replace the singular point
    phi_1(Nx1/2+1,Nx2/2+1) = sym(0);
    phi_2(Nx1/2+1,Nx2/2+1) = sym(0);
    phi_3(Nx1/2+1,Nx2/2+1) = sym(0);

    % Compute T0 using standard trapezoidal rule
    T0_1(i) = hx1*hx2*sum(sum(phi_1./r));
    T0_2(i) = hx1*hx2*sum(sum(phi_2./r));
    T0_3(i) = hx1*hx2*sum(sum(phi_3./r));

    % Compute correction coefficient
    ah(i) = sqrt(hx2^2+2-2*cos(hx1));

    % Refine grid for extrapolation
    Nx1 = Nx1*2; Nx2 = Nx2*2;
end

% Compute w0 with 16 decimals
w0_0 = (T0_1(2:end)-T0_1(1:end-1))./(ah(1:end-1)-ah(2:end));

for i = 1:5
w0_r = (2^(2*i)*w0_0(2:end)-w0_0(1:end-1))/(2^(2*i)-1);
w0_0=w0;
end

w0   = double(vpa(w0_0,16))

% Compute wc with 16 decimals
wc_0 = (T0_2(2:end)-T0_2(1:end-1))./(ah(1:end-1)-ah(2:end));

for i = 1:5
wc_r = (2^(2*i)*wc_0(2:end)-wc_0(1:end-1))/(2^(2*i)-1);
wc_0 = wc_r;
end

wc   = double(vpa(wc_0,16))

% Compute wz with 16 decimals
wz_0 = (T0_3(2:end)-T0_3(1:end-1))./(ah(1:end-1)-ah(2:end));

for i = 1:5
wz_r = (2^(2*i)*wz_0(2:end)-wz_0(1:end-1))/(2^(2*i)-1);
wz_0 = wz_r;
end

wz   = double(vpa(wz_0,16))
```

Appendix A Euler-Maclaurin formula

Theorem A.1 (Euler-Maclaurin expansion)**.** For a function $f \in C^{2p+2}([a,b])$

$$\begin{aligned}\int_a^b f(x)\mathrm{d}x =& T_h[f] + \sum_{\ell=1}^{p} \frac{h^{2\ell} b_{2\ell}}{(2\ell)!}(f^{(2\ell-1)}(b) - f^{(2\ell-1)}(a)) \\ &+ \frac{h^{2p+2}}{(2p+2)!} \int\limits_a^b B_{2p+2}\left(\left\{\frac{x-a}{h}\right\}\right) f^{(2p+2)}(x)\mathrm{d}x.\end{aligned} \tag{A.1}$$

The expression uses the Bernoulli polynomials B_p and the Bernoulli numbers defined as $b_p = B_p(0)$. The periodized versions $B_p(\{x\})$ are piecewise smooth and bounded functions, see Cohen [6, Proposition 9.3.1 and Remark 2] for more details.

From the Euler-Maclaurin expansion (A.1) we see that there are two main sources of errors in the trapezoidal rule

i) contribution to the error from the boundaries given by

$$\sum_{\ell=1}^{p} \frac{h^{2\ell} b_{2\ell}}{(2\ell)!}(f^{(2\ell-1)}(b) - f^{(2\ell-1)}(a)) \tag{A.2}$$

ii) contribution of the error which is determined by the regularity of the function

$$\frac{h^{2p+2}}{(2p+2)!} \int\limits_a^b B_{2p+2}\left(\left\{\frac{x-a}{h}\right\}\right) f^{(2p+2)}(x)\mathrm{d}x.$$

There are two common situations when the sum in (A.2) vanishes for integrands of class $C^{2p+2}(\mathbb{R})$

i) the integrand is periodic on $[a,b]$

ii) the integrand is compactly supported within (a,b)

In this case the error of the trapezoidal rule is $\mathcal{O}(h^{2p+2})$.

Appendix B Boundary corrections

Consider a one dimensional function f discretized on the interval $[0,\ a]$. The trapezoidal rule is then denoted as

$$T_h[f] = \sum_{i=0}^{N} \mathcal{W}_i(h) f(ih) \tag{B.1}$$

where $h = a/N$ and $\mathcal{W}(h) = [h/2,\ h, \dots, h,\ h/2]$. Following Alpert [3] correcting the boundaries of the trapezoidal rule can be performed using

$$\int_0^a f(x)\mathrm{d}x \approx= T_h[f] + \sum_{i=0}^{k-2} \beta_i [f(ih) + f(a - ih)] + \mathcal{O}(h^k) \tag{B.2}$$

for $k = 8$ we reproduce the values provided by Alpert $\beta_i = m_i h/d$ with $d = 120960$ and

$$\begin{aligned}&m_0 = -23681,\ m_1 = 55688,\ m_2 = -66109,\ m_3 = 57024,\\ &m_4 = -31523,\ m_5 = 9976,\ m_6 = -1375\ .\end{aligned}$$

To suit the purpose of the present work we define the corrected weights to be

$$\mathcal{W}^c = \mathcal{W}(h) + h[\beta_0, \ldots, \beta_{k-2},\ 0,\ \ldots,\ 0,\ \beta_{k-2}, \ldots, \beta_0]\ . \tag{B.3}$$

Appendix C Periodic Stokeslet

Using the Hasimoto decomposition the terms in (39) are given as

$$\Upsilon(\xi, \mathbf{x}) \quad = \quad C(\xi r)\frac{\mathbf{I}}{r} + D(\xi r)\frac{\hat{\mathbf{x}}\hat{\mathbf{x}}}{r}\ ,$$

with

$$C(\xi r) = \operatorname{erfc}(\xi r) - \frac{2\xi r}{\sqrt{\pi}}e^{-\xi^2 r^2}, \quad D(\xi r) = \operatorname{erfc}(\xi r) + \frac{2\xi r}{\sqrt{\pi}}e^{-\xi^2 r^2}$$

where we used the notation $\hat{\mathbf{x}} = \mathbf{x}/|\mathbf{x}|$, $r = |\mathbf{x}|$. The remainder $\tilde{\Upsilon}$ arises from

$$\tilde{\Upsilon}(\xi, \mathbf{x}) \quad = \quad \Upsilon(\xi, \mathbf{x}) - \mathbf{G}(\mathbf{x})\ ,$$

and to evaluate $\tilde{\Upsilon}(\xi, \mathbf{x})$ for $|\mathbf{x}| = 0$ we use the limit values

$$\lim_{|\mathbf{x}|\to 0}[\Upsilon(\xi, \mathbf{x}) - \mathbf{G}(\mathbf{x})] = -\frac{4\xi}{\sqrt{\pi}}.$$

The component to be evaluated in Fourier space is given by

$$\Phi(\xi, \mathbf{k}, \mathbf{x}) \quad = \quad B(\xi, \mathbf{k})e^{-k^2/4\xi^2}e^{-i\mathbf{k}\cdot\mathbf{x}}\ .$$

where for a wavenumber $\mathbf{k}$ is defined as $\mathbf{k} = \{2\pi(k_1/L_x,\ k_2/L_y,\ k_3/L_z),\ k_{i=1,\ldots,3} \in \mathbb{Z}\}$ and $k = |\mathbf{k}|$

$$B(\xi, \mathbf{k}) = 8\pi\left(1 + \frac{k^2}{4\xi^2}\right)\frac{1}{k^4}(k^2\mathbf{I} - \mathbf{k}\mathbf{k})\ . \tag{C.1}$$

References

[1] J. C. Aguilar. High-order corrected trapezoidal quadrature rules for functions with a logarithmic singularity on a circle. *Int. J. Contemp. Math. Sciences*, 3(23):1133–1140, 2008.

[2] J. C. Aguilar and Y. Chen. High-order corrected trapezoidal quadrature rules for the Coulomb potential in three dimensions. *Comput. Math. Appl.*, 49:625–631, 2005.

[3] B. K. Alpert. High-order quadratures for integral operators with singular kernels. *J. Comput. Appl. Math.*, 60:367–378, 1995.

[4] K. Atkinson. Quadrature of singular integrands over surfaces. *Electron. T. Numer. Ana.*, 17:133–150, 2004.

[5] C. W. J. Beenakker. Ewald sums of the Rotne-Prager tensor. *J. Chem. Phys.*, 85:1581–1582, 1986.

[6] H. Cohen. *Number Theory. Vol. II. Analytic and Modern Tools.* Springer, New York, U.S.A., 2007.

[7] L. M. Delves and J. E. Walsh. *Numerical Solution of Integral Equations.* Clarendon Press, Oxford, U.K., 1974.

[8] G. H. Golub and C. F. Van Loan. *Matrix Computations.* Johns Hopkins University Press, Baltimore, U.S.A., 1996.

[9] K. Gustavsson and A.-K. Tornberg. Gravity induced sedimentation of slender fibers. *Phys. Fluids*, 21(123301), 2009.

[10] R. Hamming. *Numerical Methods for Scientists and Engineers.* Dover Publications, Mineola, U.S.A., 1987.

[11] J. Happel and H. Brenner. *Low Reynolds Number Hydrodynamics.* Kluwer, Dordrecht, The Netherlands, 1983.

[12] H. Hasimoto. On the periodic fundamental solutions of the Stokes equations and their application to viscous flow past a cubic array of spheres. *J. Fluid Mech.*, 5:317–328, 1959.

[13] J. D. Jackson. *Classical Electrodynamics.* Wiley & Sons, Hoboken, U.S.A., 1998.

[14] R. E. Kleinman and G. F. Roach. Boundary integral equations for the three-dimensional Helmholtz equation. *SIAM Rev.*, 16(2):214–236, 1974.

[15] R. Kress. *Linear Integral Equations.* Springer, New York, U.S.A., 1999.

[16] O. Marin, K. Gustavsson, and A.-K. Tornberg. A highly accurate boundary treatment for confined Stokes flow. *Comput. Fluids*, 66:215–230, 2012.

[17] O. Marin, O. Runborg, and A.-K. Tornberg. Corrected trapezoidal rules for a class of singular functions. Paper 1 in this thesis, 2012.

[18] C. Pozrikidis. *Boundary Integral and Singularity Methods for Linearized Viscous Flow.* Cambridge University Press, Cambridge, U.K., 1992.

[19] C. Pozrikidis. Computation of periodic Green's functions of Stokes flow. *J. Eng. Math.*, 30(4):79–96, 1996.

[20] C. Pozrikidis. *A Practical Guide to Boundary-Element Methods with the Software Library BEMLIB.* Chapman & Hall/CRC Press, 2002.

[21] C. Pozrikidis. Computation of Stokes flow due to the motion or presence of a particle in a tube. *J. Eng. Math.*, 53:1–20, 2005.

[22] C. Pozrikidis. Numerical simulation of cell motion in tube flow. *Ann. Biomed. Eng.*, 33:165–178, 2005.

[23] V. Rokhlin. Endpoint corrected trapezoidal quadrature rules for singular functions. *Comput. Math. Appl.*, 20:51–62, 1990.

[24] A. Sidi. Application of class $\mathcal{S}$m variable transformations to numerical integration over surfaces of spheres. *J. Comput. Appl. Math.*, 184:475–492, 2005.

[25] A.-K. Tornberg and K. Gustavsson. A numerical method for simulations of rigid fiber suspensions. *J. Comput. Phys.*, 215:172–196, 2005.